



I. R. IRAN

ISSN: 2423-7167

e-ISSN: 1735-9244



International Journal of Engineering

Journal Homepage: www.ije.ir



TRANSACTIONS C: Aspects

Volume 34, Number 03, March 2021

Materials and Energy Research Center

INTERNATIONAL JOURNAL OF ENGINEERING

Transactions C: Aspects

DIRECTOR-IN-CHARGE

A. R. Khavandi

EDITOR-IN-CHIEF

G. D. Najafpour

ASSOCIATE EDITOR

A. Haerian

EDITORIAL BOARD

- | | | | |
|------|--|-------|---|
| S.B. | Adeloju, Charles Sturt University, Wagga, Australia | A. | Mahmoudi, Bu-Ali Sina University, Hamedan, Iran |
| K. | Badie, Iran Telecomm. Research Center, Tehran, Iran | O.P. | Malik, University of Calgary, Alberta, Canada |
| M. | Balaban, Massachusetts Ins. of Technology (MIT), USA | G.D. | Najafpour, Babol Noshirvani Univ. of Tech., Babol, Iran |
| M. | Bodaghi, Nottingham Trent University, Nottingham, UK | F. | Nateghi-A, Int. Ins. Earthquake Eng. Seis., Tehran, Iran |
| E. | Clausen, Univ. of Arkansas, North Carolina, USA | S. E. | Oh, Kangwon National University, Korea |
| W.R. | Daud, University Kebangsaan Malaysia, Selangor, Malaysia | M. | Osanloo, Amirkabir Univ. of Tech., Tehran, Iran |
| M. | Ehsan, Sharif University of Technology, Tehran, Iran | M. | Pazouki, Material and Energy Research Center, Meshkindasht, Karaj, Iran |
| J. | Faiz, Univ. of Tehran, Tehran, Iran | J. | Rashed-Mohassel, Univ. of Tehran, Tehran, Iran |
| H. | Farrahi, Sharif University of Technology, Tehran, Iran | S. K. | Sadrnezhaad, Sharif Univ. of Tech, Tehran, Iran |
| K. | Firoozbakhsh, Sharif Univ. of Technology, Tehran, Iran | R. | Sahraeian, Shahed University, Tehran, Iran |
| A. | Haerian, Sajad Univ., Mashhad, Iran | A. | Shokuhfar, K. N. Toosi Univ. of Tech., Tehran, Iran |
| H. | Hassanpour, Shahrood Univ. of Tech., Shahrood, Iran | R. | Tavakkoli-Moghaddam, Univ. of Tehran, Tehran, Iran |
| W. | Hogland, Linnaeus Univ, Kalmar Sweden | T. | Teng, Univ. Sains Malaysia, Gelugor, Malaysia |
| A.F. | Ismail, Univ. Tech. Malaysia, Skudai, Malaysia | L. J. | Thibodeaux, Louisiana State Univ, Baton Rouge, U.S.A |
| M. | Jain, University of Nebraska Medical Center, Omaha, USA | P. | Tiong, Nanyang Technological University, Singapore |
| M. | Keyanpour rad, Materials and Energy Research Center, Meshkindasht, Karaj, Iran | X. | Wang, Deakin University, Geelong VIC 3217, Australia |
| A. | Khavandi, Iran Univ. of Science and Tech., Tehran, Iran | | |

EDITORIAL ADVISORY BOARD

- | | | | |
|-------|--|-------|--|
| S. T. | Akhavan-Niaki, Sharif Univ. of Tech., Tehran, Iran | A. | Kheyroddin, Semnan Univ., Semnan, Iran |
| M. | Amidpour, K. N. Toosi Univ of Tech., Tehran, Iran | N. | Latifi, Mississippi State Univ., Mississippi State, USA |
| M. | Azadi, Semnan university, Semnan, Iran | H. | Oraee, Sharif Univ. of Tech., Tehran, Iran |
| M. | Azadi, Semnan University, Semnan, Iran | S. M. | Seyed-Hosseini, Iran Univ. of Sc. & Tech., Tehran, Iran |
| F. | Behnamfar, Isfahan University of Technology, Isfahan | M. T. | Shervani-Tabar, Tabriz Univ., Tabriz, Iran |
| R. | Dutta, Sharda University, India | E. | Shirani, Isfahan Univ. of Tech., Isfahan, Iran |
| M. | Eslami, Amirkabir Univ. of Technology, Tehran, Iran | A. | Siadat, Arts et Métiers, France |
| H. | Hamidi, K.N.Toosi Univ. of Technology, Tehran, Iran | C. | Triki, Hamad Bin Khalifa Univ., Doha, Qatar |
| S. | Jafarmadar, Urmia Univ., Urmia, Iran | S. | Hajati, Material and Energy Research Center, Meshkindasht, Karaj, Iran |
| S. | Hesaraki, Material and Energy Research Center, Meshkindasht, Karaj, Iran | | |

TECHNICAL STAFF

M. Khavarpour; M. Mohammadi; V. H. Bazzaz, R. Esfandiar; T. Ebadi

DISCLAIMER

The publication of papers in International Journal of Engineering does not imply that the editorial board, reviewers or publisher accept, approve or endorse the data and conclusions of authors.

CONTENTS:

Transactions C: Aspects

Chemical Engineering

A. Aminmahalati; Investigating the Performance of CO Boiler Burners in the 587-597
A. Fazlali; RFCC Unit with CFD Simulation
H. Safikhani

A. Poormohammadi; Photocatalytic removal of toluene from gas stream using 598-605
Z. Ghaedrahmat; chitosan/AgI-ZnO Nanocomposite fixed on glass bed
M. Ahmad Moazam; under UVA irradiation
N. Jaafarzadeh;
M. Enshayi;
N. Sharifi

Civil Engineering

M. Dadashi Haji; The Effects of BIM Maturity Level on the 4D Simulation 606-614
H. Taghaddos; Performance: An Empirical Study
M.H. Sebt;
F. Chokan;
M. Zavari

F. Marchione Enhancement of Stiffness in GFRP Beams by Glass 615-620
Reinforcement

S. Svergzova; Application of Sorbent Waste Material for Porous 621-628
N. Miroshnichenko; Ceramics Production
I. Shaikhiev;
Z. Sapronova;
E. Fomina;
N. Shakurova;
V. Promakhov

C. Jithendra; Parametric Effects on Slump and Compressive Strength 629-635
S. Elavenil Properties of Geopolymer Concrete using Taguchi Method

B.A. Mir; Mechanical Behaviour of Nano-material (Al₂O₃) 636-643
S.H. Reddy Stabilized Soft Soil

H. Y. Khudhaire; Management of Abandoned Construction Projects in Iraq 644-649
H. I. Naji Using BIM Technology

Electrical & Computer Engineering

R. Badaghei; Detection of Bikers without Helmet Using Image Texture 650-655
H. Hassanpour; and Shape Analysis
T. Askari

S.R. Salehinai; E. Afjei; A. Hekmati; H. Aghazadeh	Design Procedure of an Outer Rotor Synchronous Reluctance Machine for Scooter Application	656-666
J. Tavoosi; A. Mohammadzadeh	A New Recurrent Radial Basis Function Network-based Model Predictive Control for a Power Plant Boiler Temperature Control	667-675
Z. Nejati; A. Faraj	Actuator Fault Detection and Isolation for Helicopter Unmanned Aerial Vehicle in the Presence of Disturbance	676-681
Industrial Engineering		
A. Torabi; H. Hamidi; N. Safaie	Effect of Sensory Experience on Customer Word-of-mouth Intention, Considering the Roles of Customer Emotions, Satisfaction, and Loyalty	682-699
Material Engineering		
M.R. Shojaei; G.R. Khayati; N. Assadat Yaghubi; F. Bagheri Sharebabaki; S.M.J Khorasani	Removing of Sb and As from Electrolyte in Copper Electrorefining Process: A Green Approach	700-705
Mechanical Engineering		
E. Mohagheghpour; M. M. Larijani; M. Rajabi; R. Gholamipour	Effect of Silver Clusters Deposition on Wettability and Optical Properties of Diamond-like Carbon Films	706-713
A. Jabbar Hassan; T. Boukharouba; D. Miroud; N. Titouche; S. Ramtani	Direct Drive Friction Welding Joint Strength of AISI 304	714-720
H. Kohestani; R. Ezoji	Synthesis and Characterization of TiO ₂ /CuO/WO ₃ Ternary Composite and its Application as Photocatalyst	721-727
A. Mahmoodian; M. Durali; M. Saadat; T. Abbasian	A Life Clustering Framework for Prognostics of Gas Turbine Engines under Limited Data Situations	728-736
B. Meyghani; M. Awang; S. Emamian	Introducing an Enhanced Friction Model for Developing Inertia Welding Simulation: A Computational Solid Mechanics Approach	737-743

A. Assadi; M. Nazemizadeh	Size-dependent Vibration Analysis of Stepped Nanobeams Based on Surface Elasticity Theory	744-749
--	--	---------

Petroleum Engineering

M. A. Guzev; E. V. Kozhevnikov; M. S. Turbakov; E. P. Riabokon; V. V. Poplygin	Experimental Investigation of the Change of Elastic Moduli of Clastic Rocks under Nonlinear Loading	750-755
---	--	---------



Evaluating the Performance of CO Boiler Burners in RFCC Unit using CFD Simulation

A. Aminmahalati^a, A. Fazlali^{*a}, H. Safikhani^b

^a Department of Chemical Engineering, Faculty of Engineering, Arak University, Arak, Iran

^b Department of Mechanical Engineering, Faculty of Engineering, Arak University, Arak, Iran

PAPER INFO

Paper history:

Received 27 December 2020

Received in revised form 10 January 2021

Accepted 16 January 2021

Keywords:

CFD

Simulation

CO boiler

Mechanisms

Combustion

ABSTRACT

The combustion chamber's internal refractory in Imam Khomeini Oil Refinery Company (IKORC) was damaged in several parts, requiring operating conditions and re-inspecting the design of the combustion chamber using CFD. Simplify the combustion chamber 3D simulation, decrease in the number of calculations, the symmetry principle was applied in the simulation. The results, independent of the mesh network, were investigated via increasing the mesh nodes. The one-stage, two-stage, multi-stage and overall mechanisms, which were designated, were examined and compared to actual measured data and a calculation error of less than 8% was obtained. Ultimately, selecting overall mechanisms, the simulation results, streams mixing and length of the chamber were scrutinized, and as a result, the current design was approved. The temperature and velocity of the flows in the combustion chamber were investigated. In the combustion chamber, the farther we are from the burners, the more uniform the velocity and temperature profiles also become as the wall temperature increases. The rate of combustion reaction was evaluated with the temperature of different points in the combustion chamber. The results showed that the combustion chamber wall's temperature is in the appropriate range and has not suffered any thermal damage. Unlike the combustion chamber wall, the burner wall (at the mixing point) has an unauthorized temperature; there is the possibility of thermal damage that can be eliminated by changing the number of currents. Unsuitable thermal profiles also showed large amounts of oxygen in the exhaust gas indicated that the steam boiler performance is far from the optimal condition and specific changes would be required in the air streams. Streamline demonstrated that the primary air stream was more effective for decreasing CO and NO_x amounts in the outlet stream. The secondary air stream was also significant to prevent thermal damage to the internal coating and reduce safety hazards.

doi: 10.5829/ije.2021.34.03c.01

1. INTRODUCTION

The increasing rate of fossil fuel consumption, such as coal, crude oil and natural gas, followed by a gradual reduction in their reservoirs, has become one of the most controversial contemporary issues. Exhausting fossil fuels harm the environment and cause significant environmental damages. Their consumption leads to CO₂ and CO production, and consequently, a continuous increase in greenhouse gas emissions. Despite the highly damaging impacts of CO₂ on global warming, the effects of CO are negligible. Nevertheless, it is noteworthy to mention that CO has significant indirect impacts. It reacts

with the OH-radicals in the atmosphere, which behaves as an inhibitor for greenhouse gases, such as methane. Also, CO can boost the formation of Ozone [1]. Therefore, more improvement is vital in combustion technologies and processes [2].

There are several different codes for numerical calculations. These codes can generally be classified into LP codes and Computational Fluid Dynamics (CFD) codes. The significant advantage of CFD codes is their capability to model the turbulent flows and complex geometries. However, the most significant impediment of this class is their high computational costs. On the other hand, LP codes are suited to handle merely simple

Corresponding Author Institutional Email: a-fazlali@araku.ac.ir (A. Fazlali)

Please cite this article as: A. Aminmahalati, A. Fazlali, H. Safikhani, Investigating the Performance of CO Boiler Burners in the RFCC Unit with CFD Simulation, International Journal of Engineering, Transactions C: Aspects Vol. 34, No. 03, (2021) 587-597

geometries and their biggest strength lies in their capability of running the equation fast [3]. For example, CFD codes and other simulation methods have been used to research references [4-11]. In CFD, we attempt to model combustion utilizing simple reaction models because detailed chemical reaction mechanisms are composed of hundreds of species and side reactions that cannot accommodate reasonable costs. Moreover, an increase in the number of different reaction mechanisms adds to the overall modeling complexity [2].

According to the inherent intricacy of interaction among turbulency, combustion, convection, radiation, buoyancy and compressibility of gases, CFD combustion modeling is a complex subject. This complexity rises specifically in large chambers when natural, or forced convection must be considered. Thus, CFD combustion modeling requires being validate using physical and empirical results. Validation of CFD codes promotes certainty of users in its forecast precision. Modeling validation is of significance regarding complicated cases. However, validation tests are not applicable since they are costly and challenging to be implemented [12]. CFD focus and strength have been on predicting reaction structure, temperature, velocity and not the emission of pollutants [2].

In the oil refinery's RFCC units, a 700-800°C gaseous phase flows out of the regeneration unit. It carries less than 5% of CO and the rest includes N₂, H₂O and CO₂, which is called flue gas [12].

CO burns with fuel gas in CO boilers, generating a vast amount of heat. Hot gases from combustion are then cooled down via heat exchangers using cooling water in tubes. This interaction leads to superheated steam production and the utility units can apply the steam. Refineries deal with significant daily steam demands. Accordingly, the CO boiler steam production can mainly cut the costs down. Since then, CO boilers play a pivotal role in the RFCC process [12].

The CO boiler internal wall is installed to protect the refractory from thermal damages. The CO boiler temperature can rise to 1200°C. Furthermore, this may cause internal/external damages; for instance, high temperatures can damage central refractories [12].

A typical CO boiler generates up to 300 tons of steam per hour. This production annually reduces the expenses in the refinery by 68 million dollars [13]. The CO boiler maintenance, inspection and shut down have substantial consequences in the RFCC process and any damage would lead to a loss of 1 million dollars per day. Also, possible threats to human and environmental safety are crucial when the CO boiler is shut down [12-14]

The present study was conducted to investigate the combustion chamber performance and its effects on the refractory's internal wall. The above-mentioned CO boiler produces 270 tons of high-pressure steam an hour, RFCC unit in Imam Khomeini Oil Refinery Company

(IKORC). Two combustible streams of fuel gas and flue gas flow into the chamber. Fuel gas stream is composed of butane and lighter gases. Table 1 represents the property details of this stream .The flue gas stream is the regeneration unit output and it contains 1.25% of carbon monoxide and a small amount of oxygen and other non-combustible compounds. The required oxygen is supplied with two air streams. The required oxygen is supplied with two air streams (primary and secondary air). Table 1 contains all the mentioned streams in detail. The flue gas stream has a high temperature (702°C) and the other three streams (fuel gas, primary and secondary air) enter the combustion chamber at a temperature close to the environment. The output streamline from the combustion chamber enters the steam generator heat exchanger and its temperature is important in the amount of steam production [15].

Once the CO boiler is not in service, in addition to the enormous energy loss, a considerable amount of CO is released into the environment. Therefore, timely diagnosis and proper maintenance of internal walls in the CO boiler will decrease possible maintenance and prevent environmental pollution. The flowchart used for this research is shown in Figure 1.

Significant damages have been spotted in the refractory cover of the walls. In case of a lack of diagnosis regarding the damages, financial losses are expected, and wall ruptures may lead to operators' casualties. In this work, the chamber's flame profile was investigated and the reason for the current damages was represented. This study focuses specifically on the flame in the combustion chamber and examines its effects in the combustion chamber, especially its walls exhaust gas compositions and It also investigates the effect of flame on combustion gas compositions. In other words,

TABLE 1. Properties and components of the chamber inlet streamlines

	Unit	Flue gas	Fuel gas	Primary Air	Secondary air	
Flow	kg/s	34.2	0.41	6.5	6.5	
Temperature	C	702	60	50	50	
Compounds of constituent	H₂	%	-	13.6	-	-
	CH₄	%	-	65.22	-	-
	C₂H₆	%	-	5.16	-	-
	C₃H₈	%	-	3.24	-	-
	C₄H₁₀⁺	%	-	1.86	-	-
	CO	%	1.25	-	-	-
	CO₂	%	17.22	0.33	-	-
	N₂	%	80.3	10.59	79.81	79.81
O₂	%	0.13	-	20.19	20.19	

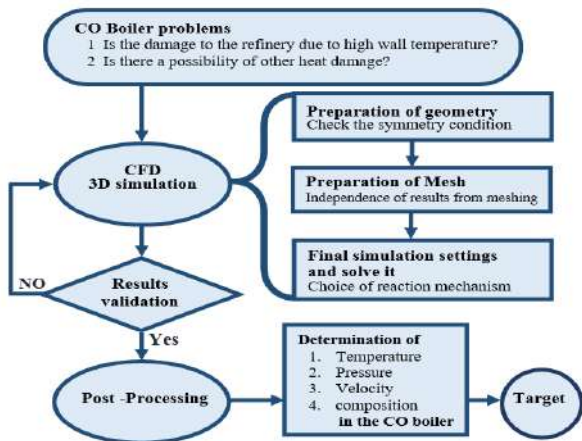


Figure 1. Flowchart of the methodology used in the present work

this study seeks to understand better the effects of flame in the combustion chamber and ways to improve the economic and environmental performance of the CO boiler.

2. BURNER MODELING

2.1. Physical Model As illustrated in Figure 2, the combustion chamber is a 900 m³ cylinder with three identical burners, in which three similar sets of burners are installed. Each group consists of 9 smaller burners, one in the center and the rest are located in the chamber circumference.

Due to the large volume of the chamber, a numerous mesh network is required. The symmetrical principles are significantly applied to cut down the simulation model volume. As shown in Figure 3, splitting the chamber into three subdivisions, streams in each burner set are not

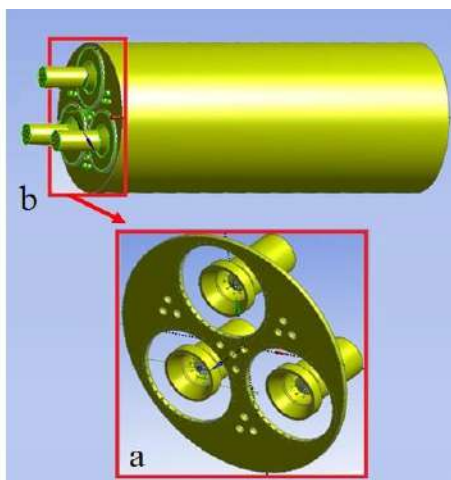


Figure 2. Stimulated boiler combustion chamber a) Overall view b) Burners zone

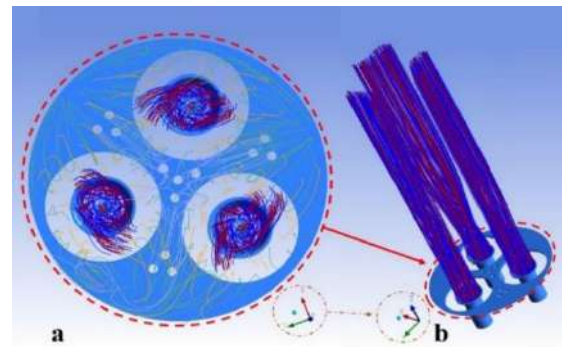


Figure 3. Co boiler streamlines. a) Streamlines overall view b) Fuel gas and primary air streamlines

intermixed. The smaller volume, there is to model, the denser the mesh network we will get. Figure 3 illustrates all the streamlines of the steam boiler. Figure 3.a indicates streamlines and symmetrical principle effects, and Figure 3.b represents the primary air and the fuel gas streams. According to Figure 3, it can be concluded that no stream intermix occurs.

Figure 4 shows all the entering streams to the chamber. Figure 4.a represents the combustion chamber, and Figure 4.b demonstrates the inlet section of the chamber. Flue gas is sprayed from the periphery of the torch, shown as α in yellow. The primary air streams inflow the burners from internal rings, while the external rings and holes located at the outer ring circumference supply the secondary air. Due to the symmetry of the combustion chamber, one-third of the combustion chamber is modeled. The secondary air is divided into two parts; part one is in the form of external rings around flue gas, depicted as the thin rings as shown β in blue in

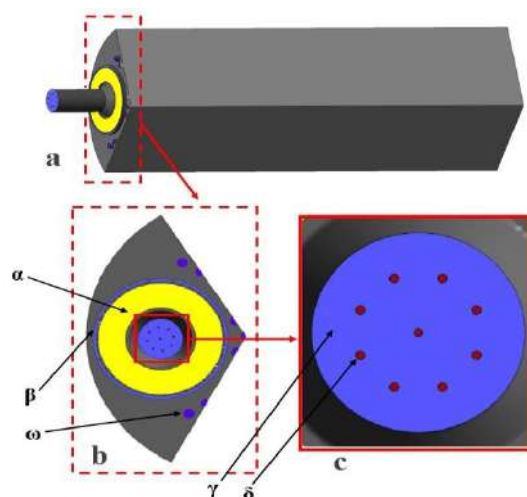


Figure 4. Simulated chamber inlet streamlines a) Overall view of the combustion chamber, b) magnified view of the inlets and c) magnified view of the inlets to the burner α -Inlet Flue gas, β -Internal ring: primary air inlet, ω -External ring and holes: secondary air inlets, γ -Primary air, δ -Inlet fuel gas

Figure 4.b. The part two ,consists of small circles shown as ω in blue. The primary air stream is illustrated in Figures 4.b and 4.c. It is shown to be charged to the burner center represented as γ in blue. The input venue for fuel gas includes nine small circles represented in Figure 4.c as δ in red.

As illustrated in Figure 5, the wall temperature was of the maximum error. When we do calculations with 3 million, this error progressively decreased to 1%. Other variable deviation errors in this node number were less than 0.3%. With the increase in mesh nodes up to 6 million, all the errors decreased to below 0.1%. Table 2 shows important information about meshing, including simulation volume, the maximum and minimum size of each mesh, the growth rate of mesh size, number of nodes and number of elements.

2. 2. Numerical Method

The ANSYS/CFX v19.0 software was used for CFD simulations by solving the numerical simulation carried out on a supercomputer with Intel Xeon CPU E5-2630L V2(2.4 GHz * 8 CPUs, 30 GB RAM). The mathematical modeling in this study is based on a steady-state condition. The turbulence equation is standard k- ϵ [16-18]. The buoyancy force was neglected in the gas type and steam boiler horizontal geometry, following the simulation results. Three different heat transfer governing equations are optionally available. Meanwhile, due to combustion reaction nature and high fluid temperature variations, the overall energy governing equation was designated.

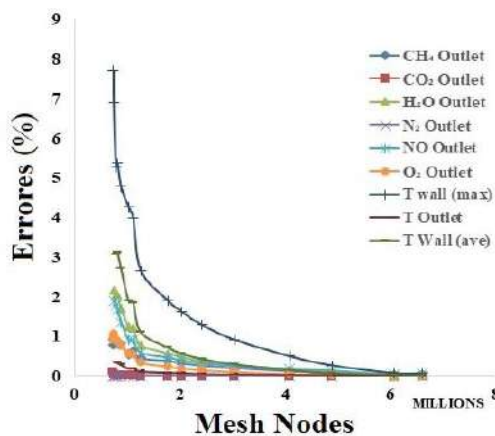


Figure 5. Mesh network independency deviation (major variables deviation) vs. nodes number

TABLE 2. Important information about meshing, which is: simulation volume, the maximum and minimum size of each mesh, the growth rate of mesh size, number of nodes and number of elements

Volume (m ³)	Max face size (mm)	Min size (mm)	Growth rate	NO. nodes	NO. elements
290.68	25	1	1.2	6.17e+6	3.45e+7

Typical and defined reactions in the simulation must cover combustions of methane, butane, ethane, propane, CO and H₂. Accordingly, the three mechanisms are suggested as follows: One-stage, two-stage and multi-stage reaction mechanism. Westbrook and Dryer [34] proposed several simplified reaction mechanisms for the oxidation of fuels, namely the WD one-step (WD1), WD two-step (WD2) and multi-step with Water-Gas Shift reaction (WGS) mechanisms. Table 3 shows the different mechanisms used for the combustion reaction in the CO boiler. All the three mechanisms, as mentioned earlier, were applied in different simulations separately; meanwhile, the fourth simulation was applied with all the mechanisms simultaneously. A brief literature review is presented in Table 4 concerning the combustion reactions in the three mechanisms.

Generally, thermal radiation with different models was studied and here, model P1 is considered [35-37]. P1 is a simple and accurate model and suitable for simulating large objects.

3. MODEL VALIDATION

Validation was confirmed by adapting actual and empirical temperature and analysis of steam boiler exhaust gases with results calculated by the simulation. Four thermometers were set up on the steam boiler. The control system gathered the mean temperature data as one of the significant parameters to control the combustion chamber. Actual and calculated temperatures are listed in Table 5. The thermometers were installed in one direction with the same distance to burners. Figure 6 illustrates the direction of the thermometer. Figure 7 simulates the thermometer's changes in the thermometer's direction. The simulation shows that it can be observed that the maximum temperature difference in the thermocouple direction was 21°C. If an accurate thermometers show more difference, they are damaged. The simulation shows that The difference between the average of the wall temperatures and the average temperature of the exhaust gas was less than 8°C. Therefore, the average of the wall temperatures is a desirable criterion for estimating the outlet temperature.

Table 5 represents the compared values for the exhaust gas analysis and four simulated reaction mechanisms. The experimental values were dry-based. The listed result in Table 5 indicates that the overall reaction mechanism results are closer to the real data. Defining the error function below (Equation (1)), the simulation's temperature error for combining mechanisms was less than 6%; however, each mechanism's deviation was estimated to be less than 7%.

$$Error = \frac{(Real\ Data - Simulation\ data)}{Real\ Data} \tag{1}$$

TABLE 3. Single-stage, two-stage and multi-stage reaction mechanisms in CO boiler

	One-stage reactions (WD1)	Two-stage reactions (WD2)	Multi-stage reactions (WGS)
Butane	$C_4H_{10} + 6.5O_2 \xrightarrow{k[O_2]^{1.6}[C_4H_{10}]^{0.15}} 4CO_2 + 5H_2O$	$C_4H_{10} + 4.5O_2 \xrightarrow{k[O_2]^{1.6}[C_4H_{10}]^{0.15}} 4CO + 5H_2O$ $CO + 0.5O_2 \xrightarrow[k[H_2O]^{0.5}[O_2]^{0.25}]{H_2O} CO_2$	$C_4H_{10} + 2O_2 \xrightarrow{k[O_2]^{1.6}[C_4H_{10}]^{0.15}} 4CO + 5H_2$ $CO + 0.5O_2 \xrightarrow[k[CO][H_2O]^{0.5}[O_2]^{0.25}]{H_2O} CO_2$ $H_2 + 0.5O_2 \longrightarrow H_2O$ $CO + H_2O \longleftrightarrow CO_2 + H_2$
Propane	$C_3H_8 + 5O_2 \xrightarrow{k[O_2]^{1.65}[C_3H_8]^{0.1}} 3CO_2 + 4H_2O$	$C_3H_8 + 3.5O_2 \xrightarrow{k[O_2]^{1.65}[C_3H_8]^{0.1}} 3CO + 4H_2O$ $CO + 0.5O_2 \xrightarrow[k[CO][H_2O]^{0.5}[O_2]^{0.25}]{H_2O} CO_2$	$C_3H_8 + 1.5O_2 \xrightarrow{k[O_2]^{1.65}[C_3H_8]^{0.1}} 3CO + 4H_2$ $CO + 0.5O_2 \xrightarrow[k[CO][H_2O]^{0.5}[O_2]^{0.25}]{H_2O} CO_2$ $H_2 + 0.5O_2 \longrightarrow H_2O$ $CO + H_2O \longleftrightarrow CO_2 + H_2$
Ethane	$C_2H_6 + 3.5O_2 \xrightarrow{k[O_2]^{1.65}[C_2H_6]^{0.1}} 2CO_2 + 3H_2O$	$C_2H_6 + 2.5O_2 \xrightarrow{k[O_2]^{1.65}[C_2H_6]^{0.1}} 2CO_2 + 3H_2O$ $CO + 0.5O_2 \xrightarrow[k[CO][H_2O]^{0.5}[O_2]^{0.25}]{H_2O} CO_2$	$C_2H_6 + O_2 \xrightarrow{k[O_2]^{1.65}[C_2H_6]^{0.1}} 2CO + 3H_2$ $CO + 0.5O_2 \xrightarrow[k[CO][H_2O]^{0.5}[O_2]^{0.25}]{H_2O} CO_2$ $H_2 + 0.5O_2 \longrightarrow H_2O$ $CO + H_2O \longleftrightarrow CO_2 + H_2$
Methane	$CH_4 + 2O_2 \xrightarrow{k \frac{[O_2]^{1.3}}{[CH_4]^{0.3}}} CO_2 + 2H_2O$ $0.5N_2 + 0.5O_2 \xrightarrow{k[N_2][CH_4][O_2]^{0.5}} NO$ $N_2 + O_2 \xrightarrow{k[N_2][O_2]^{0.5}} 2NO$	$CH_4 + 1.5O_2 \xrightarrow{k \frac{[O_2]^{1.3}}{[CH_4]^{0.3}}} CO + 2H_2O$ $CO + 0.5O_2 \xrightarrow[k[CO][H_2O]^{0.5}[O_2]^{0.25}]{H_2O} CO_2$ $0.5N_2 + 0.5O_2 \xrightarrow{k[N_2][CH_4][O_2]^{0.5}} NO$ $N_2 + O_2 \xrightarrow{k[N_2][O_2]^{0.5}} 2NO$	$CH_4 + 0.5O_2 \xrightarrow{k \frac{[O_2]^{1.3}}{[CH_4]^{0.3}}} CO + 2H_2$ $CO + 0.5O_2 \xrightarrow[k[CO][H_2O]^{0.5}[O_2]^{0.25}]{H_2O} CO_2$ $H_2 + 0.5O_2 \longrightarrow H_2O$ $CO + H_2O \longleftrightarrow CO_2 + H_2$ $0.5N_2 + 0.5O_2 \xrightarrow{k[N_2][CH_4][O_2]^{0.5}} NO$ $N_2 + O_2 \xrightarrow{k[N_2][O_2]^{0.5}} 2NO$
Monoxide Carbone	$CO + 0.5O_2 \xrightarrow[k[CO][H_2O]^{0.5}[O_2]^{0.25}]{H_2O} CO_2$	$CO + 0.5O_2 \xrightarrow[k[CO][H_2O]^{0.5}[O_2]^{0.25}]{H_2O} CO_2$	$CO + 0.5O_2 \xrightarrow[k[CO][H_2O]^{0.5}[O_2]^{0.25}]{H_2O} CO_2$
Hydrogen	$H_2 + 0.5O_2 \longrightarrow H_2O$	$H_2 + 0.5O_2 \longrightarrow H_2O$	$H_2 + 0.5O_2 \longrightarrow H_2O$

TABLE 4. Brief literature review

NO.	The subject under study	Power (MW)	WD1	WD2	WGS	Ref.
1	circulating fluidized bed (CFB) boiler	660	✓			[19]
2	circulating fluidized bed (CFB) boiler	350	✓			[20]
3	ultra-supercritical BP 680 boiler	200		✓		[21]
4	pulverized coal boilers	160		✓	✓	[22]
5	biomass boilers	35		✓		[23]
6	circulating fluidized bed (CFB) boiler	12	✓			[24]
7	reciprocating grate boiler	4		✓		[25]
8	oxy-fuel combustion with pulverized coal	2.5			✓	[26]
9	biomass combustion	0.3			✓	[27]
10	MILD combustion furnace	0.02		✓	✓	[28]
11	residential furnace	0.015			✓	[29]

12	Moderate or intense low-oxygen dilution (MILD) combustion	.0130			✓	[30]
13	combustion in a bubbling fluidized bed	-	✓	✓	✓	[31]
14	Flameless Combustion	-		✓		[2]
15	swirled burner combustion	-		✓		[32]
16	industrial low swirl burner combustion	-		✓		[1]
17	rocket combustor	-		✓		[33]
18	explosions in straight large-scale tunnels	-	✓			[17]

TABLE 5. Compared values for exhaust gas and simulated exhaust gas

Compounds	T	O ₂	CO ₂	CO
Units	°C	%	%	ppm
WD1	806.94	6.32	18.412	1

WD2	807.80	6.33	18.388	2.3
WDG	807.75	6.32	18.39	2.9
Combined Mechanisms	799.23	6.32	18.386	0.6
Real results	757	6.6	17.8	4

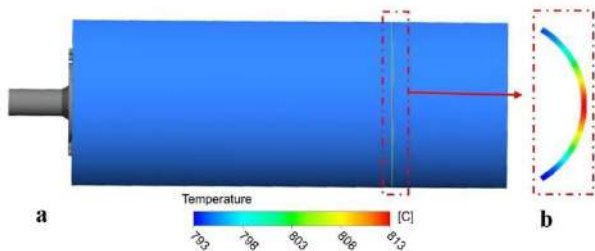


Figure 6. Thermometers' direction in the chamber. a) Overall view and thermometers direction location and b) temperature profile in the direction in the chamber

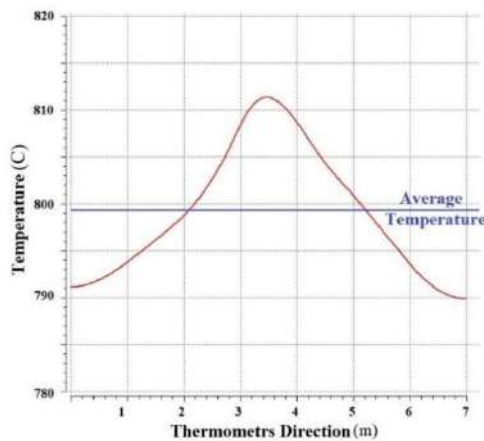


Figure 7. The temperature changes thermometers direction and averages them

Reporting stream flow in the chamber shows that the error rate of 5% is acceptable for industrial flow meters. We attempted to reduce this error by accurate calibration. This error was under 8% for CO₂ and O₂ and since the CO amount was negligible, the error function would not be a suitable option.

4. RESULTS AND DISCUSSIONS

Different streams flow in different combustion chamber sectors, which causes the flow profile to form in the combustion chamber. Combustion causes the temperature change, resulting in an amendment in the gases' velocity inside the combustion chamber. Figure 8 represents the velocity changes in the chamber, which is composed of three parts. In the upper and lower parts, the

velocity profile is shown in the cross-section, while the middle part of the figure indicates the middle section of the chamber. Additionally, each of the cross-sections is pointed out in the middle section. Figure 8 indicates that the maximum velocity was observed in burner exhausts and that the closer we got to the end of the chamber, the more uniform flow we had.

Figure 9 illustrates the wall temperature for all four mechanisms. As can be seen, the three mechanisms' general profiles were almost the same, yet it was different for the overall mechanism profile. Moreover, the reaction temperature increased as we got closer to the end of the chamber.

Temperature changes in the combustion chamber's flames can be seen through its few cross-sections in Figure 10. Figure 10 shows that firstly, the heat accumulated in the center, and then, by moving away

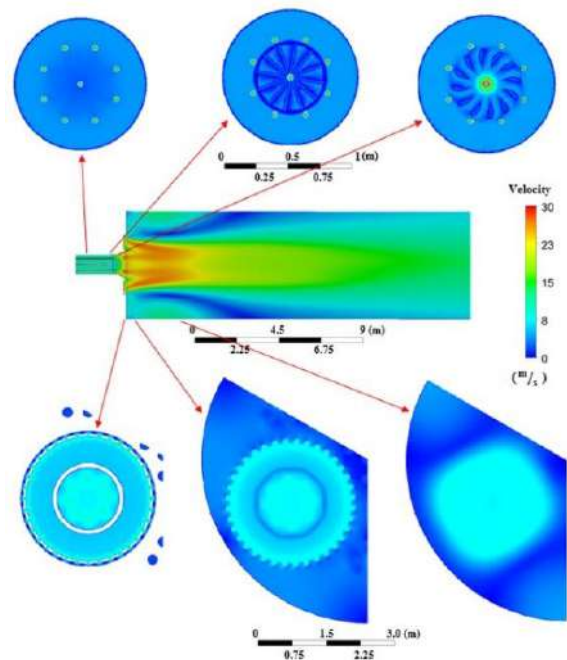


Figure 8. The velocity profiles in different cross-sections in the chamber

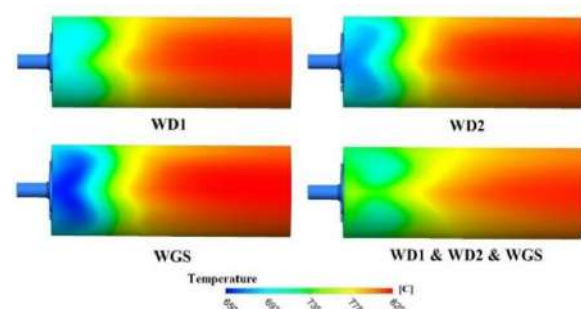


Figure 9. The chamber walls temperature profiles in different mechanisms

from the burners, the intermixing of flows reduces the temperature difference. As it can be seen in Figure 10, the burner's wall temperature increased and our calculations revealed that this temperature could reach to 1017°C . While the vendor's maximum allowable temperature in refractory is announced to be less than 982°C . This increase of 35°C indicates the possible occurrence of the damage.

Two parallel cross-sections adjoining burners are shown in Figure 11, representing flames profile changes as cold air was added to the flow. In Figure 11.a, mixing air and fuel gas is illustrated where combustion occurred around the central burner. According to Figure 11.b, the flame profile was fully developed due to air and fuel gas combustion. As shown in Figure 11, with an increase in the airflow, refractory would cool down; therefore, the temperature rising issue detected in Figure 10 was solved.

In Figure 12, we increased the burner's distance so that flame profiles would be in three cross-sections in 0.5, 5 and 15 m distance from the burner. As it can be seen in Figure 12.a, the temperature difference was higher than 1800°C while whereas this difference reduced significantly to less than 52°C according to Figure 12.c.

According to Figures.10-12, it can be concluded that in the combustion chamber, as we got approached to the end of the chamber, the temperature difference between fluid and wall decreased. In the center of the burner, the flame's core was at high temperature and the end of the chamber, no significant difference was detected. These results reveal that walls at the end of the chamber are more vulnerable to possible temperature rising damages.

Figure 13 illustrates a 3D image of the flame profile in the combustion chamber. Detecting the temperatures above a specified value, the profiles were obtained. Herein, the specified values were the temperatures above 1200 , 982 and 850°C , respectively. At temperatures above 1200°C , we only had a profile in front of the burner. At lower temperatures, the profiles were developed. A remarkable issue represented in Figure 13 is that the flame, profiles even at 850°C , is not close adequately to any walls of the chamber and the flame was

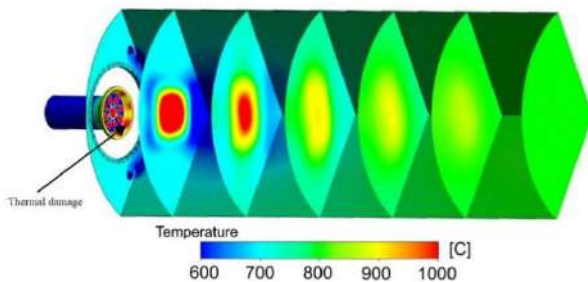


Figure 10. The flame temperature changes in different cross-sections of the chamber

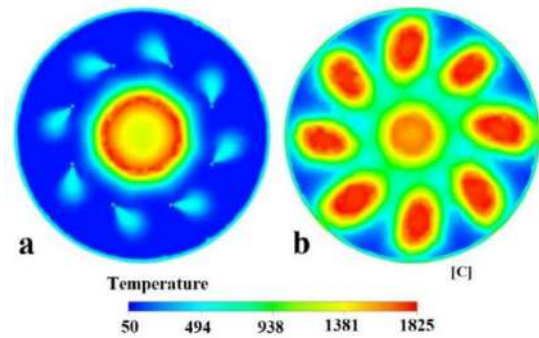


Figure 11. The temperature profile in two different sections near the burner

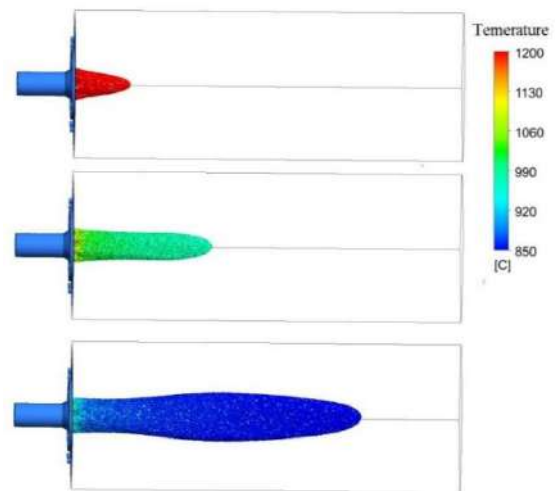


Figure 13. Flame profile 3D image

centrally developed. As mentioned before, 982°C is the maximum allowable temperature for the walls, indicating that construction problems might trigger refractory damage in sidewalls.

As mentioned, four streams enter the simulation combustion chamber, including primary air, secondary air, fuel gas and flue gas. The secondary air entered the chamber in two different spots, which can be seen in Figure 4c. The streamlines are illustrated in Figs.14 and 15. The streamline shows the path through which each stream flowed in the chamber. Figure 14 represents primary air, secondary air and their mixture streams. Figure 15 illustrates a combination of streams in which the primary air stream covered fuel gas and supplied the combustion that required oxygen. In the case of excess air, this amount of air helps obtain the full combustion of CO. Figure 15.a shows the mixture of air and fuel gas. As shown in Figure 15.b, the secondary air streams surrounded CO content flows and initially supplied this reaction, which required oxygen. In the case of excessive air, it helps fuel gas combustion. Figure 15.c illustrates all the flow mixtures.

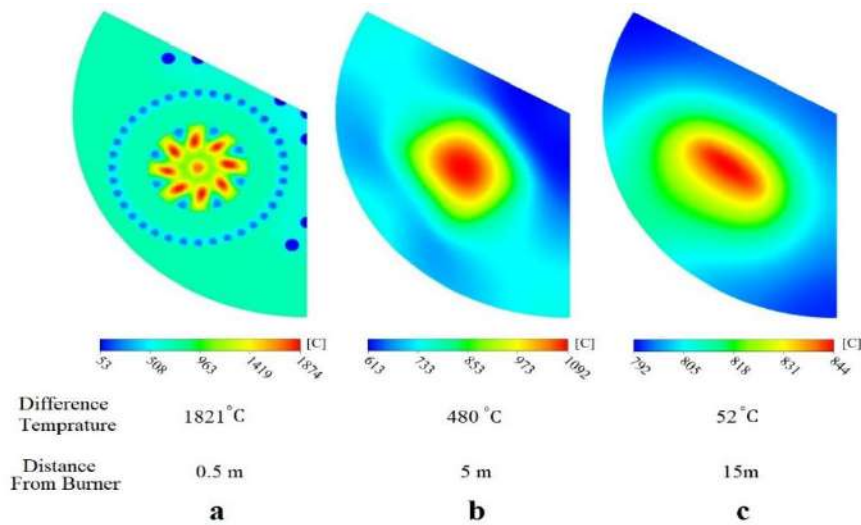


Figure 12. Temperature profile at cross-sections in different distances from the burner

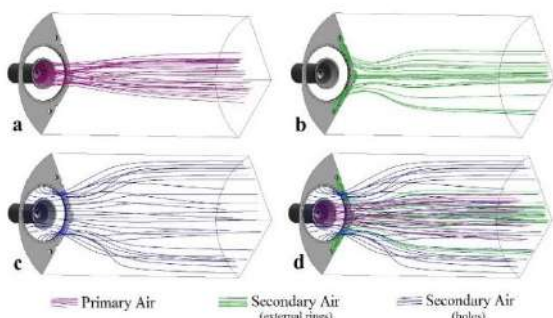


Figure 14. Inlet air streamlines. a) Primary air, b) secondary air (external ring), c) Secondary air (holes) and d) Total inlet air streamlines

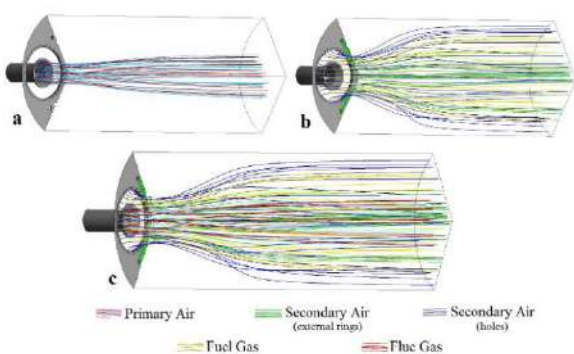


Figure 15. Inlet air streamlines. a) Primary air and fuel gas, b) Secondary air and flue gas and c) Total inlet streamlines

Figure 16 illustrates the reaction progress as a result of the reduction in reactants in the streamlines. This figure shows that molar fractions of CH_4 , C_2H_6 , C_3H_8 and

C_4H_{10} rapidly reduced, which led to a decrease in the reaction rate. Meanwhile, the CO reaction rate was far slower compared to the other components. Furthermore, according to the temperature differences of various streamlines and high CO combustion dependency on temperature, CO velocity differed from the other reactants. Figure 17 illustrates the Oxygen rate changes in the primary and secondary air streams. As could be perceived, the primary air reacted faster than the secondary one. The difference between primary and secondary air reaction rates is due to the different mixing of them with other streams.

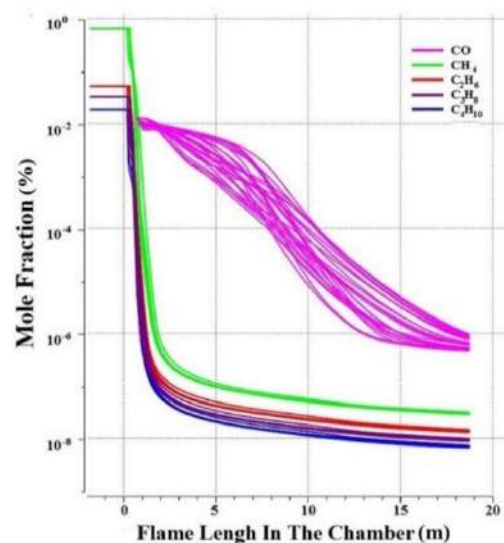


Figure 16. Reaction progress in the chamber via reactions changes

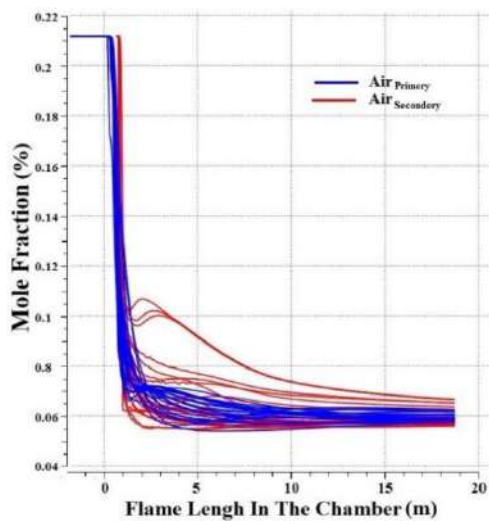


Figure 17. Oxygen level change in primary and secondary air streamlines

5. CONCLUSION

The combustion chamber of the CO boiler corresponding to the RFCC unit of the IKORC was simulated. Streamlines showed that the conditions of symmetry in the combustion chamber could be used. Also, the condition of non-dependence of the simulation results on the mesh size was investigated. The simulation results for one-stage, two-stage, multi-stage and overall combustion mechanisms showed that the closest simulation result to the actual results is the overall mechanisms. Comparison of real and simulation results shows that the simplification assumptions and calculations performed have a total error of less than 8%.

Flame velocity and temperature profiles were plotted. The results show that the flames are in the center of the combustion chamber and do not damage the combustion chamber wall, but as shown in Figure 9, there is a possibility of damage to the burner wall.

According to Figures 16 and 8, the combination of streams in the chamber was well-designed. Figure 16 also shows that the CO fraction slope decreased at the end of the chamber to reach less than 1%; thus, the chamber's length was optimally designed. Regarding Figures 14 and 15, the following results can be derived:

1. Primary air was applied for fuel gas combustion. Since then, any change in this factor altered the primarily required air.
2. Secondary air was applied for CO content stream combustion. Since then, any change in this factor alters the air required as secondary.
3. Primary air was more effective in the center, while the secondary air affects the walls. Therefore, to regulate wall temperatures, the secondary air needed to be changed. On the other hand, any other changes in CO and NO content streams require alteration of the primary air.

The maximum allowable temperature in the refractory was not observed in the burner, yet the wall temperature was much less than the allowable temperature. It can be concluded that refractory damage is not associated with functional temperature.

To prevent further damage to the burner, it is recommended to increase the primary air or modify it. Concerning the wall temperature, it is suggested to reduce the secondary air to increase thermal efficiency. The optimal amount of oxygen for burners was calculated to be approximately 3; accordingly, it is recommended to reduce the chamber's overall air entrance. This modification increases thermal efficiency and decreases fuel consumption, which ultimately reduces environmental pollution.

6. REFERENCES

1. Cellek, M.S. and Pınarbaşı, A., "Investigations on performance and emission characteristics of an industrial low swirl burner while burning natural gas, methane, hydrogen-enriched natural gas and hydrogen as fuels", *International Journal of Hydrogen Energy*, Vol. 43, No. 2, (2018), 1194-1207, DOI: 10.1016/j.ijhydene.2017.05.107.
2. Perpignan, A.A.V., Sampat, R. and Gangoli Rao, A., "Modeling pollutant emissions of flameless combustion with a joint cfd and chemical reactor network approach", *Frontiers in Mechanical Engineering*, Vol. 5, (2019), DOI: 10.3389/fmech.2019.00063.
3. Cherbański, R. and Molga, E., "Cfd simulations of hydrogen deflagration in slow and fast combustion regime", *Combustion Theory and Modelling*, Vol. 24, No. 4, (2020), 589-605, DOI: 10.1080/13647830.2020.1724336.
4. Aminoroayaie Yamini, O., Mousavi, S.H., Kavianpour, M.R. and Movahedi, A., "Numerical modeling of sediment scouring phenomenon around the offshore wind turbine pile in marine environment", *Environmental Earth Sciences*, Vol. 77, No. 23, (2018), DOI: 10.1007/s12665-018-7967-4.
5. Sengupta, A.R., Gupta, R. and Biswas, A., "Computational fluid dynamics analysis of stove systems for cooking and drying of muga silk", *Emerging Science Journal*, Vol. 3, No. 5, (2019), 285-292, DOI: 10.28991/esj-2019-01191.
6. Dirbude, S.B. and Maurya, V.K., "Effect of uniform magnetic field on melting at various rayleigh numbers", *Emerging Science Journal*, Vol. 3, No. 4, (2019), 263-273, DOI: 10.28991/esj-2019-01189.
7. Movahedi, A., Kavianpour, M.R. and Aminoroayaie Yamini, O., "Evaluation and modeling scouring and sedimentation around downstream of large dams", *Environmental Earth Sciences*, Vol. 77, No. 8, (2018), DOI: 10.1007/s12665-018-7487-2.
8. Movahedi, A., Kavianpour, M. and Aminoroayaie Yamini, O., "Experimental and numerical analysis of the scour profile downstream of flip bucket with change in bed material size", *ISH Journal of Hydraulic Engineering*, Vol. 25, No. 2, (2017), 188-202, DOI: 10.1080/09715010.2017.1398111.
9. Gharibshahian, E., "The effect of polyvinyl alcohol concentration on the growth kinetics of ktiopo4 nanoparticles synthesized by the co-precipitation method", *HighTech and Innovation Journal*, Vol. 1, No. 4, (2020), 187-193, DOI: 10.28991/hij-2020-01-04-06.
10. Jabbarzadeh Sani, M., "Spin-orbit coupling effect on the electrophilicity index, chemical potential, hardness and softness of neutral gold clusters: A relativistic ab-initio study", *HighTech*

- and Innovation Journal*, Vol. 2, No. 1, (2021), 38-50, DOI: 10.28991/hij-2021-02-01-05.
11. Trang, G.T.T., Linh, N.H., Linh, N.T.T. and Kien, P.H., "The study of dynamics heterogeneity in SiO₂ liquid", *HighTech and Innovation Journal*, Vol. 1, No. 1, (2020), 1-7, DOI: 10.28991/hij-2020-01-01-01.
 12. Yeh, C.-L., "Numerical analysis of the combustion and fluid flow in a carbon monoxide boiler", *International Journal of Heat and Mass Transfer*, Vol. 59, (2013), 172-190, DOI: 10.1016/j.ijheatmasstransfer.2012.12.020.
 13. Yeh, C.-L., "Numerical investigation of the heat transfer and fluid flow in a carbon monoxide boiler", *International Journal of Heat and Mass Transfer*, Vol. 55, No. 13-14, (2012), 3601-3617, DOI: 10.1016/j.ijheatmasstransfer.2012.02.073.
 14. Yeh, C.L. and Liang, C.W., "Nox reduction in a carbon monoxide boiler by reburning", *Procedia Engineering*, Vol. 67, (2013), 378-387, DOI: 10.1016/j.proeng.2013.12.037.
 15. Aminmahalati, A., Fazlali, A. and Safikhani, H., "Multi-objective optimization of CO boiler combustion chamber in the RFCC unit using NSGA II algorithm", *Energy*, Vol. 221, (2021), DOI: 10.1016/j.energy.2021.119859.
 16. Echi, S., Bouabidi, A., Driss, Z. and Abid, M.S., "Cfd simulation and optimization of industrial boiler", *Energy*, Vol. 169, (2019), 105-114, DOI: 10.1016/j.energy.2018.12.006.
 17. Zhu, Y., Wang, D., Shao, Z., Zhu, X., Xu, C. and Zhang, Y., "Investigation on the overpressure of methane-air mixture gas explosions in straight large-scale tunnels", *Process Safety and Environmental Protection*, Vol. 135, (2020), 101-112, DOI: 10.1016/j.psep.2019.12.022.
 18. Józwiak, P., Hercog, J., Kiedrzyńska, A. and Badyda, K., "Cfd analysis of natural gas substitution with syngas in the industrial furnaces", *Energy*, Vol. 179, (2019), 593-602, DOI: 10.1016/j.energy.2019.04.179.
 19. Ji, J., Cheng, L., Wei, Y., Wang, J., Gao, X., Fang, M. and Wang, Q., "Predictions of nox/n₂o emissions from an ultra-supercritical cfb boiler using a2-d comprehensive cfd combustion model", *Particuology*, Vol. 49, (2020), 77-87, DOI: 10.1016/j.partic.2019.04.003.
 20. Xu, L., Cheng, L., Ji, J., Wang, Q. and Fang, M., "A comprehensive cfd combustion model for supercritical cfb boilers", *Particuology*, Vol. 43, (2019), 29-37, DOI: 10.1016/j.partic.2017.11.012.
 21. Hernik, B., Zabłocki, W., Żelazko, O. and Latacz, G., "Numerical research on the impact of changes in the configuration and the location of the over fire air nozzles on the combustion process in the ultra-supercritical bp 680 boiler", *Process Safety and Environmental Protection*, Vol. 125, (2019), 129-142, DOI: 10.1016/j.psep.2019.02.029.
 22. Modlinski, N. and Hardy, T., "Development of high-temperature corrosion risk monitoring system in pulverized coal boilers based on reducing conditions identification and cfd simulations", *Applied Energy*, Vol. 204, (2017), 1124-1137, DOI: 10.1016/j.apenergy.2017.04.084.
 23. Gómez, M.A., Martín, R., Chapela, S. and Porteiro, J., "Steady cfd combustion modeling for biomass boilers: An application to the study of the exhaust gas recirculation performance", *Energy Conversion and Management*, Vol. 179, (2019), 91-103, DOI: 10.1016/j.enconman.2018.10.052.
 24. Gu, J., Shao, Y. and Zhong, W., "Study on oxy-fuel combustion behaviors in a s-co₂ cfb by 3d cfd simulation", *Chemical Engineering Science*, Vol. 211, (2020), DOI: 10.1016/j.ces.2019.115262.
 25. Karim, M.R., Bhuiyan, A.A., Sarhan, A.A.R. and Naser, J., "Cfd simulation of biomass thermal conversion under air/oxy-fuel conditions in a reciprocating grate boiler", *Renewable Energy*, Vol. 146, (2020), 1416-1428, DOI: 10.1016/j.renene.2019.07.068.
 26. Guo, J., Hu, F., Jiang, X., Li, P. and Liu, Z., "Effects of gas and particle radiation on ifrf 2.5 mw swirling flame under oxy-fuel combustion", *Fuel*, Vol. 263, (2020), DOI: 10.1016/j.fuel.2019.116634.
 27. Smith, J.D., Sreedharan, V., Landon, M. and Smith, Z.P., "Advanced design optimization of combustion equipment for biomass combustion", *Renewable Energy*, Vol. 145, (2020), 1597-1607, DOI: 10.1016/j.renene.2019.07.074.
 28. Hu, F., Li, P., Guo, J., Liu, Z., Wang, L., Mi, J., Dally, B. and Zheng, C., "Global reaction mechanisms for mild oxy-combustion of methane", *Energy*, Vol. 147, (2018), 839-857, DOI: 10.1016/j.energy.2018.01.089.
 29. Milcarek, R.J., DeBiase, V.P. and Ahn, J., "Investigation of startup, performance and cycling of a residential furnace integrated with micro-tubular flame-assisted fuel cells for micro-combined heat and power", *Energy*, Vol. 196, (2020), DOI: 10.1016/j.energy.2020.117148.
 30. Si, J., Wang, G., Li, P. and Mi, J., "Optimization of the global reaction mechanism for mild combustion of methane using artificial neural network", *Energy & Fuels*, Vol. 34, No. 3, (2020), 3805-3815, DOI: 10.1021/acs.energyfuels.9b04413.
 31. Hu, C., Luo, K., Zhou, M., Lin, J., Kong, D. and Fan, J., "Influences of secondary gas injection pattern on fluidized bed combustion process: A cfd-dem study", *Fuel*, Vol. 268, (2020), DOI: 10.1016/j.fuel.2020.117314.
 32. Franzelli, B., Riber, E., Gicquel, L.Y.M. and Poinso, T., "Large eddy simulation of combustion instabilities in a lean partially premixed swirled flame", *Combustion and Flame*, Vol. 159, No. 2, (2012), 621-637, DOI: 10.1016/j.combustflame.2011.08.004.
 33. Garby, R., Selle, L. and Poinso, T., "Large-eddy simulation of combustion instabilities in a variable-length combustor", *Comptes Rendus Mécanique*, Vol. 341, No. 1-2, (2013), 220-229, DOI: 10.1016/j.crme.2012.10.020.
 34. Fureby, C., "Large eddy simulation of turbulent reacting flows with conjugate heat transfer and radiative heat transfer", *Proceedings of the Combustion Institute*, (2020), DOI: 10.1016/j.proci.2020.06.285.
 35. Shi, Y., Zhong, W., Chen, X., Yu, A.B. and Li, J., "Combustion optimization of ultra supercritical boiler based on artificial intelligence", *Energy*, Vol. 170, (2019), 804-817, DOI: 10.1016/j.energy.2018.12.172.
 36. Paul, C., Haworth, D.C. and Modest, M.F., "A simplified cfd model for spectral radiative heat transfer in high-pressure hydrocarbon-air combustion systems", *Proceedings of the Combustion Institute*, Vol. 37, No. 4, (2019), 4617-4624, DOI: 10.1016/j.proci.2018.08.024.
 37. Perrone, D., Castiglione, T., Klimanek, A., Morrone, P. and Amelio, M., "Numerical simulations on oxy-mild combustion of pulverized coal in an industrial boiler", *Fuel Processing Technology*, Vol. 181, (2018), 361-374, DOI: 10.1016/j.fuproc.2018.09.001.

Persian Abstract

چکیده

پوشش داخلی محافظ حرارتی دیگ بخار مونواکسید کربن پالایشگاه امام خمینی (ره) شازند چندین بار دچار آسیب شده است، برای ریشه یابی علت این مشکل و تعیین شرایط جدید عملیاتی از دینامیک سالات محاسباتی (CFD) استفاده شد. برای ساده سازی شبیه سازی سه بعدی و کاهش حجم محاسبات از شرط تقارن در شبیه سازی محافظه احتراق استفاده شد، خطوط جریان نشان می دهد که استفاده از تقارن خطا در شبیه سازی ایجاد نمی کند. تعداد نقاط شبکه بهینه گردید و با استفاده از شرط استقلال نتایج شبیه سازی از تعداد نقاط شبکه، تعداد نقاط شبکه بهینه گردید. شبیه سازی با مکانیسم های احتراق تک مرحله ای، دو مرحله ای، چند مرحله ای و مجموع هر سه مکانیسم، انجام گردید و نتایج شبیه سازی با نتایج واقعی اندازه گیری شده از دیگ بخار مونواکسید کربن مقایسه شد، نتایج نشان می دهد که بهترین حالت برای شبیه سازی مجموع مکانیسم ها است که خطایی کمتر از 8٪ دارد. پروفایل سرعت و دمای شعله در قسمت های مختلف محافظه احتراق بررسی شد، نتایج نشان می دهد که هرچه از مشعل ها فاصله بگیریم پروفایل سرعت و دما یکنواخت تر می شود همچنین دمای دیواره افزایش پیدا می کند و نحوه اختلاط جریان های مختلف ورودی در محافظه احتراق از طریق رسم خطوط جریان بررسی گردید. بررسی پیشرفت واکنش احتراق و مکان یابی مناطق داغ محافظه احتراق و همچنین دمای دیواره ها نتایج نشان می دهد که دمای دیواره محافظه احتراق در محدوده مناسب است و آسیب حرارتی ندیده است. ولی دیواره مشعل در محل اختلاط جریان ها امکان آسیب جزئی دارد که با تغییر مقدار جریان ها قابل رفع است. پروفایل نامناسب حرارتی همچنین مقدار زیاد اکسیژن در گاز خروجی نشان می دهد که شرایط عملکرد دیگ بخار از شرایط بهینه فاصله دارد و نتایج شبیه سازی نشان می دهد که برای کاهش مقدار CO و NOx در جریان خروجی باید شدت جریان هوای اولیه تغییر کند و همچنین برای جلوگیری از آسیب حرارتی به پوشش داخلی و کاهش خطرات ایمنی، جریان هوای ثانویه تغییر یابد.



Photocatalytic Removal of Toluene from Gas Stream using AgI-ZnO/Chitosan Nanocomposite Fixed on Glass Bed under UVA Irradiation

A. Poormohammadi^a, Z. Ghaedrahmat^b, M. Ahmad Moazam^b, N. Jaafarzadeh^{*b,c}, M. Enshayi^b, N. Sharafi^b

^a Center of Excellence for Occupational Health, Research Center for Health Sciences, School of Public Health, Hamadan University of Medical Sciences, Hamadan, Iran

^b Department of Environmental Health Engineering, School of Health, Ahvaz Jundishapur University of Medical Sciences, Ahvaz, Iran

^c Environmental Technologies Research Center, Ahvaz Jundishapur University of Medical Sciences, Ahvaz, Iran

PAPER INFO

Paper history:

Received 16 December 2020

Received in revised form 25 January 2021

Accepted 16 February 2021

Keywords:

Toluene

Photocatalyst

Ultraviolet

Chitosan

Nanocomposite

ABSTRACT

In this study, AgI-ZnO/chitosan nanocomposite was synthesized and then was coated on 2×40×200 glass plates under UVA irradiation for the removal of toluene from air streams. The AgI-ZnO/chitosan Nanocomposite was characterized using XRD, SEM, FTIR and BET techniques. The analyses showed Zn and Ag were added to the composite structure with weight percentages of 32.02 and 7.31, respectively. The results confirmed that the AgI-ZnO/chitosan nanocomposite was successfully synthesized. According to the results, the photocatalytic process was able to remove 74.6% of toluene at an air flow rate of 1 L/min after 3.3 min. Also, by increasing the passing flow rate from 0.3 to 1.5 L/min through the photocatalytic reactor, the process efficiency for toluene removal increased. The toluene removal efficiency decreased with increasing relative humidity with respect to time. Moreover, increasing relative humidity decreased the photocatalyst capacity for the removal of the target pollutants. The results implied that the initial toluene concentration in the inlet stream played a key role on the photocatalysis of toluene and by further increase in the pollutant concentration higher than 20 ppm, its performance decreased dramatically. Therefore, the proposed process can be used and an effective technique for the removal of toluene from the polluted air stream under UV irradiation and increasing temperature up to 60 °C could increase its performance.

doi: 10.5829/ije.2021.34.03c.02

1. INTRODUCTION

Nowadays, the quality of indoor air in residential and occupational environments has become an important issue around the world [1]. Toluene as an aromatic hydrocarbon is widely found in coal tar that can pose a major threat to human health. Toluene (methylbenzene or phenyl methane) is a colorless, odorless, water-insoluble and flammable liquid, which is commonly used as a solvent in various industries such as paints, resins, solvents, thinners, silicone sealants, chemical reagents, plastics, printing inks, adhesives, lacquers and disinfectants. It can also be used in the manufacture of foam and TNT [2]. Toluene exposure is associated with many adverse effects on human health. Low-level

exposure to toluene can cause fatigue, dizziness, weakness, unbalanced behavior, memory impairment, insomnia, anorexia, and blurred vision and hearing loss. Toluene can also cause damage to liver and kidney [3]. There is no evidence at present that toluene causes cancer in humans [4]. Occupational Safety and Health Administration (OSHA) standard concentration has established a maximum exposure limit of 3 ppm for the workplace and EPA has recommended 14.3 mg/L for drinking water [5]. Due to the adverse effects of toluene on human health, it must be removed from polluted air streams before being released into the ambient air. In recent years, there has been a growing interest in the use of heterogeneous photocatalytic oxidation for indoor air purification, especially gaseous pollutants such as benzene, toluene, ethylbenzene, zylene isomers, and

*Corresponding Author Email: h.koohestani@semnan.ac.ir (H. Koohestani)

ethylene trichloride. Because the indoor pollutants can pose a serious health risk to human [6]. The use of Nano-crystalline semiconductors as photocatalysts to initiate surface reduction-oxidation reactions has gained much interest due to their unique physicochemical properties such as nano-dimensions and high specific surface area. Until now, numerous photocatalysts have been used in photocatalytic degradation of different pollutants from air and water media. Among them, zinc oxide (ZnO) nanoparticle is one of the most widely used inorganic nanoparticles, which offers good physical and chemical properties like high chemical stability, low dielectric constant, low toxicity, high electromechanical coupling coefficient, high optical absorption thresholds and high ability to degrade some organic compounds, and high catalytic activity [7-9].

ZnO as a semiconductor (type II-VI) has a band gap of 3.37 eV and an excitation binding energy of 60 eV at room temperature. Due to its non-toxicity and low-cost, it offers high potential to be used as photocatalyst. However, some limitations of ZnO such as low quantum efficiency and low visible light absorption limit its practical applications as photocatalyst. AgI is a plasmonic semiconductor that offers a narrow band gap, and hence provides excellent visible light sensitivity and photocatalytic performance. So that the combined composite of this photocatalyst can make it a more practical catalyst and boosts its application under different types of light sources [10].

Nowadays, in order to enhance the adsorption and condensation of gaseous compounds, various stabilizers such as activated carbon, bone ash, silica, alumina, zeolites are applied. In this regard, chitosan as a natural polysaccharide provides many advantages such as hydrophilicity, biocompatibility, biodegradability and antibacterial properties. Chitosan is also capable of absorbing many metal ions because its amino groups can act as a chelating site [11]. In a review study on the applicability of chitosan based nanocomposite materials as a photocatalyst, it was found that the use of natural organic materials such as chitosan in the synthesis of nano-sized material causes an interface for the charge transfer, resulting in an increase of photocatalytic efficiency [12]. Therefore, the use of chitosan as supporting material in photocatalytic process can increase the adsorption rate of pollutant molecules, and consequently increase the photocatalytic process efficiency. Recent studies have showed that Ag-based semiconductors exhibits strong visible light absorption and high photocatalytic activity under visible light due to its narrow band gap energy [13]. Until now, there has been no study investigating the performance of AgI-ZnO/chitosan nanocomposite for the removal of toluene from polluted air stream.

Therefore, this study aimed at investigating the performance of AgI-ZnO/chitosan nanocomposite fixed

on glass bed in photocatalytic degradation of toluene from polluted air stream under UVA irradiation. For this reason, on the proposed photocatalytic efficiency, the effects of various parameters, such as volumetric flow Rate, TiO₂/chitosan ratio, volumetric flow rate, and toluene concentration were investigated. Moreover, in order to evaluate the applicability of the proposed system under visible light as a cost effective and available energy, the experiments were conducted under UVA and visible light.

2. MATERIALS AND METHODS

2. 1. Materials Toluene with >99% purity were analytical grade and purchased from Merck (Darmstadt, Germany). AgI powders were purchased from Sigma Aldrich Co (USA). Chitosan was provided from tiger or pink shrimp shells that is available in the domestic markets and shrimp shops in Ahwaz city of Khuzestan province.

2. 2. Preparation of Chitosan from Chitin Chemical and biological methods are commonly used for the production of chitin and chitosan from the shrimp shell including. In this study, the chemical method was used for the production of chitosan from tiger or pink shrimp shells that is available in the domestic markets and shrimp shops in Ahwaz city of Khuzestan province. For this reason, chitin was first extracted in four steps including: 1) size reduction: In this step, the pink shrimp shells were rinsed with distilled water and stored in 0.5% sodium hydroxide solution for 4 h. Next, the resulting shells were rinsed with distilled water, dried in open air and grinded machine, 2) protein removal: 2% caustic soda solution with a weight ratio of 1:30 was used at 90 ° C for 24 h. Then, the resulting shells were rinsed and washed with distilled water until the sample pH reached near neutral and dried at 70 ° C, 3) demineralization: the shell residues were poured in 2% hydrochloric acid, mixed in 5% hydrochloric acid solution at 60 ° C for 24 h, filtered, washed to reach neutral pH and finally dried, and 4) decolorization: the obtained chitin was kept in acetone-ethanol solution (1: 1 ratio) for 24 h until the color became clear, washed to reach neutral pH, and then dried. Eventually, chitosan was obtained the deacetylation of the prepared chitin from the previous stages.

2. 2. Preparation of AgI-ZnO Nanocomposite In order to prepare 0.188 mol of silver iodide crystal, 0.578 g of zinc nitrate and 506.08 g of silver nitrate were dissolved in 100 mL of distilled water and stirred at room temperature. Then, NaOH solution (5 M) was added dropwise to the resulting solution at room temperature to reach pH of 9.5. Then, the aqueous sodium iodide

solution (0.076 g of sodium iodide dissolved in 50 mL of distilled water) was slowly added into the light brown suspension until the solution turned yellow. The resulting yellow suspension was then refluxed for 60 min at approximately 196 °C. The formed olive product was centrifuged. The obtained precipitate was removed and washed twice with distilled water and ethanol to remove unreacted reagents and dried at 60 °C for 24 h.

2. 3. Synthesis of AgI-ZnO/Chitosan Nanocomposite

In the present study, AgI-ZnO/chitosan nanocomposite was synthesized in three different ratios of 0.5: 1, 1: 1, and 1: 2 chitosan: AgI-ZnO. For preparing AgI-ZnO/chitosan nanocomposite with a ratio of 1: 1, 2 g of AgI-ZnO powder was poured into 100 mL of distilled water, and then placed in an ultrasonic bath for 5 h to form a suspension. Next, 2 g of the chitosan powder was added into 100 mL of 5% acetic acid solution and placed on a shaker at 60 rpm. Afterward, the resulting mixture was added into the AgI-ZnO suspension until white gel was formed

2. 4. Characterization of AgI-ZnO/Chitosan Nanocomposite

In this step, the prepared AgI-ZnO/chitosan nanocomposite was characterized using XRD technique (to identify crystalline compounds or phases), (to study surface morphology), FTIR (to determine functional groups) and BET (to measure specific surface area).

2. 5. Experiments

In this research, AgI-ZnO/chitosan nanocomposite was first synthesized and then was coated on 2×40×200 glass plates. Next, the glass containing harmonious nanocomposite was placed inside a plexiglass chamber with a useful volume of 1 L (5 ×8× 25 mm). All experiments were conducted in this set-up as continuous-flow reactor. The airflow was generated using the air pump (BioLite High-volume Sample Pump, SKC) and passed through the chamber containing toluene (37% toluene was used to provide various concentrations of toluene in the gas phase) and a humidifier (containing water) to provide the desirable humidity. Afterward, the humid air stream containing toluene was entered into a mixing chamber and the photocatalytic reactor. The air stream containing the compounds of interest was entered into the reactor and passed on the photocatalytic glass containing photo catalyst under UV irradiation at a wavelength of 365 nm, which provided by two UVA lamps (6 watt). The concentration of toluene in the inlet and outlet of the reactor was measured by sampling valves embedded in the inlet and outlet of the reactor using a direct-reading monitor (PhoCheck TIGER). In order to evaluate the effects of visible light on the process performance, a 30-watt fluorescent tube was applied in

the reactor. A schematic illustration of the reactor used is shown in Figure 1.

In order to determine the optimum conditions of the various parameters affecting the photocatalytic process, the experiments were performed at three different levels of each parameter under UV irradiation (Table 1). In order to determine the effect of irradiation type on process efficiency, the experiments were conducted under UV and visible irradiation. The parameter were optimized by the one-factor-at-a-time method as presented in Table 1. Moreover, in order to investigate kinetics and thermodynamics of the process, the effects of time and temperature variables under optimal conditions were also investigated. Table 2 shows how the experiments were performed. Sample size determination was based on the simplicity of the design of the experiment (combining factors to perform the experiments) based on the one-factor-at-a-time method. It should be noted that in the present study, the effect of irradiation time was evaluated by changing the duration of the use of UVA lamp in the reactor. Because, increasing the irradiation time may affect on the photocatalyst. Moreover, the effects of temperature and time (in a specific range) on the process efficiency were investigated (see Table 3).

3. RESULTS AND DISCUSSION

3. 1. Nano-composite Characterization

The AgI-ZnO/chitosan nanocomposite was characterized using XRD, FTIR and BET techniques. Figure 2 a presents the FTIR spectrum of the synthesized AgI-ZnO/chitosan nanocomposite. As observed here, the broader and stronger peak at 3425 cm^{-1} is attributed to the NH_2 and OH group stretching vibration, which may be due to the interaction between these groups and ZnO. Moreover, the presence of peaks at 2924 and 2859 cm^{-1} may be assigned to asymmetric stretching OH, CH_3 and CH_2 of chitosan polymer in the structure of the Nan-composite [14]. Moreover, the presence of peak at 1647 cm^{-1} may be assigned to addition of silver nanoparticles to the

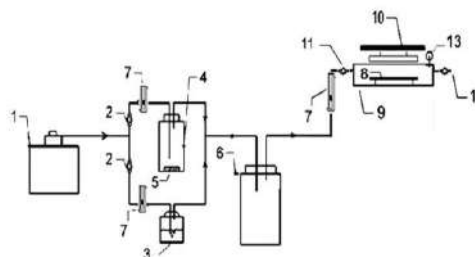


Figure 1. A schematic illustration of the reactor used (1-Air Pump, 2- Flow adjustment valve, 3- Humidifier, 4- Toluene chamber, 5- Toluene solution, 6- Mixing chamber, 7- Flowmeter, 8-Photocatalyst, 9- Reaction reactor, 10- Ultraviolet lamp, 11- Input sampling valve, 12- Output sampling valve, 13- Humidity meter)

TABLE 1. Determination of optimum parameters under UV irradiation

Volumetric flow rate (L/min)	Toluene concentration (ppm)	Relative humidity (%)	TiO ₂ /chitosan ratio	Volumetric flow rate (L/min)		
	4	60	1:1	0.2	0.6	1
Relative humidity (%)	Toluene concentration (ppm)	Volumetric flow rate (L/min)	TiO ₂ /chitosan ratio	Volumetric Flow Rate (L/min)		
	4	Optimum	1:1	20	50	80
AgI-ZnO/chitosan ratio	Toluene concentration (ppm)	Volumetric flow rate (L/min)	Relative humidity (%)	TiO ₂ /Chitosan Ratio		
	4	Optimum	Optimum	1:0.5	1:1	2:1
Total runs with 2 replicates			18			

TABLE 2. Effect of toluene concentration under optimum operating conditions on process efficiency

Irradiation source	Optimal conditions	Toluene concentration (ppm)						
UV-A	Flow, Relative humidity and Chitosan /AgI-Zno ratio	1	2	4	6	8		
Visible Light	Flow, Relative humidity and Chitosan /AgI-Zno ratio	1	2	4	6	8		
Total runs with 2 replicates			20					

TABLE 3. Effect of temperature and time on process efficiency

Optimal conditions	Irradiation source	Parameters	Levels				
Concentration, relative humidity and chitosan /AgI-ZnO ratio	UV-A	Irradiation time* (s)	60	75	100	150	300
		Temperature (° C)	25		45		65
	Visible light	Irradiation time (s)	60	75	100	150	300
		Temperature (° C)	25		45		65
Total runs with two replicates			32				

*irradiation time: Duration of use of UV lamp before sampling

proposed composite. According to the XRD analysis of the synthesized nanocomposite (Figure 1b), the peaks observed at 2θ values of 37.9002°, 47.3018°, 56.1889°, and 76.8833° that are assigned to (111), (200), (220) and (311) planes of pure silver based on the face-centered cubic structure (JCPDS, file No. 04-0783) [15,16]. Figures 2c and 2d show the EDAX analysis results of the synthesized nanocomposite. As can be seen here, Zn and Ag was added to the composite structure with weight percentages of 32.02 and 7.31, respectively, which confirmed that the AgI-ZnO/chitosan nanocomposite was successfully synthesized. Figure 2e demonstrates the SEM images of the AgI-ZnO/chitosan nanocomposite. The SEM analysis indicated spherical shape of Ag nanoparticles that the size of most particles are more than 100 nm.

3. 2. Effect of Flow Rate In this study, in order to investigate the performance of the photocatalytic process under different flow rates, the experiments were conducted under 5 flow rates (0.3, 0.5, 1, 1.5 and 2 L/min). Figure 3 presents the changes of process

efficiency with increasing flow rates with respect to time. As observed, by increasing passing flow rate from 0.3 to 1.5 L/min through the photocatalytic reactor, the process

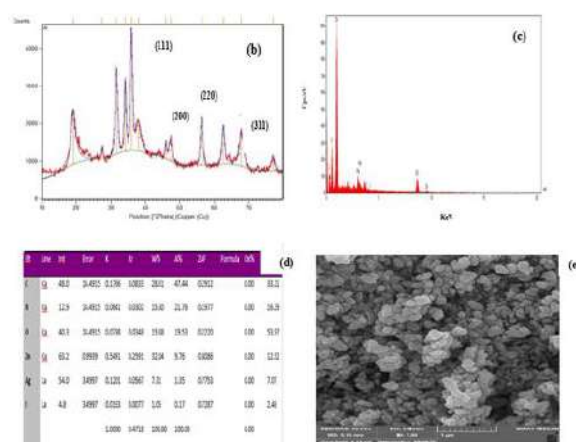


Figure 2. (a) FTIR analysis, (b) XRD, (c and d) EDAX, and (e) SEM analyses of AgI-ZnO/chitosan Nanocomposite

efficiency for toluene removal increased. Flow rate of the entrance stream to a photocatalytic reactor plays a key role in the photocatalysis of the target pollutant, due to its role in the determination of irradiation time of pollutant in the reactor. It is suspected that increasing flow rate up to certain amount provides enough irradiation time of the pollutant and sufficient mixing for the photocatalytic process. While further increasing the air flow rate can decrease the residence time of the pollutant, and thereby decreases the process efficiency. As can be seen in Figure 2, the process efficiency of the proposed photocatalytic process increased with increasing air flow rate up to 1.5 L/min, while by further increasing the air flow rate to 2 L/min, a dramatic decrease was observed in the process performance. This phenomenon may be attributed to the high speed of the air stream inside the reactor, which decreases the UV irradiation time in the reactor. According to the results, photocatalytic process increased with increasing UV irradiation time from 0 to 0.6 min and then a constant efficiency was observed with respect to time. The photocatalytic process was able to remove 74.6% of toluene in at an air flow rate of 1 L/min after 3.3 min of irradiation time. This finding indicated that the proposed process requires low contact time to remove the pollutant in the air stream and further increasing in the contact time did not have an obvious effect on increasing process efficiency. In a recent study, the synergistic effect of pollutant initial concentration and air flow rate on the plasma-photocatalytic process for ethylbenzene removal was investigated. It was found that the flow rate had a negative effect on the ethylbenzene removal efficiency. The highest performance was observed at the lowest air flow rate. This difference with our findings may be attributed to the difference in the volume of entrance air and the dimensions of the used reactor. In the present study, the effect of air flow rate was investigated in the range 0.3-2 L/min, while in the mentioned study, the effect of air flow rate was very lower (15-45 mL). On the other hand, the simultaneous effect of increasing the pollutant concentration can also be related to decrease in overall process efficiency in the mentioned study in compared to the present study [17].

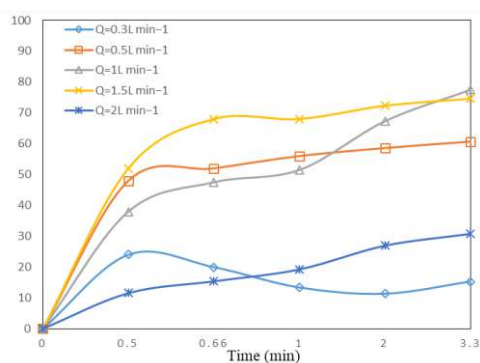


Figure 3. Effect of air flow rate on photocatalysis of toluene

3. 3. Effect of Relative Humidity Water vapor is generated as a byproduct in the most of reactions in industries such as burning in petroleum and gas refineries. The content of water vapor is measured as relative humidity in contaminated air stream. It is recommended to measure the relative humidity along with other parameters in the exhaust air flow from many industries due to its effects on the control processes. In this regard, it is necessary to evaluate relative humidity on the performance of control processes. For this reason, in the present study, the influences of different levels of relative humidity in the range 30-80% on the proposed process efficacy were investigated. Figure 4 illustrates the effects of the relative humidity on the photocatalysis of toluene with respect to time. As can be seen here, the performance of the photocatalytic process with the AgI-ZnO/chitosan nanocomposite fixed on glass bed decreased with increasing relative humidity level. Moreover, this decreasing effect increased with respect to time. Based on the results, the highest removal efficiency was obtained at 30% of relative humidity, which was about 70%. This phenomenon is clearly attributed to the competition of water molecules at higher humidity to absorb on the vacant sites on the photocatalyst surface, which decreases the available vacant sites of the photocatalyst for the target pollutant [18]. These results are in agreement with the findings of Jiancai et al. [19] study on the catalytic combustion of toluene over copper based catalysts with different supports in presence of water vapor.

3. 4. Effect of AgI-ZnO/Chitosan Ratios In this step, the effect of different ratios of Ag-ZnO/chitosan (0.5:1, 1:1 and 2:1) on the process performance in the removal of toluene from air stream was investigated. As can be seen in Figure 5, at the Ag-ZnO/chitosan ratio of 0.5:1, the photocatalytic efficiency reached about 70%. This result is due to the photocatalytic activity of the AgI-ZnO at this ratio, which can generate higher active species such as $\bullet\text{OH}$ and $\bullet\text{O}_2^-$. Various photocatalysts generate different main active species because of the difference in their band structure or phase composition.

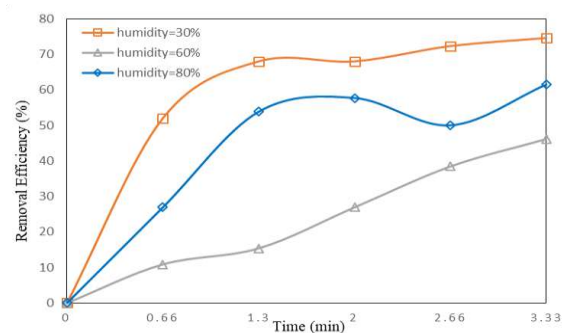


Figure 4. Effect of relative humidity on photocatalysis of toluene

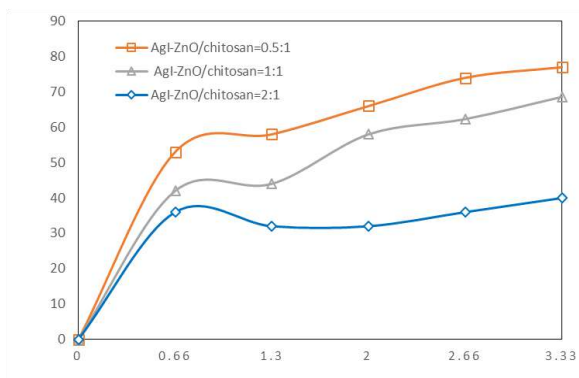


Figure 5. Effects of different ratios of AgI-ZnO /chitosan in the process performance

Therefore, the different ratio of the proposed photocatalyst can affect its photocatalytic activity. So that the process efficiency decreased by increasing AgI-ZnO/chitosan ratio and the most removal efficacy was observed at 0.5:1 ratio [9,10]. On the other hand, chitosan as supporting material in photocatalytic process can increase the adsorption rate of the pollutant molecules and consequently increase the photocatalytic process efficiency, which is consistent with our findings, because increasing chitosan with a specific ratio of AgI-ZnO in the proposed nanocomposite could increase the photocatalytic efficiency for the removal of toluene from air stream. While, further increase of AgI-ZnO could reduce the light transmittance and decrease the light penetration. Therefore, a high dosage of AgI-ZnO limits the photocatalysis of toluene in the air. This result is consistent with the finding of Xie et al. [20] study, on the enhanced photocatalytic activity of Se-doped TiO₂ under visible light irradiation. They reported that further increasing the doping concentration decreased the photocatalytic activity of the photocatalyst.

3. 5. Effect of Toluene Concentrations The efficiency of photocatalytic process for the removal of pollutants is obviously dependent to the pollutant concentration. In air purification processes using photocatalytic, due to short UV irradiation time of the pollutant inside the reactor, the pollutant concentration plays a key role in the process efficiency. For this reason, in the present study, the effects of various toluene concentration on the process performance were investigated. As observed in Figure 6, the efficiency of the proposed photocatalytic process reduced with increasing toluene concentration from 20 to 50 ppm. This is clearly due to the limited capacity of the nanocatalyst used in the process, which by increasing the pollutant concentration from a certain amount, the empty sites available on the nanocomposite surface is reduced, and hence there is no enough capacity in the nanocomposite to decompose the high concentration of the pollutant

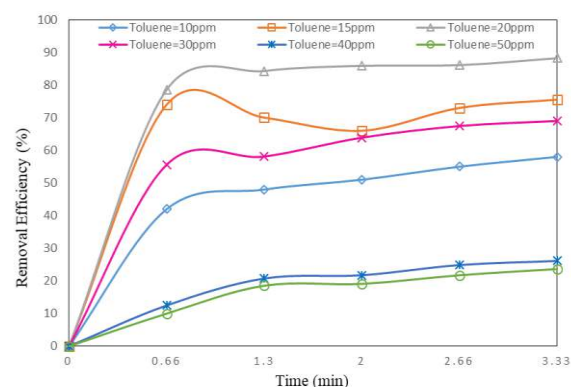


Figure 6. Effects of different toluene concentration on the process performance

molecules. This result is consistent with the findings of previous studies [1-3]. In contrast, the highest removal efficiency was obtained at 20 ppm of toluene in the inlet stream into the reactor. Indeed, the process efficiency increased with increasing toluene concentration from 10 to 20 ppm. This phenomenon can be due to the absence of the minimum concentration of contaminants at low concentrations for the reaction in the process. This result implied that this process can efficiency used for different concentrations of air pollutants up to a certain concentration without decreasing its performance. Binas et al. [21] in a similar study on the removal of toluene along with other organic and inorganic pollutants, reported that the photocatalytic process with modified TiO₂ decreased with increasing toluene concentration; however, this decreasing effect was negligible at low concentrations of toluene in the range 10-20 ppm, which is in agreement with our findings.

3. 6. Comparison of Effect of Ultraviolet Light and Visible Light

In this study due to the use of Ag in the synthesis of photocatalyst it was expected to be applicable under visible light in addition to UV irradiation. For this reason, the performance of the AgI-ZnO/chitosan nanocomposite fixed on glass bed under the UV irradiation was compared to visible light for the photocatalytic removal of toluene from gas stream. The results are presented in Figure 7. As can be see here, the photocatalytic process offered a better efficiency under UV irradiation at different temperatures compared to visible light. This result can be attributed to the high photocatalytic activity of AgI-ZnO/chitosan nanocomposite under UVA, which generates higher active species such as $\cdot\text{OH}$ and $\cdot\text{O}_2$ [9,10]. Therefore, our findings implied that the proposed photocatalyst showed higher photocatalyst activity under UVA irradiation compared to visible light, because of higher degradation rate of toluene under UVA irradiation. According to the results, the highest removal efficiency of toluene was

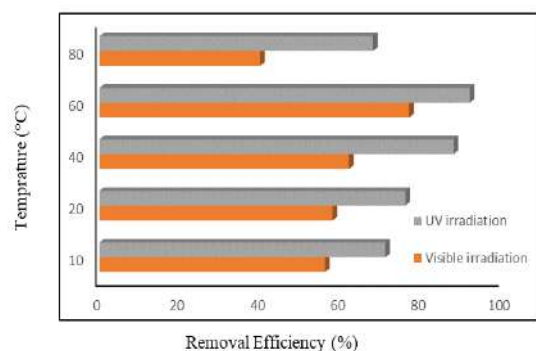


Figure 7. Effects of ultraviolet irradiation and visible light on photocatalytic removal of toluene from gas stream using AgI-ZnO/chitosan Nanocomposite fixed on glass bed

observed at 60 °C under UV irradiation. Therefore, the photocatalytic process has high performance at higher reaction temperature that can be attributed to the increase in the rate of chemical reactions at high temperatures. This result is consistent with the findings of Hu et al. [22] on the effect of reaction temperature on the photocatalytic degradation of methyl orange under UV-Vis light irradiation. In the mentioned study, it was reported that the photocatalytic efficiency increased five times by increasing reaction temperature in the range 30-100 °C [22-24]. This finding emphasize the role of solar energy in such photocatalytic processes that can be used for activation of the used catalyst simultaneously with increasing the reaction temperature.

4. CONCLUSION AND FUTURE PERSPECTIVE

In this study, AgI-ZnO/chitosan nanocomposite was first synthesized and used for photocatalytic degradation of toluene from polluted air. The laboratory experiments indicated that the process efficiency of the proposed photocatalytic process increased with increasing air flow rate up to 1.5 L/min, while by further increasing the air flow rate to 2 L/min, a dramatic decrease was observed in the process performance, and obviously decreased with increasing relative humidity. Moreover, the process efficiency was also decreased by increasing AgI-ZnO/chitosan ratio and the most removal efficacy was observed at 0.5:1 ratio. The results implied that the initial toluene concentration in the inlet stream played a key role on the photocatalysis of toluene and by further increase in the pollutant concentration higher than 20 ppm, its performance decreased dramatically. Our findings also indicated that the proposed process offered a better performance under UV irradiation compared to visible light and increasing temperature up to 60 °C could increase its performance. It can be concluded that the AgI-ZnO/chitosan nanocomposite fixed on glass bed can

effectively remove toluene from air stream under UV light, and given the synergetic effect of high temperature on the process efficiency, it is recommended to perform further study on the application of such process under sunlight as a natural and cost-effective source for UV and temperature rise. Lack of analysis of the production of by-products during photocatalytic process to determine the quality of the outlet gas and lack of investigation of the effect of other contaminants on the process efficiency are considered as the main limitations in conducting this research. Further studies are required to investigate the effect of some other parameters such as other pollutants on the AgI-ZnO/chitosan photocatalyst under UVA irradiation as well as by-products in the outlet gas of the proposed process in order to determine the quality of the process exhaust gas.

5. ACKNOWLEDGMENT

This research work was financially supported by the Environmental Technologies Research Center, Ahvaz Jundishapur University of Medical Sciences (Grant No. ETRC-9629).

6. REFERENCES

- Samarghandi, M. R., Daraee, Z., Shekher Giri, B., Asgari, G., "Reza Rahmani, A. and Poormohammadi, A., Catalytic ozonation of ethyl benzene using modified pumice with magnesium nitrate from polluted air", *International Journal of Environmental Studies*, Vol. 74, (2017) 486-499. DOI: 10.1080/00207233.2017.1316042.
- Zhu, B., Zhang, L.-Y., Li, M., Yan, Y., Zhang, X.-M. and Zhu, Y.-M., "High-performance of plasma-catalysis hybrid system for toluene removal in air using supported Au nanocatalysts" *Chemical Engineering Journal*, Vol. 381, (2020), 122599. DOI: 10.1016/j.cej.2019.122599.
- Samarghandi, M.R., Babae, S.A., Ahmadian, M., Asgari, G., Ghorbani Shahna, F. and Poormohammadi, A., Performance catalytic ozonation over the carbosieve in the removal of toluene from waste air stream, *Journal of Research in Health Sciences*, Vol. 14, (2014), 227-232.
- Pitarque, M., Vaglenov, A., Nosko, M., Hirvonen, A., Norppa, H., Creus, A., Marcos, R., "Evaluation of DNA damage by the Comet assay in shoe workers exposed to toluene and other organic solvents, Mutation", *Research/Genetic Toxicology and Environmental Mutagenesis*, Vol. 441, (1999) 115-127. DOI: 10.1016/s1383-5718(99)00042-x.
- Hsieh, G. C., Sharma, R. P., Parker, R. D., "Immunotoxicological evaluation of toluene exposure via drinking water in mice", *Environmental Research*, Vol. 49, (1989) 93-103. DOI: 10.1016/S0013-9351(89)80024-6.
- Poormohammadi, A., Bahrami, A., Ghiasvand, A., Shahna, F. G. and Farhadian, M., "Preparation of Carbotrap/silica composite for needle trap field sampling of halogenated volatile organic compounds followed by gas chromatography/mass spectrometry determination", *Journal of Environmental Health Science and Engineering*, (2019) 1-9. DOI: 10.1007/s40201-019-00418-2.

7. Salehi, R., Arami, M., Mahmoodi, N. M., Bahrami, H., Khorramfar, S., "Novel biocompatible composite (chitosan-zinc oxide nanoparticle): preparation, characterization and dye adsorption properties", *Colloids and Surfaces B: Biointerfaces*, Vol. 80, (2010), 86-93. DOI: 10.1016/j.colsurfb.2010.05.039.
8. Scharnberg, A. A., de Loreto, A. C., Alves, A. K. "Optical and structural characterization of Bi₂FexNbO₇ nanoparticles for environmental applications", *Emerging Science Journal*, Vol. 4, (2020) 11-17. DOI: 10.28991/esj-2020-01205
9. Gharibshahian, E. "The Effect of Polyvinyl Alcohol Concentration on the Growth Kinetics of KTiO₇O₄ Nanoparticles Synthesized by the Co-precipitation Method", *High Tech and Innovation Journal*. Vol. 1, (2020), 187-193. Doi: 10.28991/HIJ-2020-01-04-06
10. Lu, J., Wang, H., Dong, Y., Wang, F., Dong, S., "Plasmonic AgX nanoparticles-modified ZnO nanorod arrays and their visible-light-driven photocatalytic activity", *Chinese Journal of Catalysis*, Vol. 35, (2014), 1113-1125. DOI: 10.1016/S1872-2067(14)60055-3.
11. Yaghmaeian, K., Jaafarzadeh, N., Nabizadeh, R., Rasoulzadeh, H., Akbarpour, B., "Evaluating the performance of modified adsorbent of zero valent iron nanoparticles-Chitosan composite for arsenate removal from aqueous solutions", *Iranian Journal of Health and Environment*, Vol. 8 (2016) 535-548.
12. Nithya, A., Jothivenkatachalam, K., Prabhu, S., Jeganathan, K. "Chitosan based nanocomposite materials as photocatalyst-a review", *In Materials Science Forum*, Vol. (2014), 79-94. DOI: 10.4028/www.scientific.net/MSF.781.79.
13. Li, J., Fang, W., Yu, C., Zhou, W., Xie, Y., "Ag-based semiconductor photocatalysts in environmental purification", *Applied Surface Science*, Vol. 358, (2015). DOI: 46-56. 10.1016/j.apsusc.2015.07.139
14. Abbasipour, M., Mirjalili, M., Khajavi, R., Majidi, M. M., "Coated cotton gauze with Ag/ZnO/chitosan nanocomposite as a modern wound dressing", *Journal of Engineered Fibers and Fabrics*, Vol. 9, (2014) 155892501400900114.
15. Meng, Y., "A sustainable approach to fabricating Ag nanoparticles/PVA hybrid nanofiber and its catalytic activity", *Nanomaterials*, Vol. 5, (2015) 1124-1135. DOI: 10.3390/nano5021124.
16. Samadi, M. T., Shokoohi, R., Poormohammadi, A., Azarian, G., Harati, M., Shanesaz, S., "Removal of bisphenol, using antimony nanoparticle multi-walled carbon nanotubes composite from aqueous solutions", *Oriental Journal of Chemistry*, Vol. 32, (2016) 1015-1024. DOI : 10.13005/ojc/320227
17. Parvari, R., Ghorbani-Shahna, F., Bahrami, A., Azizian, S., Assari, M. J., Farhadian, M., "Core-Discontinuous Shell Nanocomposite as an Indirect Z-Scheme Photocatalyst for Degradation of Ethylbenzene in the Air Under White LEDs Irradiation", *Catalysis Letters*, (2020) 150, 3455-3469. DOI: 10.1007/s10562-020-03236-6.
18. Bose, R., "Methane gas recovery and usage system for coalmines, municipal land fills and oil refinery distillation tower vent stacks", *Google Patents*, 2010.
19. Jiancai, F., Xiao, C., Qibin, X., Hongxia, X., Zhong, L., "Effect of relative humidity on catalytic combustion of toluene over copper based catalysts with different supports", *Chinese Journal of Chemical Engineering*, Vol.17, (2009) 767-772. DOI: 10.1016/S1004-9541(08)60275-X.
20. Xie, W., Li, R. Xu, Q., "Enhanced photocatalytic activity of Sedoped TiO₂ under visible light irradiation", *Scientific Reports*, Vol. 8, (2018) 8752.
21. Binas, V., Venieri, D., Kotzias, D. and Kiriakidis, G., "Modified TiO₂ based photocatalysts for improved air and health quality", *Journal of Materiomics*, Vol. 3, (2017) 3-16. DOI: https://doi.org/10.1016/j.jmat.2016.11.002.
22. Hu, Q., Liu, B., Song, M., Zhao, X., "Temperature effect on the photocatalytic degradation of methyl orange under UV-vis light irradiation", *Journal of Wuhan University of Technology-Materials Science Edition*, Vol. 25, (2010) 210-213. DOI: 10.1007/s11595-010-2210-5.
23. Priscilla, S. J., Judi, V. A., Daniel, R., Sivaji, K. "Effects of chromium doping on the electrical properties of zno nanoparticles", *Emerging Science Journal*, Vol. 4, (2020), 82-88. DOI: 10.28991/esj-2020-01212
24. Sohrabi, S., Akhlaghian, F., "Fe/TiO₂ catalyst for photodegradation of phenol in water", *International Journal of Engineering, Transactions A: Basics*, Vol. 28 (2015) 499-506. DOI: 10.5829/idosi.ije.2015.28.04a.02

Persian Abstract

چکیده

در این مطالعه، نانوکامپوزیت AgI-ZnO/کیتوزان سنتز شد و روی صفحات شیشه ای $200 \times 40 \times 2$ تحت تابش UVA پوشانده شد، سپس برای از حذف تولون از جریان هوا به کار برده شد. نانوکامپوزیت کیتوزان/AgI-ZnO با استفاده از تکنیک های XRD، SEM، FTIR و BET بررسی شد. تجزیه و تحلیل نشان داد که Zn و Ag به ترتیب با درصد وزنی 32/02 و 7/31 درصد به ساختار کامپوزیت اضافه شدند که تأیید کرد که نانوکامپوزیت AgI-ZnO/کیتوزان با موفقیت سنتز شده است. با توجه به نتایج، فرآیند فوتوکاتالیستی توانست 74/6 درصد تولون را با سرعت جریان هوا 1 لیتر بر دقیقه پس از 3/3 دقیقه حذف کند. همچنین، با افزایش میزان جریان عبوری از 0/3 به 1/5 لیتر در دقیقه از طریق راکتور فوتوکاتالیستی، راندمان فرآیند حذف تولون افزایش یافت. راندمان حذف تولون با افزایش رطوبت نسبی با گذشت زمان کاهش می یابد. علاوه بر این، افزایش رطوبت نسبی ظرفیت فوتوکاتالیست را برای حذف آلانده هدف کاهش می دهد. نتایج حاکی از آن است که غلظت اولیه تولون در جریان ورودی نقش اساسی در فوتوکاتالیز تولون داشته و با افزایش بیشتر غلظت آلانده بالاتر از 20ppm، عملکرد آن به طرز چشمگیری کاهش می یابد. بنابراین، فرآیند پیشنهادی می تواند و یک تکنیک موثر برای حذف تولون از جریان هوای آلوده تحت تابش اشعه ماورا بنفش مورد استفاده قرار گیرد. و افزایش دما تا 60 درجه سانتیگراد عملکرد آن را افزایش دهد.



The Effects of BIM Maturity Level on the 4D Simulation Performance: An Empirical Study

M. Dadashi Haji^a, H. Taghaddos^{*b}, M. H. Sebt^a, F. Chokan^b, M. Zavari^a

^a Department of Civil and Environmental Engineering, Amirkabir University of Technology (Tehran polytechnic), Tehran, Iran

^b School of Civil Engineering, College of Engineering, University of Tehran, Tehran, Iran

PAPER INFO

Paper history:

Received 04 December 2020

Received in revised form 05 January 2021

Accepted 11 January 2021

Keywords:

Building Information Modeling

Simulation

Maturity Model

4D BIM

BIM Benefits

ABSTRACT

Building information modeling (BIM) has attracted considerable interest in the area of 4D simulation. The performance and benefits of the 4D simulation can be affected by different factors, such as the organizational integration of the teams involved in the project and the models' content, which is recognized as the maturity level of BIM. Despite the various advantages of implementing 4D BIM and the significance of obtaining the full potential of 4D simulation, there is a scant number of researches that have considered this issue. Thus, this study aims not only to assess the relationship between the performance of 4D simulation and different maturity levels but also to clarify the required Level of Development (LOD) and maturity level in BIM application to synchronize the BIM implementation process with its expected benefits. For this purpose, the differences in gained benefits of implementing 4D BIM in various projects, which had different BIM maturity levels, were examined. The results showed that promoting the integration of the BIM implementation process, considering suitable LOD for modeling, and clarifying the expectation from different parts of a project lead to an enhancement in the performance of BIM 4D simulation.

doi: 10.5829/ije.2021.34.03c.03

NOMENCLATURE

AIA	American Institute of Architecture	LOD	Level of development
AEC	Architecture, engineering, and construction	MEP	Mechanical, electrical, and plumbing
BIM	Building information modeling	NBIMS	The National BIM Standard
ISPS	Integrated Site Planning System	PMO	Project management office

1. INTRODUCTION

Nowadays, one of the main goals of every country is obtaining faster growth compared to others. Adopting new technologies and the need for modernization play a significant role in achieving this objective [1]. For instance, the advent of science and technology parks, which intend to develop new techniques, skills, methods, and processes used for producing goods or services or the accomplishment of objectives, provides a mechanism for sustainable development [2]. In this regard, researchers have been trying to reduce the negative impact of new technologies and improve their capabilities [3]. For example, different studies aimed to decrease global

environmental problems by offering new suggestions [4-6]. Building information modeling (BIM) as a relatively new technology in the construction industry can play a crucial role in industry development.

Before discussing any aspects of building information modeling, it is necessary to establish a clear definition of the term. Since BIM has drawn the interest of researchers in recent years, they have also attempted to define their terms that have led to a proliferation of definitions for BIM in the literature [7]. It is most frequently perceived as a tool for visualizing and coordinating architecture, engineering, and construction (AEC) tasks to avoid errors and omissions while improving the productivity, schedule, safety, cost, and quality of construction

*Corresponding Author Institutional Email: htaghaddos@ut.ac.ir (H. Taghaddos)

projects [8]. The National BIM Standard (NBIMS) presented the most common definition that conforms with the aims of this study. It defines BIM as "a digital representation of physical and functional characteristics of a facility. As such, it serves as a shared knowledge resource for information about a facility forming a reliable basis for decisions during its life-cycle from inception onward. The BIM is a shared digital representation founded on open standards for interoperability" [9]. In recent years, the use of BIM among the AEC industry for visualization has shifted from vision to realization. Moreover, according to the different levels of understanding of a construction project that a BIM model can provide, various dimensions are described. BIM technology has evolved from a basic 3D model to a more sophisticated 4D, 5D, 6D, and 7D. Every dimension has its specific purpose and usage in a project.

One of the fundamental concepts in BIM is maturity level, which is commonly defined as the quality, repeatability, and degree of excellence within a BIM capability. Differences in BIM maturity level can be distinguished by factors such as level of development (LOD), integration through the project's organization, economic purposes, and BIM implementation procedures [10]. Therefore, a literature review has been undertaken to collect available information about the benefits of 4D BIM and BIM maturity levels to form a holistic view of 4D modeling and its expected advantages, to identify the characteristics of different maturity levels, and to explore the level of development as a significant factor in modeling for visualization.

1. 1. Benefits Expected from BIM 4D Simulation

4D modeling refers to the linking of individual elements of 3D models or assemblies to the time or schedule for allowing the project team to coordinate stages of work [11]. Benjaoran and Bhokha proposed a structured method to develop 4D models. According to the method, 4D modeling starts with collecting the design information and transferring it into 3D models. Assigning different characteristic colors to groups of elements or categorizing them while undergoing the 3D modeling process not only makes it possible to identify the components quicker [12] but also facilitates the modification process of elements attributes [13]. As an instance of such grouping, different BIM software provides the possibility of placing elements in a selection set. Afterward, the previously prepared construction schedules can be integrated with the model using BIM tools to run the analysis. Based on the literature review, different research papers published within the last decade have studied the benefits of 4D BIM. Table 1 illustrates these advantages, which have been categorized into six groups.

A) 4D simulation can be used as a tool for revealing time-based risks [14, 15]. It plays a fundamental role in

TABLE 1. Benefits of 4D simulation in BIM

#	4D simulation benefits	References
A	Increasing project safety	[16-19]
B	Enhancing project site analysis and project monitoring	[20-23]
C	Improving integration of project schedule	[24-28]
D	Reducing change orders in construction phase	[11, 29, 30]
E	Reducing time due to the decrease in clashes and reworks	[11, 13, 28]
F	Improving coordination and contribution among different project stakeholders	[11, 27, 28, 31, 32]

analyzing what, when, why, and where safety measures are needed for preventing accidents [16]. Integrated safety management systems for projects during the construction phase include 4D models to automate hazard identification processes by linking models to risk data. This process would make it possible to visualize the risks of each activity [17-19].

B) A project's site analysis and monitoring can be enhanced by using 4D models. A 4D Integrated Site Planning System (4D-ISPS) allows for better control of the construction phase by integrating progress measurements with existing 4D models [20, 23]. Using technologies such as Laser Scanner can improve the controlling process by providing 3D as-built models that can be compared with 4D models [21]. Visualizing the performance metrics has also been used for representing progress deviations by superimposing 4D as-planned models over time-lapsed photographs [22].

C) 4D simulation improves the integration of the project schedule when the integrated database is used as an information resource to support improved planning of project activities. Furthermore, the capability to implement upgraded approaches, such as resource flow, during a project's progress boosted this process [24, 25]. Exploring various construction strategies to meet delivery dates, and to assure stakeholders about the achievability and accuracy of a schedule has enhanced the reliability of the constructability review process [26, 28].

D) The virtual execution of a project led the decision-makers to address construction-phase problems during the planning phase. Reducing change orders in the construction phase can unquestionably be counted as one of the benefits of 4D models [18].

E) Time-based clash detection has a significant role in verifying the planned construction sequences to confirm that activities can occur without creating conflicts [11].

F) 4D BIM modeling has also been used as a tool for improving the efficiency of decision-making meetings. Visualization techniques can allow for better

coordination among the project planners. Moreover, clarifying the activities for project teams may cause a better understanding of the expectations and would make the schedule more reliable [11].

1. 2. BIM Maturity Levels BIM maturity levels have been established to define BIM capabilities clearly in the AEC industry. These refer to quality, repeatability, and degree of excellence within a BIM capability [32]. BIM maturity levels (depicted in Figure 1) are classified into five categories: (a) Initial, (b) Defined, (c) Managed, (d) Integrated and (e) Optimized.

Each maturity level is defined concerning the content of models, procedure and strategies, integration among different parts of a project, and purposes of BIM implementation [29]:

- **Maturity Level A (Initial):** At this level, the lack or absence of an overall strategy and shortage of defined processes for BIM implementation is tangible. BIM software tools are applied without sufficient prior investigations and preparations. BIM adoption looks like separated islands through the project, and some individuals distinctively try to use the BIM tools in part of their activities. This process suffers from the lack of active and consistent support of middle and senior management. A low rate of collaboration is the main characteristic of this level. Hence, BIM implementation typically occurs with little or no pre-defined process guides or standards [29].
- **Maturity Level B (Defined):** At this level, senior managers are familiar with BIM implementation. The processes and policies have been established to utilize BIM tools. Basic BIM guidelines are available, including training manuals, workflow guides, and BIM delivery standards. Training requirements are well-defined and typically provided only when needed. Collaboration between different parts of the project increases based on mutual relationships following process guides and standards [29].
- **Maturity Level C (Managed):** The aims and processes of BIM implementation are understood by most staff at this level. Moreover, a monitoring system and a detailed action plan are being devised. Business opportunities arising from BIM are acknowledged and used in marketing efforts. Modeling, 2D representation, quantification, specifications, and analytical properties of 3D models are managed through detailed standards and quality plans. BIM managers are hired to collaborate the responsibilities based on temporary project alliances or longer-term partnerships [29].
- **Maturity Level D (Integrated):** BIM implementation requirements and processes are integrated between different parts of a project through pre-defined channels at this level. Economic purposes of implementation are adopted with the activities of all staff involved in the project, from managers to lower-level

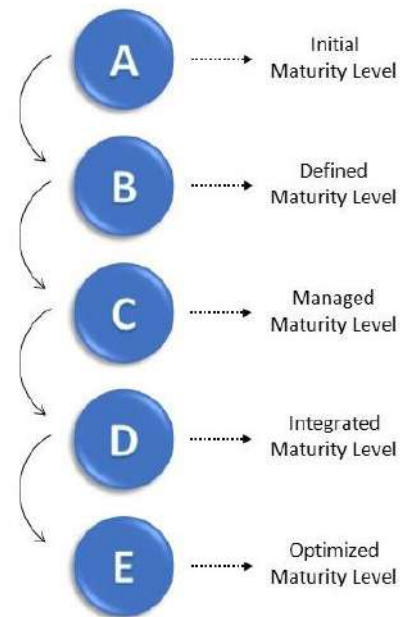


Figure 1. BIM Maturity Levels [27]

team members. Software choice follows the main objectives of the projects, not just operational requirements. Documentation of gained experiences and knowledge is carried out systematically, making it easy to access and retrieve [29].

- **Maturity Level E (Optimized):** BIM implementation at this level is pervasive among project stakeholders, as their strategies and processes are continuously monitored and revised to best match with each other. BIM software tools used in the project can change if needed to meet strategic benchmarks. Contractual models are also modified to achieve the highest value for all stakeholders [33].

1. 3. Level of Development The concept of level of development specifies the graphical representation and the information that a model must contain for its use at each phase of the project's life cycle [34]. One of the most cited definitions in the literature is related to the American Institute of Architecture (AIA), which categorizes the LOD into five levels [35, 36]: LOD100 to LOD500. At the first level, LOD100, a project model has represented generally, and some sorts of analysis (e.g., cost per square meter and building orientation) can be carried out. The next level, LOD200, is more precise than LOD100, and its generic elements can approximately represent the orientation, location, shape, size, and quantities. This level can be used for the analysis of selected systems by application of generalized performance criteria, such as investigation of the effects of colors in architecture [37]. In the third level, LOD300, building elements are specific and non-graphical

information can be added into the model, making it viable for use in documentation. The next level is LOD400, in which detailed elements can be useful for accurately representing processes such as fabrication, assembly, and installation. The last level, LOD500, is the most detailed level corresponding to a project's as-built model. Models at this level can be used for facility management and maintenance. Additionally, an intermediary level, LOD350, has been proposed between LOD300 and LOD400 to support different trades during construction by adding requirements on interfaces with other building systems [38]. LOD300 or LOD350 is sufficient for modeling during design phases unless some parts of the project deal with fabrication and assembly procedures. LOD grows during the design phase and reaches its peak during the construction phase [39]. The level of development at the design stage usually concentrates on geometrical issues, while at the construction phase, resources including equipment, materials, and labor are dominant.

The level of development is also related to the BIM maturity level, especially at the initiation of the project and contractual phases. Implementing BIM at higher maturity levels entails addressing more issues and more complicated details based on the differences in the responsibilities, relationships, collaboration level, and technologies at each level of maturity [40].

In conclusion, BIM maturity level has been clarified in different contexts, such as software platforms [41]; however, a lack of assessment of the consequences of implementing BIM at those levels was apparent in past studies. Moreover, although Dakhil and Alshawi explained BIM implementation benefits within each BIM maturity level, they neglected to quantify such implementation benefits within each maturity level [42]. Furthermore, researchers have been studying the visualization provided by BIM, but few studies have examined the distinction in the benefits gained from implementing 4D BIM simulation at different levels of maturity. Thus, this research aims to empirically measure survey data from two actual construction projects with different BIM maturity levels to investigate the expected benefits of implementing 4D simulation.

The remainder of the article is organized as follows. The research methodology is discussed in section 2. Section 3 defines the details of projects, which are considered for the case study. Section 4 demonstrates the results and discussion. In the end, some conclusions are presented in Section 5.

2. METHODOLOGY

In this study, the benefits of increasing from the initial maturity level to the integrated maturity level, and the effectiveness of BIM maturity level for profitable BIM

implementation are investigated empirically. For this intention, the BIM maturity level of two construction projects is determined. Next, the collected data about the gained benefits within each case is discussed. Figure 2 shows the proposed methodology of this study. The above two steps are further elaborated below.

For the first step, the major measuring aspects of BIM maturity level were investigated by reviewing the literature. Then, the procedure of BIM implementation, coordination, and integration between different parts of the project, the financial aims of implementation, and its perception in project organization were surveyed in both projects to determine their maturity levels.

Next, a questionnaire was designed to assess the benefits of increasing from the initial maturity level to the integrated maturity level, and the effectiveness of BIM maturity level for profitable BIM implementation based on the information gathered from the literature. Then, the questionnaire was reviewed and improved according to the comments of a group of six BIM experts, including both BIM engineers and academic researchers. Four of the BIM experts worked on both projects and also had experience in the field of building information modeling. The two others were academic experts who worked on BIM and project scheduling as their field of study. The questionnaire was distributed among 36 BIM experts chosen from design engineers, engineers of project management office (PMO), and teams of Research and Development involved in both projects. The questionnaire was distributed through individual

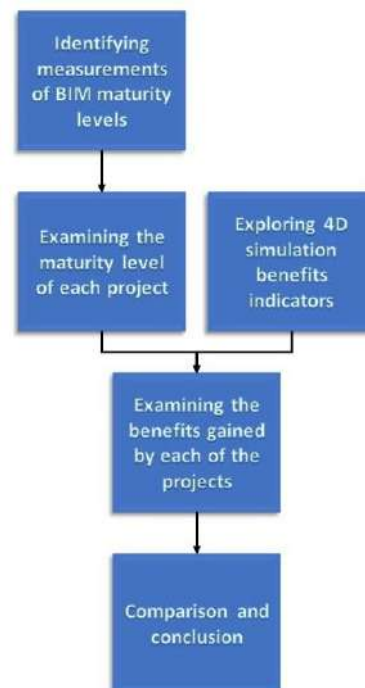


Figure 2. Flowchart of the proposed research methodology

interviews instead of sending via email, fax, or mailing them to clarify possible ambiguous questions for respondents. Ambiguities are one of the most dangerous elements of a survey that might affect the reliability and the usefulness of the results. In the survey, the following items were measured by reflective indicators with a five-point Likert scale (1= very low, 2= low, 3= medium, 4= high, 5= very high):

- improving integration of project schedule
- improving project site analysis and project monitoring
- increasing safety level in project
- reducing time-based clashes and reworks
- reducing change orders in construction phase
- enhancing coordination and contribution among different parts of the project

The reliability of the three questionnaires was measured by utilizing Cronbach's α coefficient, which is the most common measure of integral reliability when questions are asked on a Likert scale [43]. According to the definition of Cronbach's α coefficient, its normal range cannot be less than 0.0 and cannot be greater than +1.0. The reliability coefficients of 0.7 or higher are considered satisfactory, and the higher values reflect a higher degree of internal consistency.

3. CASE STUDIES

As mentioned, there are two construction projects in this study. The first case is a commercial building located in Tehran, named Atlas Mall. This project was the first of the company for BIM implementation. They utilized Autodesk products (e.g., Revit, Navisworks) to develop BIM models. The project details are as follows:

- Location of project: Tehran, Iran
- Number of floors: 19
- Total area: About 130,000 m²
- Schedule: 48 months

The second project is a commercial-therapeutic building located in Kerman, named Atlas Clinic (Figure 3). The project details are as follows:

- Location of project: Kerman, Iran
- Number of floors: 11
- Total area: About 12,000 m²
- Schedule: 48 months

4. RESULTS AND DISCUSSION

As mentioned, the survey was conducted among experts involved in two commercial construction projects undertaken by Iranian Atlas Company, a large-scale general contractor in Iran. All experts were familiar with the benefits and challenges of implementing 4D BIM in

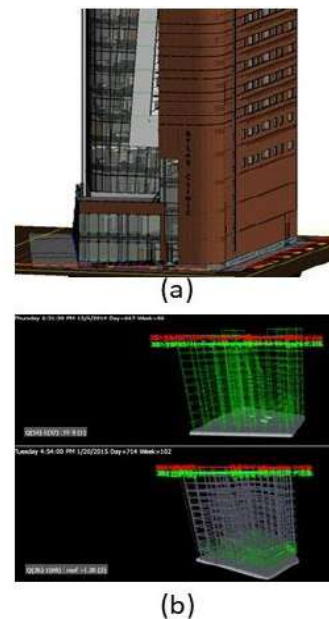


Figure 3. BIM model of Atlas Clinic project, a) 3D, b) 4D

both projects. The calculated Cronbach's α coefficient of the questionnaires was 0.876, which means that the reliability of the questionnaires was assured. Atlas Mall was the first project that was investigated for determining its level of BIM maturity. Autodesk BIM software, such as Revit, was used to model the various disciplines of the project. As it was the first attempt of the company for BIM implementation and there was a lack of experience, no specified procedure was employed within the project. Additionally, there was inconsistent LOD for different disciplines due to a lack of integration among various parts of the project. For instance, no commercial advantage was gained from detailed architectural 3D modeling, in which interior furnishing was modeled completely. While the model of mechanical, electrical, and plumbing (MEP) was not developed in detail. Thus, BIM implementation was at the initial maturity level according to the available definition of the literature.

Atlas Clinic, the second project investigated for determining its BIM maturity level, was also modeled using Autodesk products. In contrary to Atlas Mall, BIM implementation procedures and standards were set systematically by senior managers. Additionally, a procedure was established to define the duties of each part of the project organization and determine their relations. For instance, a committee that includes structural, architectural, MEP designers, a project control manager, and a representative of the scheduling team was in charge of promoting the integration between different parts of the project. They aimed to select a suitable LOD for the model based on the project's phases and needs.

In the process of 3D modeling, the most time-consuming activity was developing an architectural

model, and the wrong decision for LOD resulted in a large amount of time wasted on the first project. If the chosen LOD for the 3D model is higher than that required for scheduling, linking operations number and the length of time taken will increase. Moreover, the project schedule gains more details with the progress of the project. If any change is required in the 3D model or project scheduling, modifying the 4D simulation will be more difficult and time-consuming. Therefore, the joint committee played a significant role in better BIM implementation. The proposed LOD for the pre-construction phase was between LOD200 and LOD300, and the LOD for construction was developed from LOD100 to LOD400. One of the most significant issues noticed in the integration of design and project control sections was that LOD would not be the same for all the model's elements. For instance, in finding crane locations in the project site, LOD100 is adequate, and its increase does not impact the results.

Another challenging factor in the Atlas Clinic project was the process of matching the LOD of the 3D model to the required one for the project schedule in the 4D simulation. As the project schedule consisted of approximate activity sequences in the pre-construction phase, and it did not contain construction dates and project milestones. One of the experiences gained through this project was the preferability of providing a detailed schedule just before the construction phase. Consulting with the site manager can also be efficacious in optimizing the scheduling process. Moreover, the 4D modeler team devoted considerable effort to develop a project schedule that matches with the 3D models. Providing selection sets in 3D models and naming the elements helped reduce the amount of work necessary to link the model to the schedule. Furthermore, the anticipation of many problems and solving them before being encountered during project execution was the result of undertaking project simulation before on-site execution and caused considerable cost and time savings. The relation defined between the site and 4D modeling teams was improved by comments sent from the project's site through the BIM implementation process. Alternative solutions were assessed in 4D simulation to help managers choose the best option, such that 4D simulation played the role of decision support system. In conclusion, the Atlas Clinic project can be categorized at the fourth maturity level according to the literature. Table 2 shows a comparison of the two projects in regards to maturity criteria.

Considering the different criteria that are determinative of the BIM maturity level of a project, the maturity level of Atlas Mall and Atlas Clinic was initial and integrated, respectively. Figure 4 depicts the impacts of BIM maturity level on different benefits of BIM implementation. The chart is drawn based on the results of the questionnaire analysis. The positive effects

TABLE 2. A comparison between Atlas Mall and Atlas Clinic projects

Criteria	Atlas Mall	Atlas Clinic
BIM implementation process	No pre-defined process	BIM implementation procedure was defined concerning the integration and interaction between different parts of the project
Software selection	No strategy was defined for choosing software	The software was chosen based on the project's needs and the analysis required during project execution
Economic purposes of BIM implementation	No economic purpose	BIM models were used in the process of preselling
Systematic documentation	No BIM-based process	An internal system for communication, integration, and documentation was carried out

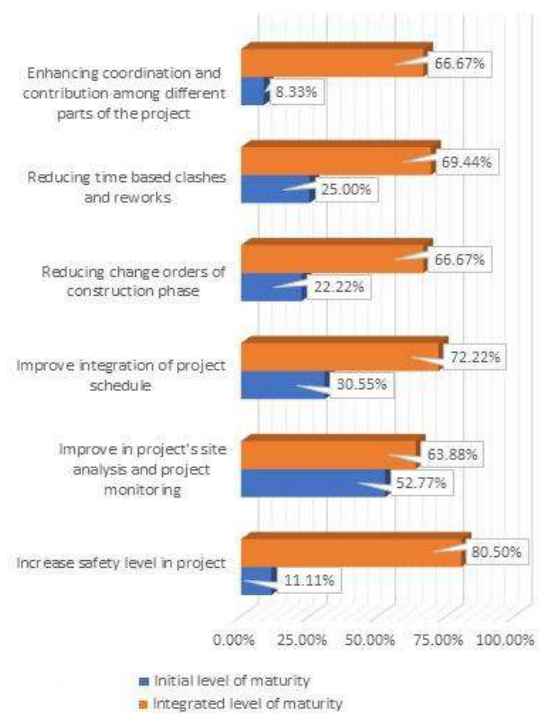


Figure 4. Effectiveness of BIM maturity level for advantageous BIM implementation

of BIM maturity level on the advantages of BIM implementation can be concluded clearly.

As shown in the chart, the 4D simulation of the Atlas Mall project had not gained the full potential of most of BIM 4D's benefits, including safety, schedule integration, change order reduction, decreased time-based clashes, and coordination improvement. However, it can be inferred that the first and most easily achieved

benefit of 4D modeling is improving project site analysis and monitoring. This benefit stems from BIM's visualization outputs provided by time-based modeling of the project. This capability allows for a visual comparison, even with low or inconsistent levels of detail among the elements, between a project's real progress and what the managers expected to see. The media representing the discrepancies between planned and actual progress of the project (e.g., charts, graphs, and still photos) may not facilitate the communication of progress information clearly and quickly, which makes the process time-consuming and distracts decision-makers from the vital task of corrective decision making [44]. A series of conceptual visualization techniques have been recently developed to facilitate the communication of progress information and decision making on corrective actions. However, it should be considered that the increase in the effectiveness of 4D BIM in the project's site analysis and monitoring was not dramatic by implementing BIM at a higher level of maturity.

The low maturity level of the Atlas Mall project caused many of the 4D modeling benefits to be marginalized, whereas Atlas Clinic had benefited remarkable advantages due to its increase in the level of maturity to the integrated stage. For instance, considering the results of time-based clash reduction and safety improvement can be concluded that in the Atlas Mall project time-based risk identification did not occur due to its initial maturity level. On the other hand, entering the high maturity level terms in the project execution process of Atlas Clinic improved BIM 4D utilization. One of the most significant applications of 4D models is discovering the time-based clashes. For instance, based on the experience of implementing BIM, simultaneous executions of a part of the roof and a lower floor's shear wall was not possible. This fact's clarification prevented unforeseen changes in the schedule during the construction phase. As shown in the result, the more detailed and integrated modeling process is, the more applicable the 4D models become.

In addition, the relationship between the number of BIM projects that each of the respondents experienced and their respective answers to the survey questions were analyzed. The results showed that former experience of working on BIM projects had a profound effect on respondents' opinions. In other words, experts with three or more years of experience on BIM-based projects had a significantly higher evaluation of the benefits of 4D BIM simulation at the integrated level of maturity. Thus, it can be implied that highly experienced experts have a deeper insight into the potential of 4D BIM simulation. Figure 5 depicts the differences between the responses of experts considering their duration of BIM involvement experience.

Finally, this study results depict the positive impact of BIM maturity level on the 4D simulation, which is

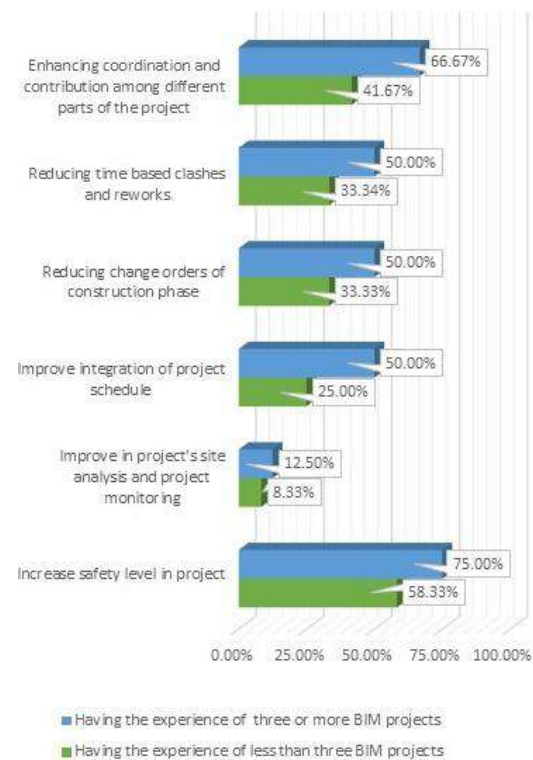


Figure 5. The effect of BIM experience on the experts' responses

consistent with existing literature. For instance, Smits et al. presented the maturity of the BIM implementation strategy as the only reliable predictor of time, cost, and quality performance [45]. In this study, other factors that would impact the project performance were examined, and their positive effects were shown. The other lesson following from this research was the significance of developing and observing specified standards and procedures for BIM implementation.

5. CONCLUSION

BIM, as a digital representation of physical and functional characteristics of a facility, has drawn exceptional attention from researchers and practitioners of the AEC industry. Among the vast area of BIM studies, 4D simulation is one of the prevalent issues that has been frequently investigated and implemented in many cases. Nonetheless, there is a lack of research that examines the relationship between the different factors, such as the BIM maturity level, and the potential benefits that can be gained from a 4D simulation of construction projects. The objective of this paper is to study the effects of BIM maturity level on the performance of the 4D simulation. For this purpose, two commercial construction projects, which were undertaken by the

Iranian Atlas Company, were selected as cases. Both projects have 4D BIM models, which were developed in different disciplines. The BIM maturity level and gained benefits of implementing the 4D simulation of each project were assessed to clarify whether there is a relationship between them.

BIM maturity level is illustrated the BIM capabilities in the AEC industry. The maturity level of projects' BIM models was investigated and determined, considering the criteria extracted from the literature. On the other hand, a questionnaire was distributed among 36 professionals engaged with both projects ask them to rate the achievability of various benefits expected from the 4D simulation. The results depict that enhancing the maturity from initial to integrated level has a profound effect on the achievement of expected benefits, such as increasing the safety level of a project, improving the integration of the project schedule, reducing change orders in the construction phase, improving coordination and contribution among different parts of projects and reducing time-based clashes and reworks. Moreover, it was notable that improving the project's site analysis and project monitoring is an advantage that can be obtained easily by implementing 4D BIM, regardless of considering inconsistent levels of detail in model elements, temporary facilities such as cranes or scaffolds, and an integrated procedure for BIM implementation. Additionally, the results showed that highly experienced experts have a deeper insight into the potential of 4D BIM simulation.

Future efforts will focus on extending the research scope to all stakeholders involved in construction projects and assessing all five levels of maturity by surveying on a higher number of projects.

6. ACKNOWLEDGEMENT

The authors would like to thank the experts and staff of the Iranian Atlas Company, who shared their time for supporting this study.

7. REFERENCES

- Aryal, K., Thapa, P.S. and Lamichhane, D., "Revisiting agroforestry for building climate resilient communities: A case of package-based integrated agroforestry practices in nepal", *Emerg Science Journal*, Vol. 3, No. 5, (2019), 303-311. doi:10.28991/esj-2019-01193
- Saryazdi, A.H.G. and Poursarrajian, D., "Qualitative system dynamics model for analyzing of behavior patterns of smes", *HighTech and Innovation Journal*, Vol. 2, No. 1, (2021), 9-19. doi:10.28991/HIJ-2021-02-01-02
- Borowski, P.F., "New technologies and innovative solutions in the development strategies of energy enterprises", *HighTech and Innovation Journal*, Vol. 1, No. 2, (2020), 39-58. doi:10.28991/HIJ-2020-01-02-01
- Burciaga, U.M., Sáez, P.V. and Ayón, F.J.H., "Strategies to reduce co2 emissions in housing building by means of cdw", *Emerging Science Journal*, Vol. 3, No. 5, (2019), 274-284. doi:10.28991/esj-2019-01190
- Procházka, L. and Boháčová, J., "Effect of admixtures on durability characteristics of fly ash alkali-activated material", *Emerging Science Journal*, Vol. 4, No. 6, (2020), 493-502. doi:10.28991/esj-2020-01247
- Burciaga, U.M., "Sustainability assessment in housing building organizations for the design of strategies against climate change", *HighTech and Innovation Journal*, Vol. 1, No. 4, (2020), 136-147. doi:10.28991/HIJ-2020-01-04-01
- Barlish, K. and Sullivan, K., "How to measure the benefits of bim—a case study approach", *Automation in construction*, Vol. 24, (2012), 149-159. doi:10.1016/j.autcon.2012.02.008
- Zuppa, D., Issa, R.R. and Suermann, P.C., Bim's impact on the success measures of construction projects, in *Computing in civil engineering* (2009). 2009.503-512. doi:10.1061/41052(346)50
- AlizadehKharazi, B., Alvanchi, A. and Taghaddos, H., "A novel building information modeling-based method for improving cost and energy performance of the building envelope", *International Journal of Engineering*, Vol. 33, No. 11, (2020), 2162-2173. doi:10.5829/IJE.2020.33.11B.06
- Alvanchi, A., Shiri, N. and Alikhani, H., "In-depth investigation of project planning and control software package application in the construction industry of iran", *International Journal of Engineering*, Vol. 33, No. 10, (2020), 1817-1825. doi:10.5829/IJE.2020.33.10A.01
- Trebbe, M., Hartmann, T. and Dorée, A., "4d cad models to support the coordination of construction activities between contractors", *Automation in construction*, Vol. 49, No., (2015), 83-91. doi:10.1016/j.autcon.2014.10.002
- Benjaoran, V. and Bhokha, S., "Enhancing visualization of 4d cad model compared to conventional methods", *Engineering, Construction and Architectural Management*, Vol. 16, No. 4, (2009), 392-408. doi:10.1108/09699980910970860
- Zhou, Y., Ding, L., Wang, X., Truijens, M. and Luo, H., "Applicability of 4d modeling for resource allocation in mega liquefied natural gas plant construction", *Automation in Construction*, Vol. 50, (2015), 50-63. doi:10.1016/j.autcon.2014.10.016
- Hernadewita, H. and Saleh, B., "Identifying tools and methods for risk identification and assessment in construction supply chain", *International Journal of Engineering*, Vol. 33, No. 7, (2020), 1311-1320. doi:10.5829/IJE.2020.33.07A.18
- El Hiri, M., En-Nadi, A. And Chafi, A., "Suppliers selection in consideration of risks by a neural network", *International Journal of Engineering*, Vol. 32, No. 10, (2019), 1454-1463. doi:10.5829/IJE.2019.32.10A.15
- Chantawit, D., Hadikusumo, B.H., Charoenngam, C. and Rowlinson, S., "4dcad-safety: Visualizing project scheduling and safety planning", *Construction Innovation*, Vol. 5, No. 2, (2005), 99-114. doi:10.1191/1471417505ci0910a
- Benjaoran, V. and Bhokha, S., "An integrated safety management with construction management using 4d cad model", *Safety Science*, Vol. 48, No. 3, (2010), 395-403. doi:10.1016/j.ssci.2009.09.009
- Zhang, J. and Hu, Z., "Bim-and 4d-based integrated solution of analysis and management for conflicts and structural safety problems during construction: 1. Principles and methodologies", *Automation in Construction*, Vol. 20, No. 2, (2011), 155-166. doi:10.1016/j.autcon.2010.09.013
- Kang, L.-S., Moon, H.-S., Kim, H.-S., Choi, G.-Y. and Kim, C.-H., Development of 5d cad system for visualizing risk degree and progress schedule for construction project, in *Computing in civil engineering* (2011). 2011.690-697. doi:10.1061/41182(416)85

20. Ma, Z., Shen, Q. and Zhang, J., "Application of 4d for dynamic site layout and management of construction projects", *Automation in Construction*, Vol. 14, No. 3, (2005), 369-381. doi:10.1016/j.autcon.2004.08.011
21. Turkan, Y., Bosche, F., Haas, C.T. and Haas, R., "Automated progress tracking using 4d schedule and 3d sensing technologies", *Automation in Construction*, Vol. 22, (2012), 414-421. doi:10.1016/j.autcon.2011.10.003
22. Golparvar-Fard, M., Peña-Mora, F., Arboleda, C.A. and Lee, S., "Visualization of construction progress monitoring with 4d simulation model overlaid on time-lapsed photographs", *Journal of Computing in Civil Engineering*, Vol. 23, No. 6, (2009), 391-404. doi:10.1061/(ASCE)0887-3801(2009)23:6(391)
23. Zhang, C. and Arditi, D., "Automated progress control using laser scanning technology", *Automation in Construction*, Vol. 36, (2013), 108-116. doi:10.1016/j.autcon.2013.08.012
24. Dawood, N., Sriprasert, E., Mallasi, Z. and Hobbs, B., "Development of an integrated information resource base for 4d/vr construction processes simulation", *Automation in Construction*, Vol. 12, No. 2, (2003), 123-131. doi:10.1016/S0926-5805(02)00045-6
25. Jongeling, R. and Olofsson, T., "A method for planning of workflow by combined use of location-based scheduling and 4d cad", *Automation in Construction*, Vol. 16, No. 2, (2007), 189-198. doi:10.1016/j.autcon.2006.04.001
26. Russell, A., Staub-French, S., Tran, N. and Wong, W., "Visualizing high-rise building construction strategies using linear scheduling and 4d cad", *Automation in Construction*, Vol. 18, No. 2, (2009), 219-236. doi:10.1016/j.autcon.2008.08.001
27. Kang, J.H., Anderson, S.D. and Clayton, M.J., "Empirical study on the merit of web-based 4d visualization in collaborative construction planning and scheduling", *Journal of Construction Engineering and Management*, Vol. 133, No. 6, (2007), 447-461. doi:10.1061/(ASCE)0733-9364(2007)133:6(447)
28. Hartmann, T. and Fischer, M., "Supporting the constructability review with 3d/4d models", *Building Research & Information*, Vol. 35, No. 1, (2007), 70-80. doi:10.1080/09613210600942218
29. Succar, B. and Kassem, M., "Building information modelling: Point of adoption", in CIB World Conference Proceedings. Vol. 1, No., (Year).
30. Zhao, Q., Li, Y., Hei, X. and Wang, X., "Toward automatic calculation of construction quantity based on building information modeling", in 2015 11th International Conference on Computational Intelligence and Security (CIS), IEEE. (2015), 482-485. doi:10.1109/CIS.2015.122
31. Mahalingam, A., Kashyap, R. and Mahajan, C., "An evaluation of the applicability of 4d cad on construction projects", *Automation in Construction*, Vol. 19, No. 2, (2010), 148-159. doi:10.1016/j.autcon.2009.11.015
32. Boton, C., Kubicki, S. and Halin, G., "Designing adapted visualization for collaborative 4d applications", *Automation in Construction*, Vol. 36, (2013), 152-167. doi:10.1016/j.autcon.2013.09.003
33. Succar, B., Sher, W. and Williams, A., "Measuring bim performance: Five metrics", *Architectural Engineering and Design Management*, Vol. 8, No. 2, (2012), 120-142. doi:10.1080/17452007.2012.659506
34. The American Institute of Architects, "AIA Document G202-2013", The American Institute of Architects, 2013.
35. Pinheiro, A.P., "Architectural rehabilitation and sustainability of green buildings in historic preservation", *HighTech and Innovation Journal*, Vol. 1, No. 4, (2020), 172-178. doi:10.28991/HIJ-2020-01-04-04
36. Solihin, W. and Eastman, C., "Classification of rules for automated bim rule checking development", *Automation in Construction*, Vol. 53, (2015), 69-82. doi:10.1016/j.autcon.2015.03.003
37. Kriphal, M. and Grilo, A., "Compatibility between design and construction building information models", *ECPPM Proceedings*, London, UK, Taylor & Francis Group, (2012), 447-452.
38. Sinclair, S., *Building information modelling (bim) & english law*. 2015, London, UK, John Wiley & Sons, Ltd. doi:10.1002/9781118838167.app3
39. Bouška, R., "Evaluation of maturity of bim tools across different software platforms", *Procedia Engineering*, Vol. 164, (2016), 481-486. doi:10.1016/j.proeng.2016.11.648
40. Dakhil, A. and Alshawi, M., "Client's role in building disaster management through building information modelling", *Procedia Economics and Finance*, Vol. 18, (2014), 47-54. doi:10.1016/S2212-5671(14)00912-5
41. Boton, C., Kubicki, S. and Halin, G., "The challenge of level of development in 4d/bim simulation across aec project lifecycle. A case study", *Procedia Engineering*, Vol. 123, (2015), 59-67. doi:10.1016/j.proeng.2015.10.058
42. AIA, A., "Document e202-2008", Building Information Modeling Protocol Exhibit, Washington, DC: American Institute of Architects, (2008).
43. Masood, R., Kharal, M. and Nasir, A., "Is bim adoption advantageous for construction industry of pakistan?", *Procedia Engineering*, Vol. 77, (2014), 229-238. doi:10.1016/j.proeng.2014.07.021
44. Fard, M.G. and Peña-Mora, F., Application of visualization techniques for construction progress monitoring, in *Computing in civil engineering* (2007). 2007.216-223. doi:10.1061/40937(261)27
45. Smits, W., van Buiten, M. and Hartmann, T., "Yield-to-bim: Impacts of bim maturity on project performance", *Building Research & Information*, Vol. 45, No. 3, (2017), 336-346. doi:10.1080/09613218.2016.1190579

Persian Abstract

چکیده

ابعاد مختلف مدل‌سازی اطلاعات ساختمان و علی‌الخصوص شبیه‌سازی چهاربعدی پروژه در سال‌های اخیر مورد توجه پژوهشگران مختلف قرار داشته‌است. اثرگذاری تفاوت‌های پیاده‌سازی مدل‌سازی اطلاعات ساختمان، که ذیل مبحث سطح بلوغ قرار می‌گیرد، می‌تواند کارکردهای مورد انتظار را تحت تأثیر قرار دهد. این تفاوت‌ها که از عوامل مختلفی از جمله یکپارچگی سازمان پیاده‌کننده و یا محتوای مدل، متأثر می‌باشد در پژوهش‌های انجام‌شده به طور کامل مورد توجه قرار نگرفته است. این پژوهش مزایای شبیه‌سازی چهاربعدی پیاده‌سازی شده در سطوح بلوغ متفاوت را مورد بررسی قرار داده است و با استفاده از تحلیل اطلاعات جمع‌آوری شده، سطح جزئیات و بلوغ مورد نیاز برای نیل به اهداف از پیش تعیین‌شده از پیاده‌سازی مدل اطلاعاتی ساختمان را تعیین می‌نماید. نتایج حاکی از این می‌باشد که یکپارچگی پیاده‌سازی مدل اطلاعاتی ساختمان در سازمان پروژه، در نظر گرفتن سطح جزئیات و شفاف‌سازی انتظارات بخش‌های مختلف سازمانی از پیاده‌سازی مدل اطلاعاتی ساختمان منجر به بهبود کارایی و اثربخشی پیاده‌سازی مدل اطلاعاتی ساختمان می‌شوند.



Enhancement of Stiffness in GFRP Beams by Glass Reinforcement

F. Marchione*

Dipartimento di Ingegneria Civile, Edile e Architettura (DICEA), Università Politecnica delle Marche, via B. Bianche, Ancona, Italy

PAPER INFO

Paper history:

Received 13 December 2020

Received in revised form 30 December 2020

Accepted 11 January 2021

Keywords:

Bending Tests

GFRP Beams

Adhesive Joint

Stiffness Enhancement

ABSTRACT

Glass is a stiff material with brittle structural behaviour. Hence, it is usually a material mostly decorative or simply structurally supported, and it is hardly ever a load-bearing element within a structure. Although in recent years there have been several experiments in its use in civil engineering, to date little data has been collected or design methodologies disseminated. The present study proposes the innovative concept of considering glass as a structural material, cooperating within a structural system thanks to the adhesive joining technique. In detail, the case of a GFRP structural beam element subjected to bending is herein considered. The evaluation of the stiffness of the mentioned element is compared with that of the same element reinforced with glass plates of different thicknesses. The results show the possibility to increase the global stiffness of the structural element. These outcomes are validated by FEM analysis, which showed excellent agreement with the analytical ones. The effectiveness of the reinforced system, thanks to the considerable stiffness characteristics, allows both the use of glass and the respect of the requirements related to the displacements of the structural elements in their service life.

doi: 10.5829/ije.2021.34.03c.04

NOMENCLATURE

URM	Unreinforced model	k	Stiffness
RM-i	Reinforced model with i-thick reinforcement	E	Young Modulus
I	Moment of inertia	b	Cross area width
t	Thickness	l	Beam Length
s	Displacement	F	Applied load

1. INTRODUCTION

Glass is a stiff material with brittle structural behaviour. In the building sector, there has been a significant increase in its use [1-3]. In fact, it is an element that allows light spaces to be created and gives a sense of lightness to the resulting element. However, despite the fact that the use of glass is very frequent (e.g. doors/windows [4], decorations, etc.) its structural applications are limited to date. In fact, in its usual applications, it is often configured as a supported object without any load-bearing function. Recent scientific and research advances are considering the development of glass or hybrid structures, characterised by the joining of glass with other traditional materials, such as timber [5-7], steel [8], GFRP [9].

However, in the study of these new structures, the main point is represented by the joints. In fact, joints are the most vulnerable points in any structure. In particular, in the case of glass structures, classical mechanical joints introduce undesirable concentrated stresses due to the brittle behaviour of glass. Stress peaks could lead to the diffusion of micro-cracks and therefore the rapid collapse of the structure or part of it for values of stresses lower than those characteristics of the material.

Therefore, the types of joints that could overcome this type of problem are the adhesive ones.

This type of joint provides several advantages, such as better and more uniform stress distribution, ease of application and little added weight to the resulting structure [10, 11].

Several papers, such as in Refs. [12, 13] show how the use of glass (a fragile material) coupled with other

*Corresponding Author Institutional Email:
f.marchione@pm.univpm.it (F. Marchione)

ductile materials (steel, GFRP, aluminium, timber) is able to create high-performance structures, capable of withstanding significant external actions both in and out of plane.

Parate [14] studied Propellant Actuated Devices (PAD), usually installed on various combat aircraft of Air Force. This study explains the development aspects of PAD, its use, function, testing and performance evaluation methodology in a suitable fabricated Velocity Test Rig (VTR). The main objective of this paper is to devise a novel method to measure actual slug velocity of the aircraft gun inside a cartridge using VTR and Doppler RADAR. Ntintakis et al. [15] studied the topology optimization by the use of 3D Printing Technology in the Product Design Process. In this study the authors initially print furniture models with different wall thicknesses using the Inject Binder technique and then we check their durability and resilience by compression tests. Then, the optimized models are redesigned in order to improve their durability. Ha [16] proposed a simple but effective trailing edge flap system. This preliminary concept uses a more practical and stable actuation system which consists of a motor-driven worm gear drive and flexible torsion bar. A preliminary level design study was performed to show the applicability of the new trailing edge flap system for wind turbine rotor blades or helicopter blade. Rastegarian et al. [17] studied the dependency of structural performance level and its corresponding inter-story drift in conventional RC moment frames. For this purpose, inter-story drift as a dependent variable and other structural characteristics have been assumed. Specimens were studied by means of pushover analysis.

Silvestru et al. [18] studied two configurations for such glass-metal façade elements, with silicone and acrylic adhesive respectively. Full-scale tests and FEA simulations are carried out for the two configurations with loads acting in three different directions, both separately and in combination. The results of the tests performed under in-plane shear load reveal a high load capacity of both configurations and show that the failure begun inside the adhesive layers.

Haldimann et al. [19] studied the performance of five adhesives for load-bearing steel-glass connections. Mechanical tests on the connections provided useful data for the selection of a suitable adhesive (silicone).

Richter et al. [20] illustrated the possibilities offered by existing hyperelastic material models for specific steel-glass components. Small-scale tests were carried out to characterise the adhesives and determine the material model for subsequent FEA.

Figure 1 illustrates the research methodology proposed.

Glass-fiber-reinforced pultruded materials (GFRP) represent innovative high-strength materials with low dead weight. However, they are particularly vulnerable

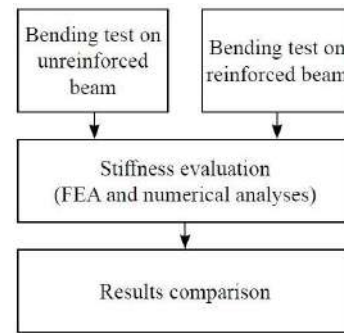


Figure 1. Research flowchart

to concentrated stresses (e.g. bolted joints). Therefore, the adhesive joint allows both to solve the problem of stress distribution and to improve the global behavior of the resulting structure, making the glass and the support beam structurally cooperating [21].

This paper illustrates the study of the problem of a GFRP beam and illustrates a simple method to improve its characteristics in terms of the overall stiffness of the structural element. This is sought through the insertion of a glass plate reinforcement at its extrados. The analytical and numerical methods for the evaluation of the stiffness of the structural configurations analysed are detailed in the following.

2. PROBLEM STATEMENT

In this section the simulations and calculations program carried out is defined.

The present paper illustrates the possibility of obtaining a significant increase in stiffness by means of an adhesive joint between a GFRP beam and a glass plate. GFRP and glass panels are bonded together by means of structural adhesive, as shown in Figure 2. The cross-section of the beam is depicted in Figure 2, and it will be analysed in the following. Numbers 1 and 2 indicate the GFRP and glass substrates, respectively. The adhesive thickness between the adherents is always considered constant and equal to 0.30 mm. The length of the beams is always considered to be 1.00 m.

Figure 3 illustrates the static scheme used in the subsequent analytical analysis. A pressure of 2.00 kPa is applied to the extrados surface of the beam.

The novelty of this concept concerns the realisation of a new type of load-bearing beam for structural uses, characterised by the coupling of a ductile material (e.g. GFRP) and a material known to be brittle (e.g. glass). The reinforcement by means of a glass plate is proposed only on the extrados of the beam both for architectural needs (e.g. transparent and light finish) and for needs related to the safety of the users.

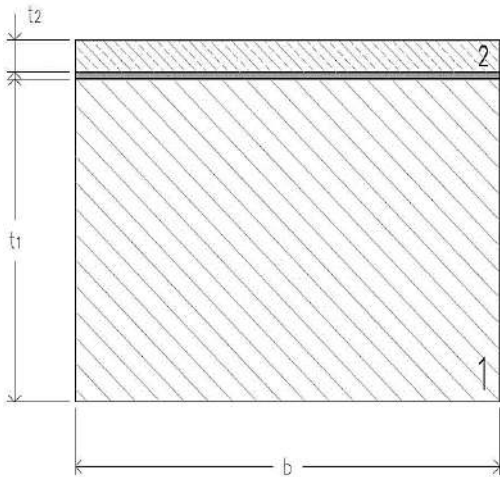


Figure 2. Beam cross section

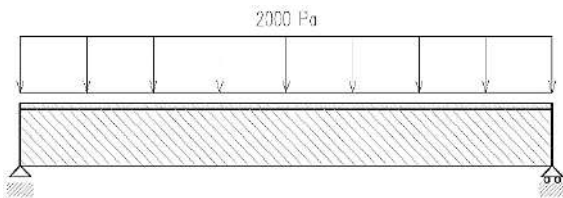


Figure 3. Static model of the beam

Table 1 shows the mechanical characteristics of the materials used in the models shown below.

Table 2 illustrates the acronyms and geometric characteristics of the beams considered in the following analyses

The results obtained from analytical calculations and FEM simulations are shown below.

TABLE 1. Materials' characteristics

	E [MPa]
Adhesive	3000
GFRP	26000
Glass	75000

TABLE 2. Beams geometric characteristics

Parameters				
Specimen	b (mm)	t ₁ (mm)	t ₂ (mm)	l (mm)
URM	70	50	-	1000
RM -10	70	50	10	1000
RM -15	70	50	15	1000
RM -20	70	50	20	1000

3. ANALYTICAL MODEL

Considering the static model of the beam (Figure 2) simply supported at its ends, the following equation could be written in relation to the value of the beam displacement:

$$s = \frac{F l^3}{48 E_b I_b} \tag{1}$$

where l is the length of the beam, E_b is the modulus of elasticity and F is the applied load. I represents the moment of inertia of the beam, given by the well-known equation:

$$I = \frac{b h^3}{12} \tag{2}$$

where b e t_b are width and length of the beam cross-section, respectively.

Stiffness k , defined as the load required to produce a unit displacement, is given by the following:

$$k = \frac{F}{s} = \frac{48 E_b I_b}{l^3} \tag{3}$$

To verify the effectiveness of the reinforcement in terms of stiffness, it is necessary to distinguish between perfectly adhesive behaviour between glass and substrate and no structural collaboration between the two elements. In the case of structural collaboration, the stiffness could be evaluated as follows:

$$k_{coop} = \frac{48}{l^3} \sum_{i=1}^2 E_i I_i^* \tag{4}$$

in which the moments of inertia are expressed as follows:

$$I_1^* = I_1 + A_1 \cdot x^2 \tag{5}$$

$$I_2^* = I_2 + A_2 \cdot \left[(t_2 - x) + \frac{t_2}{2} \right]^2 \tag{6}$$

The position of the neutral axis in relation to the centre of gravity of the section is then determined:

$$x = \frac{E_2 \cdot b \cdot t_2 \cdot \frac{t_1}{2} + E_2 \cdot b \cdot t_2^2 \cdot \frac{1}{2}}{2 E_1 \cdot t_1 \cdot t_2 + 2 E_1 \cdot b \cdot t_2 + E_1 \cdot b \cdot t_2} \tag{7}$$

In the case of non-collaborating elements, the stiffness could be expressed as follows:

$$k_{no-coop} = \frac{48}{l^3} \sum_{i=1}^2 E_i I_i \tag{8}$$

Where the moments of inertia are expressed as shown in Equation (2).

4. FEA ANALYSIS

This section illustrates finite element modeling for the above mentioned problem.

Finite element analyses are performed both in the case of unreinforced and reinforced beams, according to the geometric configurations illustrated in section 2.

The “Static Structural” module, present in ANSYS®19 is used, and the results are herein reported. The analysis is linear elastic, and the analysis is of 3D-type. The geometries illustrated are meshed with PLANE 182 elements, a 4-node structural solid and a maximum element size of 0.10 mm. Once the loads are applied, it is possible to correlate the maximum displacement with the force reactions at the ends of the beam, both for unreinforced and in reinforced beams.

4. RESULTS AND DISCUSSION

The present paragraph reports on the results obtained according to both the analytical and numerical analysis just presented.

Different geometrical characteristics have been considered in the reinforcement of the GFRP beam in the condition of cooperating reinforcement.

The beam theory is used to analyze the ductility and to evaluate the position of the neutral axis for a composite beam simply supported at its ends. The simulation validates the theoretical results by means of a linear elastic analysis of the model considered. The FEA simulation is conducted by means of the static analysis of the ANSYS®19 software. Table 3 illustrates and compares the results obtained from the different analyses.

The results obtained show a very accurate approximation of the analytical analysis for the evaluation of the stiffness increase brought by the glass reinforcement. In fact, a small evaluation error is observed for the reinforced configurations (within 15%).

Figure 4 shows the force-displacement graphs obtained from the analyses.

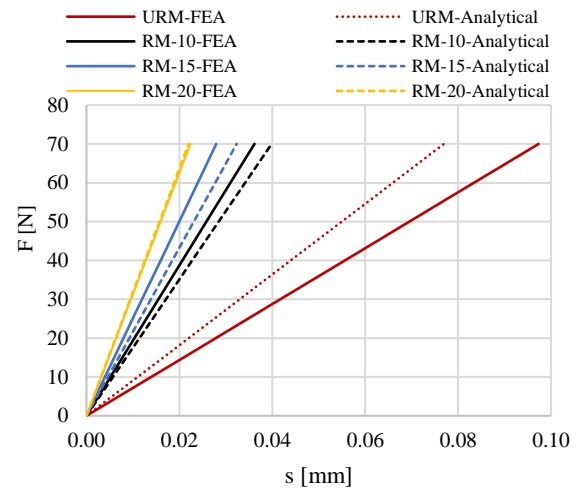


Figure 4. Load-displacement graph

TABLE 3. Analytical and FEA results

Specimen	b (mm)	t ₁ (mm)	t ₂ (mm)	l (mm)	k (N/mm)		
					ANSYS	Equation (4)	Δ (%)
URM	70	50	-	1000	719.22	910.00	-26.53
RM -10	70	50	10	1000	1934.98	1755.95	+ 9.25
RM -15	70	50	15	1000	2505.64	2165.32	+ 13.58
RM -20	70	50	20	1000	7409.29	3184.06	- 1.88

4. CONCLUSIONS

Recent legislations and technological developments lead to a continuous escalation of the technical requirements of structural elements in terms of both global and local ultimate strength. On the other hand, modern architectural language makes extensive use of glass as both a structural and purely decorative material. Indeed, glass allows the creation of luminous structures and provides an idea of lightness to the user. However, the structural applications of glass are currently very limited. The study here presented proposes a new hybrid beam in GFRP and glass for structural purpose. The result is a light and design structural element, which is therefore not relegated to a load-bearing function only, but also assumes an architectural value.

In detail, a GFRP beam in unreinforced configuration is considered and its stiffness is evaluated both numerically and analytically. Then, different combinations of glass reinforcements (i.e. plates of different thicknesses) were considered and analysed.

The main outcomes are:

- The hybrid system enables very high stiffness values to be obtained when compared with the same unreinforced structural element;
- The increase in stiffness that could be achieved makes it possible to meet very high requirements in terms of permissible displacements with the same structural elements, without introducing significant geometric changes in the section;
- FEA and analytical results are in good agreement and therefore make it possible to adequately assess

the increase in stiffness that could be achieved;

- The methodology illustrated allows for a quick and easy assessment of the stiffness contribution of the reinforcement and is therefore an effective design tool.

In conclusion, the present study provides an example of the calculation and application of glass in the field of civil engineering. The aim is to overcome the concept of glass as a material with merely decorative functions and to extend its function to the field of structures. The results reported demonstrate the effectiveness of its application in this purpose.

5. REFERENCES

1. Quini, J.G. and Marinucci, G., "Polyurethane structural adhesives applied in automotive composite joints", *Materials Research*, Vol. 15, No. 3, (2012), 434-439. doi: 10.1590/S1516-14392012005000042
2. Fecht, S., Vallée, T., Tannert, T. and Fricke, H., "Adhesively bonded hardwood joints under room temperature and elevated temperatures", *The Journal of Adhesion*, Vol. 90, No. 5-6, (2014), 401-419. doi: 10.1080/00218464.2013.836968
3. Godat, A., Légeron, F., Gagné, V. and Marmion, B., "Use of frp pultruded members for electricity transmission towers", *Composite Structures*, Vol. 105, (2013), 408-421. doi: 10.1016/j.compstruct.2013.05.025
4. Appelfeld, D., Hansen, C.S. and Svendsen, S., "Development of a slim window frame made of glass fibre reinforced polyester", *Energy and Buildings*, Vol. 42, No. 10, (2010), 1918-1925. doi: 10.1016/j.enbuild.2010.05.028
5. Rodacki, K., Tekieli, M. and Furtak, K., "Contactless optical measurement methods for glass beams and composite timber-glass i-beams", *Measurement*, Vol. 134, (2019), 662-672. doi: 10.1016/j.measurement.2018.09.061
6. Dorn, M., Enquist, B. and Serrano, E., "Load bearing timber glass composites—a woodwisdom—net project for innovative building system", in COST Action TU0905 Mid-term Conference on Structural Glass, CRC Press. (2013), 269. doi: http://dx.doi.org/10.1201/b14563-38
7. Unuk, Ž., Ivanič, A., Leskovar, V.Ž., Premrov, M. and Lubej, S., "Evaluation of a structural epoxy adhesive for timber-glass bonds under shear loading and different environmental conditions", *International Journal of Adhesion and Adhesives*, Vol. 95, (2019), 102425. doi: 10.1016/j.ijadhadh.2019.102425
8. Machalická, K., Vokáč, M. and Eliášová, M., "Influence of artificial aging on structural adhesive connections for façade applications", *International Journal of Adhesion and Adhesives*, Vol. 83, (2018), 168-177. doi: 10.1016/j.ijadhadh.2018.02.022
9. Bedon, C. and Louter, C., "Structural glass beams with embedded gfrp, cfrp or steel reinforcement rods: Comparative experimental, analytical and numerical investigations", *Journal of Building Engineering*, Vol. 22, (2019), 227-241. doi: 10.1016/j.job.2018.12.008
10. Marchione, F., "Investigation of vibration modes of double-lap adhesive joints: Effect of slot", *International Journal of Engineering*, Vol. 33, No. 10, (2020), 1917-1923. doi: 10.5829/ije.2020.33.10a.10
11. Marchione, F., "Stress distribution in double-lap adhesive joints: Effect of adherend reinforcement layer", *International Journal of Adhesion and Adhesives*, Vol. 105, (2021), 102780. doi: 10.1016/j.ijadhadh.2020.102780
12. Machalická, K. and Eliášová, M., "Adhesive joints in glass structures: Effects of various materials in the connection, thickness of the adhesive layer, and ageing", *International Journal of Adhesion and Adhesives*, Vol. 72, (2017), 10-22. doi: 10.1016/j.ijadhadh.2016.09.007
13. Marchione, F. and Munafò, P., "Experimental strength evaluation of glass/aluminum double-lap adhesive joints", *Journal of Building Engineering*, Vol. 30, (2020), 101284. doi: 10.1016/j.job.2020.101284
14. Parate, B.A., "Propellant actuated device for parachute deployment during seat ejection for an aircraft application", *HighTech and Innovation Journal*, Vol. 1, No. 3, (2020), 112-120. doi: 10.28991/HIJ-2020-01-03-03
15. Ntintakis, I., Stavroulakis, G.E. and Plakia, N., "Topology optimization by the use of 3d printing technology in the product design process", *HighTech and Innovation Journal*, Vol. 1, No. 4, (2020), 161-171. doi: 10.28991/HIJ-2020-01-04-03
16. Ha, K., "Innovative blade trailing edge flap design concept using flexible torsion bar and worm drive", *HighTech and Innovation Journal*, Vol. 1, No. 3, (2020), 101-106. doi: 10.28991/HIJ-2020-01-03-01
17. Rastegarian, S. and Sharifi, A., "An investigation on the correlation of inter-story drift and performance objectives in conventional rc frames", *Emerging Science Journal*, Vol. 2, No. 3, (2018), 140-147. doi: 10.28991/esj-2018-01137
18. Silvestru, V.A., Kolany, G., Freytag, B., Schneider, J. and Enghardt, O., "Adhesively bonded glass-metal façade elements with composite structural behaviour under in-plane and out-of-plane loading", *Engineering Structures*, Vol. 200, (2019), 109692. doi: 10.1016/j.engstruct.2019.109692
19. Haldimann, M., Luible, A. and Overend, M., "Structural use of glass, labse, Vol. 10, (2008).
20. Richter, C., Abeln, B., Geßler, A. and Feldmann, M., "Structural steel-glass facade panels with multi-side bonding—nonlinear stress-strain behaviour under complex loading situations", *International Journal of Adhesion and Adhesives*, Vol. 55, No., (2014), 18-28. doi: 10.1016/j.ijadhadh.2014.07.004
21. Alderucci, T., Terlizzi, V., Urso, S., Borsellino, C. and Munafò, P., "Experimental study of the adhesive glass-steel joint behavior in a tensegrity floor", *International Journal of Adhesion and Adhesives*, Vol. 85, (2018), 293-302. doi: 10.1016/j.ijadhadh.2018.04.017

Persian Abstract

چکیده

شیشه ماده ای سفت و سخت و دارای رفتار ساختاری شکننده است. از این رو ، این ماده معمولاً یک ماده عمدتاً تزئینی است و یا به سادگی از نظر ساختاری پشتیبانی می شود و به سختی یک عنصر باربر درون سازه است. اگرچه در سالهای اخیر چندین آزمایش در استفاده از آن در مهندسی عمران انجام شده است ، اما تاکنون اطلاعات کمی جمع آوری شده یا روشهای طراحی منتشر شده است. مطالعه حاضر مفهوم ابتکاری در نظر گرفتن شیشه به عنوان یک ماده ساختاری ، همکاری در یک سیستم ساختاری را به لطف روش اتصال چسب ارائه می دهد. به طور جزئی ، در اینجا یک مورد از عناصر پرتوی ساختاری GFRP تحت خمش مورد بررسی قرار می گیرد. ارزیابی سختی عنصر ذکر شده با همان عنصر تقویت شده با صفحات شیشه ای با ضخامت های مختلف مقایسه می شود. نتایج نشان می دهد امکان افزایش سختی جهانی عنصر سازه. این نتایج با تجزیه و تحلیل FEM تأیید می شود ، که توافق عالی با نتایج تحلیلی را نشان داد. اثربخشی سیستم تقویت شده ، به لطف ویژگی های قابل توجهی از سختی ، هم استفاده از شیشه و هم رعایت الزامات مربوط به جایجایی عناصر سازه ای را در طول عمر آنها فراهم می کند.



Application of Sorbent Waste Material for Porous Ceramics Production

S. Sverguzova^a, N. Miroshnichenko^a, I. Shaikhiev^b, Z. Saprionova^a, E. Fomina^{*a}, N. Shakurova^a, V. Promakhov^c

^a Department of Industrial Ecology, Belgorod State Technological University, Belgorod, Russia

^b Department of Environmental Engineering, Kazan National Research Technological University, Kazan, Russia

^c National Research Tomsk State University, Tomsk, Russia

PAPER INFO

Paper history:

Received 03 September 2020

Received in revised form 11 November 2020

Accepted 10 December 2020

Keywords:

Agricultural Waste

Porosity

Pumpkin Seed Husks

Waste Sorption Material

Sludge Disposal

Combustible Additive

ABSTRACT

The paper considers the application of waste sorption material utilization and pumpkin seed husks formed during the extraction of heavy metal ions from aqueous solutions, as a combustible additive to clay mixtures in production of the porous ceramics. In this regard, this study evaluates the effects of different amounts (2-8%) of the spent sorption material in the charge composition with changes in the physical and mechanical properties of ceramic samples obtained by firing at temperatures of 950-1050 °C. One finding is that the combustion of the organic additive is accompanied by the formation of voids and the release of gases with the formation of pores in the ceramic piece. Another finding is that all clay mixtures with a combustible additive allow the production of porous ceramics to meet the requirements for compressive strength, porosity, density, water absorption and linear shrinkage. It is recommended using 4 % of combustible additive in order to obtain optimal properties in terms of density and strength. During the testing of the developed porous ceramics for heavy metal leaching, the material does not pose an environmental hazard. Finally, the results of this study are applicable for the construction of internal partitions and household buildings.

doi: 10.5829/ije.2021.34.03c.05

1. INTRODUCTION

Wastewater treatment sludge is one of the most widespread and large-scale wastes. Annually, around the world, millions of tons of such wastes are generated, which are partially utilized and used later in agriculture and production cycles. However, most of them are stored at industrial landfills, disposing large areas of fertile soils and having a negative impact on the environment. In addition, construction is an industry where sewage sludge can be used. This excludes some costly and energy-intensive recycling steps and the resulting construction material is often stable and safe [1-3]. Extensive research was carried out on the use of sewage sludge in the production of building materials such as roofing tile, bricks, lightweight aggregates, cement, concrete and geopolymers [4,5]. Particular attention is paid to wastewater treatment sludge containing heavy metals. The potential hazard of heavy metals depends on the physic-chemical forms of metals in the sludge. Heavy metals are considered as one of the hazardous pollutants

because they are toxic with high persistence in the environment and food chain. In addition, these metals do not decompose and have the ability to accumulate in the environment and present one of the most dangerous pollutants in the biosphere [6,7].

The existing literature sources touch upon the issue of the economic efficiency of sorbents from agricultural crops for removing heavy metal ions from wastewater [8] and the efficiency of using agricultural waste in the construction industry [9-11]. The metal-containing wastes formed after water treatment pose an environmental hazard and necessitate their disposal. The use of organic sediments for water treatment of heavy metals is a promising option in the production of ceramic products [12,13] and porous ceramics [14]. This solution makes it possible to avoid secondary pollution and also increases the value of the waste converting it into a useful material. In addition, sewage sludge acts as a fuel during the sintering process and saves up to 40% of energy for firing [15].

*Corresponding Author Email: fomina_e.n@mail.ru (E. Fomina)

During sintering the components of organic matter coming from the sewage sludge additionally emit gases, which contribute to the formation of pores and the creation of a porous structure of ceramic material, which characterizes it as a combustive additive [16].

Recent studies in this research area reveal that the heat treatment allows the fixation of heavy metals coming from the sludge of treated wastewater in a silicate structure. When the sintering temperature of ceramics is reached, heavy metals interact with basic clay minerals (for example, alumina, kaolinite, and hematite) and form a crystalline phase of aluminosilicates and silicates [17,18]. The synthesis of various compounds can depend on temperature and basic oxide content.

One of the main trends in the literature review refers that the ceramic matrix stabilizes the mobility of heavy metals, reducing the potential hazard of their release [19,20]. According to the results of the leaching test, a low limit of extraction of metals such as Pb, Cd, Zn, Cr, Ni and Cu is noted [6], this confirms their stabilization in the ceramic structure of building material [21]. The tests carried out in the work [22] confirm the harmlessness of ceramic materials obtained using wastewater treatment sludge from heavy metals during their operation.

To provide an additional step to the advancement of knowledge in this research area and in order to expand the range of methodological approaches to the disposal of wastewater treatment sludge containing heavy metals in the production of ceramic products, we studied the effect of wastewater treatment sludge with nickel ions Ni^{2+} (WTSN), where crushed pumpkin seed husk (PSH) was used as a sorbent. The main purpose of this research is to develop porous ceramics with low density, high porosity and without significant changes in mechanical strength.

2. MATERIALS AND METHODS

We used the Yastrebovsky deposit clay (Belgorod region, Russia). The chemical composition (Table 1) was determined by X-ray fluorescence using ARL 9900 WorkStation X-ray fluorescence spectrometer with a built-in diffraction system, cobalt anode. According to the classification of clay raw materials GOST 9169-75 (Russia), this clay in terms of content ($Al_2O_3 < 15\%$) belong to acidic clay, in terms of the content of coloring oxides it belongs to a group with a high Fe_2O_3 content and a low TiO_2 content.

In order to study the features of phase formation and sintering of a ceramic piece, the measurements of heat and mass fluxes were carried out when clay samples were heated to $1000\text{ }^\circ\text{C}$. We used a STA 449 F1 Jupiter® synchronous thermal analysis by NETZSCH Proteus® software. According to the results (Figure 1) in the range from 70 to $130\text{ }^\circ\text{C}$ (peak point is $86.3\text{ }^\circ\text{C}$) the endothermic effect is observed associated with the removal of adsorbed water. The exo-effect is observed in the range from 130 - $430\text{ }^\circ\text{C}$ - organic impurities are combusted. Endoeffects characterizing the phase transitions of clay minerals occur in the ranges from 430 to $550\text{ }^\circ\text{C}$ (peak point is $469.3\text{ }^\circ\text{C}$). The endothermic effect characterizing the polymorphic transformations of quartz occurs in the range from 550 to $650\text{ }^\circ\text{C}$ (peak point is $577.8\text{ }^\circ\text{C}$). The endothermic effect of the decomposition of carbonates is observed in the range from 650 to $750\text{ }^\circ\text{C}$ (peak point is $724.6\text{ }^\circ\text{C}$). The determination of the phase composition of a clay sample, ground through a 008 sieve, was carried out by powder X-ray diffraction using ARL XTRA Termo Fisher Scientific diffractometer, copper Cu anode. In this regard, the results of X-ray of the clay are drawn in Figure 2.

TABLE 1. Clay chemical composition percentage

SiO_2	TiO_2	Fe_2O_3	CaO	MgO	Na_2O	K_2O	Al_2O_3	LOI	Σ
71.3	1.02	4.62	1.61	1.2	0.62	2.06	14.3	3.27	100.00

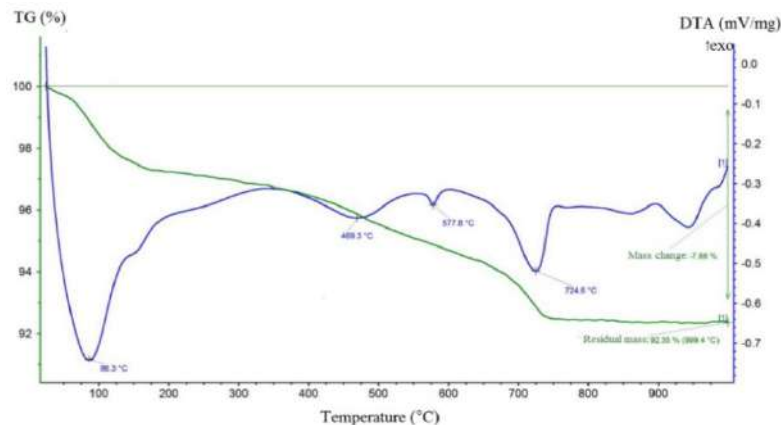


Figure 1. DTA and TG curves for the clay

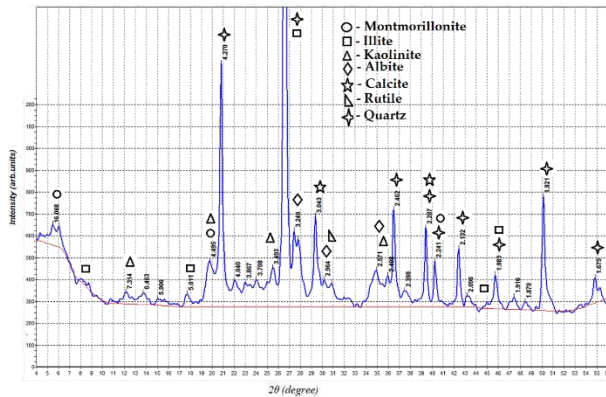


Figure 2. X-ray of the clay

In accordance with GOST 9169-75 (Russia), the following technological properties of clay were determined: plasticity; coefficient of sensitivity to drying. Based on the obtained indicators, the clay of the Yastrebovsky deposit belongs to the moderately plastic class - plasticity number $P = 15$; the studied clay is insensitive to drying with a sensitivity coefficient $K_s = 0.4$.

In addition, WTSN was obtained treating model waste water containing nickel ions. PSH was used as a sorbent. The number of Ni^{2+} ions in the solution was 100. The sorption material had a mass of 1 g. The solution with the sorbent was stirred for 20 minutes. The moisture content of the WTSN was 30%, the content of nickel ions was 0.24%. The size of the PSH particles used for cleaning was 1-2 mm. WTSN was used as a combustible additive in the preparation of porous ceramics.

In order to prepare clay samples, raw clay was roughly crushed in a laboratory jaw crusher. The crushed clay was dried to a moisture content of 7% and then dry grinding was carried out in laboratory runners of the "LM - 2e" brand, followed by sieving through a sieve No. 063. The WTSN additive was introduced in the amount of 2, 4, 6, 8 % while reducing the proportion of clay in the mixture. WTSN was mixed with clay in a mill for 15 minutes. Then the mixture of clay with the addition of WTSN was moistened with water to a moisture content of 18%. The prepared clay mass was kept for 7 days in order to complete the formation of adsorbed hydration shells. Then, the samples - cubes with a size of $30 \times 30 \times 30$ mm were molded from the clay mixture by plastic molding. Preliminary drying of the samples was carried out under natural conditions for 7 days and then in a drying cabinet at a temperature of $100-110^\circ C$ to a residual moisture content of 1% (4 hours at $T = 50-60^\circ C$ and 6 hours at $T = 110^\circ C$). The samples were fired in a SNOL-1/9 muffle furnace at temperatures of 950, 1000, $1050^\circ C$.

After firing, the samples were tested for a number of physical and mechanical properties, such as compressive

strength, average density, total porosity and water absorption in accordance with GOST 2409-95 (ISO 5017-88) (Russia). The samples without addition of WTSN were taken as control compositions.

The study of the microstructure of finished products was carried out using the method of scanning electron microscopy (SEM) by using high-resolution microscope TESCANMIRA 3 LMU.

3. MEASURES AND RESULTS

3. 1. Physical and Mechanical Properties of Ceramic Sample

With the addition of WTSN to the clay mixture, the number of voids and rounded pores of various morphology increases. Figure 3 shows the change in the structure of ceramic samples obtained at a firing temperature of $1050^\circ C$. The samples with the addition of WTSN have deep voids with broken edges with a maximum size of $100-400 \mu m$. Small micro-voids of $\leq 50 \mu m$ are noted. The size of closed pores is in the range $10-50 \mu m$.

The presence of voids is the result of the action of WTSN as a combustible additive. The micrograph of the ceramic structure of the sample fired at a temperature of $950^\circ C$ (Figure 4a) clearly shows a WTSN particle included in the clay matrix, which leaves fixed voids during combustion (Figure 4b). According to the literature [23-26], with the increase in the firing temperature of ceramic mixtures with organic combustible additives, the process of the formation of a

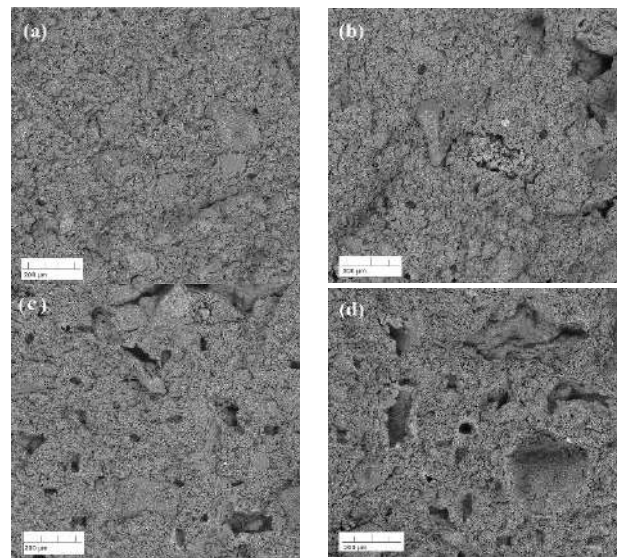


Figure 3. SEM analysis of the microstructure of ceramic samples fired at a temperature of $1050^\circ C$: (a) Without additive; (b) With the addition of 2% WTSN; (c) With the addition of 4% WTSN; (d) With the addition of 8% WTSN

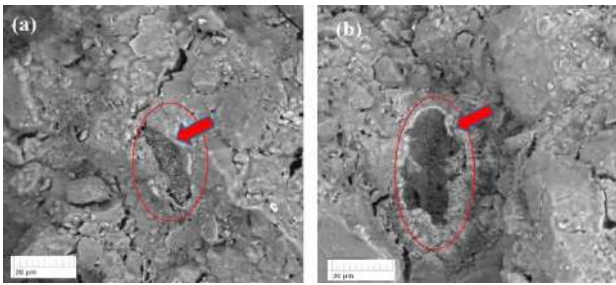


Figure 4. SEM analysis of the microstructure of ceramic samples: (a) With the addition of 4% WTSN, fired at a temperature of 950 °C; (b) With the addition of 4% WTSN, fired at a temperature of 1050 °C

liquid phase on the surface of the raw mixture particles intensifies. The formed water penetrates into pores and capillaries formed by gas release and participate in the processes of hydration of the cementing binder with the formation of thin films at the interface between the phases, contributing to the consolidation of pores and voids.

The pores in the structure of a ceramic piece are formed as a result of the participation of gaseous products of CO₂, released during the combustion of organic matter [27]. The visual analysis of ceramic brick samples is shown in Figure 5; where there is no color change and increase in the number of voids with the introduction of WTSN additive.

An increase in the concentration of voids has reflected in the total porosity of ceramic samples (Figure 6). It goes without saying that voids act as a barrier for heat flow. With an increase in the firing temperature from 950 to 1050 °C, the total porosity of the product decreases. The highest porosity of 30.9% was achieved with the addition of 8% WTSN and a firing temperature of 950 °C. The lowest values of porosity were 24.6% with the addition of 2% WTSN and a firing temperature of 1050 °C. An increase in the total porosity is reflected in the decrease in the density of ceramic samples (Figure 7). In this regard, this study uses the metal in the structure of the ceramic samples that potentially enhance thermal conductivity. It is noted that the maximum density

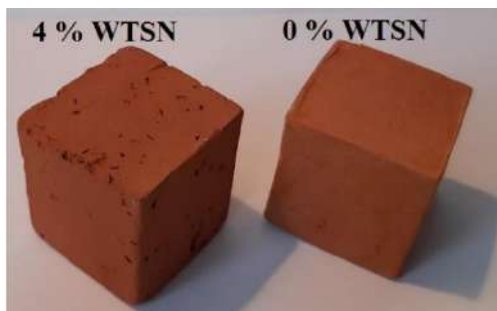


Figure 5. Samples of ceramic products based on 4% WTSN and 0% WTSN

reduction of 1590 kg/m³ is achieved with the introduction of an 8% additive and a firing temperature of 950 °C. The porous microstructure offers advantages for specific applications of the developed, such as thermal insulation or thermal resistance, which allows bricks to withstand sudden temperature changes through the reduction of the modulus of elasticity and shear [28]. Voids isolate the heat flow, causing the decrease in the thermal conductivity of the samples. The developed porous structure leads to an increase in the value of water absorption (Figure 8). It is known [29] that water absorption of a high-quality porous ceramic product should be within the range of 6 - 20% by mass. It is noted that in all studied cases, the water absorption indicators do not cross the permissible limit (20%). Figure 9 shows the change in the mechanical strength of clay samples. The strength of the samples decreases with an increase in the amount of additive and the increase in porosity, which is typical for porous ceramic materials [30]. The average compressive strength of the developed ceramic samples of the control composition (without additives) in the firing temperature range of 950-1050 °C was 21.5 MPa. Higher sintering temperatures increased compressive strength. With an increase in the concentration of WTSN in the ceramic matrix, it is accompanied by the decrease in the strength of the fired samples.

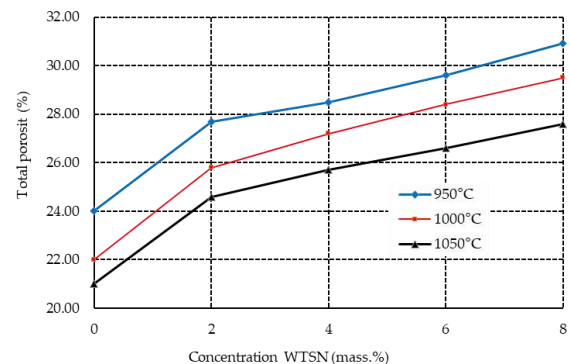


Figure 6. Change in the total porosity of ceramic samples from the composition of the charge and the firing temperature

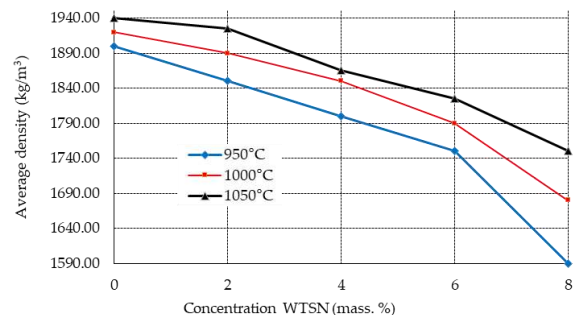


Figure 7. Change in the average density of ceramic samples from the composition of the charge and firing temperature

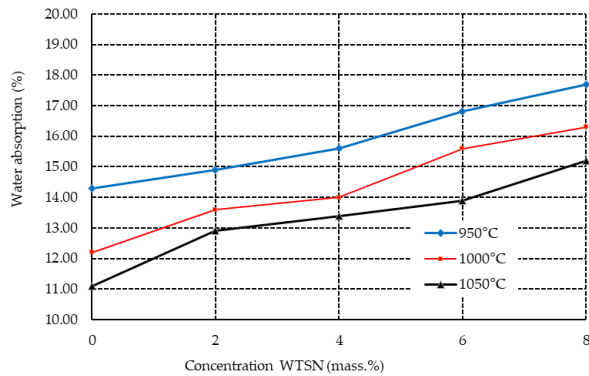


Figure 8. Change in water absorption of ceramic samples from the composition of the charge and firing temperature

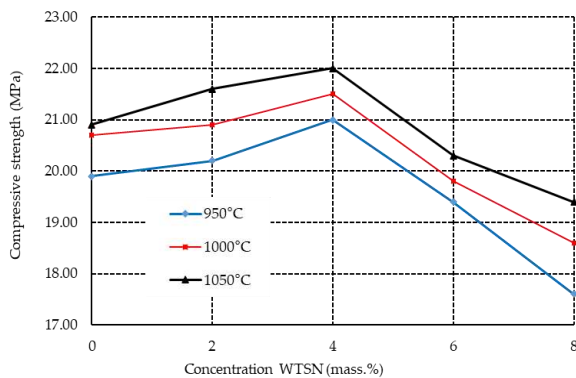


Figure 9. Change in the physical and mechanical properties of ceramic samples from the composition of the charge and firing temperature

According to the purpose of this study to obtain highly porous clay ceramics with sufficient strength, it is necessary to note that, in connection with the available data, the strength of porous ceramics with the use of organic combustible additives is in average 20-25 MPa [25,31-33].

We should admit that the optimal introduction of WTSN into the clay mixture as a combustible additive is up to 4%. In this case, the compressive strength is within acceptable limits of at least 20 MPa. The migration of gases through the matrix, obtained as a result of the combustion of WTSN in an amount of more than 4%, created a highly porous clay material, which negatively affected the mechanical strength.

In order to select the optimal firing mode and obtain ceramic objects with specified dimensions, the values of air and fire shrinkage of the dried and fired samples were determined at different firing temperatures (950-1050 °C) and different contents of the combustible additive WTSN. Shrinkage during drying is based on the amount of water in the test material. The amount of air shrinkage varies depending on the crystallinity of clay mineral. The change in the firing shrinkage based on the firing

temperature indicates the level of the caking of clay raw materials. Table 2 shows the observed shrinkage during the drying and firing cycles of clay bricks containing various concentrations of additives.

An increase in the mass fraction of WTSN in the composition of the clay mixture leads to the increase in the indicators of air and fire shrinkage. However, these changes do not lead to the deformation and deterioration in the quality of the resulting products. In accordance with GOST 530-2012 (Russia), for ceramic bricks, air shrinkage is allowed up to 8%, fire shrinkage - from 1% to 2%. All the values obtained are within the standard range. The observed relatively low values of air shrinkage of 2.27-2.79% when firing clay without additives is typical for sandy clays, such as used clay with a content of 71.3% SiO₂ (Table 1). An increase in the amount of introduced additive causes a natural increase in air and fire shrinkage, which is associated with the removal of residual and chemically combined water, as well as with the transformation of additives into ash. These chemical reactions during firing, along with rearrangement of particles and regulation in the crystal lattice, form a more compact solid texture in comparison with the initial state, which causes shrinkage deformations [34].

3. 2. Nickel Ion Leaching Testing of Porous Ceramics

The additive of waste sorption material contains compounds of heavy metals, potentially hazardous to the environment. We investigated the probability of migration into the environment of WTSN nickel ions, enclosed in the structure of a ceramic piece. Powder of porous ceramics with the addition of WTSN was ground to a particle size of less than 0.08 mm and placed in solutions of hydrochloric acid at pH = 3; 4; 5; 6, was kept for 24 hours at an aqueous medium temperature of 20 ± 0.5 °C. During the experiments, the specified pH value was maintained by acidification. Then the suspensions were filtered through a paper filter and the concentration of Ni²⁺ ions were determined by the atomic adsorption method according to GOST R 57162-2016 (Russia). The experimental results (Table 3) indicate the resistance of ceramic products to leaching of Ni²⁺ ions, which is estimated as the value of the concentration of Ni²⁺ ions in an acid solution.

TABLE 2. The impact of the content of wastewater treatment sludge in the raw mixture on the shrinkage¹ of ceramic samples

Burning temperature (°C)	Additive content in the charge percentage				
	0	2	4	6	8
950	2.27/0.80	2.28/0.90	2.99/0.98	2.84/1.12	3.04/1.20
1000	2.31/0.91	2.58/1.02	3.04/1.20	3.19/1.26	3.52/1.39
1050	2.79/1.10	3.12/1.23	3.52/1.39	3.73/1.47	4.03/1.59

¹linear air shrinkage value (%) / fire shrinkage value (%).

TABLE 3. Ion washout dynamics Ni²⁺

WTSN content in clay mixture (%)	Ion concentration Ni ²⁺ (mg/dm ³)				
	pH=3	pH=4	pH=5	pH=6	pH=7
0	0.000	0.000	0.000	0.000	0.000
2	0.000	0.000	0.000	0.000	0.000
4	0.000	0.000	0.000	0.000	0.000
6	0.000	0.000	0.000	0.000	0.000
8	0.001	0.001	0.000	0.000	0.000
16	0.001	0.001	0.000	0.000	0.000
24	0.001	0.001	0.000	0.000	0.000

The insignificant leaching of nickel from ceramic powder occurs in the samples containing more than 8% WTSN at pH=3 and 4. At pH>4, nickel is not leached out. We should note that according to GOST R 57162-2016 (Russia), the concentration of nickel ions in solutions with pH=3 and 4 is lower than the LOC for nickel water for fishery facilities (0.01 mg/dm³). Thus, the disposal of waste sorption material in the production of ceramic bricks eliminates the risk of nickel entering the environment.

4. CONCLUSION

Here, we provide the conclusion and findings of this paper as follows:

- The possibility of the use of WTSN based on pumpkin seed husks as a combustible additive to clay mixtures was investigated.
- Microstructure SEM analysis showed that the combustion of the organic additive promotes the formation of voids, and the emission of gases to the formation of pores in the ceramic piece during firing.
- The addition of WTSN and changing the firing temperature within the range of 950-1050°C is reflected in the indicators of ultimate strength in compression, water absorption, total porosity and density of ceramic samples.
- The optimal amount of WTSN as a combustible additive for the production of porous ceramics is not more than 4 %. In this case, as a result of firing at the temperature range from 950 to 1050°C, the compressive strength was 20.0-20.7 MPa, the density of the product was 1800-1860 kg/m³, and the water absorption was in the range of 15.6-13.4%. The linear shrinkage values of the resulting products were within the standard range.
- The dynamics of the washing out of heavy metal ions from the ceramic matrix began when the content of the WTSN additive was over 8% and

ended completely at pH values > 4, which eliminated the danger of their entry into the environment.

- The use of WTSN in a clay mixture allowed obtaining porous ceramics with satisfactory technical and operational characteristics, which could be used as an effective building material for the construction of internal partitions and household buildings.
- The use of optimization theory to reduce the waste materials with novel metaheuristics like red deer algorithm [35-36], water wave optimization [37-38] and social engineering optimizer [39], is another interesting idea for further research.

5. ACKNOWLEDGMENTS

The work is realized in the framework of the Program of flagship university development on the base of the Belgorod State Technological University named after V.G. Shoukhov, using equipment of High Technology Center at BSTU named after V.G. Shoukhov and by the Tomsk State University competitiveness improvement program

6. REFERENCES

1. Bauman-Kaszubska, H., & Sikorski, M. "Selected problems of waste water disposal and sludge handling in the Mazovian province" *Journal of Water and Land Development*, Vol. 13, No. 1, (2009), 149-159.
2. Valencia, J. A., González, J. P., Jimenez-Pitre, I., & Molina-Bolívar, G. "Physico-chemical treatment of waste water contaminated with heavy metals in the industry of metallic coatings" *Journal of Water and Land Development*, Vol. 43, No. 1, (2019), 171-176..
3. Yasin Mousavi, S., Tavakkoli, A., Jahanshahi, M., Dankoub, A. "Performance of High-Strength Concrete Made with Recycled Ceramic Aggregates (Research Note)." *International Journal of Engineering, Transactions C: Aspects*, Vol. 33, No. 6, (2020), 1085-1093. 10.5829/ije.2020.33.06c.05.
4. Chang, Z., Long, G., Zhou, J. L., Ma, C. "Valorization of Sewage Sludge in the Fabrication of Construction and Building Materials: A Review." *Resources, Conservation and Recycling*, Vol. 154, (2020), 104606. <https://doi.org/10.1016/j.resconrec.2019.104606>
5. Świerczek, L., Cieślík, B. M., Konieczka, P. "The Potential of Raw Sewage Sludge in Construction Industry-a Review." *Journal of Cleaner Production*, Vol. 200, (2018), 342-356. <https://doi.org/10.1016/j.jclepro.2018.07.188>
6. Foroutan, R., Mohammadi, R., Farjadfard, S., Esmaeili, H., Saberi, M., Sahebi, S., Dobaradaran, S., Ramavandi, B. "Characteristics and Performance of Cd, Ni, and Pb Bio-Adsorption Using Callinectes Sapidus Biomass: Real Wastewater Treatment." *Environmental Science and Pollution Research*, Vol. 26, No. 7, (2019), 6336-6347. <https://doi.org/10.1007/s11356-018-04108-8>
7. Lupandina, N. S., Sapronova, Z. A. "Modified Bleaching Clay as a Sorption Material." IOP Conf. Series: Earth and Environmental

- Science, 459, (2020), 042063 IOP Publishing. doi:10.1088/1755-1315/459/4/042063
8. Dai, Y., Sun, Q., Wang, W., Lu, L., Liu, M., Li, J., Yang, S., Sun, Y., Zhang, K., Xu, J. "Utilizations of Agricultural Waste as Adsorbent for the Removal of Contaminants: A Review." *Chemosphere*, Vol. 211, (2018), 235-253. <https://doi.org/10.1016/j.chemosphere.2018.06.179>
 9. Fediuk, R. S., Lesovik, V. S., Svintsov, A. P., Mochalov, A. V., Kulichkov, S. V., Stoyushko, N. Y., Gladkova, N. A., Timokhin, R. A. "Self-Compacting Concrete Using Pretreated Rice Husk Ash." *Magazine of Civil Engineering*, Vol. 79, No. 3, (2018).
 10. Chandra Paul, S., Mbewe, P. B., Kong, S. Y., Šavija, B. "Agricultural Solid Waste as Source of Supplementary Cementitious Materials in Developing Countries." *Materials*, Vol. 12, No. 7, (2019), 1112. <https://doi.org/10.3390/ma12071112>
 11. Sapronova, Z., Svergzuzova, S., Fomina, E., Fokina, E. "Carbonate-Containing Precipitate of Sugar Production from Sugar Beet as Filler for Polymer Concrete." (2018).
 12. Franus, M., Barnat-Hunek, D., Wdowin, M. "Utilization of Sewage Sludge in the Manufacture of Lightweight Aggregate." *Environmental Monitoring and Assessment*, Vol. 188, No. 1, (2016), DOI: 10.1007/s10661-015-5010-8
 13. Galvez-Martos, J.-L. "Sewage Sludge Ashes as Additives for the Cement and Ceramics Industries." *Wastewater Treatment Residues as Resources for Biorefinery Products and Biofuels*, (2019), 49.
 14. Qi, Y., Yue, Q., Han, S., Yue, M., Gao, B., Yu, H., Shao, T. "Preparation and Mechanism of Ultra-Lightweight Ceramics Produced from Sewage Sludge." *Journal of Hazardous Materials*, Vol. 176, No. 1-3, (2010), 76-84. <https://doi.org/10.1016/j.jhazmat.2009.11.001>
 15. Areias, I. O. R., Vieira, C. M. F., Colorado, H. A., Delaqua, G. C. G., Monteiro, S. N., Azevedo, A. R. G. "Could City Sewage Sludge Be Directly Used into Clay Bricks for Building Construction? A Comprehensive Case Study from Brazil." *Journal of Building Engineering*, (2020), 101374. <https://doi.org/10.1016/j.jobbe.2020.101374>
 16. Tuan, B. L. A., Hwang, C.-L., Lin, K.-L., Chen, Y.-Y., Young, M.-P. "Development of Lightweight Aggregate from Sewage Sludge and Waste Glass Powder for Concrete." *Construction and Building Materials*, Vol. 47, (2013), 334-339. <https://doi.org/10.1016/j.conbuildmat.2013.05.039>
 17. Xu, G. R., Zou, J. L., Li, G. B. "Stabilization of Heavy Metals in Sludge Ceramsite." *Water Research*, Vol. 44, No. 9, (2010), 2930-2938. <https://doi.org/10.1016/j.watres.2010.02.014>
 18. Lottollahi, M. N., Saeidi, N. "A Procedure for Preparation of Semi-Activated Carbon Fiber without Any Treatment under High Temperature." *International Journal of Engineering, Transaction A: Basics*, Vol. 27, No. 10, (2014), 1519-1526.
 19. Qiao, L., Ho, G. "The Effect of Clay Amendment on Speciation of Heavy Metals in Sewage Sludge." *Water Science and Technology*, Vol. 34, No. 7-8, (1996), 413-420. [https://doi.org/10.1016/S0273-1223\(96\)00773-1](https://doi.org/10.1016/S0273-1223(96)00773-1)
 20. Othman, M. H. D., Adam, M. R., Hubadillah, S. K., Puteh, M. H., Harun, Z., Ismail, A. F. "Evaluating the Sintering Temperature Control Towards the Adsorptivity of Ammonia onto the Natural Zeolite Based Hollow Fibre Ceramic Membrane." *International Journal of Engineering, Transaction B: Applications*, Vol. 31, No. 8, (2018), 1398-1405.
 21. Shih, K., White, T., Leckie, J. O. "Nickel Stabilization Efficiency of Aluminate and Ferrite Spinels and Their Leaching Behavior." *Environmental Science & Technology*, Vol. 40, No. 17, (2006), 5520-5526. <https://doi.org/10.1021/es0601033>
 22. Cusidó, J. A., Cremades, L. V. "Environmental Effects of Using Clay Bricks Produced with Sewage Sludge: Leachability and Toxicity Studies." *Waste Management*, Vol. 32, No. 6, (2012), 1202-1208. <https://doi.org/10.1016/j.wasman.2011.12.024>
 23. Starostina, I., Simonov, M., Volodchenko, A., Starostina, Y., Fomin, A., Fokina, E. "The Usage of Iron-Containing Sludge Wastes in Ceramic Bricks Production." *IOP Conference Series: Materials Science and Engineering*, Vol. 365, No. 3, 032066. IOP Publishing doi:10.1088/1757-899X/365/3/032066
 24. Obada, D. O., Dodoo-Arhin, D., Dauda, M., Anafi, F. O., Ahmed, A. S., Ajayi, O. A. "The Impact of Kaolin Dehydroxylation on the Porosity and Mechanical Integrity of Kaolin Based Ceramics Using Different Pore Formers." *Results in physics*, Vol. 7, (2017), 2718-2727. <https://doi.org/10.1016/j.rinp.2017.07.048>
 25. Al-Qadhi, E., Li, G., Ni, Y. "Influence of a Two-Stage Sintering Process on Characteristics of Porous Ceramics Produced with Sewage Sludge and Coal Ash as Low-Cost Raw Materials." *Advances in Materials Science and Engineering*, Vol. 2019, (2019). <https://doi.org/10.1155/2019/3710692>
 26. Obada, D. O., Dodoo-Arhin, D., Dauda, M., Anafi, F. O., Ahmed, A. S., Ajayi, O. A., Csaki, S., Bansod, N. D., Kirim, I. I., Momoh, O. J. "Crack Behaviour and Mechanical Properties of Thermally Treated Kaolin Based Ceramics: The Influence of Pore Generating Agents." *Applied Clay Science*, Vol. 194, (2020), 105698. <https://doi.org/10.1016/j.clay.2020.105698>
 27. Ahmad, S., Iqbal, Y., Muhammad, R. "Effects of Coal and Wheat Husk Additives on the Physical, Thermal and Mechanical Properties of Clay Bricks." *Boletín de la Sociedad Española de Cerámica y Vidrio*, Vol. 56, No. 3, (2017), 131-138. <https://doi.org/10.1016/j.bsecv.2017.02.001>
 28. Vakifahmetoglu, C., Semerci, T., Soraru, G. D. "Closed Porosity Ceramics and Glasses." *Journal of the American Ceramic Society*, Vol. 103, No. 5, (2020), 2941-2969. <https://doi.org/10.1111/jace.16934>
 29. Olawuyi, B. J., Olusola, K. O., Ogunbode, E. B., Kyenge, S. S. "Performance Assessment of Makurdi Burnt Bricks." *Civil Engineering*, (2014).
 30. Knudsen, F. P. "Dependence of Mechanical Strength of Brittle Polycrystalline Specimens on Porosity and Grain Size." *Journal of the American Ceramic Society*, Vol. 42, No. 8, (1959), 376-387. <https://doi.org/10.1111/j.1151-2916.1959.tb13596.x>
 31. Thalmaier, G., Cobîrzan, N., Balog, A. A., Constantinescu, H., Streza, M., Nasui, M., Neamtu, B. V. "Influence of Sawdust Particle Size on Fired Clay Brick Properties." *Materiales de Construcción*, Vol. 70, No. 338, (2020), 215. <https://doi.org/10.3989/mc.2020.04219>
 32. Chiang, K.-Y., Chou, P.-H., Hua, C.-R., Chien, K.-L., Cheeseman, C. "Lightweight Bricks Manufactured from Water Treatment Sludge and Rice Husks." *Journal of Hazardous Materials*, Vol. 171, No. 1-3, (2009), 76-82. <https://doi.org/10.1016/j.jhazmat.2009.05.144>
 33. Starostina, I. V., Simonov, M. M., Denisova, L. V. "The Use of Ferrovandium Production Sludge Wastes in Claydite Gravel Technology." *Solid State Phenomena*, No. 265, (2017), 501-506. <https://doi.org/10.4028/www.scientific.net/SSP.265.501>
 34. Chemani, B., Chemani, H. "Effect of Coal on Engineering Properties in Building Materials: Opportunity to Manufacturing Insulating Bricks." *International Journal of Materials and Metallurgical Engineering*, Vol. 8, No. 8, (2014), 805-811.
 35. Hajiaghahi-Keshтели, M., J Afshari, A., & Nasiri, E., "Addressing the freight consolidation and containerization problem by recent and hybridized meta-heuristic algorithms." *International Journal of Engineering, Transactions C: Aspects*, Vol. 30, No. 3, (2017), 403-410.
 36. Fathollahi-Fard, A. M., Hajiaghahi-Keshтели, M. & Tavakkoli-Moghaddam, R., "Red deer algorithm (RDA): a new nature-

- inspired meta-heuristic," *Soft Computing*, Vol. 24, (2020), 14637-14665. DOI: 10.1007/s00500-020-04812-z.
37. Hajiaghaei-Keshteli, M., Abdallah, K. S., & Fathollahi-Fard, A. M. (2018). "A collaborative stochastic closed-loop supply chain network design for tire industry." *International Journal of Engineering, Transaction A: Basics*, Vol. 31, No. 10, (2018), 1715-1722.
38. Zheng, Y. J. "Water wave optimization: a new nature-inspired metaheuristic." *Computers & Operations Research*, Vol. 55, (2015), 1-11. <https://doi.org/10.1016/j.cor.2014.10.008>
39. Fathollahi-Fard, A. M., Hajiaghaei-Keshteli, M., & Tavakkoli-Moghaddam, R., "The social engineering optimizer (SEO)." *Engineering Applications of Artificial Intelligence*, Vol. 72, (2018), 267-293. <https://doi.org/10.1016/j.engappai.2018.04.009>

Persian Abstract

چکیده

در این مقاله امکان استفاده از مواد جاذب زیاله - پوسته بذر کدو تنبل، که هنگام استخراج یون های فلزات سنگین از محلول های آبی ارائه شده است، که به عنوان یک افزودنی قابل احتراق برای مخلوط های رس در تولید سرامیک های متخلخل استفاده گردید. تأثیر مقادیر مختلف (2-8٪ جرم) مواد جذب شده صرف شده در ترکیب شارژ در تغییر در خصوصیات فیزیکی و مکانیکی نمونه های سرامیکی بدست آمده در دمای 950-1050 درجه سانتیگراد مورد بررسی قرار گرفت. مشخص شد که احتراق مواد افزودنی آلی موجب تشکیل حفره ها و انتشار گازها با تشکیل منافذ در قطعه سرامیکی همراه است. همه مخلوط های رس با افزودنی قابل احتراق امکان تولید سرامیک متخلخل را فراهم می آورد که شرایط لازم برای مقاومت فشاری، تخلخل، چگالی، جذب آب و انقباض خطی را برآورده می کند. توصیه می شود تا حداکثر 4 درصد وزنی استفاده گردید. درصد مواد افزودنی قابل احتراق به منظور به دست آوردن خواص بهینه از نظر چگالی و استحکام. در طول آزمایش سرامیک متخلخل توسعه یافته برای شستشوی فلزات سنگین، مشخص شد که این ماده خطری برای محیط زیست ایجاد نمی کند. مصالح ساختمانی حاصل برای ساخت پارتیشن های داخلی و ساختمانهای خانگی توصیه می شود.



Parametric Effects on Slump and Compressive Strength Properties of Geopolymer Concrete using Taguchi Method

C. Jithendra*^a, S. Elavenil^b

^a Assistant Professor, Department of Civil Engineering, CMR Institute of Technology, Bengaluru, India

^b Professor, School of Civil Engineering, Vellore Institute of Technology, Chennai, India

PAPER INFO

Paper history:

Received: 21 July 2020

Received in revised form: 23 September 2020

Accepted: 26 October 2020

Keywords:

Geopolymer Concrete

By-products

Taguchi Method

Ambient Curing

ABSTRACT

This paper represents the parametric effects on slump and compressive strength of aluminosilicate based Geopolymer concrete using by Taguchi method. A total of nine mix proportions were considered to evaluate the effect of sodium hydroxide (NaOH) solution, Solution/Binder (SB) ratio and the percentage of superplasticizer. Results indicated that the highest slump of 165 mm and 28 days compressive strength of 68.37 MPa was obtained for aluminosilicate based Geopolymer concrete with the superplasticizer, Solution to Binder (SB) ratio and extra water) parameters. By using the selected (Signal-to-Noise (SN) ratio graphs, the best combination of parameters for slump and compressive strength properties was also obtained. The mix with the best combination of parameters was considered and partially replaced with silica fume and rice husk ash. The inclusion of additional silica (in form of silica fume and rice husk ash as Ground Granulated Blast Furnace Slag (GGBFS) replacement), most significantly influenced the slump and compressive strength properties.

doi: 10.5829/ije.2021.34.03c.06

1. INTRODUCTION

There is a rapid increase in the use of Ordinary Portland Cement (OPC) as primary binder in the preparation of concrete. The OPC manufacturing industry contributes to 7% (approximately) of the total CO₂ emission as per International Energy Agency (IEA) [1,2,3]. On the other, the accumulation of industrial by-products in agricultural and residential lands poses varied threats and challenges to the country's productive development [4]. Hence, an extensive research has been initiated over the last few decades to explore alternate and suitable cementitious materials to mitigate this issue [3,5]. Thus considering a wide range of by-products in the manufacturing of concrete as a potential replacement becomes a new scope of research.

In 1978, Joseph Davidovits invented the concept of "Geopolymer" [5, 6]. Since 1978, due to its excellent properties and environmental benefits, the popularity of Geopolymer Concrete (GC) has increased as a promising

alternative to OPC concrete [7]. The production of GC has reduced the emission of CO₂ to 80% (approximately) as compared to OPC [6]. The major steps involved in the mechanism of polymerization include the dilution of Silica (Si) and Alumina (Al) in alkaline medium, the condensation of elements into monomers and the formation of polymeric structure by polycondensation of monomers [8].

A vast number of research studies have been carried out on GC that is manufactured using low calcium content fly ash as primary binding material along with alkali solution (sodium hydroxide (NaOH)/sodium silicate (Na₂SiO₃) based) cured under oven temperatures [1,7,9]. Nevertheless, the manufacturing of GC under oven curing temperatures had minimized its usage to precast concrete elements [10]. Consequently, the field of applications using GC incorporating Ground Granulated Blast Furnace Slag (GGBFS) as partial substitute to fly ash at ambient curing came into existence [10-15]. Several studies focused on setting time, workability and

*Corresponding Author Institutional Email: jithendra.c@cmrit.ac.in
(C Jithendra)

hardened properties of GGBFS/fly ash-based mortar and concrete under ambient temperature [16-20]. It is outlined that the partial substitution of GGBFS improves the setting time and compressive strength. Nevertheless a reduction in workability was also observed [16-20].

Taguchi method is a robust designing method which is used to optimize the number of experiments and to analyse the parametric effects on test results to identify the best level of each factor. It is based upon the Signal to Noise (SN) ratio. The measure of robustness is used to identify the controllable factors which minimize the variability in a product or process by reducing the effects of noise factors (uncontrollable factors). The design factors and the process parameters that can be controlled are known as control factors. The factors which cannot be controlled during production, but can be controlled during experimentation are known as noise factors. In Taguchi design experiments, noise factors that cause variability in the results facilitate the identification of optimal control factor settings. It can be identified that the higher values of the SN ratio will reduce the effects of the noise factors. There are three types of SN ratio namely, i) Larger is the better, ii) Nominal is the better, and iii) Smaller is the better. Based on the requirement the specific SN ratio should be selected as indicated in the Table 1. In this study, Larger is the better, is selected to minimize the effects of noise factors. The best combination of parameters can be analysed by an individual response using Taguchi method. Only a limited number of research studies have considered for the Taguchi method to optimize the parameters according to different properties of Geopolymer concrete, to the knowledge of the authors [21-25].

Therefore, the main aim of this paper is to identify the best combination of mixing proportion in terms of slump and compressive strength properties of GC under ambient curing. Taguchi analysis method is used to identify the best combination of mixing parameters of GC. In this study, 70% GGBFS and 30% fly ash is selected as the primary binder (after a number of trial runs done in the research laboratory). The parameters selected for this study are Solution to Binder (SB) ratio, percentage of superplasticizer and extra water content,

TABLE 1. Selection of SN ratio

Signal-to-noise ratio	Goal of the experiment	Signal-to-noise ratio formulas
Larger is better	Maximize the response	$S/N = -10 \log(\Sigma(1/Y^2)/n)$
Nominal is better	Target the response and you want to base the signal-to-noise ratio on standard deviations only	$S/N = -10 \log(\sigma^2)$
Smaller is better	Minimize the response	$S/N = -10 \log(\Sigma(Y^2)/n)$

and the properties considered are the slump and compressive strength. After achieving the best combination of mix parameters, silica fume and rice husk ash are partially replaced to GGBFS. Further, slump and compressive strength tests were carried out to understand the role of silica fume and rice husk in Geopolymer concrete.

2. EXPERIMENTAL DETAILS

2.1. Materials GGBFS, silica fume and rice husk ash is supplied by Astra chem Pvt Ltd, India. Fly ash is obtained from North Chennai Thermal Power Station, India. The elemental composition of the by-product materials is represented in Table 2. Natural river sand (Zone - II, as per IS: 383-1970) is used as fine aggregate after sieving in 1.18 mm sieve. Normal coarse aggregate with a size of 12 mm is used. The specific gravities of coarse aggregate and fine aggregate are reported as 2.6 and 2.7 respectively. Sodium based silicate solution (Na₂O-15%, SiO₂-30%, H₂O-55%, with modular ratio of 2) is obtained from Kiran Global Chem Pvt, India. The sodium hydroxide flakes with 97% purity was supplied by Sunshine Chemicals, India. The high range water reducer used in research work is commercially available Master Glenium SKY 8233 which is supplied by BASF Construction Chemicals.

2.2. Design of Experiments Taguchi method is used to design the experiments by considering three factors with three levels each using Minitab17 software. The three factors considered in this are SB ratio (0.5,

TABLE 2. Chemical composition of material binder

Components	GGBFS	Fly ash	Silica fume
CaO	33.4%	3.42%	0.001%
Al ₂ O ₃	13.02%	29%	0.04%
Fe ₂ O ₃	2.54%	11.01%	0.04%
SiO ₂	31.03%	51.4%	99.86%
MgO	7.73%	0.25%	-
Loss on Ignition	0.26%	1.44	0.015%
Glass Content (%)	91%	-	-
Specific gravity	2.86	2.74	2.63

TABLE 3. Parameters and their proportions

Factors	Proportion 1	Proportion 2	Proportion 3
SB ratio	0.5	0.55	0.6
Superplasticizer (%)	2	4	6
Water	10	12	14

0.55, 0.6), percentage of superplasticizer (2, 4, 6%) and extra water (10, 12, 14%) are reported in Table 3. A total of nine mixes were generated using Taguchi L₉(3³) array as reported in Table 4. The concentration of sodium hydroxide 12M is kept constant.

2. 3. Preparation of Samples The raw materials are mixed for 2 minutes using a pan mixer. Later, the solution content is added slowly and mixed for another 5 minutes. Immediately after mixing, the fresh concrete is tested for workability using slump cone test and then the concrete is cast in 100 mm size steel moulds with proper compaction and placed on a vibrator for 10 seconds. The specimens were subjected to ambient curing (25⁰C ± 2⁰C) for 24 hours. Following this, the specimens are removed from the moulds and kept for 7, 28, and 90 days for ambient curing.

3. RESULTS AND DISCUSSION

3. 1. Slump Value The slump value of Geopolymer concrete has been tested using a normal slump cone test as per IS 7320-1974. The dimensions of the slump cone are top diameter-10 cmm, height-30 cm and bottom diameter-20 cm. The concrete has been placed into the cone in three layers and tamped properly to remove the air voids. The cone is then lifted vertically and the readings are noted using a steel scale. The slump values of nine mixes are as shown in Figure 1. The minimum slump of 63 mm is achieved by the mix consisting of 0.5 SB ratio, superplasticizer 2% and extra water 10%. The maximum slump value of 150 mm is achieved in the mix consisting of 0.6 SB ratio, 6% superplasticizer and 12% extra water (Table 5). The slump value is significantly influenced by the three factors: SB ratio, Superplasticizer and water content. It clearly indicates that with an increase in the parameter levels, the workability also increases. However, to

analyze the individual parameter that influences the slump value, Taguchi analysis was conducted using Minitab17 software.

From Figure 2, with the help of SN ratio's the individual effect of parameters has been determined. Firstly, SB ratio significantly influences the slump

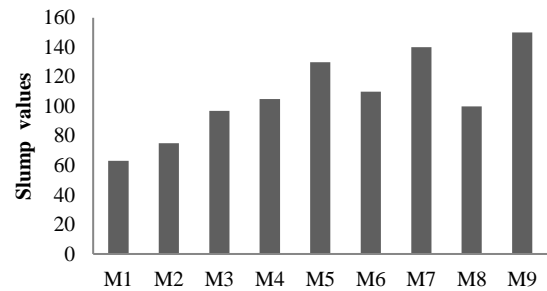


Figure 1. Slump values of Taguchi mixes

TABLE 5. Test results of Geopolymer concrete

Mix ID	Slump (mm)	Compressive strength (MPa)		
		7 days	28 days	90 days
M1	63	58	66.8	68.4
M2	75	53.1	62.2	64.2
M3	97	49.4	57.9	60
M4	105	53	60.12	62.6
M5	130	47.66	56.77	59.4
M6	110	54.8	63.4	66.74
M7	140	44.9	57.05	60.45
M8	100	54	61.45	64.87
M9	150	43.2	52.24	54.29

TABLE 4. Taguchi mix proportions

Mix Id's	SB ratio	Superplasticizer (%)	Water (%)
TM1	0.5	2	10
TM2	0.5	4	12
TM3	0.5	6	14
TM4	0.55	2	12
TM5	0.55	4	14
TM6	0.55	6	10
TM7	0.6	2	14
TM8	0.6	4	10
TM9	0.6	6	12

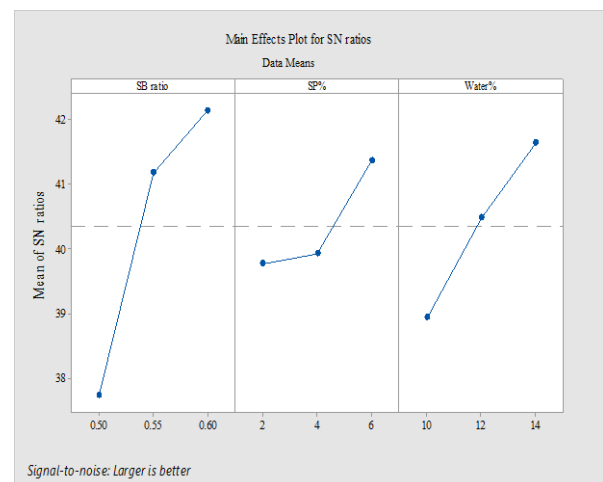


Figure 2. Main effects plot of SN ratios for slump

values. The slump value gradually increases with increase in parameter level of SB ratio from 0.5 to 0.6. The second parameter that influences the slump value is the extra water content. When extra water content is increased from 10 to 14%, there is a linear increment in the slump value. The third parameter, the percentage of superplasticizer also affects the workability properties. With a change in the parameter levels of superplasticizer from 2 to 4%, a slight increase in workability is achieved. When this is further increased from 4 to 6%, a higher rate of workability is noticed.

3. 2. Compressive Strength

A total of nine mixes (M1 to M9) have been cast and subjected to ambient curing. The compressive strength test was conducted as per to IS 516: 1959. The compressive strength of the nine mixes was tested at 7, 28, and 90-days age of concrete, and the average strength of the three specimens are reported in Table 5. The highest compressive strength of 68.4 is achieved with the mix of SB ratio-0.5, 2% superplasticizer and 10% extra water. The lowest compressive strength of 54.29 is achieved with mix that has SB ratio of 0.6, 6% superplasticizer and 12% extra water as shown in Figure 3. However, to deeply understand the effect of parameters on compressive strength, Taguchi analysis is conducted using Minitab17 software. From Figure 4, the first parameter to affect the strength properties is found to be the superplasticizer. It is observed that the strength properties gradually decrease with an increase in the superplasticizer. The second parameter that affects the strength properties is the SAS/Binder content. Even with a change from 0.5 to 0.55, there is a drastic reduction in the strength. Further increasing it from 0.55 to 0.6, indicates a slight reduction in the strength properties. However, there is not much effect of extra water (10, 12, 14%) on the strength properties.

The selection of the best mix proportion is considered in terms of both slump and compressive strength properties of GGBFS Geopolymer concrete. The mix

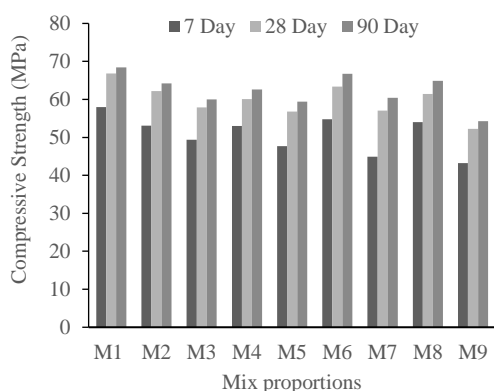


Figure 3. Compressive strength of Taguchi mixes

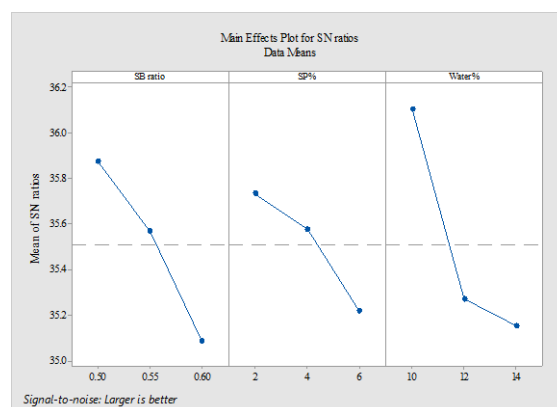


Figure 4. Main effects plot of SN ratios for compressive strength

with SB ratio of 0.5, 2% superplasticizer and 10% extra water has produced 63 mm slump and compressive strength of 66.8 MPa for 28 days. The mix with SB ratio of 0.55, 6% superplasticizer and 10% extra water content has produced 110 mm slump and compressive strength of 63.4 MPa for 28 days. The mix with SB ratio of 0.6, 4% superplasticizer and 10% extra water content has produced 100 mm slump and compressive strength of 61.45 MPa for 28 days. From Taguchi analysis, the best parameter levels are considered as follows: SB ratio 0.5, Superplasticizer 4% and extra water 14%. MID10 is designated as the optimum mix from the Taguchi analysis as reported in Table 5. Finally, the mix MID10 is seen to have achieved 165 mm slump and 68.37 MPa compressive strength at 28-days.

3. 3. Effects of Silica Fume and Rice Husk Ash

The mix MID10 is considered as the best parametric combination which is examined further with GGBFS is partially replaced by silica fume and rice husk ash such as 0, 5, 10, 15, and 20%, respectively. The test results are reported in Table 6.

TABLE 6. Effects of silica fume and rice husk ash

Mix ID	Slump (mm)	Average Compressive strength (MPa) @ 28 days
MID10	165	68.37
M10SF5	175	71.05
M10SF10	185	78.42
M10SF15	205	80.1
M10SF20	210	78.8
M10RA5	170	69.4
M10RA10	180	74.25
M10RA15	185	73.02
M10RA20	190	71.2

3. 3. 1. Effects on Slump

The Geopolymer concrete slump values are significantly influenced by silica fume and rice husk ash as shown in Figures 5 and 6. The highest slump of 205 mm was achieved with the mix of 20% silica fume as compared to the mix of 0% silica fume. The slump growth rate increases about 27.2% with 20% silica fume as compared to control mix (Table 6). On the other hand, rice husk ash also significantly affects the slump value of Geopolymer concrete. The maximum replacement of 20% rice husk ash to GGBFS results in an increase in the slump value of about 15.5% as compared to the control mix (0% rice husk ash). This is due to the large surface area of the materials with fine particles that improves the workability of the Geopolymer concrete. However, it has been observed that the slump value is highly influenced by the mixes of silica fume as compared to the mixes of rice husk ash. This is due to the larger surface area in rice husk ash as compared to silica fume. Increase in dosage of fine particles leads to an increase in the demand of water content.

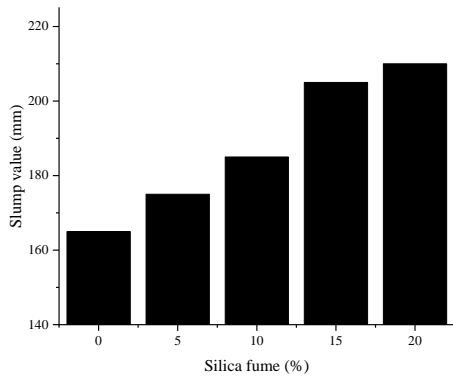


Figure 5. Effect of silica fume on slump

3. 3. 2. Effects on Compressive Strength

The test results show that the silica fume and rice husk ash play a significant impact on compressive strength of GC as represented in Figures 7 and 8. The mix 15% silica fume has achieved the highest compressive strength of 80.1 MPa at 28-days as compared to other mixes in the experiment. The growth rate of compressive strength has increased about 17.1% with partial replacement of silica fume (15%) to GGBFS. The addition of silica content in the mix leads to an improvement in the strength of GC [26]. However, the partial replacement of silica fume beyond 15% results in a slight decrease in strength. This is due to the over dose of silica content in the mixtures which hinders the geopolymerization under ambient curing [27].

On other hand, the rice husk ash also has shown significant effect on compressive strength as shown in Figure 8. The growth rate increases about 8.6% with partial replacement of 10% rice husk ash to GGBFS in the mix. Also, the partial replacement of GGBFS with rice husk ash beyond 10% tends to decrease the compressive strength. The extra rice husk ash which is rich in silica

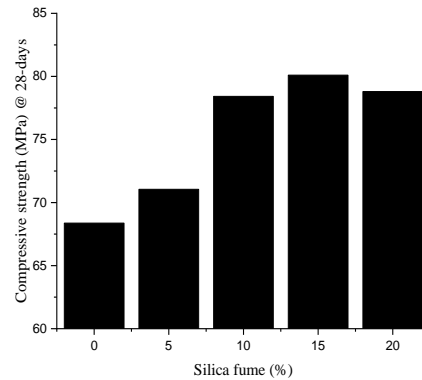


Figure 7. Effect of silica fume on Compressive strength

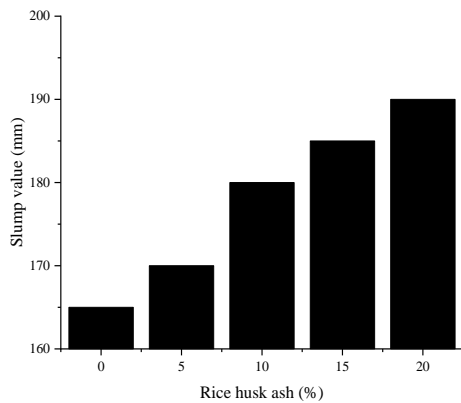


Figure 6. Effect of rice husk ash on slump

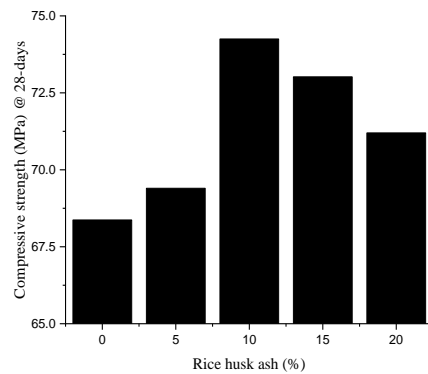


Figure 8. Effect of rice husk ash on Compressive strength

causes a problem in unreactive silica that leads to the rise in Si/Al ratio of Geopolymer concrete. This is mainly due to the effect of geopolymer concrete in the compressive strength of the mixes of rice husk ash beyond 10%. The mixes which are partially replaced with fly ash and micro silica, resulted in a decrease in the strength at ambient curing condition. The reason for decrease in strength was due to a decrease in the intensity of calcium [28], polymerization that was delayed and the hindered formation of Ca-Al-Si gel [29]. The combination of GGBFS with partial replacement of silica rich materials thus seems to be suitable under ambient curing.

4. CONCLUSION

The optimum mix M10 designed from the Taguchi analysis has achieved 165 mm slump and 68.37 MPa compressive strength at 28-days. The highest slump of 205 mm was achieved with the mix of 20% silica fume as compared to the mix of 0% silica fume. The slump growth rate increases about 27.2% with 20% silica fume as compared to control mix. The maximum replacement of 20% rice husk ash to GGBFS resulted in, an increase in the slump value of about 15.5% as compared to control mix. The growth rate of 17.1% increment in compressive strength has been observed with partial replacement of silica fume (15%) to GGBFS. Additionally, there is an 8.6% an increase in the growth rate with partial replacement of 10% rice husk ash to GGBFS in the mix. Beyond 10% replacement of the rice husk ash to GGBFS, there is decreasing trend in the growth rate under ambient curing.

5. ACKNOWLEDGEMENT

I am thankful to Vellore Institute of Technology, Chennai for providing the research facilities.

6. REFERENCES

- Part, W. K., Ramli, M., Cheah, C. B., "An overview on the influence of various factors on the properties of geopolymer concrete derived from industrial by-products", *Construction and Building Materials*, Vol. 77 (2015) 370-395. <https://doi.org/10.1016/j.conbuildmat.2014.12.065>
- Gartner, E., "Industrially interesting approaches to 'low-CO₂' cements", *Cement and Concrete Research*, Vol. 34, (2004) 1489-1498. <https://doi.org/10.1016/j.cemconres.2004.01.021>
- Huseien, G.F., Mirza, J., Ismail, M., Ghoshal, S. K., Hussein, A. A., "Geopolymer mortars as sustainable repair material: A comprehensive review", *Renewable and Sustainable Energy Reviews*. Vol. 80 (2017) 54-74. <https://doi.org/10.1016/j.rser.2017.05.076>
- Liew, K. M., A. O. Sojobi, and L. W. Zhang. "Green concrete: Prospects and challenges." *Construction and Building Materials*, Vol. 156 (2017) 1063-1095. <https://doi.org/10.1016/j.conbuildmat.2017.09.008>
- Wang, Kai-tuo, Li-qiu Du, Xue-sen Lv, Yan He, and Xue-min Cui. "Preparation of drying powder inorganic polymer cement based on alkali-activated slag technology." *Powder Technology*, Vol. 312 (2017) 204-209. <https://doi.org/10.1016/j.powtec.2017.02.036>
- Davidovits, J., "Properties of geopolymer cements.", in: First International Conference on Alkaline Cements and Concretes, Scientific Research Institute on Binders and Materials, Kiev State Technical University, Kiev, Ukraine, (1994), 131-149.
- Singh, B., Ishwarya, G., Gupta, M., Bhattacharyya, S. K., "Geopolymer concrete: A review of some recent developments." *Construction and Building Materials*, Vol. 85 (2015) 78-90. <https://doi.org/10.1016/j.conbuildmat.2015.03.036>
- Lee, N. K., Hammad R. Khalid, Haeng-Ki Lee. "Synthesis of mesoporous geopolymers containing zeolite phases by a hydrothermal treatment." *Microporous Mesoporous Materials* Vol. 229 (2016) 22-30. <https://doi.org/10.1016/j.micromeso.2016.04.016>
- Mehta, A., Siddique, R., "An overview of geopolymers derived from industrial by-products.", *Construction and Building Materials*, Vol. 127 (2016) 183-198. <https://doi.org/10.1016/j.conbuildmat.2016.09.136>
- Nath, P., Sarker, P. K., "Effect of GGBFS on setting, workability and early strength properties of fly ash geopolymer concrete cured in ambient condition", *Construction and Building Materials*, Vol. 66 (2014) 163-171. <https://doi.org/10.1016/j.conbuildmat.2014.05.080>
- Li, Z., Liu, S., "Influence of slag as additive on compressive strength of fly ash based geopolymer", *Journal of Materials in Civil Engineering*, Vol. 19 (2007) 470-474. [https://doi.org/10.1061/\(ASCE\)0899-1561\(2007\)19:6\(470\)](https://doi.org/10.1061/(ASCE)0899-1561(2007)19:6(470))
- Puligilla, S., Mondal, P., "Role of slag in microstructural development and hardening of fly ash-slag geopolymer", *Cement and Concrete Research*, Vol. 43 (2013) 70-80. <https://doi.org/10.1016/j.cemconres.2012.10.004>
- Deb, P. S., Nath, P., Sarker, P. K., "The effects of ground granulated blast-furnace slag blending with fly ash and activator content on the workability and strength properties of geopolymer concrete cured at ambient temperature", *Materials and Design*, Vol. 62, (2014), 32-39. <https://doi.org/10.1016/j.matdes.2014.05.001>
- Singh, B., Rahman, M. R., Paswan, R., Bhattacharyya, S. K., "Effect of activator concentration on the strength, ITZ and drying shrinkage of fly ash/slag geopolymer concrete", *Construction and Building Materials*, Vol. 118, (2016), 171-179. <https://doi.org/10.1016/j.conbuildmat.2016.05.008>
- Nath, P., Sarker, P. K., "Fracture properties of GGBFS-blended fly ash geopolymer concrete cured in ambient temperature", *Materials and Structures*, Vol. 50, No. 32, (2017) 1-12. <https://doi.org/10.1617/s11527-016-0893-6>
- Saha, S., Rajasekaran, C., "Enhancement of the properties of fly ash based geopolymer paste by incorporating ground granulated blast furnace slag", *Construction and Building Materials*, Vol. 146 (2017), 615-620. <https://doi.org/10.1016/j.conbuildmat.2017.04.139>
- Phoo-ngemkham, T., Maegawa, A., Mishima, N., Hatanaka, S., & Chindaprasirt, P., "Effects of sodium hydroxide and sodium silicate solutions on compressive and shear bond strengths of FA-GGBFS geopolymer", *Construction and Building Materials*, Vol. 91, (2015), 1-8. [10.1016/j.conbuildmat.2015.05.001](https://doi.org/10.1016/j.conbuildmat.2015.05.001)
- Rao, G. M., & Rao, T. G., "Final setting time and compressive strength of fly ash and GGBS based geopolymer paste and

- mortar”, *Arabian Journal of Science and Engineering*, Vol. 40, (2015), 3067-3074. <https://doi.org/10.1007/s13369-015-1757-z>
19. Khan, M. Z. N., Hao, Y., Hao, H., “Synthesis of high strength ambient cured geopolymer composite by using low calcium fly ash”, *Construction and Building Materials*, Vol. 125, (2016), 809-820. <https://doi.org/10.1016/j.conbuildmat.2016.08.097>
 20. Rafeet, A., Vinai, R., Soutsos, M., Sha, W., “Guidelines for mix proportioning of fly ash/GGBS based alkali activated concretes”, *Construction and Building Materials*, Vol. 147, (2017), 130-142. <https://doi.org/10.1016/j.conbuildmat.2017.04.036>
 21. Olivia, M., Nikraz, H., “Properties of fly ash geopolymer concrete designed by Taguchi method”. *Materials and Design*, Vol. 36, (2012), 191-198. [10.1016/j.matdes.2011.10.036](https://doi.org/10.1016/j.matdes.2011.10.036)
 22. Riahi, S., Nazari, A., Zaarei, D., Khalaj, G., Bohlooli, H., & Kaykha, M. M., “Compressive strength of ash-based geopolymers at early ages designed by Taguchi method”, *Materials and Design* Vol. 37, (2012), 443-449. <https://doi.org/10.1016/j.matdes.2012.01.030>
 23. Siyal, A. A., Azizli, K. A., Man, Z., Ullah, H., “Effects of parameters on the setting time of Fly ash based Geopolymers using Taguchi method.” *Procedia Engineering*, Vol. 148, (2016), 302-307. [10.1016/j.proeng.2016.06.624](https://doi.org/10.1016/j.proeng.2016.06.624)
 24. Dave, S. V., & Bhogayata, A. “The strength oriented mix design for geopolymer concrete using Taguchi method and Indian concrete mix design code”, *Construction and Building Materials*, Vol. 262, (2020), 120853. <https://doi.org/10.1016/j.conbuildmat.2020.120853>
 25. Onoue, K., Iwamoto, T., Sagawa, Y., “Optimization of the design parameters of fly ash-based geopolymer using the dynamic approach of the Taguchi method”, *Construction and Building Materials*, Vol. 219, (2019), 1-10. [10.1016/j.conbuildmat.2019.05.177](https://doi.org/10.1016/j.conbuildmat.2019.05.177)
 26. Hadi, M. N., Farhan, N. A., Sheikh, M. N., “Design of geopolymer concrete with GGBFS at ambient curing condition using Taguchi method.” *Construction and Building Materials*, Vol. 140, (2017), 424-431. <https://doi.org/10.1016/j.conbuildmat.2017.02.131>
 27. Cheah, C. B., Tan, L. E., Ramli, M., “The engineering properties and microstructure of sodium carbonate activated fly ash/ slag blended mortars with silica fume”, *Composites Part B*, Vol. 160, (2019), 558-572. <https://doi.org/10.1016/j.compositesb.2018.12.056>
 28. Guo, X., Shi, H., Dick, W. A., “Compressive strength and microstructural characteristics of class C fly ash geopolymer”. *Cement and Concrete Composites* Vol. 32, (2010), 142-147. <https://doi.org/10.1016/j.cemconcomp.2009.11.003>
 29. Venkatesan, R. P., Pazhani, K. C., “Strength and Durability Properties of Geopolymer Concrete made with Ground Granulated Blast furnace Slag and Black Rice Husk Ash”, *KSCCE Journal of Civil Engineering*, Vol. 20, (2016), 2384-2391. <https://doi.org/10.1007/s12205-015-0564-0>

Persian Abstract

چکیده

این مقاله نشان دهنده اثرات پارامتری بر شیب و مقاومت فشاری بتن ژئوپلیمر بر پایه آلومینوسیلیکات با استفاده از روش تاگوچی است. در مجموع نه نسبت مخلوط برای ارزیابی اثر محلول هیدروکسید سدیم (NaOH)، نسبت محلول / بایندر (SB) و درصد فوق روان کننده در نظر گرفته شد. نتایج نشان داد که بیشترین کسری 165 میلی متر و 28 روز مقاومت فشاری 68/28 مگاپاسکال برای پارامترهای فوق روان کننده، نسبت محلول به اتصال دهنده (SB) و آب اضافی برای بتن ژئوپلیمر بر پایه آلومینوسیلیکات بدست آمد. با استفاده از نمودارهای انتخاب شده نسبت سیگنال به سر و صدا (SN)، بهترین ترکیب پارامترها برای خواص مقاومت در برابر افت و فشار نیز بدست آمد. مخلوط با بهترین ترکیب پارامترها در نظر گرفته شد و تا حدی با بخار سیلیس و پوسته برنج جایگزین شد گنجاندن خاکستر اضافی سیلیس به صورت بخار سیلیس و خاکستر پوسته برنج به عنوان جایگزینی سرباره کوره بلند (GGBFS)، به طور قابل توجهی بر خصوصیات افت و مقاومت در برابر فشار تأثیر می گذارد.



Mechanical Behaviour of Nano-material (Al_2O_3) Stabilized Soft Soil

B. A. Mir, S. H. Reddy*

Department of Civil Engineering, National Institute of Technology Srinagar, J&K, India

PAPER INFO

Paper history:

Received 13 June 2020

Received in revised form 03 August 2020

Accepted 03 September 2020

Keywords:

Soft Soil

Nano-material

Stabilization

Unconfined Compressive Strength

Scanning Electron Microscopy

ABSTRACT

Rapid urbanization and requirement of infrastructure, stable construction sites are not available. Therefore, there is a dire need for improvement of marginal soils to be used as a construction material. However, weak soils comprise of saturated clays, fine silts, and loose sand, which are susceptible to failure and pose problems of stability. Therefore, this research aims to study the strength and microstructural behavior of soft soils treated with nano-alumina (Al_2O_3) additive. In this study, Al_2O_3 of different percentages (0.5, 1.0, 1.5, and 2.0%) by dry weight of soil was added to a clayey soil and subjected to compaction and unconfined compression strength tests. The compaction tests showed that nano- Al_2O_3 (< 2.0%) stabilized soils exhibit higher unit weight and lower water content compared to untreated soils. This may be attributed due to the fact that nano-materials possess higher unit weight compared to untreated soils and these materials occupy the pore spaces in-between the soil grains, which reduce soil porosity and increase the shear strength. The unconfined compressive strength test on cured treated soil specimens showed a significant increase in shear strength on the addition of nano-alumina. The scanning electron microscopic analysis on untreated and treated soil specimens showed that untreated soil samples exhibit a compact array of clay grains and nano-material treated soil display closely packed and condensed fine structure, which authenticates an increase in shear strength. Thus, with the addition of Al_2O_3 , there has been a significant improvement in the engineering properties of soft soils.

doi: 10.5829/ije.2021.34.03c.07

1. INTRODUCTION

Soil is being used as an engineered construction material and as a foundation medium to support virtually all structures, becomes an indispensable component of the construction industry and, therefore, plays a most prominent role in geotechnical engineering design. However, rapid urbanization and the requirement of infrastructure, stable construction sites are not available. Therefore, there is a dire need for improvement of marginal soils to be used as a construction material. Previous researchers have done their research by using nanomaterials with the combination of additives like Fly ash, Lime, cement, etc on the weak soils. In this present research, different percentages (0.5, 1.0, 1.5, and 2.0%) of nanomaterials were used to enhance the improvement of soft soils. But

the weak soils comprise of saturated clays, marine clays, fine silts, and loose sand, which possess low bearing capacity and are susceptible to failure and pose problems of stability [1-2]. These soils are not suitable in its in situ state to be used either as building stuff or as foundation support and pose high- risk engineers in terms of both strength and serviceability requirements [3-4]. However, their mineralogy and geotechnical properties allow using of these soils if properly characterized and improved [5]. Thus, there is a dire need for establishing suitable strategies for the improvement of weak soil deposits to avoid stability problems. Among various ground improvement techniques available, the nanotechnology is eco-friendly and sustainable improvement techniques for stabilization of soft soils in which nano-material as an additive in nanoscale can be used in soil stabilization to enhance mechanical characteristics of weak/soft soil deposits [6].

*Corresponding Author Email: hariprasad_55phd17@nitsri.net (S. H. Reddy)

Nanotechnology, as a ground improvement technique could be utilized to improve the physical and engineering properties of weak soils and to avoid the stability problems. It has been reported that the use of nanomaterials as an additive is one of the most effective and eco-friendly stabilization techniques for improving engineering behaviour of marginal soils in various geotechnical applications [7-8]. It is a well-established fact that clayey soil exhibits the smallest particle size ($< 2\mu\text{m}$) and there are also some commonly occurring soil nanoparticles classified as “nanoscale particles” formed in an uncontrolled natural environment, which possess large specific surface area and would impact the engineering behaviour of soil [9]. These soil nanoparticles or “nanoscale particles” are entirely different from the conventional type of micro-sized soil minerals in terms of engineering behaviour of soils [10]. Zohair et al. [11] in their research analyzed the slope at different angles in silty soil. The proposed methods to stabilize the existing slope are replacing soil-cement (7% by weight) by vertical layering and layering along the slope. After replacing soil-cement with both methods, the FOS improved significantly. Ekeleme et al. [12] conducted an experimental dispersion coefficient in soil by using three different soil samples which include sand, clay and silt soil. Each sample was gradually introduced into a fabricated iron column with a dimension of $30\text{cm} \times 60.96\text{cm}$. Silver nitrate solution was allowed to pass through the vertical column. Samples of soil were collected at a constant distance of 10cm and a time interval of 5mins for up to 60mins. The absorption of nitrate was taken at a constant distance of 10cm. Thereafter, the dispersion coefficient was calculated. In this research work, Kassou et al. [13], estimated the undrained shear strength of clay by using SHANSEP method as well as the slope stability analysis of embankments on soft soils during staged construction. In addition, the variations of undrained shear strength and the safety factor have been presented. However, at the nano-scale, a nano-material is a particle with one dimension at the nanometer scale (1nm-100nm) and has a very high specific surface area (SSA), contain intraparticle nanoscale voids compared to classical clay particles at micro-scale and exhibits different forms such as nanoplatelets, nanowires, nanotubes and nanodots [14]. Due to high SSA, surface charges and different formations, there is a tremendous potential of nanomaterials in various geotechnical applications, which can significantly improve the physical and engineering characteristics of soft soils [15-16]. Norazlan et al. [17] in their study reported that due to a higher ratio of surface to volume, a small proportion of nanoparticle of kaolin significantly altered the geotechnical properties of kaolin clay. Nano kaolin has been successfully used for many high-quality

constructions works in geotechnical applications for civil engineering design [18].

Many researchers have reported that adding nano-material as an additive to clayey soils reduce the swelling index of clay [19], increase index properties of soil [20], decrease permeability [21] and increase the compressive strength of the treated soft soils [22]. Lee et al. [23] conducted extensive research on the use of nanomaterials in the construction industry and found that the application of nanotechnology helps in developing unique products, which can improve conventional construction materials in terms of strength and serviceability. Arabania et al. [24] also reported that use of nano clay improved the microstructure and mechanical properties of soil stabilized by cement. Çelik [25] injected different percentages of nanoparticles of nano-silica oxide (SiO_2) and nano alumina oxide (Al_2O_3) into poorly graded sand and found that the compressive strength increased significantly at an optimum content of 0.9% of nano-silica and 0.6% of nano alumina oxide and there was a marginal effect of nanoparticles beyond optimum content. Nazari et al. [26] investigated some tests on nano alumina stabilized concrete and concluded that not only the tensile and flexural strength of concrete improved but the cement could also be replaced by adding high purity Al_2O_3 as an additive. Similar results have also been by various researchers [27-28]. Jahromi and Zahedi H [29] and Khalid et al. [30] found that Al_2O_3 as an additive in combination with cement content rapidly improved strength and CBR value at an early stage of soil stabilization, which is advantageous in completion of projects with time-bound constraints. There are extensive studies available on soft soil treated with SiO_2 nanoparticles [31-34], however, only a few results are available on soft soil treated with Al_2O_3 nanoparticles and hence more investigations are desirable. Therefore, the main objective of the aforementioned research was to study the effect of nano-alumina as a stabilizing agent on the physical and engineering characteristics of soft soils. The nano-material (Al_2O_3) was chosen as an additive for determination of the compaction parameters (e. g. maximum dry unit weight and optimum moisture content) and the unconfined compression strength (UCS) of stabilized samples at different curing periods of 0, 7, 14 and 28 days. Further, the test results were supported by conducting SEM analysis tests on untreated and treated soil samples.

2. MATERIALS AND METHODS

2. 1. Soil

In this study, disturbed and undisturbed soil samples were obtained at a depth of 0.5-1.0m below the ground surface from two sites at

Nagbal (Site: S-1) and Pampore (Site: S-2) in J&K respectively. All the basic tests, which physical properties [35-37], index properties [38], compaction characteristics [39] and strength parameters [40-41] were determined as codal procedure as given in Table-1. Scanning electron microscopy tests were conducted on untreated soil samples, which clearly depicted that soil samples collected from site-1 exhibit large size clay lumps while as soil samples from site 2 show clay particles of different arrangements. The pore void spaces are clearly observed between the soil particles and exhibits dispersed structure with no aggregations.

2. 2. Nano-material Nanomaterial (Nano- Al_2O_3) in powder form having purity higher than 99.5% was procured from M/S Nano Research Lab. Jharkhand. The average particle size (APS) of nanomaterial particle was about 30nm. The chemical properties of nanomaterial powder are given in Table 2.

Scanning electron microscopy and XRD tests were also conducted nano-alumina powder samples. The SEM images of the nanoparticles showed (Figure. 1a) that the nano Al_2O_3 are agglomerated particles with large pore voids. Also, the X-ray diffraction (XRD) analysis is used for mineral phase's identification and quantification present in a sample. In this study, XRD technique was also conducted to access the crystallite size of nano-material particles, to measure the average

TABLE 1. Properties of soil test data

Property	Site-1	Site-2
In situ or natural water content, w_n (%)	30.3	35.7
In situ or natural water content, w_n (%)	15.4	14.6
Specific Gravity, G_s	2.67	2.65
Sand (%)	01	04
Silt (%)	89	91
Clay (%)	10	5
Liquid limit, LL (%)	37	42.8
Plasticity index, PI (%)	14.4	26.3
Plasticity index of A-line, PI_A (%)	12.4	16.6
Plasticity index of A-line, PI_U (%)	26.1	31.3
Clay mineral type	Illite	Illite
Soil classification (as per USCS)	ML	ML
Consistency index, I_c	0.47	0.43
In situ cohesion by UCS test, c_u (kN/m ²)	28.6	24.3
In situ cohesion by DST test, c_u (kN/m ²)	16.7	14.9
Angle of internal friction by DST, ϕ_u (Deg)	31	25
Optimum moisture content, OMC (%)	23.1	24.9
Maximum dry unit weight, MDU (kN/m ³)	15.4	14.9

TABLE 2. Chemical Properties of Nano-Alumina Oxide (Al_2O_3)

Property	Value
Purity (%)	99.9 %
Molecular formula	Al_2O_3
Color and form	White powder
Al_2O_3	>99.5 %
CaO	<0.017 %
Fe_2O_3	<0.035 %
MgO	<0.001 %
SiO_2	<0.05 %
Average particle size	30-50 nm
Specific surface area (SSA)	120-140 m ² /g
Bulk density	1.5 g/cm ³
True density	3.97 g/cm ³
pH	7-9
Morphology	Spherical
Crystallographic structure	Rhombohedral
Atomic weight	101.96 g mol ⁻¹
Melting point	2072 °C
Boiling point	2977°C
Loss on ignition (850°C/2h)	< 0.5 %

spacings between layers of rows of atoms in a substance and to determine the orientation of an individual grain or crystal. XRD tests were performed by irradiating a crystalline sample with a beam of X-rays, which interact with the sample in such a way that these rays are diffracted from the atomic planes. The interaction of the incident rays with a certain set of atomic planes produces constructive interference when the interference angle 2θ satisfies the Bragg's Law:

$$n\lambda = 2d\sin\theta \quad (1)$$

where: n is an integer number (known as diffraction order), λ is the wavelength of the used radiation and d is the lattice spacing between the atomic planes θ is the diffraction angle.

Figure 1b shows the XRD image of the Nano- Al_2O_3 , which illustrates that the diffraction angle and the intensity of each of the diffraction peaks can be measured, processed and counted. Nine reflections were observed at 2θ angles around 19, 20, 28, 38, 41, 49, 53⁰, 64 and 71⁰ respectively. Average particle size was calculated from all peaks and was found to be 30 nm.

2. 3. Testing Materials and Research Plan The testing programme includes soil classification and preparation of test specimen [35], specific gravity [36],

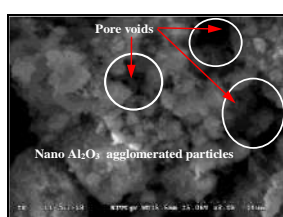


Figure 1a. SEM image of the Nano- Al_2O_3

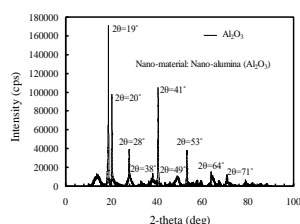


Figure 1b. XRD image of the Nano- Al_2O_3

gradation [37], the Atterberg limits [38], compaction test [39] and shear strength tests [40-41]. Table 1 shows the physical properties of the two soil samples. In this study, the experimental program includes Standard Proctor compaction tests and unconfined compression strength (UCS) tests on nano-material stabilized soil samples with varying nano- Al_2O_3 percentages (0.5, 1.0, 1.5, and 2.0%) by dry weight of soil. The soil samples admixed with different proportions of nanomaterial were prepared in a custom-designed UCS set-up of a cylindrical mold of a diameter of 38 mm and 76mm long. All soil samples for UCS tests were mixed on the basis of optimum moisture content at $0.95\gamma_{dmax}$ (Standard Proctor test) maximum dry unit weight of soft soil samples and then extruded from the cylindrical tube using a soil sample extractor carefully. The unconfined compression tests were carried out immediately on remolded soil samples and other soil samples were stored for 7, 14 and 18 days curing period in the desiccator respectively. After completion of the UCS test on uncured and cured soil samples, sample pellets were collected for the SEM analysis on/along the failure plane.

3. RESULTS AND DISCUSSIONS

3. 1. Physical and Engineering Properties of Virgin Soil Samples

Based on basic soil investigations, the soil is poorly graded clayey silt with low compressibility (ML). The specific gravity values of soil samples are in the narrow range of 2.65 to 2.67. The standard Proctor light compaction tests were carried out on untreated soil and the optimum moisture content varies between 23-25% and the maximum dry unit weight varies in the range of 14-16 kN/m^3 respectively. The unconfined compression strength and direct shear tests were carried out to determine the shear strength parameters of the in-situ soil samples as per codal procedures. Based on test results, it is seen that soil can be classified as soft consistency and as such cannot be used either as building material or as foundation support and hence needs improvement.

3. 2. Effect of Nano-material on Compaction Characteristics of Soil

The soil samples were

prepared by adding different proportions of nano-alumina (0.5, 1.0, 1.5 and 2.0%) by dry weight of soil and thoroughly mixed before compaction tests. The Standard Proctor compaction test [39] was performed to determine the maximum dry unit weight (MDU) and optimum moisture content (OMC) of nano-alumina admixed soil samples. The effect of nanomaterial additive on the compaction characteristic of stabilized soils is illustrated in Figure. 2. It is seen that OMC gradually decreases and the dry unit weight increases for both sites. The soil samples are admixed with 1.5% nano-alumina turns-out to be optimum content to yield MDU and OMC for both sites. The MDU varies in the range of 15.4 kN/m^3 to 16.4 kN/m^3 for site-1 and 14.9 kN/m^3 to 15.5 kN/m^3 for site-2. Similarly, the OMC decreased from 23 to 20% for site-1 and from 25 to 22% for site-2 respectively. This may be attributed due to the fact that nano-materials possess higher unit weight compared to untreated soils and these materials occupy the pore spaces in-between the soil grains, which reduce soil porosity and increase shear strength. However, it is also observed that the moisture content gradually increased beyond the optimum content of nano-material. This is understandable since the nano-materials exhibit a very large surface area, which absorbed more water resulting in a gradual increase in water content. Furthermore, there would be the formation of agglomeration of nano-material particles beyond the optimum limit, which would result in an increase in pore void spaces, which results in absorbing higher water content. Similar results have also been reported by various researchers [42].

3. 3. Effect of Nano-material on Strength Characteristics of Soil

The unconfined compression strength (UCS) test is the quickest test to determine the undrained shear strength of clayey soils for short-term stability analysis. The test was carried out as per BIS [40]. In this study, soil specimens were prepared and compacted under standard compaction at

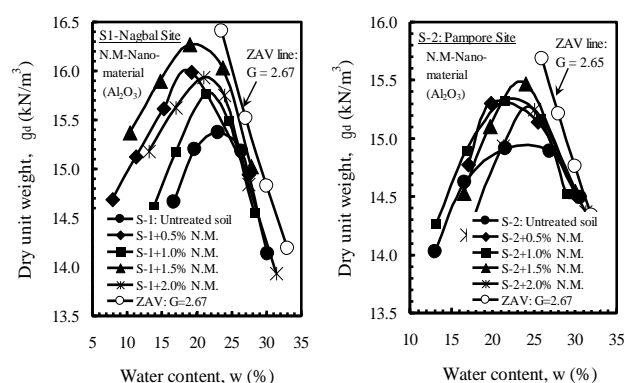


Figure 2. Compaction curves for Nano- Al_2O_3 stabilized soils for: (a). site-1 and (b). site-2

0.95 γ_{dmax} and optimum moisture content in a custom-designed UCS set-up. The UCS tests were conducted in two stages. In stage first, UCS tests were conducted immediately after preparing nano-material admixed soil specimens at varying percentages of nano-material (0.5, 1.0, 1.5, and 2.0%) by dry weight of soil material. In stage two, the UCS specimens were cured for 7days, 14days and 28days curing period before testing. The UCS tests were also carried out on cured soil specimens and specimens were collected for SEM analysis. The effect of the addition of nano-material on strength behaviour of soils for the two sites for immediate and 14 days curing period is illustrated in Figure. 3. Figure 3 demonstrates that the virgin soils possess very low shear strength and exhibit non-linear behaviour. However, the undrained strength increases and the failure strain decreases by adding nano-material with varying proportions at different curing periods. The maximum unconfined compressive strength is achieved at an optimum nano-material content of 1.5% as shown in Figure. 3. It is seen that beyond the optimum content of nano-material, the strength decreases. The undrained strength increases gradually for the initial curing period of 7 days (179 to 187 kPa), after which a rapid enhancement by curing for 14 days (187 to 236 kPa) and a rapid decrease in strength after 14 days of the curing period (236 to 128 kPa) at 28days for site-1 treated for an optimum content of nano-material of 1.5% as shown in Figure. 3. This may be attributed due to the fact that there is a very slow pozzolanic reaction between nano-materials and soil particles for initial curing period 7days and a rapid pozzolanic reaction for site-2, which indicates that soil from site-2 has higher reactive minerals compared to site-1.

The nano-material particles interact very actively with other reactive particles present in the soils, which can alter the soil behaviour. The decrease in strength beyond the optimum limit of nano-material at higher curing period may be attributed due formation of a stiffer soil matrix and flocculated structure, which resulted in lower strength. The variation of strength with

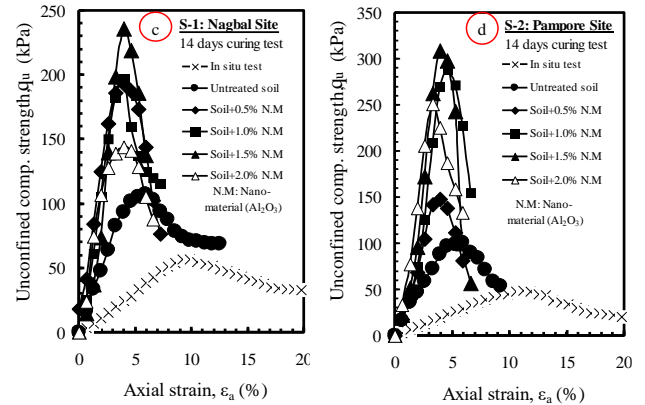
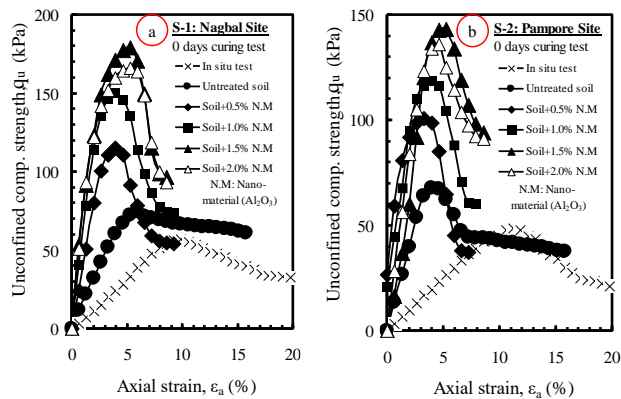


Figure 3. Effect of nano- Al_2O_3 content on stress-strain behaviour of soil collected from site-1 (a & c) & site-2 (b & d) for different curing periods (0 and 14 days)

increasing percentages of nanomaterials for both sites is shown in Figure. 4, and it is observed that 1.5% nano-material is the optimum limit for maximum strength for nano-material stabilized soils for different curing periods. Beyond the optimum limit, nano-material is not beneficial and cost-effective. Similar investigations have also been reported by various other researchers [19, 43].

3. 4. Microstructural Behaviour of Nano-material Treated Soils

In this study, SEM specimens extracted near the shear failure plane of tested untreated and treated soils were prepared as per the required pallet size of 10mmx10mm in the laboratory as shown in Figure 5.

The SEM tests were conducted in the CRF laboratory, NIT Srinagar to assess the microstructural arrangement and particle shape of untreated and treated soil specimens. The SEM images of nano-material stabilized soil specimens (1.5%) for different curing periods are shown in Figure 6. From SEM analysis, it is

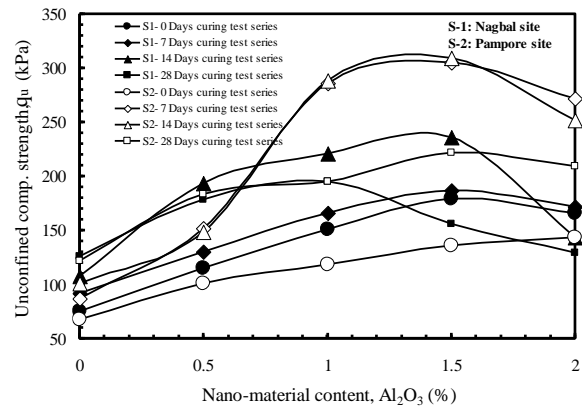


Figure 4. Variation in UCS for nano-material (Al_2O_3) stabilized soil samples

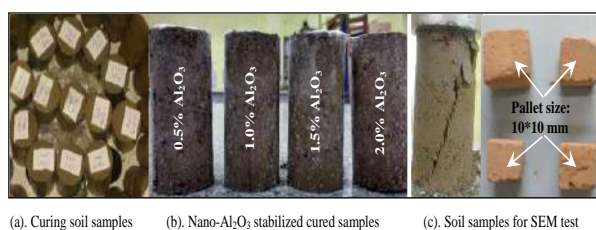


Figure 5. Cured soil samples for 28 days for UCS tests

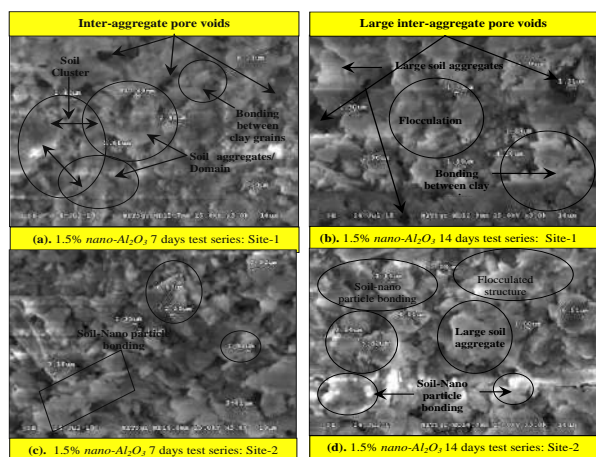


Figure 6. SEM images of nano- Al_2O_3 stabilized soil at optimum content (1.5%) during different curing periods

seen that soil samples collected from site-1 exhibit large size clay lumps while soil samples from site 2 show clay particles of different arrangements. However, the particles of treated soil specimens are closely packed with a dense microstructure with complete destructuration along the shear plane. The inter-aggregate pore void spaces are clearly seen between the soil particles and the nanomaterial particles agglomerated more than that of soil particles due to van der Waal forces between the nanoparticles. Similar investigations have also been reported by various other researchers [44, 45].

4. SUMMARY AND CONCLUSIONS

This present research provides an overview of the applications of nanometric (*Nano-alumina*) additive for the stabilization of marginal soils in Geotechnical engineering applications. The main findings are summarized as:

1. The maximum dry unit weight increased in the ratio of 1.1 for an optimum content of nano- Al_2O_3 of 1.5% for site-1 and 1.05 for site-2 respectively.
2. The unconfined compression strength of the soil improved with addition of varying proportions of nano-material (0.5, 1.0, 1.5 and 2.0%) and curing

periods (0, 7 days, 14 days and 28 days) for both sites.

3. The maximum strength was achieved for an optimum content of 1.5% nano-material. The increase ratios of the maximum strength for nano-material stabilized soil specimens cured for different curing periods (0, 7, 14 and 28 days) are 2.5, 2.1, 2.1 and 1.5 for site-1 and 2.5, 3.8, 3.1 and 1.9 for site-2 respectively for nano-material content of 0, 0.5, 1.0, 1.5 and 2.0%.
4. The SEM images demonstrated that the addition of various percentages of nano-material to the soil changes the structural arrangement of the clay particles with curing time.

5. REFERENCES

1. Munfakh, G.A. "Ground improvement engineering-the State of the US practice: Part 1- Methods." *Proceedings of the Institution of Civil Engineers-Ground Improvement*, Vol. 1, No. 4, (1997), 193-214, DOI: 10.1680/gi.1997.010402
2. Hayal, A. L., Al-Gharrawi, A. M. B. and Fattah, M. Y. "Collapse Problem Treatment of Gypseous Soil by Nanomaterials." *International Journal of Engineering, Transactions C: Aspects*, Vol. 33, No. 9, (2020), 1737-1742, doi: 10.5829/ije.2020.33.09c.06.
3. Mir, B.A. "Some studies on the effect of fly ash and lime on physical and mechanical properties of expansive clay." *International Journal of Civil Engineering-Transaction B: Geotechnical Engineering*, Vol. 13, (2015), 203-212, DOI: 10.22068/IJCE.13.3.203.
4. Mir, B. A. and Sridharan, A. "Mechanical behavior of fly ash treated expansive soil." *Proceedings of the Institution of Civil Engineers - Ground Improvement*, Vol. 172, No. 1, (2019), 12-24, DOI: 10.1680/jgrim.16.00024
5. Mir, B. A., Basit, M. Shah and Shah, F. A. "Some model studies on reinforced dredged soil for sustainable environment." In A. Kallel et al. (eds.): *Recent Advances in Environmental Science from the Euro-Mediterranean and Surrounding Regions-Advances in Science, Technology & Innovation*, (2018), DOI: 10.1007/978-3-319-70548-4_494.
6. Majeed, Z. H. and Taha, M.R. "The Effects of Using Nanomaterials to Improvement Soft Soils." *Saudi Journal of Engineering and Technology, Scholars Middle East Publishers* Dubai, United Arab Emirates, (2016), 58-63, DOI: 10.21276/sjeat.2016.1.3.1.
7. Izadia, M., Tabatabaee Ghomi, and Pircheragh, M. G. "Mechanical Strength Improvement of Mud Motor's Elastomer by Nano Clay and Prediction of the Working Life via Strain Energy." *International Journal of Engineering, Transactions B: Applications*, Vol. 32, No. 2, (2019), 338-345, DOI:10.5829/ije.2019.32.02b.20.
8. Rezaei, G. and Arab, N.B.M. "Investigation on tensile strength of friction stir welded joints in PP/EPDM/clay nanocomposites." *International Journal of Engineering-Transactions C: Aspects*, Vol. 28, No. 9, (2015), 1383-1391, DOI: 10.5829/idosi.ije.2015.28.09c.17
9. Zhang, G. "Soil nanoparticles and their influence on engineering properties of soils." *Advances in Measurement and Modeling of Soil Behavior, New Peaks in Geotechnics*, GSP 173, (2007), 1-13, DOI:10.1061/40917(236)37.

10. Majeed, Z. H. and Taha, M. R. "Effect of nanomaterial treatment on geotechnical properties of a Penang soft soil." *Asian Scientific Research*, Vol. 2, No. 11, (2012), 587-592, <http://aessweb.com/journal-detail.php?id=5003>.
11. Zohair, M, Mangnejo, D. A. and Mangi, N. "Analysis for stabilization of soil slope in silty soil with replacement of soil cement." *Civil Engineering Journal*, Vol. 5, No. 10, (2019), 2233-2246, DOI: 10.28991/cej-2019-03091407.
12. Ekeleme, A.C. and Agunwamba, J. C. "Experimental determination of dispersion coefficient in soil." *Emerging Science Journal*, Vol. 2, No. 4, (2018), 213-218, DOI:10.28991/esj-2018-01145.
13. Kassou, F., Bouziyane, J..B., Ghafiri, A. and Sabihi, A. "Slope stability of embankments on soft soil improved with vertical drains." *Civil Engineering Journal*, Vol. 6, No. 1, (2020), 164-173, DOI: 10.28991/cej-2020-03091461
14. Khalkhali, A. and Daghighi, S. "Optimum design of a coir fiber biocomposite tube reinforced with nano silica and nano clay powder." *International Journal of Engineering, Transactions C: Aspects*, Vol. 30, No. 12, (2017), 1894-1902, DOI: 10.5829/ije.2017.30.12c.11
15. Mosalman, S., Rashahmadi, S. and Hasanzadeh, R. "The effect of TiO₂ nano particles on mechanical properties of poly methyl metacrylate nanocomposites." *Internation Journal of Engineering, Transactions B: Applications*, Vol. 30, No. 5, (2017), 807-813, DOI: 10.5829/idosi.ije.2017.30.05b.22
16. Jamal, M. A. Alsharef, Taha, M. R., Firoozi, A.A. and Govindasamy P. "Potential of using nanocarbons to stabilize weak soils." *Applied and Environmental Soil Science*, Vol. 2016, 5060531, (2016), 1-9, DOI: 10.1155/2016/5060531.
17. Norazlan, K., Arshad, M.F., Mazidah, M., Kamaruzzaman, M and Kamarudin, F. "The Properties of Nano-Kaolin Mixed with Kaolin." *Electronic Journal of Geotechnical Engineering*, Vol. 19, (2014), 4247-4255, Bund. Q.
18. Fadzil, M.A., Sidek M. N. M., Norliyati, M.A., Hamidah, M. S., Wan-Ibrahim M.H., and Assrul, R.Z. "Characterization of kaolin as nano material for high quality construction." MATEC Web of Conferences, Vol. 103, No. 7, (2017), 1-9, DOI: 10.1051/mateconf/20171030 ISCEE 2016 9019.
19. Pham, H. and Nguyen, Q.P. "Effect of silica nanoparticles on clay swelling and aqueous stability of nanoparticle dispersions." *Journal of Nanoparticle Research*, Vol. 16, No. 1, 2137, (2014), 1-11, DOI: 10.1007/s11051-013-2137-9.
20. Zhang, G., Germaine, J. T., Whittle, A. J. and Ladd, C. "Index properties of a highly weathered old alluvium." *Geotechnique*, Vol. 54, No. 7, (2004), 441-451, DOI:10.1680/geot.2004.54.7.441.
21. Moradi, G. and Seyedi S. "Effect of Soils Hydraulic Conductivity on Colloidal Nano-Silica Permeation." *Biological Forum – An International Journal*, Vol. 7, No. 2, (2015), 493-497, ISSN: 2249-3239.
22. Niroumand, H., Zain M.F.M. and Alhosseini, S.N. "The influence of nano-clays on compressive strength of earth bricks as sustainable materials." *Procedia Social and Behavioral Sciences*, Vol. 89, (2013), 862-865, DOI: 10.1016/j.sbspro.2013.08.945.
23. Lee, J., Mahendra, S. and Alvarez, P. "Nanomaterials in the Construction Industry: A Review of their Applications and Environmental Health and Safety Considerations". *ACS Nano*, Vol. 4, No. 7, (2010), 3580-3590, DOI: 10.1021/nn100866w
24. Arabani, M., Haghia, A. K., Sani, A. M. and Kamboozia, N. "Use of nano clay for improvement the microstructure and mechanical properties of soil stabilized by cement". *Proceedings of the 4th International Conference on Nanostructures (ICNS4)*, Kish Island, Iran, (2012), 1552-1554.
25. Çelik, S., Alireza, N. and Mehdi, J. B. "Effect of nanoparticles on geotechnical engineering properties of granular soils by using injection method." *Journal of Biochemica Technology*, (2019), 56-60, ISSN: 0794-2328.
26. Nazari, A., Shadi, R., Sharin, R., Shamekhi, S. F. and Khademno, A. "Mechanical properties of cement mortar with Al₂O₃ nanoparticles." *Journal of American Science*, Vol. 5(7), (2009). 94-97, <http://www.americanscience.org>.
27. Jha, K. K. "An energy based nanomechanical properties evaluation method for cementitious materials." Ph.D. Dissertation, (2012), Florida International University, Miami, FL, USA.
28. Scrivener, K. L. "Nanotechnology and Cementitious Materials" In: Bittnar Z., Bartos P.J.M., Němeček J., Šmilauer V., Zeman J. (eds), *Nanotechnology in Construction 3*, (2009), Springer, Berlin, Heidelberg, DOI:10.1007/978-3-642-00980-8_4
29. Jahromi, S. G. and Zahedi, H. "Investigating the effecting of nano aluminum on mechanical and volumetric properties of clay." *Amirkabir Journal of Civil Engineering*, Vol. 50, No. 3, (2018), 597-606, DOI: 10.22060/ceej.2017.12241.5157.
30. Khalid, N., Arshad, M. F., Mukri, M., Mohamad, K. and Kamarudin, F. "Influence of nano-soil particles in soft soil stabilization." *Electronic Journal of Geotechnical Engineering*, Vol. 20, No. 2, (2015), 731-738, (2015).
31. Bahmani, S. H., Huat, B. B., Asadi, A. and Farzadnia, N. "Stabilization of residual soil using SiO₂ nanoparticles and cement." *Construction and Building Materials*, Vol. 64, (2014), 350-359, DOI:10.1016/j.conbuildmat.2014.04.086.
32. Ghasabkolaei, N., Janalizadeh, A., Jahanshahi, M., Roshan N. and Ghassemi, S. E. "Physical and geotechnical properties of cementtreated clayey soil using silica nanoparticles: an experimental study." *The European Physical Journal Plus*, Vol. 131, No. 5, (2016), 1-11, DOI 10.1140/epjp/i2016-16134-3.
33. Kong, R., Zhang, F., Gonghui, W. and Jianbing, P. "Stabilization of loess using nano-SiO₂." *Materials*, Vol. 11, No. 6, (2018). 1014, DOI:10.3390/ma11061014.
34. Reddy, H. S. and Mir, B. A. (2020). "Some studies on microstructural behaviour and unconfined compressive strength of soft soil treated with SiO₂ nanoparticles." *Innovative Infrastructure Solutions*, Vol. 5, No. 1, 34, DOI:10.1007/s41062-020-0283-3.
35. BIS: 2720-Part 1 (1980) Indian Standard Code for preparation of soil samples. *Bureau of Indian Standards*, New Delhi.
36. BIS: 2720-Part 3(1) (1980). Method of test for soils: Determination of specific gravity of fine grained soils. *Bureau of Indian Standards*, New Delhi.
37. BIS: 2720-Part 4 (1985). Method of test for soils: Determination of grain size distribution. *Bureau of Indian standards*, New Delhi.
38. BIS: 2720-Part 5 (1985). Method of test for soils: Determination of Atterberg limits. *Bureau of Indian standards*, New Delhi.
39. BIS: 2720-Part 7 (1980). Method of test for soils: Determination of Water Content-Dry Density Relation Using Light Compaction. *Bureau of Indian standards*, New Delhi.
40. BIS 2720-10 (1973). Methods of test for soils, Part 10: Determination of shear strength parameter by Unconfined compression test. *Bureau of Indian standards*, New Delhi.
41. BIS 2720-13 (1986). Methods of test for soils, Part 13: Determination of shear strength parameter by Direct shear test. *Bureau of Indian standards*, New Delhi.
42. Majeed, Z. H., Taha, M. R. and Jawad I. T. "Stabilization of soft soil using nano-materials." *Research Journal of Applied Sciences, Engineering and Technology*, Vol. 8, No. 4, (2014), 503-509, DOI: 10.19026/rjaset.8.999.

43. Mir, B. A. and Reddy, S. H. "Enhancement in Shear Strength Characteristics of Soft Soil by Using Nanomaterials." *Sustainable Environment and Infrastructure*, (2020), Springer, Cham, 421-435, DOI: 10.1007/978-3-030-51350-4_39
44. Gillott, J. E. "Study of the fabric of fine-grained sediments with the scanning electron microscope." *Journal of Sedimentary Research*, Vol. 39, No. 1, (1969), 90-105, DOI:10.1306/74D71BEA-2B21-11D7-8648000102C1865D.
45. Kamruzzaman, A. H. M., Chew, S. H. and Lee, F.H. "Microstructure of cement-treated Singapore marine clay." *Proceedings of the Institution of Civil Engineers-Ground Improvement*, ICE, UK, Vol. 10, No. 3, (2006), 113-123, DOI: 10.1680/grim.2006.10.3.113.

Persian Abstract

چکیده

شهرسازی سریع و نیاز به زیرساخت ها ، سایت های ساختمانی پایدار در دسترس نیست. بنابراین ، نیاز مبرم به بهبود خاکهای حاشیه ای وجود دارد تا به عنوان ماده ساختمانی استفاده شود. با این حال ، خاکهای ضعیف شامل رسهای اشباع ، ذرات ریز و ماسه های سست هستند که مستعد شکست هستند و مشکلات پایداری را ایجاد می کنند. بنابراین ، این تحقیق با هدف بررسی مقاومت و رفتار ریزساختاری خاکهای نرم تیمار شده با افزودنی نانو آلومینا (Al_2O_3) انجام می شود. در این مطالعه ، با Al_2O_3 درصد های مختلف (0.5% ، 1.0% ، 1.5% و 2.0%) از نظر وزن خشک خاک به خاک رسی اضافه شده و تحت آزمایشات فشردگی و مقاومت فشاری غیر محدود قرار گرفت. آزمونهای تراکم نشان داد که نانو- (Al_2O_3 (2/0%)) خاکهای تثبیت شده نسبت به خاکهای تیمار نشده دارای واحد وزن بالاتر و مقدار آب کمتری هستند. این ممکن است به دلیل این واقعیت باشد که مواد نانو در مقایسه با خاکهای تیمار نشده دارای وزن واحد بیشتری هستند و این مواد فضاهای منافذی بین دانه های خاک را اشغال می کنند ، که باعث کاهش تخلخل خاک و افزایش مقاومت برشی می شوند. آزمون مقاومت فشاری بدون محدودیت در نمونه های خاک تیمار شده ، افزایش قابل توجهی در مقاومت برشی بر افزودن نانو آلومینا را نشان داد. تجزیه و تحلیل میکروسکوپی الکترونی روبشی روی نمونه های خاک تیمار شده و تیمار نشده نشان داد که نمونه های خاک تصفیه نشده آرایه ای فشرده از دانه های رس و صفحه نمایش خاک با تیمار با مواد نانو را نشان می دهند که ساختار ظریف بسته بندی شده و متراکم شده است ، که افزایش مقاومت برشی را تأیید می کند. بنابراین ، با افزودن Al_2O_3 ، بهبود قابل توجهی در خصوصیات مهندسی خاک نرم وجود دارد.



Using Building Information Modeling to Retrofit Abandoned Construction Projects in Iraq to Achieve Low-energy

H. Y. Khudhaire*, H. I. Naji

Department of Civil Engineering, University of Diyala, Diyala, Iraq

PAPER INFO

Paper history:

Received 09 January 2021

Received in revised form 03 February 2021

Accepted 08 February 2021

Keywords:

Retrofitting Abandoned Projects

Energy Simulation

Building Information Modeling BIM

Insight 360

ABSTRACT

In recent years, the Iraqi construction sector has faced many abandoned projects that have a negative impact on stakeholders, the economy, and the environment. Retrofitting existing buildings offer significant opportunities to reduce energy consumption and carbon emissions since buildings consume the largest amount of energy. The research methodology adopting building information Modeling (BIM) technology, is one of the modern techniques for retrofitting abandoned buildings to achieve low energy buildings and reduce the environmental effect. The concept of the study is applied to one of the projects in Iraq. The author finds that the use of BIM technology is very useful in carrying out various analyses and helping to find retrofitting strategies to improve the energy efficiency of the project. The results showed that the energy savings of 24% of the total improvement compared to the baseline design situation and the most efficient alternatives are heating, ventilation and air conditioning (HVAC) systems with energy savings of 71.36 kWh/m².year.

doi: 10.5829/ije.2021.34.03c.08

1. INTRODUCTION

Globally, the construction sector is responsible for the largest environmental impacts, consumes 32% of final energy, and generates 25% of greenhouse gas emissions [1]. Therefore, the environmental effect needs to be minimized by improving energy quality and reducing energy use in the construction sector [2]. Retrofitting an abandoned building is one of the most important strategies to reduce environmental problems associated with energy use in buildings [3]. Retrofitting existing buildings improve sustainable development, decrease energy consumption, reduces maintenance costs, and mitigates climate change [4]. Retrofit of buildings has several advantages that can be classified into environmental, economic, and social benefits [5]. The traditional method of computer-aided design uses two-dimensional viewing planning does not have the capability to perform energy simulation during the initial phase of design [6]. Building Information Modeling (BIM) is a digital representation of the

physical and functional characteristics of the facility, which constitutes a shared and accurate knowledge platform for conducting sustainability measures and the analysis of energy performance at an early stage of design [7]. BIM is an innovative technology that uses several methods that can accurately measure energy efficiency in buildings [8]. BIM Technology has many tools for performance analysis (Insight 360, Autodesk Green Building Studio (GBS), Design Builder) [9]. BIM technology can create a virtual environment similar to the actual work site environment which helps in the early stages of the project to identify and solve safety problems [10]. BIM technology has the ability to effect the energy of the school building in the retrofit phases [11]. Fuzzy inference method for the indeterminacy model has the potential to solve the health and safety, and environmental risk in the construction sector [12]. In recent years, a lot of research has used BIM technology in various aspects of construction, the technology of BIM can be applied to retrofitting the building to minimize energy demand [13], identify and assess sustainable design parameters based on the tools provided by Building Information Modeling to improve sustainability in the building sector [14], use the BIM

*Corresponding Author Email: hudaeng3@gmail.com (H. Y. Khudhaire)

approach to achieve a sustainable design by using alternative waste from demolished buildings in the construction process [15], documentation using GIS and BIM data [16]. The use of the BIM technique to suggest construction alternatives to lower electricity consumption in Iraq, for example, the selection of the best construction materials for walls and roofs. It is found that the rock block is the best alternative for walls, and the Autoclaved Aerated Concrete Block (AAC block) rib slab is the best alternative for roofing [17].

In recent years, the construction sector in Iraq has faced several problems associated with an increase in the number of abandoned construction projects that have had negative impacts on the environment and increased consumption of electricity and natural resources. So, the authors of this study adopt BIM technology as one of the modern technologies to retrofitting abandoned projects to reduce environmental impacts and to improve energy efficiency in Iraq.

2. RESEARCH METHODOLOGY AND CASE STUDY

In this section, the authors present a description of the methodology for this study and also illustrate the case study.

2. 1. Research Methodology

This methodology consists of two parts, the first part is the theoretical part and the second part is the experimental part, as shown in Figure 1. data collection consists of BIM data and this data includes all building information (Quantities Schedule, 2D Drawings) through interviews with specialist construction engineers at Diyala governorate and the creation of the BIM 3D case study model using the Revit Software 2020, energy analysis and simulation was performed with the plug in for Rivet, Insight 360. Finally, clarify the conclusions that the authors have reached.

2. 2. Case Study

In order to achieve the objective of the study, one of the residential buildings at Diyala is selected as a case study. The work has started in 2010 project and in 2013 the construction work in the project is stopped with a total area of 2845,22 m², consisting of four floors, four apartments on each floor. Creating a 3D model for a case study, completion of about 55% of the work is shown in Figure 2. The benefit from the possibilities offered by BIM to complete work of the abandoned buildings is shown in Figure 3. The other information about the project is summarized as follows:

- Project location: Diyala, Iraq
- Height of Buildings 12.45 m

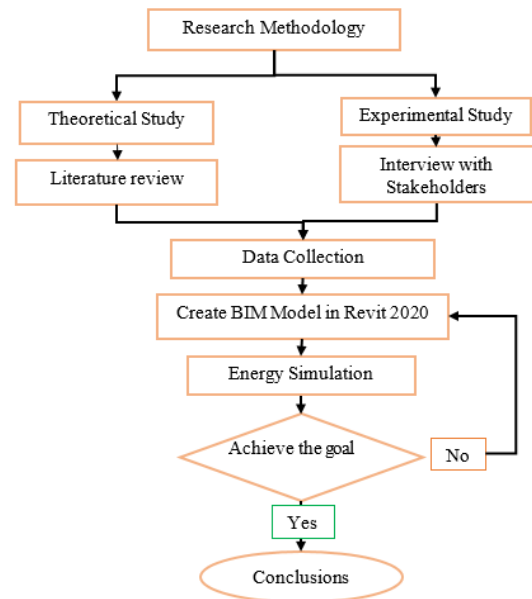


Figure 1. Research Methodology



Figure 2. 3D model of the case study



Figure 3. BIM 3D model finish work of the building

- Project supervision: engineers of the headquarters of the ministry of construction and housing at Diyala

- Type of contract: unit price contract
- The project is unfinished and is abandoned because of the country's economic crisis.
- Details of construction were used for the model building shown in the Table 1.

3. BUILDING ENERGY MODEL

Energy analysis and simulation of the building was performed with the plug in for Rivet, Insight 360. The energy analysis steps are as follows:

- Creating the BIM 3D model of the case study using Revit Software 2020.
- Selection of the building's geographical location and weather station data in Revit as shown in Figure 4.
- Creating the space and energy model of the building in Revit as shown in Figures 5 and 6.
- Select the optimizing panel in Rivet 2020 to run the energy analysis in Insight360.

4. RESULTS AND DISCUSSION

The findings of this study are based on the energy settings in Revit 2020 and retrofit alternatives which are selected in Insight 360 cloud, as shown in Figure 7.

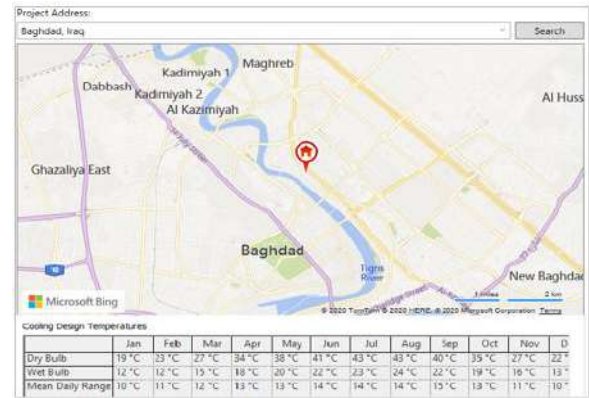


Figure 4. Building's geographical location and weather station in Revit

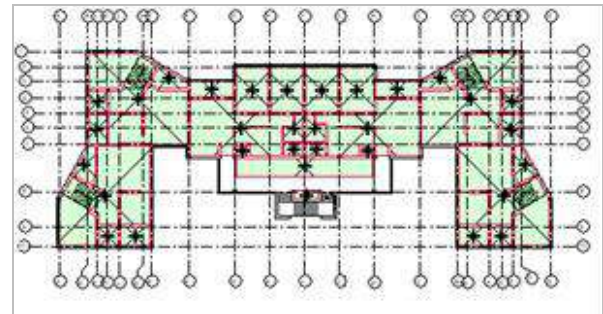


Figure 5. Analytical spaces of the building energy model in Revit

TABLE 1. Detailed construction of case studies

Construction	Details		Conductivity (W/m k)	Specific heat J/(kg·°C)
	Materials	Thickness (m)		
External Wall	Brick	0.24	0.54	840
	Cement mortar	0.02	0.72	840
	Gypsum	0.02	0.65	840
	Oil paint	0.01	0.51	960
Interior walls 1	Brick cement plaster	0.24	0.54	840
	Gypsum	0.01	0.72	840
	Plaster	0.02	0.65	840
	Brick	0.24	0.54	840
Interior walls 2	Ceramic tiles	0.02	1.2	850
	Concrete	0.15	1.046	657
	Asphalt	0.03	1.15	840
	Sand	0.02	0.335	100
Roof	Concrete tiles	0.04	1.046	657
	Concrete	0.15	1.046	657
	Mosaic Tile	0.03	0.8	850
Floor				
Window	Single-glass	0.06	1.2	840



Figure 6. Building energy model in Revit

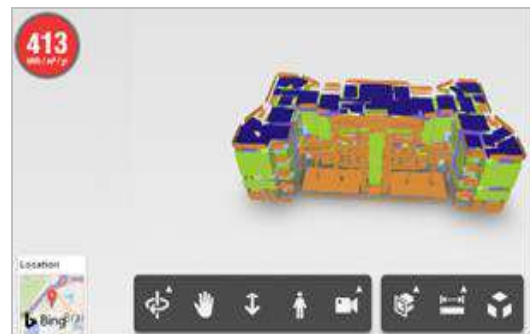


Figure 7. The building and findings obtained on platform insight 360

4. 1. Energy Simulation of Baseline Design

Energy simulation uses the basic building materials of the case-study residential building. The results showed that energy consumption is equal to 413 kWh/(m² year) as illustrated in Figure 8.

4. 2. Retrofitting Alternatives

Many abandoned projects in Iraq are designed and constructed according to criteria which do not take into account the reduction of energy consumption or sustainability. Therefore, the retrofitting of existing projects is necessary to minimize environmental impacts and to improve sustainability. Retrofitting alternatives for the case study are selected in consultation with experts and evaluated on the 360 insight platform.

4. 2. 1. Lights System

The lighting system affects the use of energy and causes a large amount of depletion of energy in the building. The retrofitting consists of the replacement of existing fluorescent luminaires with another LED system. The results of energy simulation after the improvement has achieved energy consumption 397.16 kWh/(m² year) and energy-saving 15.52 kWh/(m² year), as shown in Figure 9.

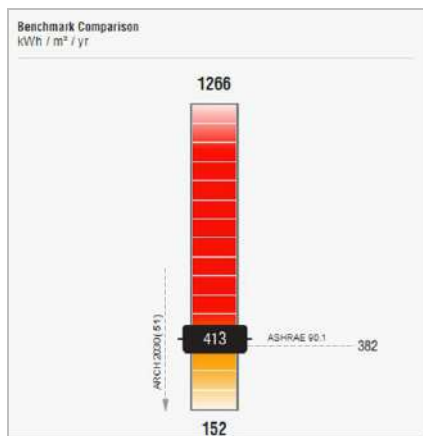


Figure 8. Energy simulation on insight 360 platform

4. 2. 2. HVAC System

One of the key components of energy usage is the heating, ventilation, and air conditioning (HVAC) system and influences the quality of indoor air and air temperature in the building. Retrofitting consists of replacing the existing building HVAC systems with a modern system based on highly efficient heat pumps. After improving, the energy consumption is 325.81 kWh/(m² year) and energy savings by 71.36 kWh/(m² year). It should be noted that this measure has produced significant energy savings and is actually one of the main components of energy consumption and has an impact on indoor air quality and the temperature of the air in the building as shown in Figure 10.

4. 2. 3. Window Glass

The type of window glass plays a major role in how much heat gain and loss in construction and its effect on energy consumption. The retrofitting consists of replacing existing single-glass windows with triple Low-E glass. After improving, the energy consumption is 303.41 kWh/(m² year) and energy savings of 12.47 kWh/(m² year) as shown in Figure 11.

In summary, as shown in Figure 12, the various scenarios examined in the applied energy simulation can be graphically represented. This section shows the various

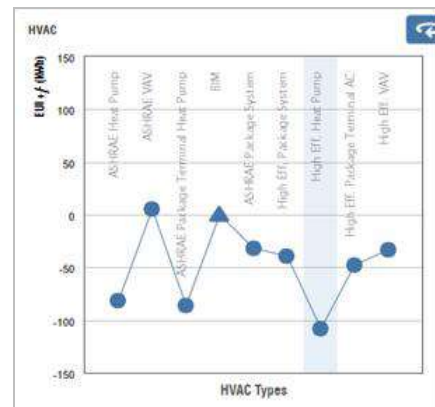


Figure 10. HVAC improvement in insight 360

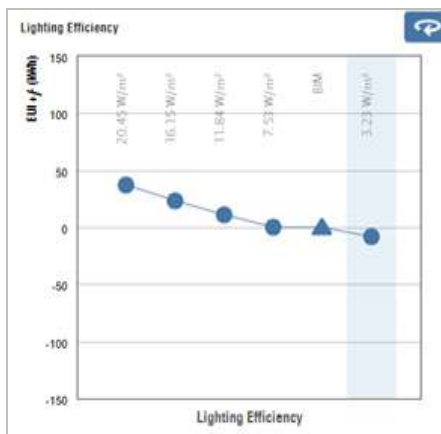


Figure 9. lighting improvement selected in insight 360

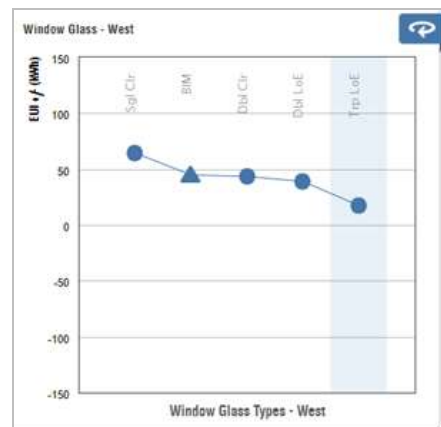


Figure 11. Window improvement selected in insight 360

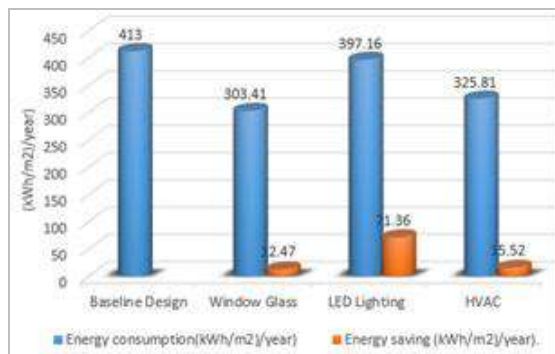


Figure 12. Various retrofit alternatives analyzed for the building

energy simulation retrofitting alternatives analyzed, where one can see the energy savings of 24% of the total improvement compared to the baseline design situation.

5. CONCLUSION

One of the largest contributors to energy use and environmental impact is the building industry. Therefore, by applying modern techniques such as BIM techniques, the authors try to renovate abandoned buildings to achieve low-energy buildings. The authors concluded that the findings are stated as in the following:

- Insight 360 is used effectively with BIM technology which is very useful to evaluate retrofitting alternatives and it enables designers and owners to the simulation of the energy efficiency of the building
- The results illustrate that the most efficient alternatives are HVAC systems with energy savings of 71.36 kWh/(m² year).
- The results clarified that the energy savings of the total improvement compared to the baseline design situation is 24%.

6. REFERENCES

1. Haruna, A., Shafiq, N. and Montasir, O., "Building information modelling application for developing sustainable building (multi criteria decision making approach)", *Ain Shams Engineering Journal*, (2020), <https://doi.org/10.1016/j.asej.2020.06.006>.
2. Pérez-Lombard, L., Ortiz, J. and Pout, C., "A review on buildings energy consumption information", *Energy and Buildings*, Vol. 40, No. 3, (2008), 394-398. <https://doi.org/10.1016/j.enbuild.2007.03.007>
3. Vizzari, C. and Fatiguso, F., "A multicriteria model description for the refurbishment of abandoned industries", in 2019 IEEE International Conference on Systems, Man and Cybernetics (SMC), IEEE., 970-975. <https://doi.org/10.1109/smc.2019.8914318>
4. Akande, O.K. and Olagunju, R.E., "Retrofitting and greening existing buildings: Strategies for energy conservation, resource management and sustainability of the built environment in nigeria", *Journal of Sustainable Architecture and Civil Engineering*, Vol. 15, No. 2, (2016), 6-12. <https://doi.org/10.5755/j01.sace.15.2.15557>
5. Amstalden, R.W., Kost, M., Nathani, C. and Imboden, D.M., "Economic potential of energy-efficient retrofitting in the swiss residential building sector: The effects of policy instruments and energy price expectations", *Energy Policy*, Vol. 35, No. 3, (2007), 1819-1829. <https://doi.org/10.1016/j.enpol.2006.05.018>
6. Azhar, S. and Brown, J., "Bim for sustainability analyses", *International Journal of Construction Education and Research*, Vol. 5, No. 4, (2009), 276-292. <https://doi.org/10.1080/15578770903355657>
7. Schlueter, A. and Thesseling, F., "Building information model based energy/exergy performance assessment in early design stages", *Automation in Construction*, Vol. 18, No. 2, (2009), 153-163. <https://doi.org/10.1016/j.autcon.2008.07.003>
8. Najjar, M.K., Tam, V.W., Di Gregorio, L.T., Evangelista, A.C.J., Hammad, A.W. and Haddad, A., "Integrating parametric analysis with building information modeling to improve energy performance of construction projects", *Energies*, Vol. 12, No. 8, (2019), 1515. <https://doi.org/10.3390/en12081515>
9. Østergård, T., Jensen, R.L. and Maagaard, S.E., "Building simulations supporting decision making in early design—a review", *Renewable and Sustainable Energy Reviews*, Vol. 61, (2016), 187-201. <https://doi.org/10.1016/j.rser.2016.03.045>
10. Abed, H.R., Hatem, W.A. and Jasim, N.A., "Adopting bim technology in fall prevention plans", *Civil Engineering Journal*, Vol. 5, No. 10, (2019), 2270-2281. <https://doi.org/10.28991/cej-2019-03091410>
11. Di Giuda, G.M., Villa, V. and Piantanida, P., "Bim and energy efficient retrofitting in school buildings", *Energy Procedia*, Vol. 78, (2015), 1045-1050. <https://doi.org/10.1016/j.egypro.2015.11.066>
12. Ardeshir, A., Farnood Ahmadi, P. and Bayat, H., "A prioritization model for hse risk assessment using combined failure mode, effect analysis, and fuzzy inference system: A case study in iranian construction industry", *International Journal of Engineering*, Vol. 31, No. 9, (2018), 1487-1497. <https://doi.org/10.5829/ije.2018.31.09c.03>
13. Ma, Z., Cooper, P., Daly, D. and Ledo, L., "Existing building retrofits: Methodology and state-of-the-art", *Energy and Buildings*, Vol. 55, (2012), 889-902. <https://doi.org/10.1016/j.enbuild.2012.08.018>
14. Taha, F., Hatem, W. and Jasim, N., "Adoption of bim technology to develop sustainable buildings in the iraqi construction sector", *Indian Journal of Science and Technology*, Vol. 13, No. 15, (2020), 1596-1606. <https://doi.org/10.17485/ijst/v13i15.223>
15. Jalil, Z.A., Naji, H.I. and Mahmood, M.S., "Developing sustainable alternatives from destroyed buildings waste for reconstruction projects", *Civil Engineering Journal*, Vol. 6, No. 1, (2020), 60-68. <https://doi.org/10.28991/cej-2020-03091453>
16. Abd, A.M., Hameed, A.H. and Nsaif, B.M., "Documentation of construction project using integration of bim and gis technique", *Asian Journal of Civil Engineering*, Vol. 21, No. 7, (2020), 1249-1257. <https://doi.org/10.1007/s42107-020-00273-9>
17. Naji, H.I., Mahmood, M. and Mohammad, H.E., "Using bim to propose building alternatives towards lower consumption of electric power in iraq", *Asian Journal of Civil Engineering*, Vol. 20, No. 5, (2019), 669-679. <https://doi.org/10.1007/s42107-019-00134-0>

Persian Abstract

چکیده

در سال های اخیر ، بخش ساخت و ساز عراق با بسیاری از پروژه های رها شده مواجه شده است که تأثیر منفی بر سهامداران ، اقتصاد و محیط زیست دارد. مقاوم سازی ساختمانهای موجود فرصتهای قابل توجهی را برای کاهش مصرف انرژی و انتشار کربن فراهم می کند ، زیرا ساختمانها بیشترین میزان انرژی را مصرف می کنند. روش تحقیق با استفاده از فناوری مدل سازی اطلاعات ساختمان (BIM)، یکی از تکنیک های مدرن برای مقاوم سازی ساختمانهای متروکه برای دستیابی به ساختمانهای کم انرژی و کاهش اثرات زیست محیطی است. مفهوم مطالعه در یکی از پروژه های عراق اعمال شده است. نویسنده دریافت که استفاده از فناوری BIM در انجام تجزیه و تحلیل های مختلف و کمک به یافتن استراتژی های مقاوم سازی برای بهبود بهره وری انرژی پروژه بسیار مفید است. نتایج نشان می دهد که صرفه جویی در انرژی 24٪ از بهبود کل در مقایسه با وضعیت طراحی پایه و کارآمدترین گزینه ها ، سیستم های HVAC با صرفه جویی در انرژی 71.36 کیلووات ساعت بر(مترمربع سال) است.



Detection of Bikers without Helmet Using Image Texture and Shape Analysis

R. Badaghi^a, H. Hassanpour^{*a}, T. Askari^b

^a Faculty of Computer Engineering and IT, Shahrood University of Technology, Shahrood, Iran

^b Computer Science Department, Faculty of Mathematics and Computer, Higher Education Complex of Bam, Bam, Iran

PAPER INFO

Paper history:

Received 11 November 2020

Received in revised form 04 January 2021

Accepted 14 January 2021

Keywords:

Helmet

Biker

Detection

Local Binary Pattern

Local Variance

Histogram of Oriented Gradient

ABSTRACT

Helmet are essential for preventing head injuries in bikers. Traffic laws are applied in most countries to bikers who don't wear a helmet. Manually checking bikers for the usage of a helmet is a very costly and tedious task. In this regard, several helmet detection methods were developed in literature for detecting bikers violating the law in recent years. This paper proposes an image processing method based on the Local Binary Pattern (LBP), Local Variance (LV), and Histogram of Oriented Gradient (HOG) descriptors for detection of bikers without a helmet. The innovation of the proposed method is mainly on the feature extraction step, which leads the classification towards appropriately discriminating between the two classes of helmet and non-helmet. The experimental results show our method is superior to the existing methods for helmet detection. The accuracy of the proposed helmet detection method is 98.03% using the Support Vector Machine classifier.

doi: 10.5829/ije.2021.34.03c.09

1. INTRODUCTION

Biker safety helmets are very effective at preventing head injuries in road accidents [1]. Due to its effectiveness, laws in many countries enforce bikers to wear a safety helmet. Unfortunately, some bikers refuse to wear it for various reasons.

Image processing techniques can be used to automatically detect violators [2]. Several studies have been conducted on the recognition of bikers without helmets using image processing techniques. The low quality of traffic images is one of the dilemmas for the detection task. To reduce the processing time for helmet detection, only the area containing the biker's head is considered. In most methods, this issue is considered by using the 1/5 (one-fifth) top of the image as the Region of Interest (ROI) (the area containing the biker's head) [3-6]. The process of helmet detection contains three steps: pre-processing, feature extraction, and classification. Different lighting and climate conditions cause unwanted data, such as noise, on traffic images. Therefore, a pre-process is required before the feature extraction step. Feature extraction is the most important step in the bikers' helmet detection. Most of the existing

approaches use several descriptors, based on color, texture, and the geometric shape of the helmet, to extract the features from ROI. Local Binary Pattern (LBP), Histogram of Oriented Gradient (HOG), Circle Hough Transform (CHT), Scale-Invariant Feature Transform (SIFT), and Haar Wavelet are common descriptors in this context [2-6].

This paper proposes a method to detect the biker without a helmet. After a simple pre-processing of images, LBP, Local Variance (LV), and HOG descriptors are used to extract features from the ROI. In order to evaluate the extracted features, a Support Vector Machine (SVM) classifier is used. The rest of the paper is organized as follows. In Section 2, we review previous works on helmet detection. The proposed method is described in Section 3. The results of applying the proposed method on a dataset are provided in Section 4. Finally, the paper is concluded in Section 5.

2. RELATED WORKS

Dinesh et al. provided a method for automatic detection of bikers' non-use of safety helmet [3]. After

*Corresponding Author Institutional Email:
h.hassanpour@shahroodut.ac.ir (H. Hassanpour)

differentiating motorcycles from the other vehicles, the candidate area (head area) from the biker's image is considered for helmet detection. SIFT, LBP, and HOG descriptors were used to extract the features from the head area. The achieved feature vector was employed for classification using SVM. Silva *et al.* suggested the use of CHT technique to determine the position of the biker's head from 1/5 (one-fifth) of the top image [7]. The LBP, HOG, and Wavelet Transform (WT) descriptors were used for feature extraction. They used several classifiers to evaluate the output of the descriptors. Although the computational complexity of the method is significant, the accuracy of the detection is acceptable. Shine and Jiji provided a method for the detection of bikers without helmets [8]. After determining the ROI, the extracted features using the LBP, HOG, and Haarlick descriptors were used for classification. The accuracy of this method is higher than the method proposed by Silva et al. [7].

In another study, Talaulikar et al. used image processing and machine learning techniques to detect the biker's helmet, [9]. They applied median filtering, flood fill, erode and dilate on the ROI. The region area was divided into four quadrants, and the average of intensities and hues were measured in each quadrant. The Principal Component Analysis (PCA) method was applied on the derived features. The accuracy of the method was suitable.

A method was provided to identify construction workers that didn't use safety helmets [10]. Although the purpose of this system is different from our research, the feature extraction step gives useful insights. In this method, the CHT technique is used to detect circular objects inside the image. Since safety helmets used by construction workers are in certain unique colors, i.e. yellow, blue, or red, the circular areas detected by the CHT are searched for helmets in these colors. Color is not a reliable feature for helmet detection in bikers, because the biker's hair may also be the same color as the helmet. The use of CHT technique lonely increases the number of false-positive (FP) predictions in helmet detection, because both the helmet and head are circular.

A study was conducted on workers without helmets in construction sites [11]. Statistical features were calculated from the Gray Level Co-occurrence Matrix (GLCM) after achieving the LBP image. The statistical features include contrast, correlation, entropy, energy, and homogeneity. To evaluate the method, an Artificial Neural Network (ANN) was used. Although the image texture is well analyzed using statistical features, but high time complexity is the disadvantage of the method.

In another study, a method was provided for detecting power substation perambulatory workers without a safety helmet [12]. From the head area, color space transformation and color feature discrimination were extracted. For the color segmentation, the HSV color space (with three channels of Hue, Saturation, and Value)

is more robust than the other color spaces, because this model can easily distinguish the desired color from the range of other colors. Hence, the images were transformed from the RGB to HSV color space. In this method, to segment various colors, two different thresholds were used for the Hue and Saturation channels. The threshold value for the Hue channel (which represents the color) was set manually, whereas the threshold value for the Saturation channel was automatically determined by the OTSU thresholding algorithm. By employing the color segmentation on the two channels, it can be recognized whether the workers are wearing helmets or not.

A detection method for bikers without helmets was proposed using image processing and Convolutional Neural Network (CNN) [13]. Initially, the method identifies bikers using the HOG and the SVM classifier. Then, by applying a CNN to the area of interest, bikers without helmets are identified. While in another method, CNN is used in two steps: discriminating bikers from other vehicles; and the detection of the bikers without helmets. The algorithm was less accurate for motorcycles with a large number of riders or motorcycles with an uncommon passenger position [14].

3. PROPOSED METHOD

In this paper, we propose a new method for detecting bikers not wearing a helmet. After a simple pre-processing, we focus on the feature extraction step. Three descriptors are used to describe samples of the two classes, i.e. helmet and non-helmet.

The SVM is used for classification. Therefore, the proposed method consists of three steps: preprocessing, feature extraction and classification. Each of the three steps is described below.

The LBP extracts homogeneous patterns from the image and pays less attention to heterogeneous patterns. In contrast, heterogeneous patterns in the image are well extracted using the variance [15]. So, simultaneous use of these descriptors can be effective for image texture analyzing and for extracting useful information. On the other hand, the HOG specifies the local shape and the direction of the edges in the image. Hence, this descriptor can describe samples of the two classes. The final descriptor is the feature vector achieved from the descriptors detailed below.

3.1. Database

The database used in this work, thankfully provided by Silva et al. [7], contains 255 images of bikers' head. There are 152 images with helmet, and 103 images without helmet, in the database. Some of the images contain bikers wearing casual hats, which are classified into the non-helmet category. A number of these images are shown in Figure 1. The

images have been captured under different lighting and climate conditions. Also, surveillance cameras were installed far from the road, and they have a low image quality, hence, as seen, the captured images are in low resolution.

3. 2. Pre-processing Initially, images are resized to 40×40 pixels. Usually, shape, texture, and color are used for object feature extraction. Safety helmets are in different colors, but the biker’s hair may be in the same color range as the helmet. So the color is not a trustable feature for this purpose. The descriptors used in the next step are independent of the color space, therefore we obtained gray level images from the RGB color space.

3. 3. LBP Operator The LBP operator is a powerful descriptor to analyze texture information from low-resolution images. The operator is locally applied, reflecting the appearance and the structure of the various regions in the image. The original method is applied on windows of size 3×3 pixels. The LBP uses a thresholding method in which the value of the central pixel is considered as the threshold. The neighboring pixels within the window are labeled considering the threshold value. The pixel is labeled as 0 if its value is smaller than the threshold, otherwise it is labeled as 1. Then, the resulting LBP can be expressed in decimal form as follows:

$$LBP_{P,R} = \sum_{i=0}^{P-1} (S(g_i - g_c)) 2^i, \tag{1}$$

where g_i and g_c are the gray-level values of neighboring pixels and the central pixel, respectively. P is the number of neighborhoods and R is neighborhood radius, where $P = 8$ and $R = 1$ in this research. Function $S(x)$ is a sign function defined as:

$$S(x) = \begin{cases} 0, & x < 0 \\ 1, & x \geq 0 \end{cases} \tag{2}$$

The decimal value obtained from the encoded bit string (in clockwise direction) replaces the central pixel in the window. Since the LBP is applied to the gray level image, the resulting value is between 0 and 255 (see Figure 2). This process is repeated for all pixels in the image and



Figure 1. Samples of images from the database used in the paper

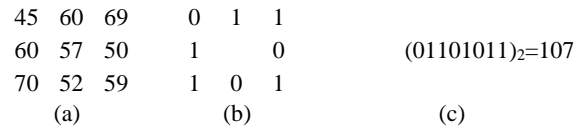


Figure 2. Example of the LBP descriptor calculation. (a) a sample window. (b) Thresholding considering the central pixel. (c) Pattern computed from the threshold result

the histogram obtained from the LBP image is used as a descriptor.

A Uniform Local Binary Pattern (ULBP) that can describe uniform patterns, is one of the basic LBP extensions. In the LBP, a pattern with a maximum of two bitwise transitions is called uniform. For example, the patterns 00000000 (0 transition), 11111110 (1 transition) and 11100111 (2 transitions) are uniform, whereas 00110010 (4 transitions), 10110110 (5 transitions) are not. ULBP operator is based on the original LBP in which neighborhood radius and the number of neighbors can be more than the basis (3×3 neighborhood). The descriptor considers a bin for each uniform pattern. Hence, the number of bins from 256 (different labels that can be obtained with the basic LBP) is reduced to a smaller number [8]. The number of patterns obtained using the descriptor depends on the number of neighbors. For P neighbors, $P \times (P - 1) + 3$ bins are obtained, where the last bin is used for all non-uniform patterns. For example, for $P = 8$, 59 patterns are obtained [16]. We used the LBP_{U2} where $U2$ means uniform, P is the number of neighbors and R is the neighborhood radius (in this paper the best value of P and R are 8 and 1 that were obtained empirically (see Figure 3)).

A biker head image can be represented as a combination of micro-patterns by an LBP histogram. Using one histogram for the whole image cannot encode the shape information and indicate locations of these micro-patterns in the image [17]. Hence, the image is divided into neighboring cells (in a 5 × 5 window) and the LBP histogram is calculated in each cell. In this research, 59 features were extracted. Eventually, these histograms are concatenated into a single histogram feature vector (as shown in Figure 4).

3. 4. Local Variance The Local Variance (LV) defines the gray level distribution between pixels within

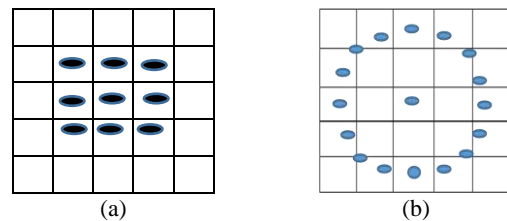


Figure 3. Examples of the Uniform LBP operator; (a) the circular (8, 1) and; (b) the circular (16, 2) neighborhoods

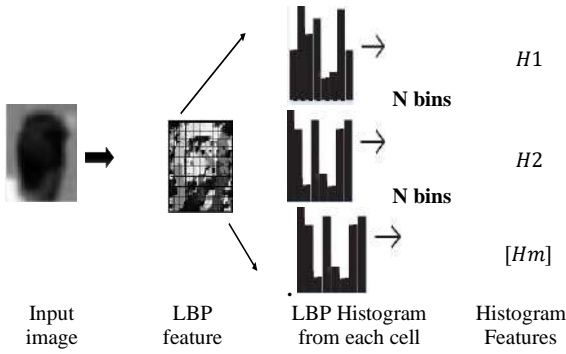


Figure 4. LBP-based image descriptor.

a neighborhood. The smaller the variance, the closer the gray level of pixels within the neighborhood, and vice versa [16]. As mentioned earlier, image variance can extract non-homogeneous patterns. On the other hand, ULBP analyzes homogeneous patterns. The descriptors can be good supplements for extracting the image’s textural patterns. In our approach, a local variance is used with a window size of 4. The window moves on each row of the image, horizontally across each column, and the variance of each image pixel is computed. The second row of Figure 5 shows the heterogeneous regions. Equation (3) shows the calculation of a pixel variance, where A is a vector made up of N scalar observations. In this paper, the value of N is considered as 4.

$$V = \frac{1}{N-1} \cdot \sum_{i=1}^N |A_i - \mu|^2 \tag{3}$$

$$\mu = \frac{1}{N} \cdot \sum_{i=1}^N A_i \tag{4}$$

Also, μ is the mean in the vector, shown in Equation (4). The dimensions of this vector is 1×36 . A number of variance images are shown in Figure 5.

3. 5. Histogram Descriptor The HOG feature descriptor is an efficient and popular method for object detection. The main idea behind the algorithm is to identify the local object shape and appearance using the distribution of local intensity gradients or edge directions [18]. This descriptor works even without knowing the edge’s precise position. The steps for implementation of the HOG descriptor are as follows:

- (1) Dividing the image into small regions (cells). In the paper, cell size is 8×8 pixels and the cell histogram is computed using nine bins.

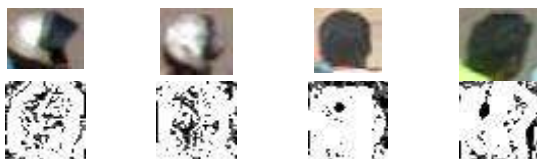


Figure 5. A number of images (top row) with their variance (bottom row)

- (2) Calculating the gradient in x and y directions for each pixel within the cell, and putting them into a x -bin histogram. Value of x depends on the gradient orientation. For the unsigned gradients, this value is 9, else it is 18. Because larger values of x cannot get the important information, we used the unsigned gradients [19]. The range of orientation is from 0 to 180 degrees. The mask array used for computing the gradient is $[-1, 0, +1]$.
- (3) For invariance to illumination and shadows, a group of adjacent cells is considered as a block, then all the cells in the block are normalized (as shown in Equation (5) and Equation (6)). We used blocks with 2×2 cells, where each of them contains 16×16 pixels; for more robust results, blocks have a 50% overlap. In total, each block contains a histogram with 36 bins (4×9). See Figure. 6.

3. 6. Image Classification

Our dataset consists of bikers wearing and not-wearing a helmet, so we use binary classifiers to classify the images. The classifier’s input is the extracted feature vector from the hybrid descriptor, which consists of LBP, HOG and LV. The linear SVM classifier is used for the classification. SVM is a supervised learning model which is used in classification and regression. Data is divided into two categories: train and test. The technique produces a model based on training data and their labels, and uses this model to predict test data labels. If the data are linearly separated, SVM uses a linear hyper plane, otherwise, using a kernel function, SVM can separate the data using a non-linear hyper plane. The data is transferred to a higher-dimensional space; in which data can be linearly separable in the new space [20].

$$H_{B1} = \left[\frac{HC1}{NB1}, \frac{HC2}{NB1}, \frac{HC5}{NB1}, \frac{HC6}{NB1} \right] \tag{5}$$

$$FV = [H_{B1,2}, H_{B3}, \dots] \tag{6}$$

4. EXPERIMENTAL RESULTS

By applying the proposed method on the introduced data, we evaluated the effectiveness of this method. The cross

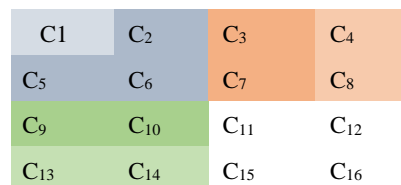


Figure 6. Example of cells and blocks, C_1 is a cell and $[C_1, C_2, C_5, C_6]$ are a block

validation technique has been used to separate train and test samples. In this technique, the original samples are divided into K equal parts, the model learns from the training samples ($K-1$ parts), and is evaluated using the test samples (one part). The process of model learning and testing is repeated K -times, so that each time the $K-1$ parts are used for training and one part is used for the test [21]. Each sample is used once for testing which makes the results reliable. Eventually, the average of this K -iterations is reported as the final result. We used the basic state of this technique with the value of K equal to 10. This method is evaluated using SVM classifier. We evaluated SVM with different kernels (linear kernel, tangent sigmoid, polynomial and radial basis function) and the linear kernel gave the best result.

In this paper, the measures used for evaluation are: True Positive Rate or Sensitivity (S), Specificity (SP) or true negative rate, Positive Predictive Value (PPV) or Precision, Negative predictive value (NPV) and Accuracy (A). These measures are described below.

$$\text{Sensitivity(S)} = \text{TP} / (\text{TP} + \text{FN}) \quad (7)$$

$$\text{Specificity (SP)} = \text{TN} / (\text{TN} + \text{FP}) \quad (8)$$

$$\text{PPV} = \text{TP} / (\text{TP} + \text{FP}) \quad (9)$$

$$\text{NPV} = \text{TN} / (\text{TN} + \text{FN}) \quad (10)$$

$$\text{Accuracy(A)} = (\text{TP} + \text{TN}) / (\text{TP} + \text{TN} + \text{FN} + \text{TN}) \quad (11)$$

$$\text{F-measure (F)} = 2 \times (\text{S} \times \text{PPV} / (\text{S} + \text{PPV})) \quad (12)$$

By using the linear SVM classifier, 99 out of 103 images were correctly classified as bikers not wearing a helmet (True Positive -TP) and 151 out of 152 images were correctly classified as bikers wearing a helmet (True Negative - TN).

TABLE 1. Confusion matrix for SVM classifier

Method	S (%)	SP (%)	PPV (%)	NPV (%)	F-measure	A
The method introduced by Silva et al. [7]	94.00	-	91.61	91.00	92.81	91.37
The proposed method	96.11	99.34	99.00	97.41	97.53	98.03

TABLE 2. Images classification results

	Predicted	
	Positive	Negative
Actual	Positive	99
	Negative	4
		151

Hence, the values of TN, TP, FP and FN were obtained as 151, 99, 1 and 4, respectively. Confusion matrix for the classifier is shown in Table 1. The best result was obtained using the SVM classifier with the accuracy rate of 98.03.

We have also compared the performance of our method with the method proposed by Silvi *et al.* [7], and the results are shown in Table 2. The accuracy of the proposed method was improved more than 6% on the dataset by using the SVM classifier. To evaluate the computational complexity of the two approaches, both methods were implemented in MATLAB on a computer with an Intel(R) core(TM) i3 processor operating at 2.40 GHz clock frequency, and 6.00 GB of RAM. The execution time is 2.32 seconds and 8.37 seconds respectively for the proposed method and the method introduced by Silvi *et al.* [7].

5. CONCLUSION

In this paper, an approach was proposed for detecting bikers not wearing a helmet. The proposed method consists of three steps: preprocessing, feature extraction and classification. Novelty of the proposed method is mainly on the feature extraction step, which leads to the classification method appropriately discriminating the two classes of helmet and non-helmet. We used a hybrid descriptor which contained HOG, LBP and LV feature extractors. Experimental results have shown that the proposed method improved helmet detection in bikers both in terms of accuracy and computational complexity.

6. REFERENCES

1. Waranusas. R, Bundon. N, Tintong. V, Tangnoi. C, and Pattanathaburt. P, "Machine vision techniques for motorcycle safety helmet detection", 28th International Conference on Image and Vision Computing New Zealand (IVCNZ), (2013), 35-40. doi: 10.1109/IVCNZ.2013.6726989
2. Doungmala. P, and Klubsuwan. K, " Helmet wearing detection in Thailand using Haar like feature and circle hough transform on image processing", International Conference on Computer and Information Technology (CIT), (2011), 611-614. doi:10.1109/CIT.2016.87
3. Dahiya. K, Singh. D, and Mohan. C. K, "Automatic detection of bike-riders without helmet using surveillance videos in real-time", International Joint Conference on Neural Networks (IJCNN), 3046-3051, (2016), doi: 0.1109/IJCNN.2016.7727586
4. Silva. R, Aires. K, Santos.T, Abdala. K, Veras. R, and Soares. A," A. Automatic detection of motorcyclists without helmet", Latin American Computing Conference (CLEI), 1-7, (2013), doi: 10.1109/CLEI.2013.6670613
5. Silva. R, Aires. K, Veras. R, Santos. T, Lima. K, and Soares. A, "Automatic motorcycle detection on public roads", *CLEI Electronic Journal*, Vol. 16, No. 3, (2013), doi: 10.1109/clei.2012.6427165
6. Marayatr. T, and Kumhom.P, "Motorcyclist's Helmet Wearing Detection Using Image Processing", In *Advanced Materials*

- Research**, Vol. 931, (2014), 588-592, doi:10.4028/www.scientific.net/AMR.931-932.588
7. Silva. R. V, Aires. K. R. T, and Veras. R. D.M, "Helmet detection on motorcyclists using image descriptors and classifiers", 27th Conference on Graphics, Patterns and Images, (2014), 141-148. doi:10.1109/sibgrapi.2014.28
 8. Shine. L, and Jiji. C.V," Automated detection of helmet on motorcyclists from traffic surveillance videos: a comparative analysis using hand-crafted features and CNN", *Journal of Multimedia Tools and Applications*, Vol. 1380, (2020), 1-21, doi: 10.1007/s11042-020-08627-w
 9. Alaulikar. A.S, Sanathanan. S, and Modi. C.N," An enhanced approach for detecting helmet on motorcyclists using image processing and machine learning techniques", In *Advanced Computing and Communication Technologies*, Vol. 702, (2019), 109-119, doi: 10.1007/978-981-13-0680-8_11
 10. Rubaiyat. A.H, Toma. T.T, Kalantari-Khandani. M, Rahman. S.A, Chen. L, Ye. Y, and Pan. C.S., "Automatic detection of helmet uses for construction safety", WIC/ACM International Conference on Web Intelligence Workshops (WIW), (2016), 135-142. doi: 10.1109/WIW.2016.045
 11. JIANG. X, XUE. H, ZHANG. L, and ZHOU. Y," A Study of Low-resolution Safety Helmet Image Recognition Combining Statistical Features with Artificial Neural Network", *International Journal of Simulation-Systems, Science and Technology*, Vol. 17, No. 37, (2016), 1473-8031, doi: 10.5013/IJSSST.a.17.37.11
 12. Li. K, Zhao. X, Bian. J, and Tan. M," Automatic Safety Helmet Wearing Detection", arXiv labs:experimental projects with community collaborators, 1802.00264, (2014).
 13. Raj. K. D, Chairat. A, Timtong. V, Dailey. M. N, and Ekpanyapong. M, "Helmet violation processing using deep learning", International Workshop on Advanced Image Technology (IWAIT), (2018), 1-4, doi: 10.1109/IWAIT.2018.8369734
 14. Siebert. F.W, and Lin. H," Detecting motorcycle helmet use with deep learning", *Journal of Accident Analysis and Prevention*, Vol. 134, (2020), doi:10.1016/j.aap.2019.105319
 15. Shakour.M. H and Tajeripour. F," Local entropy pattern to extract textural images features", Vol. 3, No. 2, (2016), 73-85.
 16. Lenc. L, and Král. P," Automatically detected feature positions for LBP based face recognition", In *IFIP International Conference on Artificial Intelligence Applications and Innovations*, (2014), 246-255, doi: 10.1007/978-3-662-44654-6_24
 17. Huang.D, Shan. C, Ardabilian. M, Wang. Y, and Chen. L, "Local binary patterns and its application to facial image analysis: a survey", *Journal of Transactions on Systems, Man, and Cybernetics, Part C (Applications and Reviews)*, Vol. 41, No. 6, (2011), 765-781, doi: 10.1109/TSMCC.2011.2118750.
 18. Dalal, N, and Triggs. B," Histograms of oriented gradients for human detection", Computer Society Conference on Computer Vision and Pattern Recognition, (2005), 886-893.
 19. Başa. B," Implementation of Hog Edge Detection Algorithm Onfpga's", *Procedia-Social and Behavioral Sciences*, Vol. 174, (2015), 1567-1575, doi: 10.1016/j.sbspro.2015.01.806
 20. Boser. B. E, Guyon. I. M, and Vapnik. V. N, "A training algorithm for optimal margin classifiers", In Proceedings of the fifth annual workshop on Computational learning theory, (1992), 144-152. doi: 10.1145/130385.130401
 21. Ellis. R. P, and Mookim. P. G, "Cross-validation methods for risk adjustment models", Mimeo, Boston University, (2008).

Persian Abstract

چکیده

کلاه ایمنی برای جلوگیری از آسیب های ناحیه سر موتورسواران ضروری است. در اکثر کشورها برای موتورسوارانی که از کلاه ایمنی استفاده نمی کنند، قوانینی وضع شده است. بررسی موتورسواران متخلف به صورت دستی کاری وقت گیر و پرهزینه است. در این راستا، در طی سال های اخیر چندین روش تشخیص موتورسواران بدون کلاه ایمنی ارائه شده است. در این مقاله یک روش بر حسب پردازش تصویر برای شناسایی موتورسواران بدون کلاه ایمنی پیشنهاد شده است. این روش از توصیفگرهای الگوی دودویی محلی، واریانس محلی و هیستوگرام مبتنی بر گرادینان استفاده می کند. نوآوری این روش اساسا در مرحله استخراج ویژگی است که باعث می شود طبقه بندی دو کلاس با و بدون کلاه ایمنی بهتر انجام شود. نتایج تجربی نشان می دهد که روش پیشنهادی ما نسبت به روش های موجود دیگر، دارای برتری در تشخیص و طبقه بندی است. دقت روش پیشنهادی برای تشخیص کلاه ایمنی با استفاده از دسته بند ماشینی بردار پشتیبان 98.03 درصد است.



Design Procedure of an Outer Rotor Synchronous Reluctance Machine for Scooter Application

S. R. Salehinia^a, S. E. Afjei^{*a}, A. Hekmati^b, H. Aghazadeh^a

^a Department of Power Electrical Eng., Faculty of Electrical Engineering, University of Shahid Beheshti, Tehran, Iran

^b Electric Machine Research Group Niroo Research Institute

PAPER INFO

Paper history:

Received 21 June 2020

Received in revised form 23 September 2020

Accepted 30 December 2020

Keywords:

Finite Element Method

Magnetic Flux Barrier

Synchronous Reluctance Motor

Torque Ripple

ABSTRACT

Synchronous reluctance motors, despite their cost-effective types and wide range of speed, generally have a considerable torque ripple due to changes in magnetic resistance between the flux barriers and the stator teeth. Given the numerous possible rotor combinations with different forms of flux barriers, designing an optimal synchronous reluctance motor without the use of mathematical equations and a clear algorithm will be very time-consuming. In this study, a comprehensive method is used to design a synchronous reluctance motor with an external rotor and a flux barrier shape adopted from the behavior of fluids around a solid rotor. According to the new topology, an external rotor synchronous reluctance motor is designed. Multi-objective Taguchi optimization algorithm based on finite element analysis (FEM) is used to maximize the average torque and reduce the torque ripple. This motor is designed for 300 W electric scooters with a six-pole rotor, a 36-slot stator, and a distributed winding. Finally, a prototype of the proposed motor is constructed to validate the results of simulations. The experimental results confirm the accuracy of the design method.

doi: 10.5829/ije.2021.34.03c.10

NOMENCLATURE

	Average Torque (N.m)	Greek Symbols	
T_{av}	Average Torque (N.m)	ρ	Mass density (kg/m ³)
<i>SynRM</i>	Synchronous Reluctance Motor	η	Efficiency
<i>EX – SynRM</i>	External rotor Synchronous Reluctance Motor	ψ	potential(m ² /s ²)
TR	Torque ripple	ξ	differential operator with the flow field
FEM	Finite Element Method	ν	Kinematic viscosity (m ² /s)
MMF	Magneto-motive force	μ	viscosity coefficient(kg/(m.s))
g	Air-gap width (mm)	Subscripts	
I	Rated current (A)	k	flux barriers number
f	Average MMF	m	flux barriers number
P_r	Pressure(kg/m ³)	q	along the q-axis
S	Iron parts thickness	d	along the d-axis
N_s	Rated Speed (rpm)		

1. INTRODUCTION

Simplicity the synchronous reluctance motor, with no need for a squirrel cage in the rotor and permanent magnet, and the similarity of its stator production line

with the widely used induction motor [1-4], have attracted the electric motors' designers and manufacturers in recent years. Most studies into the basics of this motor have been carried out on internal rotor models and there are a limited number of articles regarding external rotor architecture [5-9]. However, external rotor electric motors, thanks to their higher torque compared to the internal rotor architecture, have

*Corresponding Author Institutional Email: e-afjei@sbu.ac.ir (S.E Afjei)

more practical applications, especially in electrical vehicles [10, 11].

Limited amounts of studies are conducted in the field of reluctance motor design with external. The proposed method in considers the thickness of the flux barrier to be equal along the flux barrier. The chief reason behind this design is said to be mechanical strength. While it is shown that the closer the flux barrier shape is to the behavior of the flux lines in the rotor, the more optimized the design procedure is discussed in literature [12]. In this paper, the shape of flux barriers is designed based on the fluid-liquid velocity equation. By selecting the appropriate parameters and optimizing, a comprehensive design for the external rotor synchronous motor is presented. The present study intends to introduce a new comprehensive design method for the Ex-SynRM based on the formation in the shape of flux barriers in the solid rotor using its similarity to the pattern of fluid velocity equations around a solid object. To design external rotors in a synchronous reluctance motor (SynRM), it is tried to block the flux along the q-axis and maximize the magnetic conductance along the d-axis [12, 13]. The flux barriers in the rotor are designed in three steps: (i) determining the flux barriers shape using mathematical equations, (ii) barriers placement on the q-axis, and (iii) optimizing the designed rotor. Then, the shape of flux barriers between the d and q axes is determined through defining some equations that depend on the radius and angle of the points on the flux barrier line in the rotor. The flux barriers start from the q-axis and end around the d-axis. All points between the start and endpoints on the flux barrier line have their own radius, angle and a constant parameter (parameter C). Figure 1 depicts a mathematical definition used for the internal rotor in more details are discussed in literature [14,15]. The design is further optimized through the optimization method, so that the closer the shape of the generated flux barriers is to the shape of the flux lines, the higher average torque discussed in literature [14]. The proposed design procedure of the external rotor is shown in Figure 2.

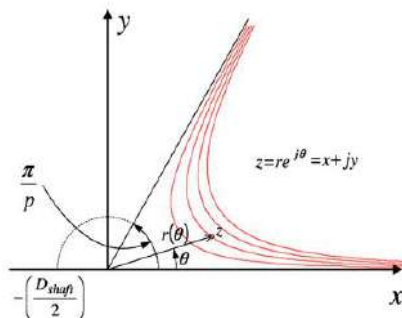


Figure 1. Mathematical definition of the parameters describing the barriers line in a two-pole machine [15]

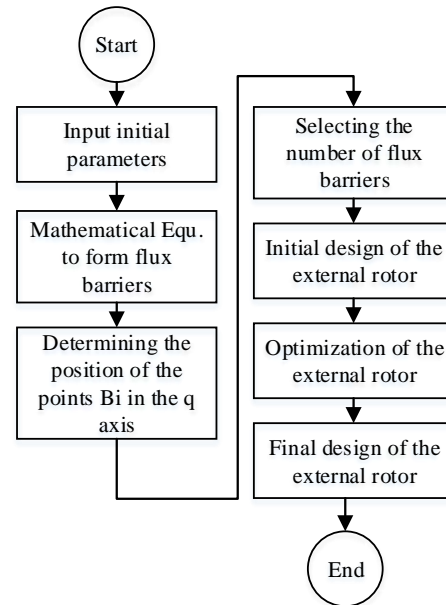


Figure 2. Design procedure of the proposed EX-SynRM

In this regard, this paper presents a new strategy for the design and analysis of EX-SynRM. The contents are organized as follows. The flux barriers shape in the rotor is provided in the second section of the proposed mathematical equations, considering some variables for improvement of the motor performance. Then the variables are evaluated through finite element analysis. In the last part of this section, the number of flux barriers is determined. Section 4 pertains to optimization through Taguchi method taking numerous variables into account. Finally, the proposed design is constructed for an electric scooter and the results of finite element analysis are compared with those of the manufactured motor.

2. MATHEMATICAL APPROACH

As a symmetric Stokes flow around a solid sphere shown in Figure 3a [16], the fluid flow lines around a solid sphere are similar to the magnetic flux lines distribution in Figure 3b. The equations expressing the motion of the fluid, with two properties of adhesion and incompressibility can be expressed as follows [16].

$$\nabla \cdot V = 0 \quad (1)$$

$$\rho \frac{DV}{Dt} = -\nabla Pr + \mu \nabla^2 V \quad (2)$$

$$Pr = pr + \rho \psi \quad (3)$$

where $V(\text{m}^2/\text{s})$ is the liquid instantaneous velocity, $Pr(\text{kg}/\text{m}^3)$ is the liquid natural pressure, $\rho \psi$ is the

gravitational potential energy per unit volume (the combination of these two pressures is known as the effective pressure) Equation (3), ρ is the liquid mass density, μ (kg/(m.s) is the liquid viscosity coefficient which is calculated experimentally, and ψ (m²/s²) is the gravitational potential [16]. Assume a solid sphere of radius a in the standard spherical coordinates plane with the components r , θ , and ϕ . The fluid flow surrounds the sphere ($r > a$), which is an example of the axial Stokes flow [16]. the symmetric axial Stokes flow, the fluid velocity equation can be considered as follows.

$$V(r) = v_r(r, \theta)e_r + v_\theta(r, \theta)e_\theta \quad (4)$$

According to literature [16] and assuming an incompressible liquid:

$$V = \nabla \phi \times \nabla \psi \quad (5)$$

where $\psi(r, \theta)$ is the Stokes flow function. Then,

$$v_r(r, \theta) = -\frac{1}{r^2 \sin \theta} \frac{\partial \psi(r, \theta, \phi)}{\partial \theta} \quad (6)$$

$$v_\theta(r, \theta) = \frac{1}{r \sin \theta} \frac{\partial \psi(r, \theta, \phi)}{\partial r} \quad (7)$$

Consider $\omega_r = \omega_\theta = 0$

$$\omega_\phi(r, \theta) = \frac{1}{r} \frac{\partial(rv_\theta)}{\partial r} - \frac{1}{r} \frac{\partial v_r}{\partial \theta} = \frac{\zeta(\psi)}{r \sin \theta} \quad (8)$$

$$\zeta = \frac{\partial^2}{\partial r^2} + \frac{\sin \theta}{r^2} \frac{\partial}{\partial \theta} \frac{1}{\sin \theta} \frac{\partial}{\partial \theta} \quad (9)$$

where ζ is a differential operator with the flow field symmetry outside the sphere having an axial symmetry, i.e. $\partial \phi / \partial \phi = 0$. In other words, here is $V_\phi = 0$ (V_ϕ is component in spherical coordinates) and it behaves like a cylindrical coordinate system due to symmetry. Evaluation of physical boundary around the sphere surface results in:

$$v_r(a, \theta) = 0 \quad (10)$$

$$v_\theta(a, \theta) = 0 \quad (11)$$

Which indicates zero speed on the sphere surface and a long distance from the sphere surface; it can be stated that:

$$v_r(r \rightarrow \infty, \theta) \rightarrow -V \cos(\theta) \quad (12)$$

$$v_\theta(r \rightarrow \infty, \theta) \rightarrow -V \sin(\theta) \quad (13)$$

According to Equation (5) discussed in literature [16], the specifications of the axial stocks flow can be expressed by the following equation.

$$\zeta^2(\psi) = 0 \quad (14)$$

By writing the boundary conditions from Equations (4) to (7), one can write:

$$\left. \frac{\partial \psi}{\partial r} \right|_{r=a} = 0, \left. \frac{\partial \psi}{\partial \theta} \right|_{r=a} = 0 \quad (15)$$

$$\psi(r \rightarrow \infty, \theta) \rightarrow \frac{1}{2} V r^2 \sin^2 \theta \quad (16)$$

$$v_r(r, \theta) = -\frac{\cos \theta V r^2}{r^2}, v_\theta = \frac{\sin \theta (V r^2)}{2r} \frac{dr}{dr} \quad (17)$$

Equation (2) can be summarized as follows [16]:

$$\nabla \text{Pr} = -\mu \nabla \times \omega = \mu \nabla \phi \times \nabla (\omega_\phi r \sin \theta) \quad (18)$$

Therefore,

$$\frac{\partial \text{Pr}}{\partial r} = -\frac{3\mu V a \cos \theta}{r^3} \quad (19)$$

$$\frac{\partial \text{Pr}}{\partial \theta} = -\frac{3\mu V a \sin \theta}{2r^2} \quad (20)$$

This means that the pressure distribution in that fluid is:

$$\text{Pr}(r, \theta) = p_0 + \frac{3\mu V a \cos \theta}{2r^2} \quad (21)$$

where p_0 is initial pressure Figure 3a shows the axial stocks flow lines under the influence of the effective pressure on the x-z plane around a solid sphere using Equation (21).

As shown in Figure 3a, each stokes flow line is affected by constant pressure and velocity in Equation (21); therefore, the parameters Pe , p_0 , V , and μ in Equation (21) are in a fixed line, and hence Equation (21) can be properly converted to an appropriate equation for the barrier's lines.

$$C = \frac{\cos(\theta * \frac{p}{2})}{2r^{2p}} \quad (22)$$

$$\theta = \frac{2 * \cos^{-1}(2C.r^{2p})}{p} \quad (23)$$

In the above equations, C is a constant function of the point coordinates through which the curve passes, p is the number of poles. The initial shape of the flux barriers is presented using mathematical equations and parameter C is determined. The results of FEM analysis for the solid rotor and the designed six-pole rotor with three flux barriers are compared in Figure 4. As can be seen, the flux barriers shape is similar to the flux lines shape in the solid rotor. It should be noted that this step,

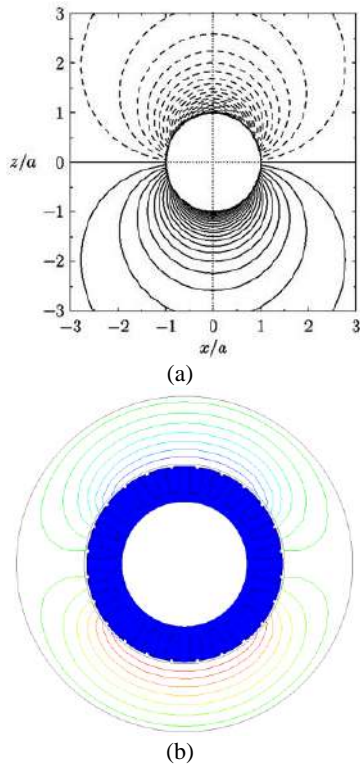


Figure 3. (a) Stokes under pressure $P-p_0$ around a sphere, (b) Magnetic flux line in the external rotor SynRM with two poles without flux barriers

i.e. designing the flux barriers, is the starting point for rotor design to achieve an optimal design with the least number of simulations. Figures 3b and 4a depict the flux lines in the solid rotor when there are no barriers in the rotor. Since the flux lines in the solid rotor and the fluid pressure lines are similar at equal velocities [16], the fluid velocity and pressure line pattern in fluid mechanics are used to design the flux barriers shape in the external rotor SynRM.

General specifications of the prototype motor suitable for electric scooters are given in Table 1. Design procedure is initiated according to the selected

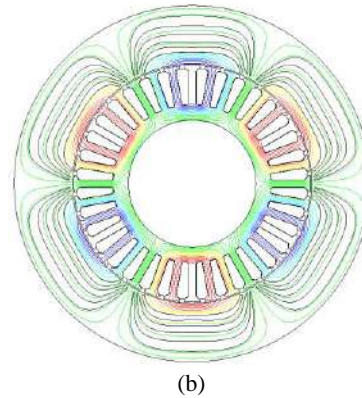
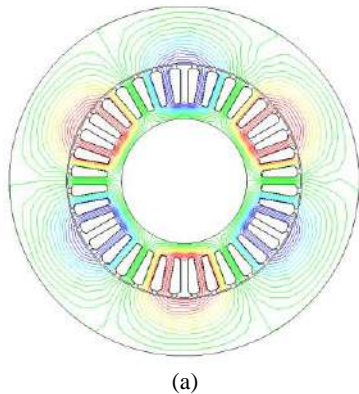


Figure 4. (a) Magnetic flux line in the external rotor SynRM with six poles without flux barriers, (b) Initial model of the six-pole design with three flux barriers

dimensions in Table 1. Based on the rotor flux lines shape and Equations (22) and (23), the general sketch of the proposed rotor output with the k number of flux barriers is shown in Figure 5.

The angle is equal to $\pi/2p$ along the q -axis, where p is the number of the rotor pole pairs. The position of $Bk_1, Bk_2, \dots,$ and Bk_n (Bk_i in which B and k denote the barrier and the selected flux barriers number, respectively) along the q -axis can be determined by Equations (25)-(31).

Definition of the parameters for determining the size and position of flux barriers in the external rotor is as follows: g is the air gap length, S_i is the iron parts thickness in each section, WB_k is the K th barrier width, B_k is the flux barriers initial and end points on the q -axis, and β is a constant value that determines the flux barrier's arc length.

Selecting insulation ratio in the q -axis (k_{wq} , which is defined as the ratio of the thickness of total insulation

TABLE 1. General specifications of the designed motor

Parameter	Definition	Value
R_{sh}	Shaft outer diameter	20 mm
R_{st}	Stator outer diameter	120.5 mm
R_{or}	Rotor outer diameter	168 mm
R_{inr}	Rotor inner diameter	121 mm
L	Stack Length (L Stack)	40 mm
P_o	Power	290 W
N	Number of turns	29turns/slot
N_s	Rated Speed	1500 rpm
I	Rated current	6 A
P	Number of pole pairs	3
η	Efficiency	0.84
g	Air-gap width(g)	0.5 mm

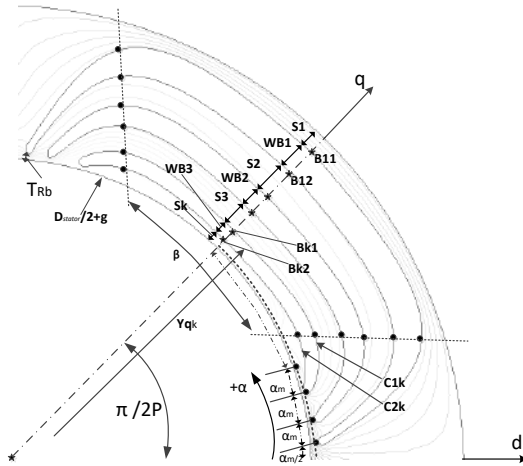


Figure 5. General rotor layout

over total iron conducting material inside the rotor) is the most fundamental and effective part in the rotor design which is defined in literature [17-19]:

$$k_{wq} = \frac{((R_{rotor} - R_{shaft}) - \sum_{n=1}^{k+1} S_i)}{\sum_{n=1}^{k+1} S_i} \quad (24)$$

The initial design is done by selecting the insulation ratio, and the tangential ribs T_{Rb} , shown in Figure 5, are decided according to the practical values which are 0.5 and 0.25mm.

Equation (22) pertain to the calculation of the C_{1k} and C_{2k} potential curves of the flux barrier edges with the starting point of B_{ki} on the q-axis. The flux barriers width and iron parts along the q-axis can be calculated through the equations shown in as follows [18].

$$\frac{WB_k}{WB_m} = \frac{\Delta f_k}{\Delta f_m} \sqrt{\frac{S_k}{S_m}} \quad (25)$$

$$\Delta f_k = f_{q+1} - f_{qk} \quad (26)$$

The gaps between the flux barriers, displayed as S_k , can be calculated by Equation (30), where f_{dh} is the magneto-motive force along the d-axis [19].

$$\frac{2S_1}{S_2} = \frac{fd_1}{fd_2}, \frac{S_h}{S_{h+1}} = \frac{fd_h}{fd_{h+1}}, h=1,2,..k \quad (27)$$

The magneto-motive force (MMF) along the d-axis in each section is equal to the average magnetic driving force by that piece. Therefore, f_{dk} can be calculated through averaging the magneto-motive force between the two end-points of the kth piece; the calculations can be found in literature [18]. The flux barriers width along

the q-axis can be considered W_{BK} [19].

$$\frac{WB_h}{WB_{h+1}} = \left(\frac{\Delta f_h}{\Delta f_{h+1}} \right)^2, h=1,2,..k-1 \quad (28)$$

$$\sum_{h=1}^k WB_h = l_a = \frac{(r_{out} - 2r_{in} - g)}{1 + \frac{1}{k_{wq}}} \quad (29)$$

where Δf_k is the difference between the average MMF per unit and $\sin(p\alpha)$ is the coverage over the Kth barrier in which p is the number of the rotor pair poles. As in Equations (30) and (31), the flux barriers width along the q-axis is, directly and indirectly, a function of k_{wq} , and f_{dh} is the average MMF of the hth piece from MMF_d. According to literature [19] for the best insulation distribution, i.e. the flux barriers width, the flux barriers should have a constant and equal permeability; therefore:

$$\frac{p_i}{p_j} = (cte.) = 1 \Rightarrow \frac{W_{bi}}{W_{b1}} = \left(\frac{\Delta f_i}{\Delta f_1} \right)^2, i=1,2,..,k \quad (30)$$

$$\Delta f_i = f_{qi+1} - f_{qi} \quad (31)$$

By determining the flux barriers width and the gap between the barriers along the q-axis, the radius of a point with the q-axis angle of one of the potential curves is defined and the potential curve can be plotted from the q-axis to the rotor end edge using Equations (22) and (23) and calculation of the C constant.

The initial values of the motor design and dimensions are considered as input parameters. Then, using the Equation (23) expressed in this part, the shape of flux barriers and the positions of the flux barrier in the q axis are determined. Accordingly, the number of flux barriers is selected based on FEM analysis. Consequently, the initial rotor is designed using the Equations (24)-(31). As shown in Figure 2 in the next step, finally, the appropriate parameters for rotor optimization are selected and the rotor is optimized.

3. FEM ANALYSIS RESULT

This section pertains to FEM analysis of the effect of three parameters on the SynRM performance. Each analysis is performed separately to show better insight into the impact each parameter contributes to the torque production. In the last part of this section, the effect of flux barriers number on the rotor is assessed using the results of finite element analysis, and the number of flux barriers is determined for the rotor.

3. 1. Effect of q-axis Insulation Ratio on the Torque Production

The effect of insulation ratio in the q-axis (k_{wq}) on the average torque and torque ripple of the selected external rotor SynRM with six poles in a rotor with one flux barrier and the constant β is considered in the above equations, the results of which are shown in Figure 6. As can be seen, the maximum torque (2.2 N.m) and with peak to peak torque ripple of 1.3(N.m) value is related to $k_{wq}=0.7$.

3. 2. Effect of the Flux Barriers Arc Length on the Torque Production

The effect of changing of the flux barriers arc length (β) on the average torque and peak to peak torque ripple, when k_{wq} is set to the optimal value ($k_{wq}=0.7$), is shown in Figure 7.

As shown in Figure 7, $\beta = 3$ is the best choice for a rotor with one flux barrier, resulting in the maximum average of 2.2 (N.m) torque and the minimum torque ripple of 1.38 (N.m). It is worth mentioning that higher amounts of β may lead to flux barriers interference.

3. 3. Effect of the Number of Flux Barriers on the Torque Production

The effect of the number of flux barriers for a special external rotor SynRM on

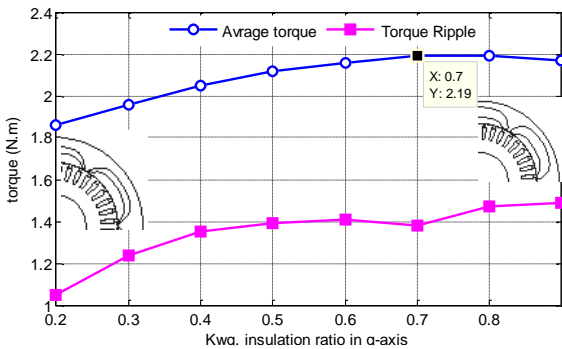


Figure 6. Average Torque and peak to peak torque ripple for different values of k_{wq} for a special β

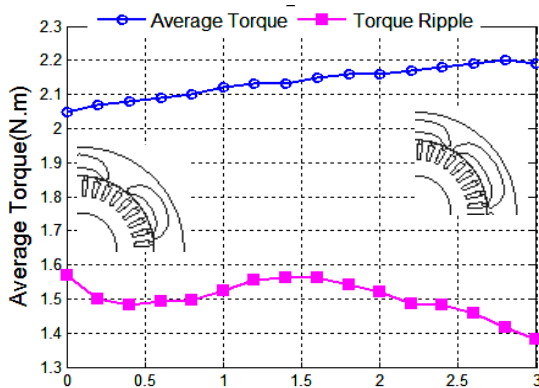


Figure 7. Torque and peak to peak torque ripple (FEM) for different values of β when k_{wq} is 0.7

average torque and torque ripple should be investigated because all design parameters can be affected. For the preliminary study, the calculated optimal values of the q-axis insulation ratio and the optimal arc length coefficient are assumed equal for all cases. Then, a motor with already mentioned characteristics is analyzed with equal parameters and different numbers of flux barriers through the finite element method, the results of which are depicted in Figure 8.

According to the results and considering the average torque and torque ripple values at the same time, a rotor with two flux barriers is the most logical and simplest choice.

4. MULTI-OBJECTIVE OPTIMIZATION OF THE EXTERNAL ROTOR SYNRM

In order to optimally design the motor, the main effective parameters should be analyzed simultaneously. The design variables in this study are the insulation ratio in the q-axis (k_{wq}), the flux barriers arc length (β), the flux barriers width (ΔWB), the displacement of the flux barrier center from the motor shaft center (ΔYq), and the magnetic thickness of the rib from the rotor edges (TRb) as shown in Figure 5.

In this design, the average amounts of torque and torque ripple are considered as the main goals in the fitness function, when the percentage of torque ripple can be expressed as follows:

$$T_R \% = \frac{(T_{Max} - T_{min})}{T_{ave}} \cdot 100 \tag{32}$$

Where T_{Max} , T_{min} , and T_{ave} are the maximum torque, minimum torque, and average torque, respectively. The Taguchi method involves the following steps [20]: (a) defining the number of levels of factors, (b) choosing the number of factors, (c) selecting a suitable orthogonal array and construct the matrix, (d) calculating signal-to-noise (S/N) ratio, (e) analysis of Variance (ANOVA),

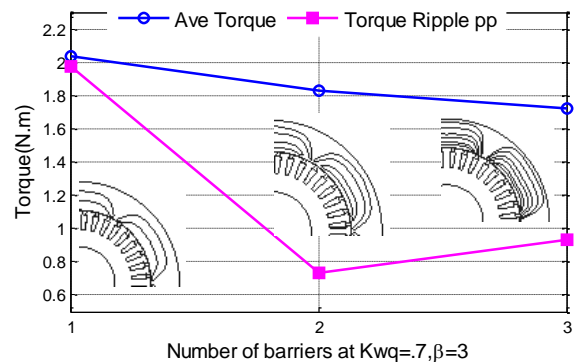


Figure 8. Average torque and torque ripple (FEM) for different values of k , where k is the number of barriers

(f) identifying the control factors and their levels, and (g) analysis of the results. Therefore, Taguchi method involves the identification of proper control factors to obtain the optimum results of the process. According to Figure 5, the rotor with two flux barriers is selected, resulting in 9 parameters for optimization. This experiment has 9 variables at 3 different levels which are shown in Table 2.

A full factorial experiment would require $3^9 = 19683$ combinations of factor levels which takes long time to analyze all the cases. To overcome this problem, Taguchi suggested a special method to take the effects of all mentioned states into consideration in less time to consider all conditions called orthogonal array. The experiment is arranged as $L27 = (3^9)$ in which L represents an orthogonal table with 27 scenarios consisted of nine variables having three levels, the details of which are shown in Table 3.

After performing the experiments according to the orthogonal scenarios, mean effects of optimization parameters on the average torque and torque ripple are plotted.

The type of the control functions related to S/N are “large is the better” and “smaller is the better” for the average torque and torque ripple, respectively [21].

TABLE 2. The levels of design variables

Variable	Level 1	Level 2	Level 3
k_{wq}	0.5	0.6	0.7
ΔY_{q1} (mm)	-2	0	+2
ΔY_{q2} (mm)	-2	-1	0
ΔWB_1 (mm)	-1	0	1
ΔWB_2 (mm)	-1	0	1
β_1 (°)	0	1.5	3
β_2 (°)	0	1.5	3
ΔTR_{b1} (mm)	0.25	0.5	1
ΔTR_{b2} (mm)	0.25	0.5	1

TABLE 3. Experimental plan of L27

N o.	k_{wq}	ΔY_{q1}	ΔY_{q2}	ΔW_{B1}	ΔW_{B2}	β_1	β_2	ΔTR_{b1}	ΔTR_{b2}
1	1	1	1	1	1	1	1	1	1
2	1	1	1	1	2	2	2	2	2
3	1	1	1	1	3	3	3	3	3
.....									
25	3	3	2	1	1	3	2	3	2
26	3	3	2	1	2	1	3	1	3
27	3	3	2	1	3	2	1	2	1

Typical mean effect plots of parameters with respect to torque and torque ripple for motors are shown in Figure 9. As it can be seen, for achieving the maximum torque, the best combination is as follows: 1^{set} level of ΔWB_2 , β_2 , ΔTR_{b1} and ΔTR_{b2} , 2^{set} level of ΔY_{q1} , ΔY_{q2} and β_1 , and 3^{set} level of k_{wq} and ΔWB_1 .

Considering Figure 9b, Minimum torque ripple is obtained as follows: 1^{set} level of k_{wq} and ΔTR_{b2} , 2^{set} level of ΔY_{q1} , ΔWB_1 , β_1 and ΔTR_{b1} , 3^{set} level ΔY_{q2} , ΔWB_2 , β_2 .

Using ANOVA can be useful to determine the effect of input parameter on output results. Then, according to Equations (33) to (35), the sum of the squares of each factor can be calculated [20-22]:

$$T = \sum_{i=1}^n y_i \tag{33}$$

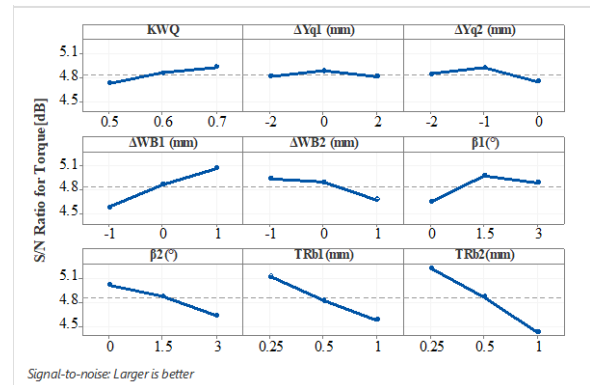
$$SS_A = \frac{1}{t} \sum_{i=1}^m A_i^2 - \frac{T^2}{n} \tag{34}$$

$$SS_T = \sum_{i=1}^n y_i^2 - \frac{T^2}{n} \tag{35}$$

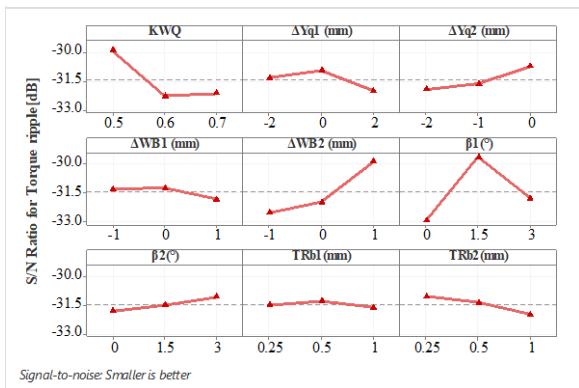
where m is the number of levels of factor A , n is the total number of tests performed, A_i is the sum of the outputs corresponding to the i th level of factor A , t is the number of tests performed at the i th level of factor A , T is equal to the total output of all tests, y_i is the output of the i th test, and SS_T is the sum of all squares.

The effects of the impact weight of all design variables on the desired output obtained through calculations are presented in Table 4.

The selection of appropriate levels of variables is done by comparing the S/N analysis results shown in Figure 9 and the results obtained in Table 3. Then, the optimization variables are selected to achieve the best design results for both average torque and torque ripple. Consequently, 1^{set} level of k_{wq} , β_2 , TR_{b1} , and TR_{b2} , 2^{set} level of ΔY_{q1} and β_1 , and 3^{set} level of ΔY_{q2} , ΔWB_1 , and ΔWB_2 .



(a)



(b)

Figure 9. S/N ratio of the optimization parameters for: (a) average torque, (b) torque ripple

TABLE 4. Impact weight of design variables

Variable	Impact weight on average torque	Impact weight on average torque ripple
k_{wq}	2.41%	20.55%
ΔY_{q1}	0.27%	5.66%
ΔY_{q2}	1.89%	5.82%
ΔWB_1	14.82%	1.28%
ΔWB_2	4.90%	24.34%
β_1	7.55%	34.08%
β_2	9.02%	0.80%
ΔTR_{b1}	19.44%	0.93%
ΔTR_{b2}	39.70%	6.53%

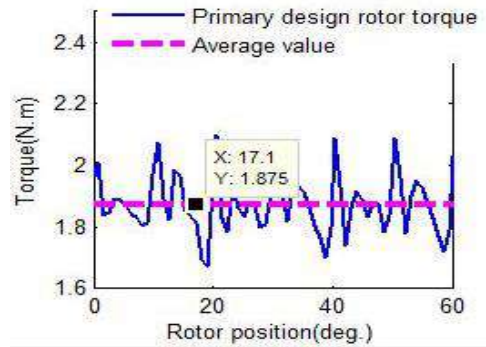
The comparison of the optimized motor with the initial design is presented in Table 5. It is worth mentioning, the variable k_{wq} is set to 0.5, TR_{b1} and TR_{b2} are set to 0.25 mm and the other variables are set to zero for the initial design.

As shown in Figure 10, it is obvious that the optimization of the external rotor motor, with 9 simultaneous effective variables and an acceptable number of tests, is performed well. Accordingly, the primary average torque and torque ripple are improved by 2.6% and 17.7%, respectively.

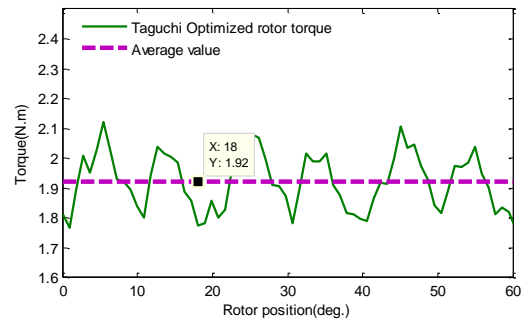
The magnetizing inductances along the d and q axes are the most important parameters in creating torque of the SynRM. As Figure 11 shows by increasing the air gap length L_d decreases while due to the presence of flux barriers in the q axis L_q remains unchanged.

TABLE 5. Comparison of the initial and optimized motors

Definition	Primary motor	Optimized motor
Ave. Torque (N.m)	1.87	1.92
Torque ripple (%)	22.62%	18.61%



(a)



(b)

Figure 10. Torque of Ex-SynRM (a) primary design, (b) Optimized by Taguchi method

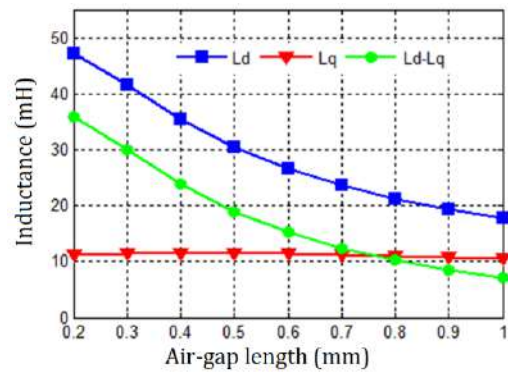


Figure 11. Effect of air-gap on the inductances of Ex-SynRM

Figure 12 shows the maximum flux density on the stator at the rated current is 1.5 Tesla, which is lower than 1.7 Tesla.

5. THE PROTOTYPED MOTOR AND THE EXPERIMENTAL RESULTS

Experimental verification the results of the initial test and a prototype motor with the same dimensions of the optimal design are presented in this section. Figure 13 shows the rotor and stator laminations of the manufactured motor.

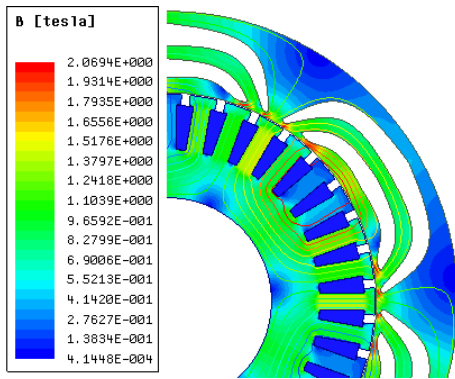


Figure 12. Flux density on the stator and rotor of Ex-SynRM

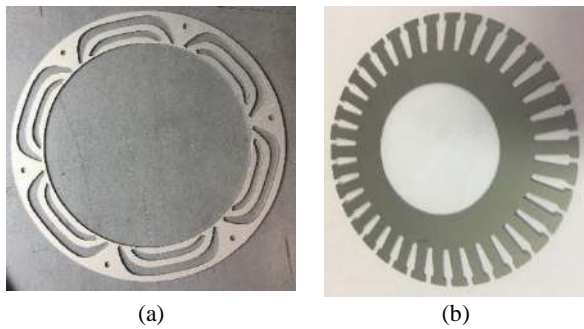


Figure 13. The laminations of (a) rotor and (b) stator

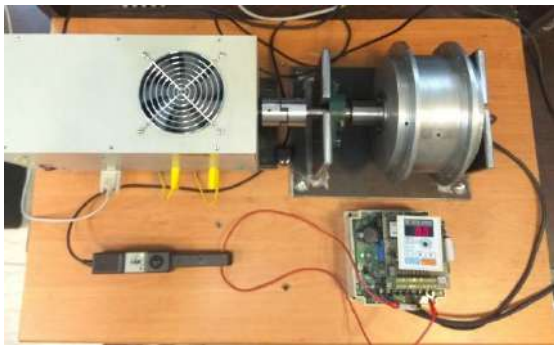


Figure 14. The experimental setup for testing the prototype external rotor SynRM

A 0.3 kW motor is constructed in this study as a prototype motor. The motor is tested in a test setup (shown in Figure 14) equipped with the ABB ACS140 Multi drive system where the current electric angle is 50 degrees. The results of the FEM analysis and measured comparisons are given in Table 7 and Figure 15. The torque measured with FEM is almost the same. The copper loss difference between the practical test and the FEM analysis can be attributed to the difference between the estimated current and the amount required for torque generation of the shaft in the practice. Regarding the iron loss difference, the lamination manufacturing and wire cutting, the accuracy of the rotor and stator assembly processes can be pointed out.

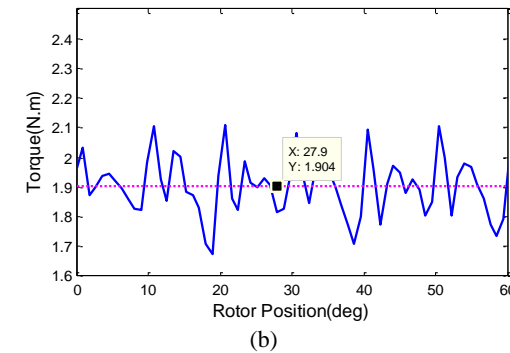
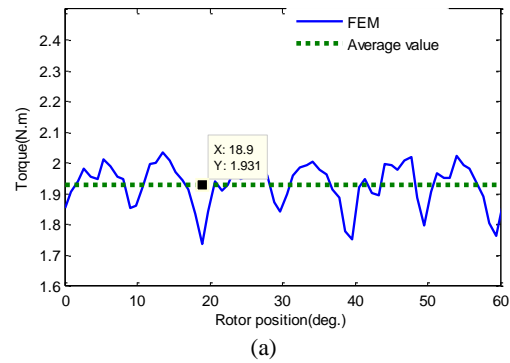


Figure 15. Torque of Ex-SynRM (a) FEM result, (b) Experimental result

TABLE 7. Comparison of the simulation results and experimental results

Definition	FEM	measurement
Ave. Torque (N.m)	1.93	1.90
Torque ripple (%)	22%	23%
Pout (W)	303	294
$\eta\%$	76	71.5
PCu (W)	48.4	56.2
PF	0.74	0.69

Finally, in order to be more accurate in practical results, more specific experiments are needed to accurately examine the core losses and the mechanical losses which data were lost during the experiments.

6. CONCLUSION

The present study proposes a new method for designing an external rotor SynRM. Given the similar behaviors of a fluid around a solid object in fluid mechanics and electromagnetic magnetic flux lines and duality relations between fluid pressure lines and potential electric lines, some simplified equations were provided for further predicting the flux lines in external rotor

reluctance synchronous motors. In the next step, considering the concept of reluctance in SynRMs, certain parameters are considered in the presented equations for controlling the position and shape of the flux barriers in the rotor body. The experiments were performed through Taguchi optimization method using the FEM analysis of an external rotor SynRM. Finally, the selected cases are analyzed and an appropriate rotor model was identified and designed for use in electric scooters. The proposed method is applied for construction of a motor which confirmed through comparing the measured practical results and the design procedure.

7. REFERENCES

- Boglietti, A., Cavagnino, A., Pastorelli, M., and Vagati, A.: 'Experimental comparison of induction and synchronous reluctance motors performance', Fourtieth IAS Annual Meeting. Conference Record of the 2005 Industry Applications Conference, Vol. 1, (2005), 474-479. DOI; 10.1109/IAS.2005.1518350.
- Boglietti, A., and Pastorelli, M.: 'Induction and synchronous reluctance motors comparison', 2008 34th annual conference of IEEE industrial electronics, (2008), 2041-2044. DOI; 10.1109/IECON.2008.4758270.
- Sahebjam, M., Sharifian, B., Feyzi, M.R., and Sabahi, M.: 'Novel Unified Control Method of Induction and Permanent Magnet Synchronous Motors', *International Journal of Engineering, Transactions B: Applications* Vol. 32, (2019), pag no. 256-269. DOI; 10.5829/ije.2019.32.02b.11.
- Arehpanahi, M., and Kheiry, E.: 'A New Optimization of Segmented Interior Permanent Magnet Synchronous Motor Based on Increasing Flux Weakening Range and Output Torque (Research Note)', *International Journal of Engineering, Transactions C: Aspects* Vol. 33, No. 6 (2020), 1122-1127. DOI; 10.5829/ije.2020.33.06c.09.
- Chan, C.: 'The state of the art of electric and hybrid vehicles', Proceedings of the IEEE, Vol. 90, (2002), 247-275. DOI; 10.1109/JPROC.2007.892489.
- Zaim, M.E.H.: 'High-speed solid rotor synchronous reluctance machine design and optimization', *IEEE Transactions on Magnetics*, Vol. 45, (2009), 1796-1799. DOI; 10.1109/TMAG.2009.2012824.
- Kolehmainen, J.: 'Synchronous reluctance motor with form blocked rotor', *IEEE Transactions on Energy Conversion*, Vol. 25, (2010), 450-456. DOI; 10.1109/TEC.2009.2038579.
- Taghavi, S.M., and Pillay, P.: 'A mechanically robust rotor with transverse laminations for a wide-speed-range synchronous reluctance traction motor', *IEEE Transactions on Industry Applications*, Vol. 51, (2015), 4404-4414. DOI; 10.1109/TIA.2015.2445819.
- Aghazadeh, H., Afjei, E., and Siadatan, A.: 'Sizing and detailed design procedure of external rotor synchronous reluctance machine', *IET Electric Power Applications*, Vol. 13, (2019), 1105-1113. DOI; 10.1049/iet-epa.2018.5802.
- Deshpande, Y., and Toliyat, H.A.: 'Design of an outer rotor ferrite assisted synchronous reluctance machine (Fa-SynRM) for electric two-wheeler application', IEEE energy conversion congress and exposition (ECCE), (2014), 3147-3154. DOI; 10.1109/ECCE.2014.6953828.
- Sankestani, M.M.R., and Siadatan, A.: 'Design of outer rotor synchronous reluctance motor for scooter application', 2019 10th International Power Electronics, Drive Systems and Technologies Conference (PEDSTC), (2019). 132-137. DOI; 10.1109/PEDSTC.2019.8697636.
- Moghaddam, R.-R., and Gyllensten, F.: 'Novel high-performance SynRM design method: An easy approach for a complicated rotor topology', *IEEE Transactions on Industrial Electronics*, Vol. 61, (2013) 5058-5065. DOI; 10.1109/TIE.2013.2271601.
- Moghaddam, R.-R.: 'Design optimization of SynRM with Ladybird rotor', 2017 International Conference on Optimization of Electrical and Electronic Equipment (OPTIM) & 2017 Intl Aegean Conference on Electrical Machines and Power Electronics (ACEMP), (2017), 317-323. DOI; 10.1109/OPTIM.2017.7974990.
- Dziechciarz, A., and Martis, C.: 'Magnetic equivalent circuit of synchronous reluctance machine', ELEKTRO, (2016), 500-503. DOI; 10.1109/ELEKTRO.2016.7512126.
- Rajabi Moghaddam, R.: 'Synchronous reluctance machine (SynRM) in variable speed drives (VSD) applications', KTH Royal Institute of Technology, 2011
- Fitzpatrick, R.: 'Theoretical fluid mechanics' (2017). DOI; 10.1088/978-0-7503-1554-8.
- Moghaddam, R.R., Magnussen, F., and Sadarangani, C.: 'Theoretical and experimental reevaluation of synchronous reluctance machine', *IEEE Transactions on Industrial Electronics*, Vol. 57, (2009), 6-13. DOI; 10.1109/TIE.2009.2025286.
- Aghazadeh, H., Afjei, E., and Siadatan, A.: 'Comprehensive Design Procedure and Manufacturing of Permanent Magnet Assisted Synchronous Reluctance Motor', *International Journal of Engineering, Transactions C: Aspects* Vol. 32, No. 9 (2019),. 1299-1305. DOI; 10.5829/ije.2019.32.09c.10. 1.
- Moghaddam, R.R., Magnussen, F., and Sadarangani, C.: 'A FEM 1 investigation on the Synchronous Reluctance Machine rotor geometry with just one flux barrier as a guide toward the optimal barrier's shape', IEEE EUROCON, (2009), 663-670. DOI; 10.1109/EURCON.2009.5167704.
- Ajamloo, A.M., Ghaheri, A., and Afjei, E.: 'Multi-objective Optimization of an Outer Rotor BLDC Motor Based on Taguchi Method for Propulsion Applications', 2019 10th International Power Electronics, Drive Systems and Technologies Conference (PEDSTC), (2019), 34-39. DOI; 10.1109/PEDSTC.2019.8697586.
- Arkadan, A., and Al Aawar, N.: 'Taguchi-EM-AI Design Optimization Environment for SynRM Drives in Traction Applications', International Applied Computational Electromagnetics Society Symposium (ACES), (2020). 1-2. DOI; 10.23919/ACES49320.2020.9196111.
- Mansoursamaei, M., Hadighi, A., and Javadian, N.: 'A New Approach Applying Multi-Objective Optimization using a Taguchi Fuzzy-based for Tourist Satisfaction Management', *International Journal of Engineering, Transactions C: Aspects* Vol. 32, (2019), 405-412. DOI; 10.5829/ije.2019.32.03c.08.

Persian Abstract

چکیده

موتور سنکرون رلوکتانسی یک موتور اقتصادی با عملکرد در محدوده وسیع سرعت می‌باشد. اما به طور عمومی ریپل گشتاور این نوع از موتورها به دلیل تغییر مقاومت مغناطیسی بین موانع شار و دندان استاتور قابل ملاحظه است. دستیابی به طراحی بهینه یک ماشین سنکرون رلوکتانسی از میان تمامی ترکیب‌های ممکن روتور با اشکال مختلف موانع شار و بدون استفاده از روابط تئوری ریاضی و الگوریتم مشخص طراحی کاری بسیار زمان‌بر است. در این مطالعه یک روش جامع برای طراحی روتور موتور سنکرون رلوکتانسی با ساختار روتور بیرونی با شکل موانع شار الگو گرفته شده از رفتار مایعات جاری اطراف یک جسم جامد ارائه شده است. با استفاده از این روش جدید طراحی، یک طرح روتور بیرونی پیشنهاد و در ادامه با استفاده از الگوریتم چند هدفه تاگوچی مبتنی بر تحلیل المان محدود (FEM) با هدف به حداکثر رساندن مقدار متوسط گشتاور و کاهش ریپل گشتاور تولیدی بهینه سازی شده است. در انتها برای اعتبارسنجی صحت نتایج حاصل از شبیه‌سازی های صورت گرفته یک نمونه اولیه از موتور پیشنهادی برای اسکوتر برقی ۳۰۰ وات و ۶ قطب، با روتوری با تعداد دو لایه مانع مغناطیسی و با استاتور ۳۶ شیار همراه با سیم پیچی توزیع شده ساخته شده است. مقایسه نتایج عملی به خوبی درستی نتایج شبیه‌سازی را تأیید می‌کند.



A New Recurrent Radial Basis Function Network-based Model Predictive Control for a Power Plant Boiler Temperature Control

J. Tavoosi*^a, A. Mohammadzadeh^b

^a Department of Electrical Engineering, Ilam University, Ilam, Iran

^b Department of Electrical Engineering, University of Bonab, Bonab, Iran

PAPER INFO

Paper history:

Received 23 November 2020

Received in revised form 25 December 2020

Accepted 08 February 2021

Keywords:

Boiler Temperature

Model Predictive Control

Parameter Uncertainty

Radial Basis Function Network

ABSTRACT

In this paper, a new radial basis function network-based model predictive control (RBFN-MPC) is presented to control the steam temperature of a power plant boiler. For the first time in this paper the Laguerre polynomials are used to obtain local boiler models based on different load modes. Recursive least square (RLS) method is used as observer of the Laguerre polynomials coefficient. Then a new locally recurrent radial basis function neural network with self-organizing mechanism is used to model these local transfer function and it used to estimate the boiler future behavior. The recurrent RBFN tracks system is dynamic online and updates the model. In this recurrent RBFN, the output of hidden layer nodes at the past moment is used in modelling, So the boiler model behaves exactly like a real boiler. Various uncertainties have been added to the boiler and these uncertainties are immediately recognized by the recurrent RBFN. In the simulation, the proposed method has been compared with traditional MPC (based on boiler mathematical model). Simulation results showed that the recurrent RBFN-based MPC perform better than mathematical model-based MPC. This is due to the neural network's online tracking of boiler dynamics, while in the traditional way the model is always constant. As the amount of uncertainty increases, the difference between our proposed method and existing methods can clearly be observed.

doi: 10.5829/ije.2021.34.03c.11

NOMENCLATURE

p	Time scale factor	$M(k)$	Gain matrix in RLS
Φ_i	Laguerre functions	$\mu_i(k)$	the coefficients of the functions in MPC
$Y_m(s)$	Laplace transform of system's output	H_i	The horizon sample
C_i	Output matrices	$u(k)$	Control input
$U(s)$	Laplace transform of system's input	$\phi_i(u)$	Output of RBF neurons
$l_i(s)$	Terms of Laguerre Ladder network	w_i	Weights in RBFN
τ_i	Time constant of the system	$y_m(k)$	Output of the model

1. INTRODUCTION

Boilers are used in many industries such as power plants. Power plants use boilers to generate steam for electrical power in steam turbines. The more precise control of the boiler outlet temperature is crucial. If the outlet steam temperature is not properly controlled, the pressure needed to rotate the turbines may not be reached or the

efficiency of the boiler and turbine may be reduced. Due to the long history of using boilers in various industries, which reaches more than 150 years, naturally, various methods have been proposed to control outlet temperature. From simple methods such as PID [1] to model free methods such as variable structures adaptive control [2], are each proposed to control the boiler system. The above methods do not require an accurate

*Corresponding Author Institutional Email: j.tavoosi@ilam.ac.ir
(J. Tavoosi)

mathematical model of the boiler, but do not perform well in the face of instantaneous changes in the boiler parameters (or uncertainty) as well as different boiler operating conditions. In contrast, various model-based methods for boiler control have been proposed, from coordinated control system [3] to nonlinear model predictive control [4]. Model-based methods can accurately control the boiler; but, if for any reason the boiler dynamics changed or the boiler parameters changed, these methods are not accurate. To solve the above problems, one solution can be the use of computational intelligence. Computational intelligence seems to be a useful tool for precise control of a system [5-7]. Fuzzy logic [8-10] and neural network [11-12] or a combination of the two [13-15] have been used in various papers to identify systems dynamics and control [16-19]. Today, due to the complexity of systems, mathematical model-based approaches alone do not work. Thus, by combining traditional control methods with computational intelligence-based tools, more precise control methods can be proposed [20-21]. Various works have been discussed in the field of boiler and heating system control [22]. In the following we will discuss some of the latest results. Sunil et al. [23] focused on improving the performance of boiler-drum level control over a wide range of operation using the quantitative feedback theory (QFT) approach. A dynamic boiler model has established and validated with values measured from a real power plant [24]. In the mentioned paper, a reheating steam control method is proposed that takes into account changes in heat storage in boiler metals and steam temperature deviations. A fuzzy control has been implemented in the combustion air flowrate of a large boiler in the Tereos group, to maintain the oxygen content in the combustion products within the optimum range [25]. The boiler turbine system is usually subject to the tight input constraint, the strong nonlinearity and the complex disturbance, which makes the control a challenging task. To this end, a disturbance observer based fuzzy model predictive control scheme is proposed for the boiler system in literature [26]. Support vector machine based control by combination the ability of fuzzy logic and learning ability of neural network have been used for boiler control in [27]. Shi [28] has applied a new fuzzy clustering method to boiler temperature control. They used type-2 fuzzy because this tool has high capacity on handling with uncertainty. Uncertainty in the parameter or structure of a system is one of the most challenging issues in control engineering [29]. In the past, the uncertainty of a system was not considered. The reason for this was either insufficient knowledge or negligence. That is why in the past, control systems did not provide the desired and suitable answer. It is clear that most systems that need to be controlled are dynamic and have multiple parameters. Some of these parameters change over time or may change for a moment and then

return to the previous state [30]. If the values of the parameters are considered constant in the designed control system, the desired answer will not be obtained in a practical system. Therefore, a control system is successful when it considers as many parametric and systematic changes as possible and has a plan for these changes [31]. Adaptive control systems and robust control systems work well with parametric and structural changes. But these methods require a mathematical and relatively accurate model of the system [32]. In contrast, methods based on computational intelligence (fuzzy logic, neural nets, etc.) have the ability to update themselves and can provide good performance in the face of uncertainties [33-35]. In the following, we will analyze the articles related to applications of neural network in boiler control. A multilayer perceptron neural network model has been developed to envisage the corrosion rate and oxide scale deposition rate in economizer tubes of a coal-fired boiler [36]. The mentioned paper does not talk about temperature control, but parametric sensitivity is well modeled by the neural network. A two layer perceptron neural network has been used to control of a boiler in literature [37]. In the mentioned paper, the inputs of neural network are temperature, pressure and carbon monoxide of the boiler and the outputs are percentage of valve opening for fuel gas supply to the boiler and percentage of valve opening for air supply to the boiler. Unfortunately, load uncertainty are not considered in this article. In literature [38] the perceptron neural network is used to control of a boiler as a two inputs - three outputs system. Inputs are: temperature, pressure and carbon dioxide and outputs are: percentage of valve opening for fuel gas supply and percentage of valve opening to supply air. In the mentioned article, no uncertainty has been applied neither in the parameters nor in the load, also the training and testing error of the neural network is relatively high. A neural network-based controller has been designed for a power boiler to save fuel consumption [39]. In the mentioned article, a proper training and test error has been obtained but any uncertain load has not been applied. A multilayer feed-forward neural network is trained to identify the inverse dynamic model of a boiler system [40]. In the mentioned paper, a perceptron-type three-input-three-output neural network has been used for this purpose, and a completely practical and laboratory work has been done, but unfortunately no uncertainty has been considered for the model.

There is no article that has used the recurrent radial basis neural network to be used in model predictive control of boiler system, and therefore our proposed method is quite original, but very few articles have used the conventional radial basis neural network to model or control the boiler, some of which are discussed in continue. Kouadri et al. [41] have been able to use the high capability of the radial basis function neural network to model and system identification of the boiler system.

In the mentioned paper, an ordinary (not recurrent) radial base function neural network with training based on genetic algorithm has been used. In literature [42], the ordinary radial base function neural network has been used to inverse control of a boiler system. In the mentioned paper the load uncertainty is not considered and the boiler equations are not clear. An ordinary radial basis function neural network has been performed to identify the boiler system and then use it in the optimal control of the boiler, but not any type of uncertainty (load or parameters) is considered [43]. We have justified by reviewing the above articles that there are shortcomings in this regard. Therefore, in this paper, we proposed a new method to eliminate them. The innovations of our proposed method are as follows:

- In most of the articles, general feedback was used in recurrent RBFNs, while in our proposed method, local feedback was used. In general feedback, the information from the past moment of the last layer is applied as input to the first layer, but in local feedback, the information from the past moment of the output of the neuron itself is used as the input of the same neuron. It should be noted that neural network training with local feedback is far more complex than training with general feedback.
- The second innovation of our method is the use of structural training (Self-Organizing) in regulating the number of neurons in the middle layer of the neural network. In this way, starting from one neuron and due to the complexity of the data, the number of neurons increases, until we achieve the desired minimum error.
- The third innovation is using the Laguerre polynomials to obtain the local boiler models for different boiler load modes.
- The fourth innovation is proposed a new structure for MPC based on RBFN. The innovation of this section is using difference formulation for MPC.
- Considering the parameters of a real boiler with real uncertainty is fifth innovation. All numerical and parametric values were measured from a laboratory and practical boiler.

In this paper, the main focus is on the load uncertainty problem. First, the dynamic equations of the boiler system are expressed. Then, the radial basis function neural network prediction model control system is presented. Finally, simulations and conclusions are presented.

2. MATHEMATICAL MODELING OF SUPER HEATED STEAM OF POWER PLANT

In this section, first the Laguerre functions are introduced; then, the boiler modeling method is

expressed using these functions. Laguerre functions are a complete set of orthogonal functions in Judicial $L_2(0, \infty)$ which are widely used because of the simple and easy expression of its network. These functions come in a series of functions [44]:

$$\Phi_i(t) = \sqrt{2p} \frac{e^{pt} t^{i-1}}{(i-1)! dt^{i-1}} [t^{i-1} \cdot e^{2pt}], \quad i = 1, 2, \dots, \infty \quad (1)$$

are defined where p is a constant called the time scale factor. The laplace transform of Equation (1) is:

$$\Phi_i(t) = \mathcal{L}\{\Phi_i(t)\} = \sqrt{2p} \frac{(s-p)^{i-1}}{(s+p)^i}, \quad i = 1, 2, \dots, \infty \quad (2)$$

Every open loop system can be approximated by Laguerre functions as Equation (3):

$$Y_m(s) = \sum_{i=1}^n C_i \Phi_i(s) U(s) = \sum_{i=1}^n C_i l_i(s) \quad (3)$$

There are several ways to express the Laguerre Ladder network. However, it is desirable for us to express the Laguerre ladder network in the state space so that it can directly predict the outputs of the system. The system state space expression using the Laguerreithmic functions after discretization is as follows [44]:

$$\begin{aligned} L(k+1) &= AL(k) + Bu(k) \\ y(k) &= CL(k) \end{aligned} \quad (4)$$

In Equation (4), the system state vector is $L(k)$ of the order n and $u(k)$ is the input of the system. The matrix A is the lower triangular matrix of $N \times N$. Also B is the matrix of input coefficients of the system ($N \times 1$) whose elements are determined by line-off. This way the amount of computation is greatly reduced. If T is the system sampling period, therefore [44]:

$$\begin{aligned} \tau_1 &= e^{-pT} \\ \tau_2 &= T + \frac{2}{p} (e^{-pT} - 1) \\ \tau_3 &= Te^{-pT} - \frac{2}{p} (e^{-pT} - 1) \\ \tau_4 &= \sqrt{2p} \frac{(1-\tau_1)}{p} \\ a &= \tau_1 \tau_2 + \tau_3 \end{aligned} \quad (5)$$

Then the system description matrices for Equation (4) are expressed as follows:

$$\begin{aligned} A &= \begin{bmatrix} \tau_1 & 0 & \dots & 0 \\ -\frac{a}{T} & \tau_1 & \dots & 0 \\ \vdots & \vdots & \ddots & \vdots \\ \frac{(-1)^{N-1} \tau_2^{N-2} a}{T^{N-1}} & \dots & -\frac{a}{T} & \tau_1 \end{bmatrix} \\ B &= \left[\tau_1 \quad \left(\frac{-\tau_2}{T}\right) \tau_4 \quad \dots \quad \left(\frac{-\tau_2}{T}\right)^{N-1} \tau_4 \right]^T \end{aligned} \quad (6)$$

$$L(k) = [l_1(k) \quad l_2(k) \quad \dots \quad l_N(k)]^T$$

$$C = [c_1 \quad c_2 \quad \dots \quad c_N]$$

The vector C , which is the system observer coefficients vector with $N + 1$ dimensional, is determined by using

the recursive least squares (RLS) to express the relationship between the Laguerre model and the desired system.

$$C(k) = C(k - 1) + \{M(k)[y(k) - C(k - 1)L(k)]\}^T$$

$$M(k) = \frac{P(k-1)L(k)}{\lambda + L^T(k)P(k-1)L(k)} \quad (7)$$

$$P(k) = \frac{1}{\lambda} [P(k - 1) - M(k)L^T(k)P(k - 1)]$$

where λ is forgetting factor. From Equations (1) to (7), a model of a boiler system can be obtained. As it is clear from the above equations, the obtained model is dynamic and with exponential coefficients and can be a relatively accurate mathematical model of a practical boiler.

3. MODEL PREDICTIVE CONTROL

Model predictive control has rules similar to classical prediction control, as both methods use a model to predict the future output of the system. Model predictive control considers the structure of control law as a linear combination of a set of basic functions. Then the weight of the coefficients of the basic functions in the linear combination has to be calculated. The selection of basic functions is also based on the process properties and the desired reference inputs. The structure of the control law can be considered as follows.:

$$u(k + i) = \sum_{n=1}^N \mu_n u_{bn}(i) \quad (8)$$

where the μ_n is the coefficients of the functions with is linear in sequence and specifies the number of base types ($u_{bn}(i)$). The values of the basic functions are instantaneous $k+i$ ($u(k + i)$). The choice of these basic functions depends on the nature of the process and the reference input and generally uses step-slope and parabolic functions. In most cases, however, using two steps to the step and the ramp is sufficient:

$$u(k + i) = \mu_1(k) + \mu_2(k) * i \quad (9)$$

The model predictive control algorithm finds the sum of future control variables in such a way that the output of the process is as close to the reference sequence as possible. The feedback correction sequence is computed by an exponential relation:

$$y_p(k + i) = y_m(k + i) - \lambda^i [y_m(k) - y(k)] \quad (10)$$

where $i = 1, 2, \dots, H_i$ are the total number of matching points. $y_p(k + i)$ are the values of the feedback correction sequence at time $k + i$, $y_m(k)$ is also the model outputs (RBFN output) and $y(k)$ are process outputs. $\lambda^i = e^{-\frac{T_s}{T_r}}$ which is T_s the sampling time and T_r the expected response time to the reference sequence .

By combination of Equations (4) and (9), the future output can be obtained.

$$y_m(k + i) = CA^i L(k) + C[A^{i-1} + A^{i-2} + \dots + I]B\mu_1(k) + C[A^{i-2} + 2A^{i-3} + \dots + (i - 1)I]B\mu_2(k) \quad (11)$$

where $y_m(k + i)$ is output of the model at $k + i$.

MPC is a control strategy that explicitly uses the process model to predict the future behavior of the process output in a finite horizon, and the control effort is achieved by minimizing the interaction between the predicted output of the model and the reference sequence at a given time horizon. The predictive control law is generally computed by minimizing the axial scaling:

$$J = \sum_{i=H_1}^{H_2} [y_p(k + i) + e(k + i) - y_r(k + i)]^2 \quad (12)$$

In relation to the control effort, only two coefficients of the basic functions, $\mu_1(k)$ and $\mu_2(k)$, are uncertain. In order to determine these unknown parameters, we rewrite the above relations [44]:

$$J = [y_p(k + H_1) + e(k + H_1) - y_r(k + H_1)]^2 + [y_p(k + H_2) + e(k + H_2) - y_r(k + H_2)]^2 \quad (13)$$

We will have the following relationship by replacing the reference sequence and predicting the process output.

$$[X_1(k) + M_{11}\mu_1(k) + M_{12}\mu_2(k)]^2 + [X_2(k) + M_{12}\mu_1(k) + M_{22}\mu_2(k)]^2 \quad (14)$$

In this regard:

$$X_1(k) = CA^{H_1}L(k) + e(k + H_1) - y_r(k + H_1)$$

$$X_2(k) = CA^{H_2}L(k) + e(k + H_2) - y_r(k + H_2)$$

$$M_{11} = C(A^{H_1-1} + A^{H_1-2} + \dots + I)B$$

$$M_{12} = C(A^{H_1-2} + 2A^{H_1-3} + \dots + (H_1 - 1)I)B \quad (15)$$

$$M_{21} = C(A^{H_2-1} + A^{H_2-2} + \dots + I)B$$

$$M_{22} = C(A^{H_2-2} + 2A^{H_2-3} + \dots + (H_2 - 1)I)B$$

From Equation (15), all required coefficient and variables in Equation (14) are calculated. Now, by deriving the relation to the unknown parameters, we obtain:

$$\mu_1(k) = S_y y(k) + S_L L(k) + S_W W(k) \quad (16)$$

In this regard

$$S_y = Q(Q_3 M_{12} - Q_2 M_{11})(1 - \alpha^{H_1}) + Q(Q_3 M_{22} - Q_2 M_{21})(1 - \alpha^{H_2})$$

$$S_L = Q(Q_3 M_{12} - Q_2 M_{11})C(A^{H_1} - I) + Q(Q_3 M_{22} - Q_2 M_{21})C(A^{H_2} - I)$$

$$S_w = -S_y \quad (17)$$

$$Q_1 = M_{11}^2 + M_{21}^2$$

$$Q_2 = M_{12}^2 + M_{22}^2$$

$$Q_3 = M_{11}M_{12} + M_{21}M_{22}$$

$$Q = 1/(Q_1 Q_2 - Q_3^2)$$

Using the above relationships, we can write the following relation for control effort:

$$u(k) = \mu_1(k) = S_y y(k) + S_L L(k) + S_w w(k) \tag{18}$$

Note that only the parameter ($\mu_1(k)$) can be specified if (Q) exists, so in selecting the free controller parameters, H_1 and H_2 , care should be taken to select the matrix (Q) would have existed. There are three main factors that can affect the output temperature of the boiler: load, steam flow and boiler internal steam temperature. The effect of load is more than others. Each change in load leads to a different behavior from the boiler. In such a way that for each load, the boiler will have a different conversion function. Other factors such as: the temperature of the injected water, the temperature of the injected steam into the super heater, the pollution on the walls, the sediment in the steam pipes, etc. can all be of uncertainty sources. Five local transfer functions with different load percentages are summarized in Table 1. For five different load modes, five transfer functions can be obtained.

Thus, all five transfer function can be modeling in one model by using recurrent RBFN. The proposed recurrent RBFN is shown in Figure 1.

In the middle layer containing RBF neurons, the neuron-governing relationship is as follows:

$$\phi_i(u) = \exp\left(-\frac{\|u - c_i\|^2}{\sigma_i^2}\right), \quad i = 1, \dots, m \tag{19}$$

TABLE 1. Five local transfer function

Load %	Equivalent Transfer Function
30	$\frac{-11.24}{1 + 124.4s} e^{-115s}$
40	$\frac{-10.16}{1 + 91.8s} e^{-101s}$
60	$\frac{-9.55}{1 + 80.7s} e^{-94.5s}$
80	$\frac{-7.61}{1 + 78.1s} e^{-82.1s}$
100	$\frac{-4.59}{1 + 53.83s} e^{-58.5s}$

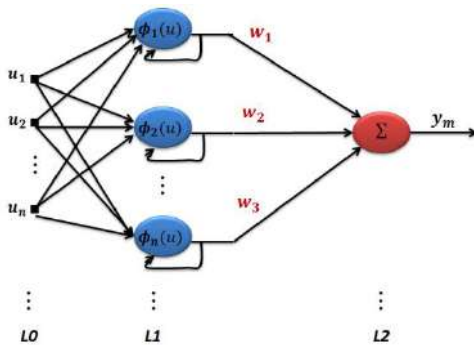


Figure 1. The proposed recurrent RBFN

where $\sigma_i \in \mathbb{R}$ the width of the neuron is, $c_i = [c_{1i}, c_{2i}, \dots, c_{ni}]^T$ is the center vector of the neuron and $u = [u_1, u_2, \dots, u_n, \phi(u(k-1))]^T$ is the network input. In the last layer, the output is calculated.

$$y = \sum_{i=1}^m w_i \phi_i(u) \tag{20}$$

Here the output from the given weight of the nonlinear bases is $\phi_i(u)$ which it must be orthogonal. In the structural training (Self-Organizing) of the radial basis function neural network, there is initially only one neuron. Upon entering the first data, the Euclidean distance of this data from the center of the neuron is calculated. If this data belonged to an existing neuron then the next data is coming, but if it did not belong, a new neuron will be created for this data. This process of adding neurons continues until the end of training and applying the latest data. For more details of RBFN training one can refer to literature [7].

The overall goal is to reduce the error between the actual system and the model.

$$e(k+i) = y(k) - y_m(k) \tag{21}$$

The structure of the proposed control system is shown in Figure 2.

The process is as follows: first, all transfer functions (here are 5 functions) are modeled by a single recurrent RBF neural network (green block in Figure 2), and so this neural network simultaneously includes all models. Therefore, if the boiler load changes, the recurrent RBF neural network immediately generates the appropriate signal and assists the controller. The boiler block (red block in Figure 2) contains the transfer functions in Table 1. The feedback correction block (orange block in Figure 2) performs the calculations for Equation (10). Finally, the optimization algorithm (blue block in Figure 2) performs the calculations for Equation (18).

4. SIMULATIONS

In this section, simulation of the boiler with the proposed control method in MATLAB software is discussed. The parameters of boiler are shown in Table 2.

In continue, the performance of the proposed control system, i.e. the neural network-based MPC, as well as the

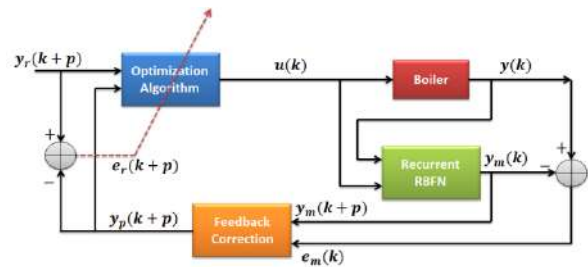


Figure 2. The structure of the proposed control system

TABLE 2. System parameter values

Nominal power	100 MW
Vapor flow rate	120 kg/sec
Steam pressure	120 kg/cm ²
Steam temperature	510 °C
Drum size	30 m ³
Water mass	30000 kg
Steam mass under pressure	1500 kg
Inlet water temperature	37 °C
Fuel flow rate	12 kg/sec

performance of the conventional MPC, are compared. It is expected that in our proposed method, the existence of a RBF neural network will lead to a more precise handling of the uncertainty and follow the changes well, and it should perform better than the traditional method. Figure 3 shows the boiler temperature control by recurrent RBFN-based MPC and traditional MPC without load uncertainty.

For greater clarity, part of Figure 3 is enlarged and shown in Figure 4.

According to Figures 3 and 4, the complete superiority of the proposed MPC method based on RBFN over the traditional MPC is clear. As can be clearly seen in Figure 4, in the traditional MPC method the boiler temperature range is from 870 to 923, while in the RBFN-based method this range is from 890 to 905. In other

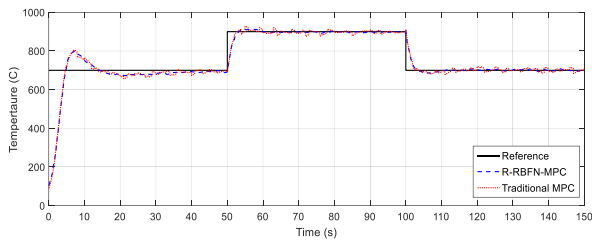


Figure 3. Simulation results of recurrent RBFN-MPC and traditional MPC for temperature boiler control without any uncertainty

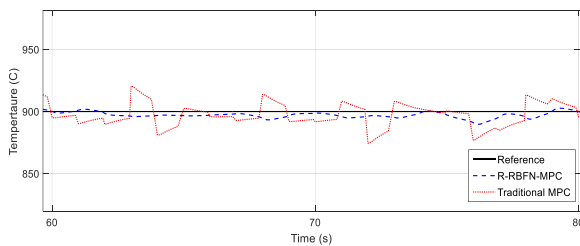


Figure 4. Zoom in on part of Figure 3

words, the RBFN softens some of the controller switching. In continue, the performance of both traditional MPC and RBFN-based MPC are challenged with uncertainty in load. It is assumed that the boiler load will change randomly by $\pm 15\%$. Figure 5 shows the boiler temperature control by recurrent RBFN-based MPC and traditional MPC $\pm 15\%$ in load uncertainty.

For greater clarity, part of Figure 5 is enlarged and shown in Figure 6.

In order to evaluate the performance of the controllers by increasing the load uncertainty, the uncertainty value of the boiler load is increased randomly to $\pm 25\%$. Figure 7 shows the boiler temperature control by recurrent RBFN-based MPC and traditional MPC $\pm 25\%$ in load parameter uncertainty.

For greater clarity, part of Figure 7 is enlarged and shown in Figure 8.

Finally, increase the uncertainty on the boiler load to $\pm 50\%$ and you will see the result in Figure 9.

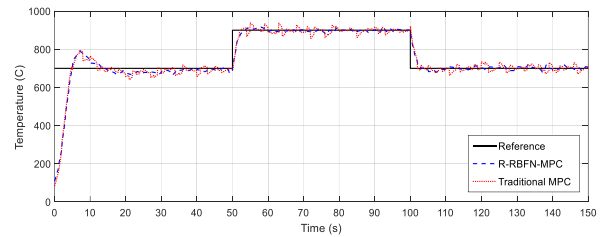


Figure 5. Simulation results of recurrent RBFN-MPC and traditional MPC for temperature boiler control with $\pm 15\%$ in load uncertainty

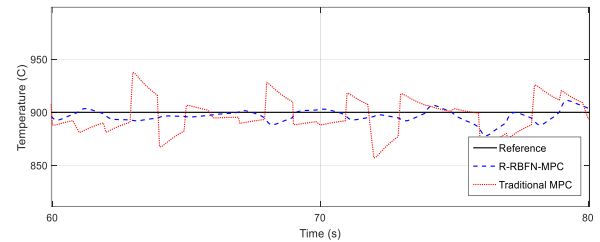


Figure 6. Zoom in on part of the Figure 5

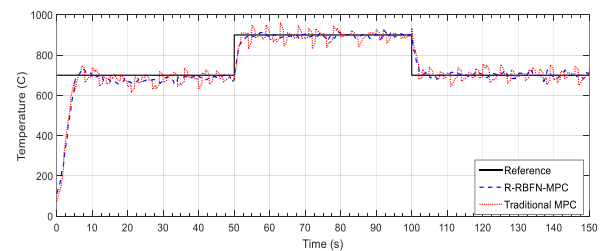


Figure 7. Simulation results of recurrent RBFN-MPC and traditional MPC for temperature boiler control with $\pm 25\%$ in load uncertainty

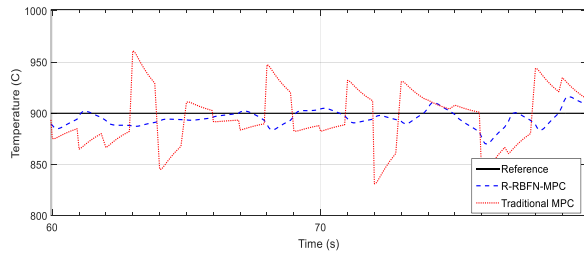


Figure 8. Zoom in on part of the Figure 7

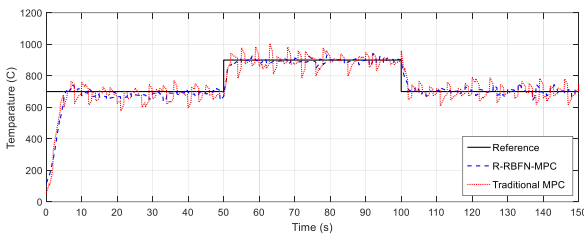


Figure 9. Simulation results of recurrent RBFN-MPC and traditional MPC for temperature boiler control with $\pm 50\%$ in load uncertainty

For greater clarity, part of Figure 9 is enlarged and shown in Figure 10.

From Figures 3 to 10 can be conclude that if the more uncertainty of the load, the greater the superiority of the recurrent RBFN-MPC over the traditional MPC. When the uncertainty reaches $\pm 50\%$, the traditional MPC is practically useless, because the tepraturate changes from 800 °C to 1000 °C instead of being fixed at 900 °C. See Table 3 for further comparison of the proposed method with some of the existing works. In this table, the measurement criterion is the root mean square tracking error (RMSE) [20].

As shown in Table 3, the use of computational intelligence (neural network, fuzzy logic, etc.) as a complement to a control system can be very useful. Boiler is a highly nonlinear system with uncertain parameters. As shown in the simulation results, for a real boiler can not be considered a fixed model with fixed parameters. It seems that the traditional MPC method behaves like this, but by combining it with computational intelligence, changes can be tracked immediately. This becomes especially critical when the rate of change is

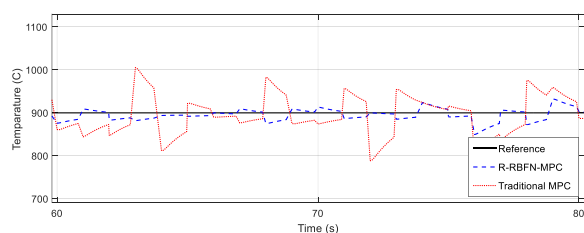


Figure 10. Zoom in on part of Figure 9

TABLE 3. Comparison of the proposed method with some of the existing works

	No. load	$\pm 15\%$ uncertainty	$\pm 25\%$ uncertainty	$\pm 50\%$ uncertainty
Method of [23]	2.271	2.441	3.318	4.776
Method of [25]	1.421	1.948	2.559	2.985
Method of [37]	1.258	1.882	2.052	2.891
Method of [42]	1.326	1.691	2.174	2.221
Alone MPC	1.545	1.962	2.498	2.993
Our proposed method	0.855	1.121	1.573	1.989

high and traditional methods do not respond well at all. Neural networks, if properly trained with appropriate and useful data, can well approximate a function and estimate future moments, and this is very useful in controlling systems.

5. CONCLUSION

In this paper, a combination of computational intelligence with model predictive control was used to control the power plant boiler. In this method, a self-organizing recurrent radial base function neural network was used for online modeling of the boiler. First, several local transfer functions of the boiler were created using the Laguerre polynomials method, then the recurrent RBF neural network was used to approximate these models. Laguerre polynomial coefficients are calculated and updated by the recursive least squares algorithm (RLS). The recurrent RBFN can estimate future moments for the model predictive method and use it to accurately control the boiler. As observed in the simulation results, when we have uncertainty in the load, the neural network-based model predictive control works better than the traditional model predictive control, especially when the uncertainty is high. All numerical values of the parameters and their mathematical relations are based on a real boiler system. Therefore, the proposed method in this paper has the capability to implement hardware and practice.

REFERENCES

1. Gao J.L., "Research on Boiler Water Supply Control System Based on AT89C55 and Fractional order PID Algorithm", *Procedia Computer Science*, Vol. 154, (2019) 173-180. DOI: 10.1016/j.procs.2019.06.026

2. Tavoosi, J., "Sliding mode control of a class of nonlinear systems based on recurrent type-2 fuzzy RBFN", *International Journal of Mechatronics and Automation*, Vol. 7, No. 2, (2020), 72-80. DOI: 10.1504/IJMA.2020.108797
3. Gao, Y., Zeng, D., Ping, B., Zhang, L., Liu, J., "Research on coordinated control system of drum boiler units considering energy demand decoupling", *Control Engineering Practice*, Vol. 102, (2020). DOI: 10.1016/j.conengprac.2020.104562
4. Siddiqui, I., Ingole, D., Sonawane, D., Agashe, S., "Offset-free Nonlinear Model Predictive Control of A Drum-boiler Pilot Plant", *IFAC-PapersOnLine*, Vol. 53, No. 1, (2020), 506-511, DOI: 10.1016/j.ifacol.2020.06.085
5. Tavoosi, J., Azami, R., "A New Method for Controlling the Speed of a Surface Permanent Magnet Synchronous Motor using Fuzzy Comparative Controller with Hybrid Learning", *Journal of Computational Intelligence in Electrical Engineering*, Vol. 10, (2019), 57-68. DOI: 10.22108/isee.2019.112834.1148
6. Mohammadzadeh, A., Kayacan, E., "A novel fractional-order type-2 fuzzy control method for online frequency regulation in ac microgrid", *Engineering Applications of Artificial Intelligence*, Vol. 90, (2020), DOI: 10.1016/j.engappai.2020.103483
7. Hesarian, M.S., Tavoosi, J., "Green Technology used in Finishing Process Study of the Wrinkled Cotton Fabric by Radial Basis Function neurons. (Experimental and Modeling analysis)", *Advances in Environmental Technology*, Vol. 5, No. 1, (2019), 35-45. DOI: 10.22104/aet.2019.3730.1183
8. Hesarian, M.S., Tavoosi, J., Hosseini, S.H., "Neuro-fuzzy Modelling and Experimental Study of the Physiological Comfort of Green Cotton Fabric Based on Yarn Properties", *International Journal of Engineering, Transactions C: Aspects*, Vol. 33, No. 12, (2020), 2443-2449. DOI:10.5829/ije.2020.33.12c.02
9. Tavoosi, J., "A New Type-2 Fuzzy Sliding Mode Control for Longitudinal Aerodynamic Parameters of a Commercial Aircraft", *Journal Européen des Systèmes Automatisés*, Vol. 53, No. 4, (2020), 479-485. DOI:10.18280/jesa.530405
10. Mohammadzadeh, A., Rathinasamy, A., "Energy management in photovoltaic battery hybrid systems: A novel type-2 fuzzy control", *International Journal of Hydrogen Energy*, Vol. 45, No. 41, (2020), 20970-20982. DOI:10.1016/j.ijhydene.2020.05.187
11. Tavoosi, J., Suratgar, A.A., and Menhaj, M.B., "Nonlinear System Identification Based on a Self-Organizing Type-2 Fuzzy RBFN," *Engineering Applications of Artificial Intelligence*, Vol. 54, (2016), 26-38. DOI: 10.1016/j.engappai.2016.04.006
12. Tavoosi, J., Suratgar, A.A., and Menhaj, M.B., "Stable ANFIS2 for Nonlinear System Identification," *Neurocomputing*, Vol. 182, (2016), 235-246. DOI: 10.1016/j.neucom.2015.12.030
13. Tavoosi, J., Suratgar, A.A., and Menhaj, M.B., "Stability Analysis of Recurrent Type-2 TSK Fuzzy Systems with Nonlinear Consequent Part?" *Neural Computing and Applications*, Vol. 28, No.1, (2017), 47-56. DOI: 10.1007/s00521-015-2036-3
14. Tavoosi, J., Suratgar, A.A., and Menhaj, M.B., "Stability Analysis of a Class of MIMO Recurrent Type-2 Fuzzy Systems", *International Journal of Fuzzy Systems*, Vol. 19, No. 3, (2017), 895-908. DOI: 10.1007/s40815-016-0188-7
15. Tavoosi, J., A. Shamsi Jokandan, and M. A. Daneshwar, "A New Method for Position Control of a 2-DOF Robot Arm Using Neuro-Fuzzy Controller," *Indian Journal of Science and Technology*, Vol. 5, No. 3, (2012), 1-5. DOI: 10.17485/ijst/2012/v5i3.10
16. Tavoosi, J., "PMSM speed control based on intelligent sliding mode technique", In *COMPEL - The international journal for computation and mathematics in electrical and electronic engineering*, Vol. 39 No. 6, (2020), 1315-1328. DOI:10.1108/COMPEL-04-2020-0137
17. Tavoosi, J., and F. Mohammadi, "Design a New Intelligent Control for a Class of Nonlinear Systems", In 6th International Conference on Control, Instrumentation and Automation (ICCIA), Sanandaj, Iran, (2019), 1-5, DOI: 10.1109/ICCIA49288.2019.9030868
18. Tavoosi, J., and F. Mohammadi, "A 3-PRS Parallel Robot Control Based on Fuzzy-PID Controller", In 6th International Conference on Control, Instrumentation and Automation (ICCIA), Sanandaj, Iran, (2019), 1-4, DOI: 10.1109/ICCIA49288.2019.9030860
19. Asad, Y.P., Shamsi, A., Tavoosi, J., "Backstepping-Based Recurrent Type-2 Fuzzy Sliding Mode Control for MIMO Systems (MEMS Triaxial Gyroscope Case Study)", *International Journal of Uncertainty, Fuzziness and Knowledge-Based Systems*, Vol. 25, No. 2, (2017), 213-233. DOI: 10.1142/S0218488517500088
20. Tavoosi, J., Badamchizadeh, M.A., "A class of type-2 fuzzy neural networks for nonlinear dynamical system identification", *Neural Computing & Applications*, Vol. 23, (2013) 707-717. DOI: 10.1007/s00521-012-0981-7
21. Tavoosi, J., "A New Type-2 Fuzzy Systems for Flexible-Joint Robot Arm Control", *AUT Journal of Modeling and Simulation*, Vol. 51, No. 2, (2019). DOI: 10.22060/miscj.2019.14478.5108
22. Nasiri Soloklo, H., Bigdeli, N., "A PFC-based Hybrid Approach for Control of Industrial Heating Furnace", *Journal of Electrical and Computer Engineering Innovations*, Vol. 7, No. 1, (2019), 81-92. DOI: 10.22061/jecei.2020.5744.253
23. Sunil, P.U., Desai, K., Barve, J., Nataraj, P.S.V., "An experimental case study of robust cascade two-element control of boiler drum level", *ISA Transactions*, Vol. 96, (2020), 337-351. DOI: 10.1016/j.isatra.2019.06.016
24. Wang, C., Qiao, Y., Liu, M., Zhao, Y., Yan, J., "Enhancing peak shaving capability by optimizing reheat-steam temperature control of a double-reheat boiler", *Applied Energy*, Vol. 260, (2020). DOI: 10.1016/j.apenergy.2019.114341
25. Mello, F.M., Cruz, A.G.B., Sousa, R., "Fuzzy Control Applied to Combustion in Sugarcane Bagasse Boilers", Editor(s): Anton A. Kiss, Edwin Zondervan, Richard Lakerveld, Leyla Özkan, *Computer Aided Chemical Engineering*, Vol. 46, (2019), 1135-1140. DOI: 10.1016/B978-0-12-818634-3.50190-9
26. Kong, L., Yuan, J., "Generalized Discrete-time nonlinear disturbance observer based fuzzy model predictive control for boiler-turbine systems", *ISA Transactions*, Vol. 90, (2019), 89-106. DOI: 10.1016/j.isatra.2019.01.003
27. Annadurai, S., Arock, M., "Fuel Classification based on Flame Characteristics using a Time Series Analysis with Fuzzy Support Vector Machine Algorithm", *Asia-Pacific Journal of Chemical Engineering*, Vol. 15, No. 5, (2020). DOI: 10.1002/apj.2395
28. Shi, J., "Identification of Circulating Fluidized Bed Boiler Bed Temperature Based on Hyper-Plane-Shaped Fuzzy C-Regression Model", *International Journal of Computational Intelligence and Applications*, Vol. 19, No. 4, (2020). DOI: 10.1142/S1469026820500297
29. Guo, C., Xie, X.J., "Output feedback control of feedforward nonlinear systems with unknown output function and input matching uncertainty", *International Journal of Systems Science*, Vol. 51, No. 6, (2020), 971-986. DOI: 10.1080/00207721.2020.1746438
30. Hu, M., Wang, F., "Maximum Principle for Stochastic Recursive Optimal Control Problem under Model Uncertainty", *SIAM Journal on Control and Optimization*, Vol. 58, No. 3, (2020), 1341-1370. DOI: 10.1137/19M128795X
31. Chaoui, H., Yadav, S. "Adaptive Control of a 3-DOF Helicopter Under Structured and Unstructured Uncertainties", *Journal of Control, Automation and Electrical Systems*, Vol. 31, (2020), 94-107. DOI: 10.1007/s40313-019-00544-0

32. Zhang, S., Hui, Y., Chi, R., Li, J., "Nonholonomic dynamic linearisation based adaptive PID-type ILC for nonlinear systems with iteration-varying uncertainties", *International Journal of Systems Science*, Vol. 51, No. 5, (2020), 903-921. DOI: 10.1080/00207721.2020.1746434
33. Sajedi, S., Sarfaraz, A., Bamdad, S., Khalili-Damghani, K. Designing a Sustainable Reverse Logistics Network Considering the Conditional Value at Risk and Uncertainty of Demand under Different Quality and Market Scenarios, *International Journal of Engineering, Transactions B: Applications*, Vol. 33, No. 11, (2020), 2252-2271. DOI: 10.5829/ije.2020.33.11b.17
34. Tavoosi, J., "A Novel Recurrent Type-2 Fuzzy Neural Network Stepper Motor Control", *Mechatronic Systems and Control*, Vol 49, No. 1, (2021), DOI: 10.2316/J.2021.201-0097
35. Choug, N., Benagoune, S., Belkacem, S., "Hybrid Fuzzy Reference Signal Tracking Control of a Doubly Fed Induction Generator", *International Journal of Engineering, Transactions A: Basics*, Vol. 33, No. 4, (2020), 567-574. DOI: 10.5829/ije.2020.33.04a.08
36. Kumari, A., Das, S.K. and Srivastava, P.K., Data-driven modeling of corrosion and scale deposition rate in economizer, *Anti-Corrosion Methods and Materials*, Vol. 64 No. 2, (2017), 178-187. DOI: 10.1108/ACMM-11-2015-1595
37. Yu, W., Zhao, F., Xu, H., Xu, M., Yang, W., Siah, K.B., Prabakaran, S., "Predictive control of CO₂ emissions from a grate boiler based on fuel nature structures using intelligent neural network and Box-Behnken design", *Energy Procedia*, Vol. 158, (2019), 364-369. DOI: 10.1016/j.egypro.2019.01.116
38. Sharipov, M., "Steam Boiler Control Using Neural Networks", In *International Multi-Conference on Industrial Engineering and Modern Technologies (FarEastCon)*, Vladivostok, Russia, (2019), 1-7. DOI: 10.1109/FarEastCon.2019.8934742
39. Savargave, S.B. and Lengare, M.J., Modeling and Optimizing Boiler Design using Neural Network and Firefly Algorithm, *Journal of Intelligent Systems*, Vol. 27, No. 3, (2018), 393-412. DOI: 10.1515/jisys-2016-0113
40. Muravyova, E.A., Uspenskaya, N.N. Development of a Neural Network for a Boiler Unit Generating Water Vapour Control. Opt. Mem. *Neural Networks*, Vol. 27, (2018), 297-307. DOI: 10.3103/S1060992X18040070
41. Kouadri, A., Namoun, A. and Zemat, M. , "Modelling the nonlinear dynamic behaviour of a boiler-turbine system using a radial basis function neural network", *International Journal of robust and nonlinear Control*, Vol. 24, (2014), 1873-1886. DOI:10.1002/rnc.2969
42. Tavoosi, J., "An experimental study on inverse adaptive neural fuzzy control for nonlinear systems", *International Journal of Knowledge-based and Intelligent Engineering Systems*, Vol. 24, No. 2, (2020). DOI: 10.3233/KES-200036
43. Liao, B., Peng, K., Song, S., Lin, X. Optimal Control for Boiler Combustion System Based on Iterative Heuristic Dynamic Programming. In: *Advances in Neural Networks. Lecture Notes in Computer Science*, Vol. 6675. Springer, Berlin, Heidelberg, (2011). DOI: 10.1007/978-3-642-21105-8_49
44. Wang, L., "Model Predictive Control System Design and Implementation Using MATLAB", 1st edition, Springer Publishing Company, Incorporated, (2009). DOI: 10.1007/978-1-84882-331-0

Persian Abstract

چکیده

در این مقاله، مدل جدید کنترل پیش‌بینی مبتنی بر شبکه تابع پایه شعاعی (RBFN-MPC) برای کنترل دمای دیگ بخار نیروگاهی ارائه شده است. برای اولین بار در این مقاله از چند جمله‌ای لاگر برای بدست آوردن مدل‌های محلی دیگ بخار بر اساس حالت‌های مختلف بار استفاده شده است. از روش حداقل مربعات بازگشتی (RLS) جهت برورسانی ضرایب چند جمله‌ای لاگر استفاده می‌شود. سپس برای مدل‌سازی محلی از شبکه عصبی تابع پایه شعاعی بازگشتی با مکانیزم خودتنظیمی استفاده شده و از آن برای تخمین رفتار آینده دیگ بخار استفاده می‌شود. در این RBFN بازگشتی، از خروجی گره‌های لایه پنهان در لحظه گذشته در مدل‌سازی استفاده می‌شود، بنابراین مدل دیگ بخار دقیقاً مانند یک دیگ بخار واقعی رفتار می‌کند. عدم قطعیت‌های مختلفی به دیگ بخار اضافه شده و این عدم قطعیت‌ها بلافاصله توسط RBFN بازگشتی شناسایی می‌شوند. در شبیه‌سازی، روش پیشنهادی با MPC سنتی (بر اساس مدل ریاضی دیگ بخار) مقایسه شده است. نتایج شبیه‌سازی نشان می‌دهد که MPC مبتنی بر RBFN بازگشتی عملکرد بهتری نسبت به MPC سنتی بر مدل ریاضی دارد. این به دلیل ردیابی آنلاین دینامیک دیگ بخار توسط شبکه عصبی است، در حالی که به روش سنتی، مدل همیشه ثابت است. با افزایش میزان عدم اطمینان، تفاوت بین روش پیشنهادی ما و روش‌های موجود بیشتر مشخص می‌شود.



Actuator Fault Detection and Isolation for Helicopter Unmanned Aerial Vehicle in the Present of Disturbance

Z. Nejati, A. Faraji*

Department of Electrical and Computer Engineering, University of Kashan, Kashan, Iran

PAPER INFO

Paper history:

Received 21 August 2020

Received in revised form 11 November 2020

Accepted 18 January 2021

Keywords:

Actuator Faults

Fault Detection

Fault Isolation

Helicopter Unmanned Aerial Vehicle

Unknown Input Observer

ABSTRACT

Helicopter unmanned aerial vehicle (HUAV) are an ideal platform for academic researches. Abilities of this vehicle to take off and landing vertically while performing hover flight and various flight maneuvers have made them proper vehicles for a wide range of applications. This paper suggests a model-based fault detection and isolation for HUAV in hover mode. Moreover in HUAV, roll, pitch and yaw actuator faults are coupled and affect each other, hence, we need a method that decouples them and also separates fault from disturbance. For this purpose, a robust unknown input observer (UIO) is designed to detect bias fault and also catastrophic fault such as stuck in actuators of HUAV. The robust UIO isolates roll and pitch actuator faults from yaw actuator fault. The novelty of this manuscript is the design of two UIO observers to detect and decouple the faults of helicopter actuators, one for lateral and longitudinal actuators and the other for pedal actuator. Also the proposed method is compared with extended Kalman filter (EKF). Simulation results show effectiveness of the proposed method for detection and isolation of actuator faults with less number of observers and it is able to decouple fault and disturbance effects.

doi: 10.5829/ije.2021.34.03c.12

NOMENCLATURE

d_{col}	collective input	a_{1f}, b_{1f}	Longitudinal and lateral stabilizer flapping angles
d_{lon}	longitudinal input	g	gravity acceleration
d_{lat}	lateral input	k_{β}	Main rotor blade restoring spring constant
d_{ped}	pedal input	h_{mr}	Height of main rotor hub above center of mass
$W^B = [p \quad q \quad r]^T$	Roll, pitch, and yaw rates in body frame	h_r	Height of tail rotor axis above center of mass
T_{mr}^h, T_{tr}^h	main and tail rotor thrust	Q_{mr}^h, Q_{tr}^h	main and tail rotor counter-torque

1. INTRODUCTION

To provide a safe flight with a helicopter unmanned aerial vehicle (HUAV), it is necessary to detect its faults and make emergency landings on time. The fault may occur in sensors, controllers, or actuators. Loss of control is the most important factor in air events [1]. This paper addresses the additive faults such as bias and stuck in case of an external disturbance.

In case of a bias fault, the control level always has a constant difference between the actual and expected deviation. In the stuck fault, the actuator is locked in a

place. In the last decade, some FDI methods have been proposed to deal with actuator faults and enhance the safety of various unmanned aerial vehicles UAVs.

A sliding mode observer (SMO) is designed for detection, isolation and estimation of the actuator faults for the quadrature nonlinear Lipschitz model for an incipient fault that is more difficult to detect [1, 2]. Multiple model adaptive estimation (MMAE) method is used to detect and isolate actuator or sensor faults [3, 4]. Two systematic algorithms, intelligent Output-Estimator and Model-Free technique were presented that detect and isolate actuator fault of quadrotor UAV [5]. Lee and Choi

*Corresponding Author Institutional Email: ar.faraji@kashanu.ac.ir (A. Faraji)

[6] used the Interactive Multiple Neural Adaptive Observer for Sensor and Actuator Fault Detection and Isolation of quadcopter. Zhong et al. [7] have presented a robust actuator fault detection and diagnosis (FDD) scheme for a quadrotor UAV (QUAV) in the case of external disturbances. In literature [8, 9] an applicable method was proposed for detecting an incipient fault in the QUAV.

Avram et al. [10] designed a nonlinear adaptive estimation technique for a quadrotor that consists of a nonlinear fault detection estimator and a bank of nonlinear adaptive fault isolation estimators .

In general, the major problem in HUAV actuator FDI methods is the detection of various faults when HUAV is in a windy environment. HUAVs almost have small size and lightweight and external disturbance affects their correct operation. So, detecting actuator fault and the external disturbances separating faults and disturbances is more difficult. Also, in this model, roll, pitch and yaw actuators faults are coupled and affect each other. Unknown input observers (UIOs) are used to separate FDI from external disturbances. The major contribution of this paper is the design of just two UIOs for decoupling actuator faults.

The rest of this paper is organized as follows. Section 2 describes plant model. The UIO is designed in Section 3 for detecting actuator faults. Section 4 presents simulation of the designed observers. Finally, the results are given in Section 5.

2. HUAV MODEL DESCRIPTION

HUAVs are categorized in terms of weight and size, and have four input references to perform various flight maneuvers that are collective input and change the reference value of the main rotor thrust. In fact, this input changes the thrust vector and HUAV flight height, The longitudinal input and lateral input that causes the device to move forward and backward right and left respectively and the pedal input that changes the tail rotor thrust value as a result of which, the HUAV rotates around it [11]. This inputs are applied to HUAV with four servo actuators, including the collective pitch servo, elevator servo, aileron servo and rudder servo.

2. 1. Mathematical Model

Equations of the helicopter are explained in literature [12, 13]. The cross-coupling terms are neglected as they small in hover mode and are summarized in a single $\dot{x} = f(x, u)$ expression as Equation (1).

$$\begin{aligned} \dot{p} &= \frac{1}{J_{xx}} ((T_{mr}^h h_{mr} + k_{\beta})(K_B d_{lat} + K_F b_{1f}) - T_{tr}^h h_{tr}) \\ \dot{q} &= \frac{1}{J_{yy}} ((T_{mr}^h h_{mr} + k_{\beta})(K_B d_{lon} + K_F a_{1f}) - Q_{mr}^h) \end{aligned} \quad (1)$$

$$\dot{r} = \frac{1}{J_{zz}} (T_{tr}^h d_{tr} - Q_{mr}^h)$$

$$\dot{a}_{1f} = -\frac{a_{1f}}{\tau_f} - q + \frac{K_H}{\tau_f} d_{lon}$$

$$\dot{b}_{1f} = -\frac{b_{1f}}{\tau_f} - p + \frac{K_H}{\tau_f} d_{lat}$$

The main rotor thrust (T_{mr}^h) and counter-torque (Q_{mr}^h) are in the following form:

$$T_{mr}^h = C_{mr}^h (C_c d_{col} + D_c) + \frac{(D_{mr}^T)^2}{2} - \dots \quad (2)$$

$$D_{mr}^T \sqrt{C_{mr}^T (C_c d_{col} + D_c) + \frac{(D_{mr}^T)^2}{4}}$$

$$Q_{mr}^h = C_{mr}^Q (T_{mr}^h)^{3/2} + D_{mr}^Q, \quad (3)$$

where C_{mr}^T , D_{mr}^T , C_{mr}^Q and D_{mr}^Q are constant, and depend on the density of air and some characteristic of the HUAV main rotor including the radius of disc, angular rotation rate, lift curve slope and blade chord length. The tail rotor thrust and counter-torque is in following form.

$$T_{tr}^h = C_{tr}^h (C_t d_{ped} + D_t) + \frac{(D_{tr}^T)^2}{2} - \dots \quad (4)$$

$$D_{tr}^T \sqrt{C_{tr}^T (C_t d_{ped} + D_t) + \frac{(D_{tr}^T)^2}{4}}$$

$$Q_{tr}^h = C_{tr}^Q (T_{tr}^h)^{3/2} + D_{tr}^Q, \quad (5)$$

where C_{tr}^T , D_{tr}^T , C_{tr}^Q and D_{tr}^Q are constant, and depend on density of air and some characteristic of HUAV tail rotor such as the radius of disc, angular rotation rate, the lift curve slope and blade chord length.

3. UNKNOWN INPUT OBSERVER

According to the study on fault detection, one of the best methods for fault detection in systems is the use of observers. The UIO observer is a robust observer that can detect or estimate faults and is robust to external disturbances and uncertainties. Assuming the use of output sensors, two UIO observers can be used to detect the faults of helicopter operators, one for lateral operators and the other for pedal operators. The observer's function is such that the third input in the first observer and the first and second inputs do not play a role in the second observer.

3. 1. Unknown Input Observer Design

Unknown input Observer (UIO) is design as state estimation error vector $e(t)$ approaches zero asymptotically, regardless of the presence of the unknown input or disturbance in the system. Suppose equation of system is described as:

$$\begin{cases} \dot{x} = Ax(t) + Bu(t) + Ed(t) \\ y(t) = Cx(t) \end{cases} \quad (6)$$

The structure for a full-order observer is described as:

$$\begin{cases} \dot{z} = Fz(t) + TBu(t) + Ky(t) \\ \hat{x} = z(t) + Hy(t) \end{cases} \quad (7)$$

where \hat{x} and z are estimated state vector and state of observer respectively. For error we have

$$\begin{aligned} \dot{e}(t) &= \dot{x}(t) - \dot{\hat{x}}(t) \\ &= Ax(t) + Bu(t) + Ed(t) - \dot{z}(t) - H\dot{y}(t) \end{aligned} \quad (8)$$

With substituting Equations (6) and (7) into Equation (8), we obtain:

$$\begin{aligned} \dot{e}(t) &= Ax(t) + Bu(t) + Ed(t) - Fz(t) - TBu(t) \\ &\quad - KCx(t) - HC(Ax(t) + Bu(t) + Ed(t)) \end{aligned} \quad (9)$$

With adding and subtracting $(A - HCA - KC)\hat{x}(t)$ from Equation (9), we have

$$\begin{aligned} \dot{e}(t) &= (A - HCA - KC)e(t) \\ &\quad + (A - HCA - KC - F)z(t) + (A - HCA - KC)Hy \\ &\quad + (B - TB - HCB)u(t) + (I - HC)Ed(t) \end{aligned} \quad (10)$$

F, T, K and H are matrices to be designed as the state estimation error vector $e(t)$ which approaches zero asymptotically and the following relation must be true.

$$\begin{aligned} (HC - I)E &= 0 \\ T &= I - HC \\ F &= A - HCA - K_1C \\ K_2 &= FH \\ K &= K_1 + K_2 \end{aligned} \quad (11)$$

Necessary and sufficient conditions to design and prove of observer stability have been demonstrated by Ducard [4] and are not mentioned here.

3. 2. Robust Actuator Fault Isolation Schemes

System equation with actuator fault can be described using the following equation for $i = 1, 2, \dots, r$.

$$\begin{cases} \dot{x} = Ax(t) + B^i u^i(t) + B^i f_a^i(t) + b_i(u_i(t) + f_{ai}(t)) + Ed(t) \\ y(t) = Cx(t) \end{cases} \quad (12)$$

where b_i is i_{th} column of the matrix B, B^i is obtained from the matrix B by deleting the i_{th} column b_i , u_i is i_{th} component of u , u^i is obtained from the vector u by deleting the i_{th} component u_i . If we define

$$\begin{aligned} E^i &= [E \quad b_i], d^i(t) = \begin{bmatrix} d(t) \\ u_i(t) + f_{ai}(t) \end{bmatrix} \\ \begin{cases} \dot{x} = Ax(t) + B^i u^i(t) + B^i f_a^i(t) + E^i d^i(t) \\ y(t) = Cx(t) \end{cases} \end{aligned} \quad (13)$$

Based on the above system description, r UIO-based residual generators can be constructed as:

$$\begin{cases} \dot{z}^i(t) = F^i z^i(t) + T^i B^i u^i(t) + K^i y(t) \\ r^i(t) = (I - CH^i)y(t) - Cz^i(t) \end{cases} \quad (14)$$

where F^i, T^i, K^i and H^i ($i=1, 2, \dots, r$) are obtained in each observer as before.

4. SIMULATION RESULTS

In order to validate the RThSEKF approach, seven scenarios are simulated on an unmanned helicopter. In this paper, model parameters are adopted from the literature [14] which describes the ANCL helicopter.

The wind gust model block implements a wind gust of standard "1-cosine" shape [14].

$$A = \begin{bmatrix} 0 & 0 & 0 & 0 & 2.78(0.2112T_{mr} + 80.52) \\ 0 & 0 & 0 & 0.67(0.2112T_{mr} + 80.52) & 0 \\ 0 & 0 & 0 & 0 & 0 \\ 0 & -1 & 0 & -7.14 & 0 \\ -1 & 0 & 0 & 0 & -7.14 \end{bmatrix}$$

$$B = \begin{bmatrix} 2.78(0.0288T_{mr} + 10.98) & 0 & -0.3336 \\ 0 & 0.67(0.0288T_{mr} + 10.98) & 0.075 \\ 0 & 0 & 0.8798 \\ 0 & 2 & 0 \\ 2 & 0 & 0 \end{bmatrix}$$

$$C = \begin{bmatrix} 1 & 0 & 0 & 0 & 0 \\ 0 & 1 & 0 & 0 & 0 \\ 0 & 0 & 1 & 0 & 0 \end{bmatrix}, E = \begin{bmatrix} 0 \\ 0 \\ -0.83Q(T_{mr}) \\ 0 \\ 0 \end{bmatrix}$$

The goal is to hold the helicopter in hover and check the actuator's fault. The state vector and the input vector that we use in this goal are in the form of Equation (7): $x = [p, q, r, a_{lf}, b_{lf}]$ and $u = [d_{lon}, d_{lat}, T_{tr}]$. For designing UIO, according to [14] and considering the fact that the collective actuator is healthy and considering that the fault in the longitudinal and lateral actuator results in the change of the pitch angle of the main rotor blades and the fault in the pedal actuator results in the change of the pitch angle of tail Rotor blades, two UIO are used to detect faults. The design method is described below. The UIO 1 is used to detect faults in longitudinal and lateral actuator, and the UIO 2 is used to detect a fault in the pedal actuator.

UIO 1: The dynamic equation for the first UIO is:

$$\dot{z}^1(t) = F^1 z^1(t) + K^1 y(t) + T^1 \begin{bmatrix} b_1 & b_2 \end{bmatrix} \begin{bmatrix} u_1(t) \\ u_2(t) \end{bmatrix}$$

where b_1 and b_2 are the first two columns of B, and the parameter matrix for this UIO are:

$$H^1 = \begin{bmatrix} 0.9995 & -0.0225 & 0 \\ -0.0225 & 0.0005 & 0 \\ 0 & 0 & 1 \\ 0 & 0 & 0 \\ 0 & 0 & 0 \end{bmatrix}, T^1 = \begin{bmatrix} 0.0005 & 0.0225 & 0 & 0 & 0 \\ 0.0225 & 0.9995 & 0 & 0 & 0 \\ 0 & 0 & 0 & 0 & 0 \\ 0 & 0 & 0 & 1 & 0 \\ 0 & 0 & 0 & 0 & 1 \end{bmatrix}$$

$$F^1 = \begin{bmatrix} -10 & 0 & 0 & 1.6618 & .1551 \\ 0 & -20 & 0 & 73.8759 & 6.8951 \\ 0 & 0 & -30 & 0 & 0 \\ 0 & -1 & 0 & -7.14 & 0 \\ -1 & 0 & 0 & 0 & -7.14 \end{bmatrix}, K^1 = \begin{bmatrix} 0.0051 & 0.2248 & 0 \\ 0.4497 & 19.9899 & 0 \\ 0 & 0 & 0 \\ 0.0225 & -0.0005 & 0 \\ -0.9995 & 0.0225 & 0 \end{bmatrix}$$

The third element of vector z^1 (z_3^1) has no inputs of y , u_1 and u_2 , hence it will stay at zero if the initial values of z_3^1 is zero and the observer matrix F^1 is designed to be stable. The full-order UIO can be reduced to:

- The state estimation is:

$$\begin{bmatrix} \dot{z}_1^1 \\ \dot{z}_2^1 \\ \dot{z}_4^1 \\ \dot{z}_5^1 \end{bmatrix} = \begin{bmatrix} -10 & 0 & 1.6618 & 0.1551 \\ 0 & -20 & 73.8759 & 6.8951 \\ 0 & -1 & -7.14 & 0 \\ -1 & 0 & 0 & -7.14 \end{bmatrix} \begin{bmatrix} z_1^1 \\ z_2^1 \\ z_4^1 \\ z_5^1 \end{bmatrix} + \begin{bmatrix} 0.0211 & 0.2266 \\ 0.9402 & 10.074 \\ 0 & 2 \\ 2 & 0 \end{bmatrix} \begin{bmatrix} u_{lat} \\ u_{lon} \end{bmatrix} + \begin{bmatrix} 0.0051 & 0.2248 \\ 0.4497 & 19.9899 \\ 0.0225 & -0.0005 \\ -0.9995 & 0.0225 \end{bmatrix} y$$

$$\hat{x}^1 = \begin{bmatrix} z_1^1 + .9995y_1 - .0225y_2 \\ z_2^1 - .0225y_1 + .0005y_2 \\ y_3 \\ z_4^1 \\ z_5^1 \end{bmatrix}$$

- The residual is generated by:

$$r^1 = y_1 - \hat{y}_1 = y_1 - \hat{x}_1 = z_1^1 + .9995y_1 - .0225y_2 = 0.0005y_1 - z_1^1 + 0.0225y_2$$

As is clear, this relationship only depends on the first and second inputs and outputs. The third input and output do not play a role in this observer, so in the event of a fault, the third input does not represent a diagnostic observer. Also, disturbance does not appear in the residual, and fault in the UIO observer are completely separate.

UIO 2: The dynamic equation for the second UIO is:

$$\dot{z}^2(t) = F^2 z(t) + K^2 y(t) + T^2 b_3 u_3(t)$$

where b_3 is the third column of B, and the parameter matrices for this UIO are:

$$H^2 = \begin{bmatrix} 1 & 0 & 0 \\ 0 & 1 & 0 \\ 0 & 0 & 0 \\ 0 & 0.1984 & 0 \\ 0.0478 & 0 & 0 \end{bmatrix}, T^2 = \begin{bmatrix} 0 & 0 & 0 & 0 & 0 \\ 0 & 0 & 0 & 0 & 0 \\ 0 & 1 & 0 & 0 & 0 \\ 0 & -0.1984 & 0 & 1 & 0 \\ -0.0478 & 0 & 0 & 0 & 1 \end{bmatrix}$$

$$F^2 = \begin{bmatrix} 0 & 0 & 0 & 0 & 0 \\ 0 & 0 & 0 & 0 & 0 \\ 0 & 0 & -30 & 0 & 0 \\ 0 & -2 & 0 & -21.8067 & 0 \\ -2 & 0 & 0 & 0 & -21.8067 \end{bmatrix}, K^2 = \begin{bmatrix} 0 & 0 & 0 \\ 0 & 0 & 0 \\ 0 & 0 & 0 \\ 0 & -5.3271 & 0 \\ -2.0429 & 0 & 0 \end{bmatrix}$$

Similar to UIO 1 the first and the second states can be eliminated, and the UIO2 can also be reduced as:

$$\begin{bmatrix} \dot{z}_3^2 \\ \dot{z}_4^2 \\ \dot{z}_5^2 \end{bmatrix} = \begin{bmatrix} -30 & 0 & 0 \\ 0 & -21.8067 & 0 \\ 0 & 0 & -21.8067 \end{bmatrix} \begin{bmatrix} z_3^2 \\ z_4^2 \\ z_5^2 \end{bmatrix} + \begin{bmatrix} 0.8798 \\ -0.0015 \\ 0.016 \end{bmatrix} \begin{bmatrix} u_{ped} \\ 0 \\ -2.0429 \end{bmatrix} + \begin{bmatrix} 0 & 0 & 0 \\ 0 & -5.3271 & 0 \\ 0 & 0 & 0 \end{bmatrix} y$$

The residual is generated by:

$$r^3 = y_3 - \hat{y}_3 = y_3 - \hat{x}_3 = y_3 - z_3^2$$

This relationship indicates that the residual only depends on the third input, and the change indicates the occurrence of a fault in the system. Various types of fault are introduced to the system in two scenarios in following. In these scenarios we suppose $d = 0.001 \sin(t) + 0.005 \cos(2t)$ and also we compare the designed method with the EKF [3].

4. 1. Scenario 1: Bias Faults

In this scenario, small bias faults are simulated for three actuator inputs in the case of disturbances. From $t=5-10s$, lateral servo has a bias fault at 0.02. For $t=10-15s$, longitudinal servo has a bias fault near to the equilibrium position in the no fault mode in 0.01. For $t=15-20s$, ruder servo has a bias fault whose value equals 0.05. Figure 1 shows residuals for the UIO 1 and UIO 2 for this scenario. As can be seen, the method is capable of accurately diagnosing the faults by the two observers, and the disturbance dose not affect it, in other words it is robust but in EKF we need more observers and it is not decoupled from disturbance.

4. 2. Scenario 2: Actuator Stuck Faults

In order to apply stuck fault to the HUAV actuator, the control between the actuator and the controller is disconnected, and the actuator stuck at a point. In this scenario, starting from $t=5-10s$, the lateral servo (d_{lat}) has a stuck fault in position 0.01. Figure 2 shows that the method is able to detected faults in the presence of disturbance. As it is shown that disturbance is decoupled from the fault in UIO, but in EKF disturbance affect on the residuals.

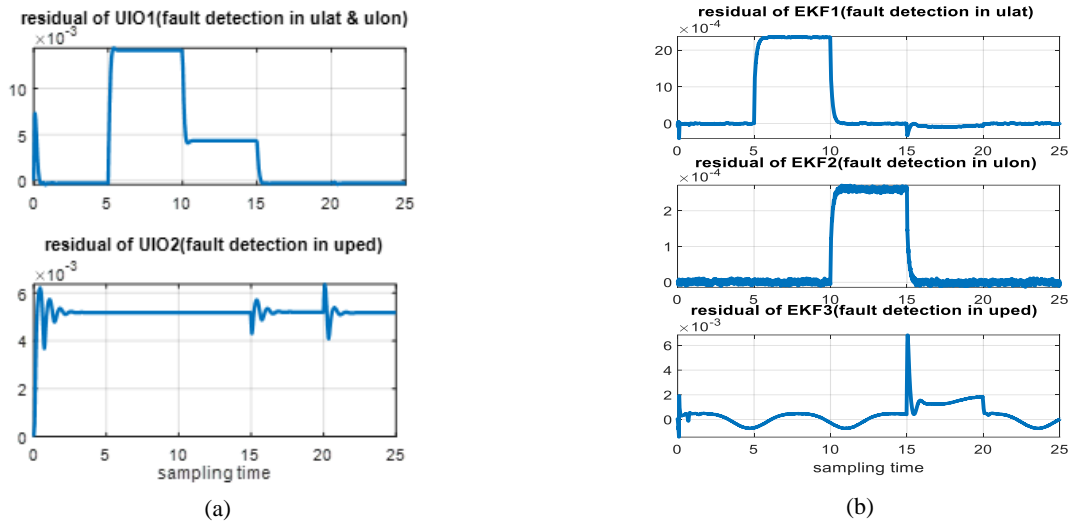


Figure 1. Residuals for Scenario 1: (a) UIO,(b): EKF

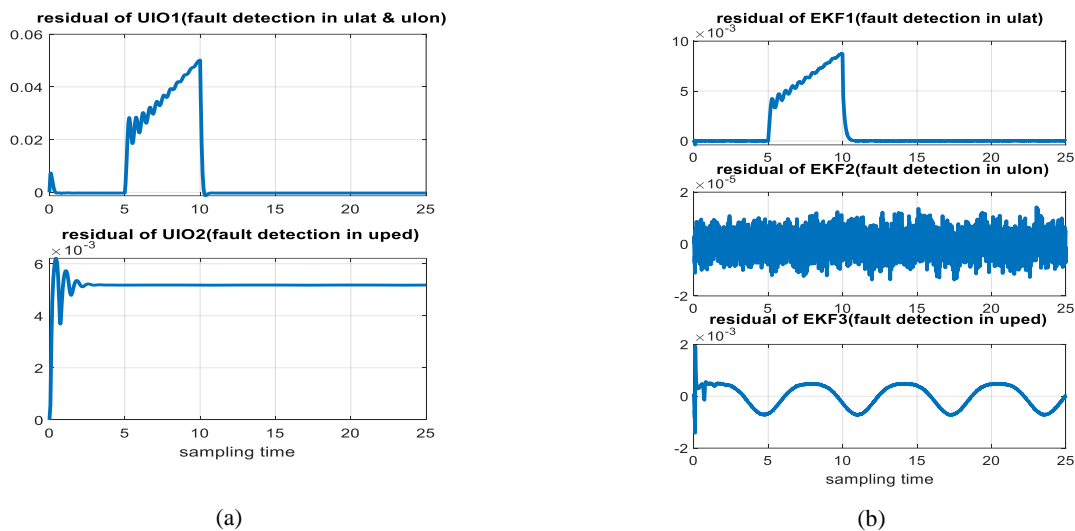


Figure 2. Residuals for scenario 2: (a) UIO,(b): EKF

5. CONCLUSION

This paper describes FDI for HUAV actuators for detecting and isolating additive faults such as bias and stuck in the presence of external disturbances in hover mode. It is important that, actuator fault detection can be decoupled and separated from disturbance. For this purpose, the unknown input observer is proposed. Two unknown input observers are designed for decoupling actuator faults. Results show effectiveness of the proposed method for various faults in HUAV actuators in comparison to the EKF. In EKF, we need three observers and it is not decoupled from disturbance. The proposed method can be used for other plants with additive faults.

6. REFERENCES

1. Liu, C., Jiang, B., and Zhang, K., "Incipient Fault Detection Using an Associated Adaptive and Sliding-Mode Observer for Quadrotor Helicopter Attitude Control Systems", *Circuits, Systems, and Signal Processing*, Vol. 35, No. 10, (2016), 3555–3574. doi:10.1007/s00034-015-0229-8
2. Zhang, Y. M., Chamseddine, A., Rabbath, C. A., Gordon, B. W., Su, C.-Y., Rakheja, S., Fulford, C., Apkarian, J., and Gosselin, P., "Development of advanced FDD and FTC techniques with application to an unmanned quadrotor helicopter testbed", *Journal of the Franklin Institute*, Vol. 350, No. 9, (2013), 2396–2422. doi:10.1016/j.jfranklin.2013.01.009
3. Ducard, G., and Geering, H. P., "Efficient Nonlinear Actuator Fault Detection and Isolation System for Unmanned Aerial Vehicles", *Journal of Guidance, Control, and Dynamics*, Vol.

- 31, No. 1, (2008), 225–237. doi:10.2514/1.31693
4. Ducard, G. J. J., "Fault-tolerant Flight Control and Guidance Systems", Practical Methods for Small Unmanned Aerial Vehicles, London, Springer London, (2009). doi:10.1007/978-1-84882-561-1
 5. Younes, Y. Al, Noura, H., Rabhi, A., and Hajjaji, A. El, "Actuator Fault-Diagnosis and Fault-Tolerant-Control using intelligent-Output-Estimator Applied on Quadrotor UAV", 2019 International Conference on Unmanned Aircraft Systems (ICUAS), (2019), IEEE, 413–420. doi:10.1109/ICUAS.2019.8798232
 6. Lee, W.-C., and Choi, H.-L., "Interactive Multiple Neural Adaptive Observer based Sensor and Actuator Fault Detection and Isolation for Quadcopter", 2019 International Conference on Unmanned Aircraft Systems (ICUAS), (2019), IEEE, 388–396. doi:10.1109/ICUAS.2019.8797779
 7. Zhong, Y., Zhang, Y., Zhang, W., Zuo, J., and Zhan, H., "Robust Actuator Fault Detection and Diagnosis for a Quadrotor UAV With External Disturbances", *IEEE Access*, Vol. 6, (2018), 48169–48180. doi:10.1109/ACCESS.2018.2867574
 8. He, Z., Wei, J., and Hou, B., "Detecting Incipient Faults in Quadrotor Unmanned Aerial Vehicle Based on Detrending and Denoising Techniques", 2018 IEEE 7th Data Driven Control and Learning Systems Conference (DDCLS), (2018), IEEE, 959–964. doi:10.1109/DDCLS.2018.8515954
 9. Yi, Y., and Zhang, Y., "Fault diagnosis of an unmanned quadrotor helicopter based on particle filter", 2017 International Conference on Unmanned Aircraft Systems (ICUAS), (2017), IEEE, 1432–1437. doi:10.1109/ICUAS.2017.7991322
 10. Avram, R. C., Zhang, X., and Muse, J., "Quadrotor Actuator Fault Diagnosis and Accommodation Using Nonlinear Adaptive Estimators", *IEEE Transactions on Control Systems Technology*, Vol. 25, No. 6, (2017), 2219–2226. doi:10.1109/TCST.2016.2640941
 11. McLean, D., "Aircraft flight control systems", *The Aeronautical Journal*, Vol. 103, No. 1021, (1999), 159–166. doi:10.1017/S0001924000064976
 12. Barczyk, M., Nonlinear State Estimation and Modeling of a Helicopter UAV, Doctoral dissertations, University of Alberta, (2012).
 13. Faraji, A., Nejati, Z., and Abedi, M., "Actuator Faults Estimation for a Helicopter UAV in the Presence of Disturbances", *Journal of Control, Automation and Electrical Systems*, Vol. 31, No. 5, (2020), 1153–1164. doi:10.1007/s40313-020-00621-9
 14. Cai, G., Chen, B. M., and Lee, T. H., Unmanned Rotorcraft Systems, London, Springer London, (2011). doi:10.1007/978-0-85729-635-1

Persian Abstract

چکیده

بالگردهای بدون سرنشین سیستمی کاربردی برای تحقیقات دانشگاهی می‌باشد. توانایی این وسیله در فرود و فراز عمودی و همچنین قابلیت پرواز در حالت هاور و مانورهای پروازی مختلف، آن را به وسیله محبوبی در بسیاری از کاربردهای تبدیل کرده است. این مقاله یک روش تشخیص و جداسازی عیب برای بالگردهای بدون سرنشین در حالت پروازی هاور ارائه می‌دهد. در این وسیله عملگرهای رول، پیتچ و یاو کوپل بوده و عیب‌های آن‌ها روی یکدیگر تاثیر می‌گذارد بنابراین ما نیاز به روشی داریم که آن‌ها را از هم کوپل کند و همچنین قادر به جداسازی عیب از اغتشاش باشد. برای این منظور مشاهده‌گر ورودی ناشناخته مقاوم ارائه شده است که قادر به تشخیص عیب‌های بایاس و عیب‌های مهمتر مانند قفل عملگر می‌باشد. این مشاهده‌گر ورودی ناشناخته عیب‌های جانبی را از عیب یاو جدا می‌کند. نوآوری مقاله در طراحی تنها دو مشاهده‌گر برای این جداسازی می‌باشد یکی برای عیب‌های جانبی و دیگری برای یاو. همچنین این مشاهده‌گر با کالمن فیلتر توسعه یافته مقایسه شده است. نتایج عملکرد خوب مشاهده‌گر را با تعداد کمتر مشاهده‌گر و دکوپله کردن اثر عیب و اغتشاش را نشان می‌دهد.



Effect of Sensory Experience on Customer Word-of-mouth Intention, Considering the Roles of Customer Emotions, Satisfaction, and Loyalty

A. Torabi, H. Hamidi*, N. Safaie

Faculty of Industrial Engineering, K.N. Toosi University of Technology, Tehran, Iran

PAPER INFO

Paper history:

Received 08 October 2020

Received in revised form 18 December 2020

Accepted 14 January 2021

Keywords:

Customer Emotions

Customer Loyalty

Customer Satisfaction

Customer Sensory Experience

Customer Word-of-mouth Intention

ABSTRACT

Although word-of-mouth (WOM) intention has been studied as an outcome variable of some constructs such as loyalty, satisfaction, and trust in retail businesses but less attention has been given to the investigating the effect of sensory experience on customer WOM intention. Since studying concurrently the effects of sensory experience on customer emotions and customer WOM intention in retail chain stores are rare, the purpose of this paper is to study how customer sensory experience affect customer WOM intention in retail chain stores, considering the mediating role of customer emotions. For this purpose, 306 valid questionnaires were collected and analyzed from customers of one of the largest and oldest retail chain stores in Iran (ETKA chain stores). The proposed conceptual model of this research is developed on the basis of S-O-R model. Structural Equation Modeling (SEM) and multiple regression analysis used to examine the conceptual model of research. This model has been tested using the Partial Least Squares (PLS) approach by SmartPLS software. The results demonstrate that customer sensory experience directly and significantly affects customer emotions. It was also found that the direct effect of customer sensory experience on customer WOM intention is not very considerable but customer sensory experience indirectly affects customer WOM intention through customer emotions, satisfaction, and loyalty. In addition, regression analysis demonstrates that among the five sensory experiences (taste, touch, sight, sound, and smell), taste has the most effect on customer positive emotions. After taste experience, touch, sight, and sound have the most effect on customer positive emotions, respectively. Similarly, it was found that taste and touch experiences have negative and significant effect on customer negative emotions, and the effect of taste experience is stronger than the effect of touch experience.

doi: 10.5829/ije.2021.34.03c.13

1. INTRODUCTION

Initially the major attraction of retail chain stores for customers in the world was the low price of products due to the economy of scale advantage. But nowadays, due to the increase in number of these stores and consequently the intensification of competition among them, it is not possible to compete in this market with only low pricing strategy. Delivering the best services and creating a distinctive and enjoyable customer experience, as well as gaining satisfaction, trust, and thereby creating a loyal customer is one of the major competitive strategies in service businesses. There are a lot of research in this area; for example Terblanche [1], Thuan et al. [2], Choi et al. [3], Baser et al. [4], and Kim et al. [5].

The last century is considered the age of experience economy, where marketing activities are expected to create valuable experiences for customers [6]. In experiential marketing, the customer is seen as both rational and emotional person, in which the marketer seeks to create an emotional experience for the customer by creating an emotional connection between the customer and the brand [6]. Creating a distinctive experience in the services providing will make the brand lasting in the customer's mind. Brand experience comes from a set of customer interactions with a brand, and involves sensations, feelings, cognitions, and behavioral responses evoked by brand related stimuli that are part of a brand's design, identity, packaging, communications, and environments [7]. Brand experience consists of four

*Corresponding Author Institutional Email: h-hamidi@kntu.ac.ir
(H. Hamidi)

dimensions: sensory, affective, intellectual, and behavioral experience [7]. Sensory experience as one of the subsets of brand experience focuses on the five senses of human such as sight, sound, smell, touch and taste [8]. Studying about customer sensory experience creation is related to the sensory marketing scope, where the marketer seeks to influence customer perception, judgment and behavior by stimulating the customer's five senses through sensory stimuli [9]. In recent years, some research has been conducted on the impact of sensory experience on customer behavior in different businesses. For example, Iglesias et al. [10] in banking industry, Yoganathan et al. [11] in ethical brands, Chen and Lin [6] in chain coffeehouses, and Moreira et al. [12] in catering industry studied the impact of sensory experience on customer behavior.

Based on the stimulus-organism-response (S-O-R) model that was developed by Mehrabian and Russell [13], environmental stimuli elicit an emotional response that results in the behavioral response of individuals. The S-O-R model consists of three parts: stimuli, a set of interface or mediator variables, and response variables that must be conceptually explicit and comprehensive and measurable operationally [13]. One application of the S-O-R model is its use in marketing science and customer behavior analysis; for example, Choi and Kandampully [14] based on the S-O-R model concluded that a hotel atmosphere such as social and room design, influences customer satisfaction and subsequently customer WOM intention. Also, according to the study of Ha and Im [15] based on the S-O-R model to examine the role of website design quality on customer satisfaction and WOM intention in online shopping, revealed that website design quality as an external stimulus through the three mediators such as pleasure, arousal, and perceived quality of information influences customer satisfaction and customer WOM intention. In addition, some research has used S-O-R model to examine the effect of external stimuli on customer behavior. For example, Chen and Lin [6] and Han et al. [16] used the S-O-R model to examine customer behavior in coffeehouses. Jang and Namkung [17], Liu and Jang [18], and Kim and Moon [19] have used this model to examine customer behavior in restaurants environment (See Table 1).

In this research, we consider sensory experience as an external stimulus; emotion as an organism, and customer behaviour such as WOM intention as a response on the basis of S-O-R model.

In this research, we attempted to study the relationships between customer sensory experience, customer emotions, and customer WOM intention based on the proposed model. In addition, the role of customer emotions as a mediator variable in the relationships between customer sensory experience and customer WOM intention was examined. Also, we determined the

effect of each of the customer's five senses on customer emotions by means of regression analysis.

This paper is organized as follows: In the second section, the literature of the research are reviewed and in the third section, the research model and hypotheses are presented. Section forth provides research method and results, and section fifth discusses about findings and conclusions. In the final section, limitations of the research and suggestions for future research are presented.

TABLE 1. References using S-O-R model

References	S-O-R Variables	Research area
Chen and Lin [6]	<p>S: Sensory experience (Sight, Sound, Smell, Touch, Taste)</p> <p>O: Positive emotions, Negative emotions</p> <p>R: Behavioral intentions, Buying behavioral</p>	Chain coffee house
Choi and Kandampully [14]	<p>S: Atmosphere (Social, Public design, Room design, Ambience)</p> <p>O: Customer satisfaction</p> <p>R: Customer engagement (Willingness to suggest, Word of mouth)</p>	Upscale Hotel
Ha and Im [15]	<p>S: Website design</p> <p>O: Pleasure, Arousal, Perceived quality of information</p> <p>R: Satisfaction, Word of mouth intention</p>	Online shopping website
Han et al. [16]	<p>S: Cognitive drivers (Brand awareness, perceived quality, Brand image, Perceived value)</p> <p>O: Affective drivers (Pleasure, Arousal)</p> <p>R: Brand satisfaction, Brand loyalty, Relationship commitment</p>	Chain coffee shop
Jang and Namkung [17]	<p>S: Product quality, Service quality, Atmospherics</p> <p>O: Positive emotions, Negative emotions</p> <p>R: Behavioral intentions</p>	Restaurant
Liu and Jang [18]	<p>S: Dining atmospherics</p> <p>O: Positive emotions, Negative emotions, Perceived value</p> <p>R: Behavioral intentions</p>	Chinese restaurant
Kim and Moon [19]	<p>S: Service scape (Facility aesthetics, Layout, Electric equipment, Seating comfort, Ambient Condition)</p> <p>O: Pleasure-Feeling, Perceived service quality</p> <p>R: Revisit intention</p>	Restaurant

2. LITERATURE REVIEW

2.1. Customer Sensory Experience

Sensory marketing is a type of marketing strategy that aims to influence customer perception, behavior and judgment by engaging the five senses such as sight, sound, taste, touch and smell [9]. These five senses are the basis of creating customer sensory experience. Lindstrom [20] has stated that creating a sensory experience is vital to building an emotional relationship between customer and product. According to Brakus et al. [7], brand sensory experience is one of four subsets of brand experience that focuses on the customer's senses. In this paper customer sensory experience defines as customer sensory perception that is stimulated by the store environment.

Most research focused on only two aspects of the visual and auditory of customer sensory experience. For example, Iglesias et al. [10], and Ong et al. [21] focused on the visual dimension of the customer sensory experience. Yoganathan et al. [11] in addition to examining the impact of visual and auditory cues on the willingness to pay for ethical brands in online shopping, examined tactile cues in the form of a tactile priming statement. But in limited research the impact of all five types of sensory experience on customer behavior has been analyzed. For example, Chen and Lin [6] in the vision section examined the impact of color, interior design, lighting, layout, staff clothing, and store logo; in the auditory section examined the impact of store background music; in the smell section examined the impact of aromas; in the touch section examined the impact of store temperature and the texture of the table, chairs, and other item in store; and in the taste section, examined the impact of the taste of coffee and other foods which sold in the store. So in general we can say that, in a shop or store atmosphere all visual cues, sounds and aromas of the environment, the taste and quality of the foods and the ambient temperature and anything related to the customer's sense of touch can be considered as a sensory stimulus for creating customer sensory experience. One study found that 37% of respondents feel that sight is the most important sense, followed by smell (23%), sound (20%), taste (15%), and touch (5%) respectively [20]. But this may not be true in different environments. For example, according to Chen and Lin [6] the sense of taste has the greatest impact on customer positive emotion; then sight, sound and, touch are the most effective senses respectively in coffeehouses.

Multi-sensory experience occurs when more than one sense help customers to perception sensory experience. Hulten et al. [22] stated that each of the five senses can affect and be affected by other senses. According to Yoganathan et al. [11], the influence of two sensory cues is greater than one cue and the influence of three sensory cues is greater than two cues.

2.2. Customer WOM Intention

Markovic et al. [23] stated that usually when a customer is loyal to the brand or product, he or she tends to convey positive emotion to others. The concept of word of mouth is defined as oral and person-to-person communication about a brand, product or service between a receiver and a communicator whom the receiver perceives as non-commercial [24]. WOM refers to informal interpersonal communication regarding the evaluation of a store, product, service, and related experience [25]. WOM is the exchange of information and experiences among customers that helps them make purchasing decisions [26]. WOM as one of the most common non-trading behaviors, plays a fundamental role in disseminating information about products and services [27]. WOM is defined as providing a particular brand or product by customers that can be positive or negative; positive WOM is the result of customer satisfaction and loyalty, and negative WOM is caused by customer dissatisfaction with a particular brand or product [23]. Positive WOM not only helps to create a positive image of the brand or firm, but also increases the confidence of customers who are unfamiliar with the brand or firm [28]. Creating positive WOM among Consumers, has become an important marketing strategy, due to its important impact on Consumer Purchasing Decision [15]. A study found that WOM is nine times more effective than traditional advertising [29]. It was also found that customers who are affected by WOM have a higher chance of purchasing a product than customers who watch its advertising [30].

In many papers, customer loyalty and satisfaction have been considered as predictors of customer WOM. For example Choi and Kandampully [14], Markovic et al. [23], and De Matos and Rossi [31]. For this reason, in this paper WOM is defined as a result of customer satisfaction and loyalty based on three components of saying good things about the store, encouraging friends and relatives, and recommending the store to them.

2.3. Customer Emotions

Emotion is a mental state of readiness that arisen from the cognitive appraisal of events or thoughts [32]. Understanding customers' emotional responses to a product is very important, because it influences customer buying decisions [33]. Customer emotion is considered as a key element for perception of service experiences [34]. Positive emotions lead to positive responses and less thinking about decision [35]. Consumers' emotional responses not only appear briefly but lingers in their consciousness and is more persuasive than cognitive messages in switching consumer behavior [6]. In this paper, customer emotions is defined as customer's affective responses to the environmental stimuli available in the store.

According to Mehrabian and Russell [13] in the S-O-R model, emotion is considered as mediator variable between environmental stimuli and individual behavior.

They stated that the main structures of emotional response are pleasant, arousal, and dominance. The modified S-O-R model stated that emotional response can be interpreted as pleasure and arousal [36]. According to previous studies, there are two different approaches to emotion segmentation: the unipolar view and the bipolar view. In the bipolar view, according to the S-O-R model, emotions are divided into two poles: pleasant and unpleasant, or arousal and non-arousal. In unipolar View Unlike bipolar view, emotions are in one pole, for example, Plutchik [37] suggested eight basic emotions: fear, anger, joy, sadness, acceptance, disgust, expectancy, and surprise. According to Izard [38] suggestion, there are ten Primary emotions: interest, joy, surprise, sadness, anger, disgust, contempt, fear, shame, and guilt. According to the unipolar approach of Differential Emotions Scale (DES), he categorized these ten emotions into two groups of positive and negative emotions, namely positive emotions: interest, joy, and surprise, and negative emotions: sadness, anger, disgust, contempt, fear, shame, and guilt. Dividing emotions into two poles has some limitations, for example, individuals may have neither a pleasant emotion nor an unpleasant emotion towards a stimulus. In addition, the occurrence of a positive emotion does not prevent the occurrence of negative emotion in the individual [17]. In general, using a unipolar approach with differential emotion scales is more appropriate than a bipolar approach for studying customer emotions. For this reason, in this paper like some other papers, such as Chen and Lin [6], Jang and Namkung [17], and Liu and Jang [18], DES approach has been used for studying customer emotions.

2. 4. Customer Satisfaction The concept of satisfaction in marketing was introduced by Cardozo for the first time in 1965 [39]. Traditionally, customer satisfaction is defined as the post-consumption evaluation of a brand, firm or their offer that depends on the perceived value, quality, and consumer expectations [10]. Satisfaction is a judgment of the product or service feature, or the product or service itself, that providing a high or low level of consumer pleasure. Customer satisfaction refers to fulfilling a consumer's needs and desires, and is a fundamental factor in marketing [3]. Customer satisfaction can be defined as customer response to the perceived discrepancy between prior expectations and actual product performance observed after consumption [40]. It is also stated that customer satisfaction is based on the comparing product or service profitability with customer expectations, and satisfaction is achieved if the profitability is equal to or greater than the customer expectations [41]. The level of customer satisfaction depends on the relationship between expectations and actual consumption experiences [42].

Customer emotions (e.g., pleasure and arousal) and customer cognition (e.g., perception of the retail

environment) are prerequisites of satisfaction [15]. In some papers customer satisfaction is defined as customer emotional and affective responses. For example, it has been stated that customer satisfaction is the result of positive or negative emotional responses and cognitive dissonance. Satisfaction or dissatisfaction is determined by the level of difference after comparing expected functions before purchase and the actual function experienced after purchase [5]. It is also stated that satisfaction is a positive emotional response to the result of past experience [43]. In this paper customer satisfaction defines as customer emotional and psychological state after sensory experiences in the store.

2. 5. Customer Loyalty In marketing, loyalty is defined as the intention to perform a diverse set of behaviors that indicate the motivation to maintain relationship with a brand or company [44]. Loyalty can be attributed the attitude of customers who are satisfied by a brand's products or services and use the same products and services continuously and repeatedly [5]. Brand loyalty refers to the consumer willingness to repurchase a brand product [3]. Customers with a high level of loyalty tend to repurchase a particular product or brand or continue to use a particular service or brand over a wide range of times. Loyal customer tends to continue shopping even when the cost or packaging of the product changes, but the non-loyal customer tends to buy other products without the slightest change or even no change. Despite the situational impact and marketing efforts, a loyal customer does not tend to change behavior [45]. In some papers, loyalty is defined as a kind of customer commitment. For example, Thuan et al. [2] defined loyalty as the customer commitment to buy a product or choose a service. Customer loyalty has been expressed as a deep commitment to repurchase a product or service consistently in the future, resulting in repeated purchases from the same brand or set [40]. Customer loyalty is a key goal for strategic market planning and an important basis for developing a sustainable competitive advantage, because it is possible to achieve long-term profits by loyal customers and making meaningful relationships with them [46]. Loyal customers do not think pay more; because they believe comparing brands will never offer unique value that obtain from their loyal brand [47]. Loyal customers tend to pay more money for a particular product or brand. Loyal customers will continue to buy and use the brand as long as they are satisfied with the brand; in addition, a loyal customer tends to pay more for a particular brand because thinks other brands cannot offer the same offers as the brand [4]. Jacoby explored the psychological meaning of loyalty and introduced a concept of brand loyalty that encompasses both behavioral and attitudinal components. Behavioral loyalty is measured by probability of repurchase, probability of long-term choice, or switch in customer

behavior and attitudinal loyalty is defined as brand preference or emotional commitment, therefore measured by repurchase intention, resistance against better options, WOM intention, or price tolerance [48].

In the marketing literature, repeat purchase, preference, commitment, and allegiance used as alternatives to loyalty [49]. Ong et al. [21] defined loyalty based on three indicators of willingness to pay more, WOM, and repurchase intention. Customer loyalty is considered as the most important metric for developing marketing strategies, and refers to continued consumer patronage for a particular brand. In this paper customer loyalty is defined as the result of customer satisfaction and is operationalized based on the three components of shop non-change, price sensitivity, and repurchase intention.

Due to the importance of customer loyalty in marketing, a lot of research has been done in this scope. In most of which satisfaction has been mentioned as the most important factor affecting customer loyalty. What matters in marketing science is how to build loyalty and create positive WOM among customers. Research in this field has examined the impact of various variables as a key factor of loyalty and subsequently positive WOM in customers, such as service quality, product price, employee attitudes, brand image, product diversity, and etc. But the impact of customer sensory experience on customer WOM intention has not been extensively explored in past research. In addition, it is rare to study this topic in retail chain stores environment. Therefore, the purpose of this paper is to investigate the effect of customer sensory experience on WOM intention by considering customer emotions as a mediator.

3. RESEARCH MODEL AND HYPOTHESES

3. 1. Relationships between Sensory Experience and Emotions

The influence of customer sensory experience from surrounding environment as an external stimulus on customer emotions has been studied in some papers. Studies conducted at some Starbucks coffeehouses in Taiwan found that customer sensory experience has direct and significant effect on customer positive and negative emotions, also became clear in this research that the taste experience has the most influence on customer positive emotions among the five sensory experiences [6]. In restaurants, the service scape (such as facility aesthetics, layout, electric equipment, seating comfort, and ambient conditions) directly and positively affects customer pleasure-feeling [19]. It was also found in another study, that in the restaurant environment, atmospherics and service quality as external stimuli increase customer positive emotions, and product quality decrease customer negative emotions [17]. Liu and Jang [18] concluded that dining atmospherics (such as interior

design, ambience, spatial layout, and human elements) as external stimuli directly and significantly affect customer positive and negative emotions and customer perceived value. Studying the influence of sensory experience on customer emotions is not limited to restaurants and coffeehouses, Iglesias et al. [10] found that sensory experience directly and positively influences customer affective commitment in a service business environment such as bank industry. In the research that conducted in three markets such as laptops, sneakers, and cars; stated that sensory experience positively and significantly affects customer affective commitment [50]. In the university environment, the space design style has an active role in the affective experience of students [51]. In addition, the impact of sensory experience on emotions has been studied in the digital environments; for example, Ha and Im [15] stated that the website design as a visual stimulus has a positive and direct effect on the customer emotions in an online shopping website. Therefore, the following hypotheses are proposed:

H1: Customer sensory experience has a positive and direct effect on customer positive emotions.

H2: Customer sensory experience has a negative and direct effect on customer negative emotions.

3. 2. Relationships between Emotions and Satisfaction

The direct effect of customer emotions on customer satisfaction has not been studied in many papers. Terblanche [1] stated that customer in-shop emotions as one of the subsets of shopping experience have a strong and significant relationship with customer satisfaction in the supermarket environment. According to Lin and Liang [34] that examined the effect of physical and social environment on customer emotions, satisfaction, and behavioral intentions; both environments affect customer emotion, satisfaction, and subsequently their behavioral intentions. Moreover, Lin and Liang [34] stated customer emotion directly and positively affect customer satisfaction in both environments. In the coffee shop environment, two affective drives of pleasure and arousal that induced by cognitive drives have positive and significant effect on brand satisfaction, while the effect of pleasure is stronger than arousal [16]. Ha and Im [15] found that the pleasure and arousal of the website design quality have positive and significant effect on customer satisfaction in an online shopping context. Therefore, the following hypotheses are proposed:

H3: Customer positive emotions have a positive and direct effect on customer satisfaction.

H4: Customer negative emotions have a negative and direct effect on customer satisfaction.

3. 3. Relationships between Sensory Experience and Three Behavioral Responses (Satisfaction, Loyalty, and WOM)

Numerous studies have been

conducted to investigate the effect of brand experience on customer satisfaction, customer loyalty, and to some extent on customer WOM; but the effect of customer sensory experience as a separate construct on these three variables less studied in the previous papers. For example, in a study on customers of four brands such as Apple, Coca-Cola, Nike, and PlayStation, it was found that sensory experience directly and positively affects customer satisfaction, trust, and loyalty [4]. Brakus et al. [7] found that brand sensory experience as one of the subsets of brand experience directly influences brand satisfaction and loyalty, they also stated that brand sensory experience indirectly influences brand loyalty through brand satisfaction as a mediator variable. Similarly, Kim et al. [5] found that in shopping malls, brand sensory experience as one of the subsets of brand experience directly influences brand satisfaction and loyalty, and indirectly influences brand loyalty through brand satisfaction. According to Sahin et al. [49] regarding the impact of brand experience on brand satisfaction, trust, and loyalty in several global brands, it was stated that brand experience directly and positively affects brand satisfaction, trust, and loyalty. In addition, it was specified that brand experience indirectly affects brand loyalty through two separate path with two mediators, namely satisfaction and trust (satisfaction is a better mediator than trust). In studies that conducted in several US coffee shops, specified that brand sensory experience as a subset of brand experience indirectly affects brand satisfaction, trust, and attitudinal loyalty through brand prestige as a mediator variable. It was also specified that attitudinal loyalty directly and significantly affects behavioral loyalty [3]. In the three categories of laptop, sneakers, and cars markets, brand sensory experience as a subset of brand experience directly (and indirectly through affective commitment) affects brand loyalty [50]. Ong et al. [19] in studies that explored the impact of brand experience on customer loyalty with three dimensions such as willingness to pay more, WOM, and repurchase intentions in restaurant industry, found that brand sensory experience has a significant and positive effect on customer willingness to pay more and repurchase intentions, but doesn't have significant effect on WOM. According to Mukerjee [29], brand sensory experience directly and positively affects customer loyalty and WOM, and indirectly affects customer WOM through customer loyalty in the banking industry.

In addition, some research has been conducted on the impact of customer sensory experience separately, as well as the impact of the environment and interior design as a sensory stimulus on customer satisfaction, loyalty, and WOM. For example, it was clarified that in the banking industry, brand sensory experience has a direct and positive influence on customer satisfaction, and satisfaction plays a mediating role in the influence of brand sensory experience on brand equity [10].

Elsewhere, it was stated the sensory experience has a direct and positive effect on customer satisfaction, and has an indirect effect through this mediator on customer loyalty in the supermarket environment [2]. In addition, it has been stated that internal shop environment as a sensory stimulus has a significant and positive effect on customer satisfaction in supermarkets [1]. In hotels, the room design as a visual stimulus has a direct and positive effect on customer satisfaction and has an indirect effect on customer WOM through customer satisfaction variable [14]. Moreover, the results of an experimental study clarified that store design and store novelty influence brand loyalty in retail fashion stores [52]. In addition to physical environments, website design as an external stimulus indirectly affects customer satisfaction and WOM intention through customer emotions and perceived quality of information [16]. Therefore, the following hypotheses are proposed:

H5: Customer sensory experience has a positive and direct effect on customer satisfaction.

H6: Customer sensory experience has a positive and direct effect on customer loyalty.

H7: Customer sensory experience has a positive and direct effect on customer WOM intention.

3. 4. Relationships between Satisfaction, Loyalty, and WOM

A lot of research has been done to investigate the relationships between customer satisfaction, loyalty, and WOM intention. For example, Baser et al. [4] found that satisfaction and trust from customer brand experience, positively and significantly affect customer loyalty. A study conducted at several US coffee shops found that customer satisfaction has a direct and positive effect on attitudinal and behavioral loyalty, as well as an indirect effect through attitudinal loyalty on behavioral loyalty [3]. According to Han et al. [16] regarding the process of customer loyalty generation by studying a case in a chain coffee shops in South Korea, it was found that customer satisfaction directly and indirectly affects customer loyalty. Another study also found that in social media, customer loyalty affected by customer satisfaction and behavioral intentions. Studies of several global brands have specified that satisfaction and trust from brand experience have positive effect on brand loyalty [49]. In the tourism industry, customer satisfaction directly and indirectly through affective commitment influences customer loyalty [40]. In a research conducted in five Asian countries, it was found that in all five countries, service quality has a positive and significant effect on customer satisfaction, which in turn leads to loyalty and customer happiness [53]. Some other research has also confirmed the direct and positive effect of customer satisfaction and brand satisfaction on customer loyalty [2, 5, 7].

In addition to the relationship between customer satisfaction and loyalty, some papers have examined the

impact of either or both of these variables on customer WOM. For example, based on a meta-analytic review, De Matos and Rossi [31] found that customer satisfaction and loyalty have a strong and significant effect on customer WOM activity. In addition, they found that satisfaction has stronger relationship with positive WOM than loyalty, whereas disloyalty has stronger relationship with negative WOM than dissatisfaction. A survey of eight categories of different service businesses, specified that customer loyalty directly and positively affects customer positive WOM [23]. Choi and Kandampully [14] stated that customer satisfaction has a positive correlation with customer WOM behavior. In addition, Mukerjee [29] stated that in the banking industry, brand loyalty directly and significantly influences customer WOM recommendations. In online shopping websites, customer satisfaction directly and positively influences customer WOM intention [15]. Therefore, the following hypotheses are proposed:

H8: Customer satisfaction has a positive and direct effect on customer loyalty.

H9: Customer satisfaction has a positive and direct effect on customer WOM intention.

H10: Customer loyalty has a positive and direct effect on customer WOM intention.

The proposed conceptual model, based on the S-O-R model, consists of three parts: external stimuli (sensory experience), mediating organism (emotions), and behavioral responses (satisfaction, loyalty, and WOM). The model consists of ten hypotheses that examine the relationships between six variables, which described in the previous section. The proposed conceptual model is shown in Figure 1. According to this model, the independent variable is customer sensory experience; the mediating variables are customer positive and negative emotions, satisfaction, and loyalty; and the dependent variables are customer satisfaction, loyalty, and WOM intention.

4. RESEARCH METHOD AND RESULTS

4. 1. Questionnaire Development

The final questionnaire consisted of 6 primary questions about demographic characteristics and then 30 questions about research conceptual model variables. Most of these

questions were selected based on previous studies related to the subject of research and some of them were slightly modified according to society condition, country culture and environment of study in order to be tangible and acceptable for respondents (See Appendix Table A for list of constructs and items used in the questionnaire). The answers of conceptual model questions were collected by a Likert’s 7-point scale and analyzed by SmartPLS software.

4. 2. Samples and Data Collection

Since we have used a quantitative approach to investigate the effect of customer sensory experience on customer WOM intention in this study, Samples randomly selected from customers of three branches of ETKA chain stores in Tehran. A Pilot study conducted on a population of 25 store managers, staff and customers to identify possible defects through feedback and suggestions, and improve the questionnaire. After passing this stage, according to the achieved results, four questions that reduced the validity and reliability of the research deleted. After that, 320 questionnaires (in Farsi language) provided to customers of these three branches. Questionnaires completed by direct interview and personal answering.

From 320 distributed questionnaires, 306 completed questionnaires returned to the researchers. In a few of these questionnaires, there were one, two or three unanswered questions. In order to fix this defect, the average of the total answers given to the same question, replaced for that item. According to Table 2, the mean of all constructs except the construct of negative emotions was higher than the median (4.240 to 4.837). This is due to the negative nature of questions of negative emotions section. The standard deviation of all constructs is from 1.172 to 1.521, which represents a narrow band around the mean. In addition, the skewness and kurtosis values of the constructs, which are the criteria for measuring the data normality, are in the range of (-0.670, 0.209) and (-0.197, 0.518), respectively. Data is normal when the skewness and kurtosis values are in the range of (-1, 1) [54], therefore this condition is confirmed in this study.

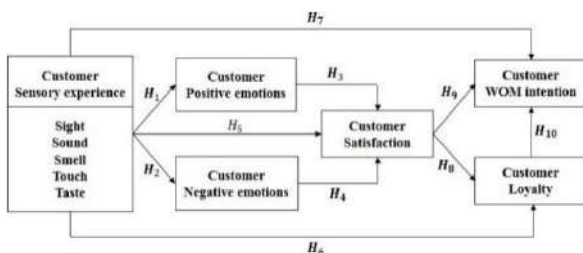


Figure 1. Research conceptual model

TABLE 2. Descriptive statistics

Construct	Mean	Standard deviation	Variance	Skewness	Kurtosis
Sensory experience	4.763	1.250	1.577	-0.368	0.518
Positive emotions	4.765	1.172	1.375	-0.254	0.313
Negative emotions	2.769	1.180	1.400	0.209	-0.082
Satisfaction	4.837	1.311	1.720	-0.670	0.515
Loyalty	4.240	1.521	2.332	-0.179	-0.197
WOM intention	7.758	1.328	1.767	-0.439	0.278

Table 3 shows different values for mean, standard deviation, variance, skewness coefficient and kurtosis.

4. 3. Respondent Profile

Among 306 respondents, 65.36% are male and 34.64% are female. 18.95% are single and 81.05% are married. Approximately the age of 66% are in the range of 30 to 49 years, from the rest of the respondents, approximately 18% are less than 30 years old and 16% are 50 years or older. In addition, many have a college or university education (77.78%). It is necessary to mention that 67.32% live in a family of three or four, 16.67% live in a family of two, 11.67% live in a family of five or six and

4.25% live alone or in families with more than six members. Family monthly expenditure of 18.63% are under two million tomans, 35.62% are between two and three million, 34.31% are between three and five million, 7.52% are between five and seven million and the rest are more than seven million tomans. All demographic statistics are shown in Table 3.

4. 4. Data Analysis

As mentioned earlier, structural equation modeling approach has been used in this research. According to Hsu et al. [55], there are two different approaches to analysis in structural equation modeling: Covariance-based and variance-based. In this research, we used partial least squares method, due to the accuracy and appropriateness of the variance-based approach in small-scale cases and predictive purposes [54]. According to Hair et al. [56], partial least square analysis consists of two parts: measurement model (outer model) and structural model (inner model). The measurement model examines the quality of all constructs for evaluating validity and reliability, and the structural model examines the relationships between different model constructs for hypothesis analysis [56].

4. 4. 1. Measurement Model Analysis (Outer Model)

According to the model analysis algorithm in PLS method, two main criteria of reliability and validity have to examine for outer model evaluation. Cronbach's alpha, factor loadings, and composite reliability (CR) are the criteria for measuring reliability. In addition, average variance extracted (AVE) and composite reliability calculated as convergent validity criteria, and the Fornell-Larcker criterion and HTMT ratio of correlation computed to assess discriminant validity [57] (Tables 4-6). The version 3.2.6 of SmartPLS software used to calculate Cronbach's alpha, factor loadings, and composite reliability. According to Bagozzi and Yi [58] the factor loading of each indicator should be greater than 0.5. Based on Table 5, the factor loadings obtained in this research are above 0.5 (Three indicators above 0.6 and others above 0.7). The value of Cronbach's alpha coefficient can be between 0 and 1 and how much is closer to 1, shows higher internal consistency [59]. According to Moazanzadeh and Hamidi [60], the acceptable value of alpha coefficient in exploratory research is 0.7 or more. Based on Table 5, the alpha coefficients obtained in this research are above 0.7. The third step to assess reliability is to calculate composite reliability. The minimum accepted value for composite reliability is 0.7 [61]. Based on Table 5, the composite reliability of all constructs are higher than 0.7.

According to Fornell and Larcker [62], the AVE value for each construct should be greater than 0.5, in addition Hamidi and Chavoshi [63] believe that to confirm convergent validity, the CR value should be greater than AVE. In this study, the AVE of all structures

TABLE 3. Demographic profile of respondents

Characteristics	Range	Number	%
Gender	Male	200	65.36
	Female	106	34.64
Age	<18	2	0.65
	18-29	53	17.32
	30-39	121	39.54
	40-49	82	26.80
	50-59	31	10.13
	>60	17	5.56
Marital status	Single	58	18.95
	Married	248	81.05
Level of education	Under high school diploma	9	2.94
	High school diploma	59	19.28
	Associate degree	40	13.07
	Bachelor of Science degree	118	38.56
	Master of science degree	64	20.92
	Doctor of Philosophy degree	16	5.23
Number of family member	1	10	3.27
	2	51	16.67
	3 or 4	206	67.32
	5 or 6	36	11.76
	≥ 7	3	0.98
	<2	57	18.63
Family monthly expenditure (million tomans)	2-3	109	35.62
	3-5	105	34.31
	5-7	23	7.52
	>7	12	3.92

is greater than 0.5 and the CR of each construct is greater than the AVE of the same construct. The results of convergent reliability and validity calculation are shown in Table 5. Based on these results, it can be concluded that convergent validity and reliability have been confirmed.

After examining the convergent validity, we assessed the discriminant validity using heterotrait-monotrait (HTMT) ratio of correlation and Fornell-Larcker criterion. Version 3.2.6 of SmartPLS software has been used for this purpose. The Fornell-Larcker method evaluates discriminant validity at the latent variables

TABLE 4. Descriptive, reliability and convergent validity

Construct	Indicator	F. loading	α	CR	AVE
Sensory experience	SEV.1	0.817	0.901	0.917	0.503
	SEV.2	0.747			
	SEV.3	0.764			
	SEA.1	0.667			
	SEA.2	0.687			
	SES.1	0.732			
	SES.2	0.766			
	SES.3	0.742			
	SETO.1	0.619			
	SETO.2	0.657			
Positive emotions	SETA.1	0.683	0.940	0.955	0.808
	PE.1	0.865			
	PE.2	0.926			
	PE.3	0.936			
	PE.4	0.889			
Negative emotions	PE.5	0.877	0.941	0.955	0.809
	NE.1	0.848			
	NE.2	0.922			
	NE.3	0.951			
	NE.4	0.916			
Satisfaction	NE.5	0.856	0.916	0.947	0.855
	SA.1	0.913			
	SA.2	0.929			
Loyalty	SA.3	0.933	0.854	0.911	0.774
	LO.1	0.925			
	LO.2	0.776			
WOM intention	LO.3	0.930	0.958	0.973	0.923
	WOM.1	0.947			
	WOM.2	0.970			
	WOM.3	0.966			

level [64]. This method compares the square root of AVE with the correlation of latent variables and states that the square root of each construct's AVE should be greater than the correlations with other latent variables [64]. Based on Table 5, in this research the square root of each construct's AVE is greater than the correlations with other latent variables. HTMT is able to achieve higher specificity and sensitivity rates compared to the Fornell-Larcker [64]. If all ratios in the HTMT matrix are less than 0.9, the discriminant validity of measurement model is confirmed. HTMT values close to 1, indicates a lack of discriminant validity [64]. Based on Table 6, all ratios in the HTMT matrix are less than 0.9.

4. 4. 2. Structural Model Analysis (Inner Model)

The structural model describes the relationship between latent variables. According to Malekinezhad and Bin [65], in evaluation of structural model, β (path coefficient), R^2 (determination coefficient), f^2 (effect size) and Q^2 (predictive relevance) should be calculated. In this research, all criteria were calculated using version 3.2.6 of SmartPLS software.

Table 7 shows the path coefficients (β) between the constructs in the conceptual model. The path coefficient indicates the existence of a relationship, intensity, and direction of the relationship between two latent variables.

TABLE 5. Discriminant validity, Fornell-Larcker criterion

	1	2	3	4	5	6
Loyalty	0.880					
Negative emotions	-0.538	0.900				
Positive emotions	0.723	-	0.899			
Satisfaction	0.762	-	0.610	0.925		
Sensory experience	0.651	-	0.684	0.673	0.709	
WOM intention	0.819	-	0.738	0.786	0.649	0.961

TABLE 6. Discriminant validity, Heterotrait-Monotrait Ratio

	1	2	3	4	5	6
Loyalty						
Negative emotions	0.577					
Positive emotions	0.790	0.674				
Satisfaction	0.840	0.655	0.835			
Sensory experience	0.721	0.533	0.729	0.719		
WOM intention	0.888	0.620	0.777	0.683	0.683	

TABLE 7. Structural model’s hypotheses

NO.	Hypothesis	Path coefficient	t-value	p-value	Supported
1	SE->PE	0.684	18.666	0.000	Yes
2	SE->NE	-0.500	9.502	0.000	Yes
3	PE->SA	0.502	8.496	0.000	Yes
4	NE->SA	-0.169	3.751	0.000	Yes
5	SE->SA	0.245	4.261	0.000	Yes
6	SE->LO	0.252	4.477	0.000	Yes
7	SE->WOM	0.095	2.031	0.043	Yes
8	SA->LO	0.593	10.949	0.000	Yes
9	SA->WOM	0.347	5.307	0.000	Yes
10	LO->WOM	0.492	8.428	0.000	Yes

We used bootstrapping method by version 3.2.6 of SmartPLS software to analyze path correlations. As shown in Table 7, all t-statistics pass from ±1.96 and all p-values are less than 0.05, so according to Zare et al. [66], all research hypotheses are confirmed.

From the path analysis, it can be stated that the sensory experience has a direct and positive effect on customer positive emotions with significant β value of 0.684 (t = 18.666 >1.96, p <0.001), thus the H1 hypothesis is supported. It was also found that the sensory experience has a direct and negative effect on customer negative emotions with significant β value of -0.500 (t = 9.502 >1.96, p <0.001), thus the H2 hypothesis is supported. Customer positive emotions have a direct and positive effect on customer satisfaction with significant β value of 0.502 (t = 8.496 >1.96, p <0.001) and customer negative emotions have a direct and negative effect on customer satisfaction with significant β value of -0.169 (t = 3.751 >1.96, p <0.001), thus the H3 and H4 hypotheses are supported. From the results it can be deduced that the sensory experience has a direct and positive effect on customer satisfaction with significant β value of 0.245 (t = 4.261 >1.96, p <0.001), hence H5 hypothesis is supported. In addition, this construct has direct and positive effect on customer loyalty and customer WOM intention with significant β value of 0.252 (t = 4.477 >1.96, p <0.001) and 0.095 (t = 2.031 >1.96, p <0.05), respectively, thus the H6 and H7 hypotheses are supported. Moreover, it was specified that customer satisfaction has direct and positive effect on customer loyalty and customer WOM intention with significant β value of 0.593 (t = 10.949 >1.96, p <0.001) and 0.347 (t = 5.307 >1.96, p <0.001), respectively, thus the H8 and H9 hypotheses are supported. In addition, It can be deduced from the results that customer loyalty has a direct and positive effect on customer WOM intention with significant β value of 0.492 (t = 8.428 >1.96, p <0.001), thus the H10 hypothesis is supported.

The R^2 value is a criterion used to connect the measurement and structural components of structural equation modeling and indicates the influence of an independent variable on a dependent variable. The value of R^2 is between 0 and 1, and the higher the R^2 , the better the independent variable predicts for the dependent variable [67]. The values of 0.75, 0.5 and 0.25 for R^2 indicate respectively that the model is substantial, moderate and weak [67]. In addition, the values of R^2 larger than 0.35 represent a substantial model. According to Figure 2, the model is approximately substantial.

After evaluating hypotheses, the effect of each independent variable on dependent variables should be calculated. We can measure the of an independent variable on a dependent variable by f^2 criterion [67]. The values of 0.02, 0.15 and 0.35, indicate small, medium and large effect size. According to Table 8, there are three variables with medium effect size and three variables with large effect size in model.

Q^2 criterion indicates the predictive relationships of model. We calculated Q^2 by blindfolding process of SmartPLS. If the value of Q^2 is greater than zero, the dependent variable has predictive relevance [56]. According to Hair et al. [56], the three values of 0.02, 0.15 and 0.35 are considered as low, medium and high predictive relevance. As shown in Table 9, all predictive relationships are high except one, that is medium.

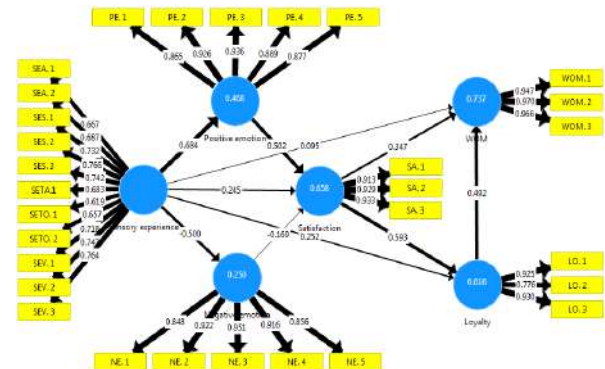


Figure 2. Obtained values of β and R^2 through SmartPLS

TABLE 8. Effect size of independent variables

	1	2	3	4	5	6
Loyalty						0.354
Negative emotions				0.049		
Positive emotions				0.308		
Satisfaction	0.501					0.167
Sensory experience	0.091	0.333	0.879	0.092		0.017
WOM intention						

TABLE 9. Indicator of model's predictive relevance

Dependent variable	Q ²
Positive emotions	0.352
Negative emotions	0.187
Satisfaction	0.528
Loyalty	0.445
WOM intention	0.641

4. 4. 3. Mediating Effect Analysis

The indirect effect is examined in paths that exist one or more mediator variables. In the following, the effect of positive emotions, negative emotions, and loyalty as partial mediator variables are examined. According to Baron and Kenny [68] the existence of a partial mediator variable is confirmed: if the total effect is significant (The sum of direct and indirect effects), the indirect effect is significant (from independent variable to mediator and from mediator to dependent variable), and the direct effect is significantly less than the total effect.

We used regression analysis to examine how customer sensory experience affects customer satisfaction through two mediator variables of customer positive and negative emotions and how customer satisfaction affects customer WOM intention through customer loyalty as a mediator variable. According to Baron and Kenny [68] and as shown in Table 10, the existence of three partial mediator variables: customer positive emotions, customer negative emotions and

TABLE 10. verification of mediators

NO.	Hypothesis	Path coefficient	Standard deviation	t-value	p-value
Sensory experience->Positive emotion->Satisfaction					
1*	SE->SA	0.676	0.031	21.543	0.000
2	SE->PE	0.685	0.034	20.016	0.000
3	PE->SA	0.590	0.050	11.708	0.000
4**	SE->SA	0.272	0.055	4.912	0.000
Sensory experience->Negative emotion->Satisfaction					
1*	SE->SA	0.678	0.032	21.363	0.000
2	SE->NE	-0.503	0.050	10.085	0.000
3	NE->SA	-0.359	0.048	7.473	0.000
4**	SE->SA	0.497	0.048	10.424	0.000
Satisfaction->Loyalty->WOM					
1*	SA->WOM	0.787	0.028	28.508	0.000
2	SA->LO	0.764	0.026	29.599	0.000
3	LO->WOM	0.524	0.055	9.555	0.000
4**	SA->WOM	0.387	0.061	6.344	0.000

*Total effect, **Direct effect

customer loyalty confirmed. Thus, it is clarified that sensory experience has indirect effect on customer satisfaction through customer positive and negative emotions, and customer satisfaction has an indirect effect on customer WOM intention through customer loyalty. It can be deduced that positive sensory experience promote positive emotions and relieve negative emotions, leading to customer satisfaction. Moreover, it can be deduced that satisfaction strengthens customer WOM intention through customer loyalty. Therefore, sensory experience is a strong and critical antecedent of three customer behavioral responses, especially customer WOM, and focus on this aspect can help retail businesses owner to improve his/her business.

4. 4. 4. Effect of Five Types of Customer Sensory Experiences on Customer Emotions

According to Chen and Lin [6], we used regression analysis to examine the effect of five types of customer sensory experiences on customer positive and negative emotions. Each of these effects will discuss below.

4. 4. 4. 1. Effect on Customer Positive Emotions

In this regression analysis, sensory experiences have been considered as independent variables and positive emotions as dependent variable. As shown in Table 11, all VIF values are less than 2.5, indicating no notable collinearity in the regression model. The regression model is highly significant with the determination coefficient of 52.7%. According to Table 11, the greatest effect of sensory experience on customer positive emotions is taste experience, and subsequently touch, sight, and sound experiences, respectively. It should be noted that the effect of smell experience on positive emotions is not significant.

4. 4. 4. 2. Effect on Customer Negative Emotions

Similarly, we considered sensory experiences as independent variables and positive emotions as dependent variable. As shown in Table 12, all VIF values are less than 2.5, indicating no notable collinearity in the regression model. The regression model is highly significant with the determination coefficient of 29.6%. According to Table 12, only the effect of touch and taste

TABLE 11. regression analysis of five types of sensory experience on positive emotions

Sensory experience	β	t-value	p-value	R ²	VIF
Sight	0.134	2.053	0.041		1.998
Sound	0.134	2.058	0.038		2.360
Smell	0.062	0.942	0.347	0.527	2.453
Touch	0.193	3.600	0.000		1.798
Taste	0.386	7.019	0.000		1.542

TABLE 12. regression analysis of five types of sensory experience on negative emotions

Sensory experience	β	t-value	p-value	R^2	VIF
Sight	-0.041	0.579	0.563		1.979
Sound	-0.114	1.328	0.185		2.337
Smell	-0.023	0.245	0.806	0.296	2.449
Touch	-0.248	3.874	0.000		1.765
Taste	-0.251	3.814	0.000		1.547

experiences on customer negative emotions are significant, while the effect of taste on customer negative emotions is slightly greater than the effect of touch experience.

5. DISCUSSION AND CONCLUSIONS

As mentioned earlier, the purpose of this study is to examine the effect of sensory experience on customer WOM intention in retail chain stores. Structural equation modeling (SEM) and questionnaire have been used to achieve this purpose. Version 3.2.6 of SmartPLS software used to test the hypotheses and calculate path coefficients. We describe the research findings below, and then the results related to the effect of sensory experience on customer emotions in the retail chain stores is compared with similar results obtained in the chain coffeehouses by Chen and Lin [6]. In the last part, the conclusions of this research will be express.

5. 1. Findings Related to Customer Sensory Experience

According to the path analysis carried out in section four of the paper, hypothesis 1 (SE-> PE) and hypothesis 2 (SE-> NE) are confirmed, which indicates that, sensory experience in the retail chain stores directly and significantly affects customer positive and negative emotions. These results are supported by the results of Chen and Lin [6] in coffeehouses, and Liu and Jang [18] in restaurant environments. According to the path analysis, hypothesis 5 (SE-> SA) is confirmed, which shows the direct and positive effect of customer sensory experience on customer satisfaction. This result is supported by the results of Iglesias et al. [10] in banking industry and Thuan et al. [2] in supermarket environments. In addition, it was found that sensory experience indirectly affects customer satisfaction through partial mediators of customer positive emotions and customer negative emotions. According to Variance Accounted For (VAF) proposed by Zhao et al. [69], and path coefficients, over 51% ($0.684 \times 0.502 / 0.673$) of the total effect of sensory experience on customer satisfaction is transmitted through customer positive emotions, and approximately 13% ($-0.500 \times -0.169 / 0.673$)

of the total effect of sensory experience on customer satisfaction is transmitted through customer negative emotions (so approximately 64% of the total effect is transmitted through customer emotions), and the rest of the total effect is transmitted directly. Finally based on the path coefficients and VAF, it can be concluded that customer positive emotions mediator is better than customer negative emotions mediator, and the major effect of customer sensory experience on customer satisfaction is transmitted indirectly through customer positive emotions. The path analysis also shows that hypothesis 6 (SE-> LO) and hypothesis 7 (SE-> WOM) are confirmed, that reflect the direct and positive effect of customer sensory experience on customer loyalty and customer WOM intention. Due to the calculated path coefficients, it can be stated that, the direct effect of sensory experience on customer loyalty is considerable, but the direct effect of sensory experience on customer WOM intention is not very considerable, and much of the total effect (with coefficient of 0.649) is transmitted indirectly through available mediators on the path, such as emotions, satisfaction and loyalty. According to VAF and path coefficients, it can be concluded that approximately 85.5% of the total effect of sensory experience on customer WOM intention is transmitted indirectly, that is described separately below:

- 18.5% of the total effect is transmitted through the path of sensory experience-> positive emotions-> satisfaction-> WOM ($0.684 \times 0.502 \times 0.347 / 0.649$).
- 15.5% of the total effect is transmitted through the path of sensory experience-> positive emotions-> satisfaction-> loyalty-> WOM intention ($0.684 \times 0.502 \times 0.593 \times 0.492 / 0.649$).
- 4.5% of the total effect is transmitted through the path of sensory experience-> negative emotions-> satisfaction-> WOM intention ($-0.500 \times -0.169 \times 0.347 / 0.649$).
- 4% of the total effect is transmitted through the path of sensory experience-> negative emotions-> satisfaction-> loyalty-> WOM intention ($-0.500 \times -0.169 \times 0.593 \times 0.492 / 0.649$).
- 13% of the total effect, is transmitted through the path of sensory experience-> satisfaction-> WOM intention ($0.245 \times 0.347 / 0.649$).
- 11% of the total effect is transmitted through the path of sensory experience-> satisfaction-> loyalty-> WOM intention ($0.245 \times 0.593 \times 0.492 / 0.649$).
- 19% of the total effect is transmitted through the path of sensory experience-> loyalty-> WOM intention ($0.252 \times 0.492 / 0.649$).

5. 2. Findings Related to Customer Satisfaction, Loyalty and WOM Intention

According to the path analysis carried out in section four, Hypothesis 8 (satisfaction-> loyalty) and Hypothesis 9 (satisfaction-> WOM intention) are confirmed, which indicates that

customer satisfaction in the retail chain stores directly and positively affects customer loyalty and WOM intention. The positive effect of customer satisfaction on customer loyalty is similar to the results of Choi et al. [3], Baser et al. [4], Brakus et al. [7], Han et al. [16], Richard and Zhang [40], LV et al. [46], and Gong and Yi [53] in different businesses. In addition, the positive effect of customer satisfaction on customer WOM intention is similar to the results of Choi and Kandampully [14], Ha and Im [15], and De Matos and Rossi [31]. Based on the calculated path coefficients, it can be concluded that both effects are significant, but the direct effect of customer satisfaction on customer loyalty is greater than the direct effect of customer satisfaction on customer WOM intention, which is justified by considering the mediating role of customer loyalty in the indirect effect of customer satisfaction on customer WOM intention. In addition, according to the path analysis Hypothesis 10 (loyalty->WOM intention) is confirmed, indicating a direct and positive effect of customer loyalty on customer WOM intention. This result is supported by the results of Markovic et al. [23], Mukerjee [29], and De Matos and Rossi [31]. Based on the results, it can be inferred that customer loyalty is a partial mediator in the relationship between customer satisfaction and customer WOM intention; according to the concept of VAF, it can be concluded that approximately 46% ($0.593 \times 0.492 / 0.639$) of the total effect of customer satisfaction on customer WOM intention is transmitted through the customer loyalty. In general, it can be stated that satisfaction affects customer loyalty and this loyalty will lead to customer WOM intention.

5. 3. Comparison of The Effect of Sensory Experiences on Customer Emotions in Two Different Environments

In this section, we compare the regression analysis performed in this study with the similar regression analysis performed by Chen and Lin [6]. According to Table 13, in this study, all VIF values (variance inflation factor) are less than 2.5, which is similar to study of Chen and Lin [6]. In addition, the value of R^2 obtained in both studies are approximately equal. Based on the results of this analysis, and similar to study of Chen and Lin [6], the effect of smell experience on positive emotions is not significant but the effects of the other four senses on positive emotions are significant. In both studies, taste experience has the most effect on positive emotions, but unlike result of Chen and Lin [6], touch experience has more effect on positive emotion than the other two senses. In addition, it is specified that in this study, the effects of sight and sound experiences on positive emotions are approximately equal, that is not the case in Chen and Lin [6]. The differences in the effect of five type of sensory experiences on positive emotions between two different environments of retail chain stores and chain coffeehouses are shown in Table 13.

TABLE 13. Comparison of two different environments (PE)

Proposed model				
Sensory experience	β	t-value	R^2	VIF
Sight	0.134	2.053*		1.998
Sound	0.134	2.058*		2.360
Smell	0.062	0.942	0.527	2.453
Touch	0.193	3.600***		1.798
Taste	0.386	7.019***		1.542
Chen and Lin [6] model				
Sensory experience	β	t-value	R^2	VIF
Sight	0.284	6.798***		2.065
Sound	0.134	3.494**		1.741
Smell	0.055	1.390	0.524	1.846
Touch	0.111	2.566*		2.212
Taste	0.298	7.469***		1.887

Significance levels: * $p < 0.05$, ** $p < 0.01$, *** $p < 0.001$

Similar to the analysis performed in the positive emotions section, in the negative emotions section, all VIF values are less than 2.5, which is similar to the result obtained in Chen and Lin [6] (See Table 14). In this study, the effects of taste and touch experiences on negative emotions are significant and approximately equal, but in the research of Chen and Lin [6], only the effect of sight experience on negative emotions is significant. In addition, the regression analysis performed in this study revealed that the R^2 value of customer negative emotions is approximately three times the R^2 value of customer negative emotions in the regression analysis performed by Chen and Lin [6].

Regression analysis suggests that among the five senses related to the customer sensory experience, the sense of taste has the most effect on positive emotions. After that, touch has the most effect on positive emotions. Sight and sound are the next. From these results, it can be inferred that the taste and quality of food products sold in retail chain stores have the greatest effect on positive emotions. Moreover, the feature that customers in the retail chain stores can touch goods before buying, as well as the condition of ventilation and temperature of the store have the greatest effect on the positive emotions after taste and quality of food products. Sight experience that affects the sense of vision, such as the lighting, cleanliness of the store and the layout of products, and sound experience that affects the sense of auditory, such as music playing or annoying sounds in the store, have less effect on positive emotions than taste and touch experiences. In addition, according to regression analysis, it can be stated that like positive emotions, the

TABLE 14. Comparison of two different environments (NE)

Proposed model				
Sensory experience	β	t-value	R^2	VIF
Sight	-0.041	0.579		1.979
Sound	-0.114	1.328		2.337
Smell	-0.023	0.245	0.296	2.449
Touch	-0.248	3.874***		1.765
Taste	-0.251	3.814***		1.547
Chen and Lin [6] model				
Sensory experience	β	t-value	R^2	VIF
Sight	-0.269	-4.703***		2.065
Sound	0.009	0.180		1.741
Smell	-0.069	-1.281	0.106	1.846
Touch	0.039	0.662		2.212
Taste	0.066	-1.215		1.887

Significance levels: * $p < 0.05$, ** $p < 0.01$, *** $p < 0.001$

sense of taste has the most effect on negative emotions and the sense of touch is next. It means that the good taste and high quality of food products will reduce the negative emotions more than desirable touch of goods before buying or favorable temperature and ventilation of the store.

6. CONCLUSIONS

In this research, it is concluded that among the three constructs related to customer behavioral responses namely satisfaction, loyalty, and WOM intention; customer satisfaction acts as a strong predictor of customer loyalty and customer WOM intention. In addition, due to the indirect effect of customer sensory experience on customer satisfaction through partial mediators of customer positive and negative emotions, it can be concluded that sensory experience as an external stimulus, affects customer satisfaction as a behavioral response and predictor of two other behavioral responses (loyalty and WOM). Moreover, according to the research findings, it can be concluded that taste and touch experiences have the most effect on customer positive and negative emotions respectively. Smell does not affect either positive or negative emotions, in addition, sight and sound do not affect negative emotions. In general, it can be concluded that engaging five senses of customers as a sensory marketing strategy can affect customer emotions, and consequently, based on the proposed model it can be used as a way to develop customer loyalty programs in retail chain stores and subsequently create positive WOM.

7. LIMITATIONS AND FUTURE RESEARCH

Usually in any research, obstacles and limitations placed on the way to the researchers. This research is not an exception, so the limitations of the research will discuss:

- One of the limitations is the community under study. The focus of this research was on customers of three branches of a retail chain store in Tehran. So due to the differences in culture, attitude, shopping behavior, etc. of the customers under study, compared to the customers of other retail chain stores or even customers of other branches of this store, different results may be obtained. Thus, future research could explore this topic in other retail chain stores.
- The inherent limitations of questionnaire, such as superficial attitude to the actual events and scalability of the responses, could prevent the results from being real. In addition, respondents may answer questions with their own understanding. Because of this issue, newer methods of data collection, such as neuromarketing could be used in future research. Moreover, the total questionnaires distributed for data collection was 320 copies, out of which 306 analyzed. Naturally, increasing the number of questionnaires and consequently increasing the available data can increase the consistency and validity of the results.
- It should note that the present study used only the opinions of customers and did not use the views of business owners and marketers, therefore in future research, researchers can collect other views and compare these results with customer opinions. In addition, it should not overlooked that the moderator variable not used in this study. In general, using moderator variables could provide more comprehensive and accurate results.
- Variables affecting WOM intention include a wide range, that in this study, we sought to investigate the effect of sensory experience on this variable. Future research can examine the effect of other independent variables such as service quality, price, technological facilities, etc., along with sensory experience, and compare these effects with each other.

8. REFERENCES

1. Terblanche, N. S., "Revisiting the supermarket in-store customer shopping experience", *Journal of Retailing and Consumer Services*, Vol. 40, (2018), 48–59. doi:10.1016/j.jretconser.2017.09.004
2. Luu Tien Thuan, Nguyen Huynh Bao Ngoc, and Nguyen Thu Nha Trang, "Does Customer Experience Management Impact Customer Loyalty Shopping at Supermarket? The Case in the Mekong Delta, Vietnam", *Economics World*, Vol. 6, No. 1, (2017), 13–21. doi:10.17265/2328-7144/2018.01.002
3. Choi, Y. G., Ok, C. "Michael", and Hyun, S. S., "Relationships between brand experiences, personality traits, prestige,

- relationship quality, and loyalty", *International Journal of Contemporary Hospitality Management*, Vol. 29, No. 4, (2017), 1185–1202. doi:10.1108/IJCHM-11-2014-0601
4. Başer, İ. U., Cintamür, İ. G., and Arslan, F. M., "Examining the effect of brand experience on consumer satisfaction, brand trust and brand loyalty", *Marmara University Journal of Economic & Administrative Sciences*, Vol. 37, No. 2, (2016), 101–128. doi:10.14780/iibd.51125
 5. Kim, J. W., Lee, F., and Suh, Y. G., "Satisfaction and Loyalty From Shopping Mall Experience and Brand Personality", *Services Marketing Quarterly*, Vol. 36, No. 1, (2015), 62–76. doi:10.1080/15332969.2015.976523
 6. Chen, H.-T., and Lin, Y.-T., "A study of the relationships among sensory experience, emotion, and buying behavior in coffeehouse chains", *Service Business*, Vol. 12, No. 3, (2018), 551–573. doi:10.1007/s11628-017-0354-5
 7. Brakus, J. J., Schmitt, B. H., and Zarantonello, L., "Brand Experience: What is It? How is it Measured? Does it Affect Loyalty?", *Journal of Marketing*, Vol. 73, No. 3, (2009), 52–68. doi:10.1509/jmkg.73.3.052
 8. Hultén, B., "Sensory marketing: the multi-sensory brand-experience concept", *European Business Review*, Vol. 23, No. 3, (2011), 256–273. doi:10.1108/09555341111130245
 9. Krishna, A., "An integrative review of sensory marketing: Engaging the senses to affect perception, judgment and behavior", *Journal of Consumer Psychology*, Vol. 22, No. 3, (2012), 332–351. doi:10.1016/j.jcps.2011.08.003
 10. Iglesias, O., Markovic, S., and Rialp, J., "How does sensory brand experience influence brand equity? Considering the roles of customer satisfaction, customer affective commitment, and employee empathy", *Journal of Business Research*, Vol. 96, (2019), 343–354. doi:10.1016/j.jbusres.2018.05.043
 11. Yoganathan, V., Osburg, V.-S., and Akhtar, P., "Sensory stimulation for sensible consumption: Multisensory marketing for e-tailing of ethical brands", *Journal of Business Research*, Vol. 96, (2019), 386–396. doi:10.1016/j.jbusres.2018.06.005
 12. Moreira, A. C., Fortes, N., and Santiago, R., "Influence of sensory stimuli on brand experience, brand equity and purchase intention", *Journal of Business Economics and Management*, Vol. 18, No. 1, (2017), 68–83. doi:10.3846/16111699.2016.1252793
 13. Mehrabian, A., and Russell, J. A., "The Basic Emotional Impact of Environments", *Perceptual and Motor Skills*, Vol. 38, No. 1, (1974), 283–301. doi:10.2466/pms.1974.38.1.283
 14. Choi, H., and Kandampully, J., "The effect of atmosphere on customer engagement in upscale hotels: An application of S-O-R paradigm", *International Journal of Hospitality Management*, Vol. 77, (2019), 40–50. doi:10.1016/j.ijhm.2018.06.012
 15. Ha, Y., and Im, H., "Role of web site design quality in satisfaction and word of mouth generation", *Journal of Service Management*, Vol. 23, No. 1, (2012), 79–96. doi:10.1108/09564231211208989
 16. Han, H., Nguyen, H. N., Song, H., Chua, B.-L., Lee, S., and Kim, W., "Drivers of brand loyalty in the chain coffee shop industry", *International Journal of Hospitality Management*, Vol. 72, (2018), 86–97. doi:10.1016/j.ijhm.2017.12.011
 17. Jang, S. (Shawn), and Namkung, Y., "Perceived quality, emotions, and behavioral intentions: Application of an extended Mehrabian–Russell model to restaurants", *Journal of Business Research*, Vol. 62, No. 4, (2009), 451–460. doi:10.1016/j.jbusres.2008.01.038
 18. Liu, Y., and Jang, S. (Shawn), "The effects of dining atmospherics: An extended Mehrabian–Russell model", *International Journal of Hospitality Management*, Vol. 28, No. 4, (2009), 494–503. doi:10.1016/j.ijhm.2009.01.002
 19. Kim, W. G., and Moon, Y. J., "Customers' cognitive, emotional, and actionable response to the servicescape: A test of the moderating effect of the restaurant type", *International Journal of Hospitality Management*, Vol. 28, No. 1, (2009), 144–156. doi:10.1016/j.ijhm.2008.06.010
 20. Lindstrom, M., "Broad sensory branding", *Journal of Product & Brand Management*, Vol. 14, No. 2, (2005), 84–87. doi:10.1108/10610420510592554
 21. Ong, C. H., Lee, H. W., and Ramayah, T., "Impact of brand experience on loyalty", *Journal of Hospitality Marketing & Management*, Vol. 27, No. 7, (2018), 755–774. doi:10.1080/19368623.2018.1445055
 22. Hultén, B., Broweus, N., and van Dijk, M., "What is Sensory Marketing?", *Sensory Marketing*, London, Palgrave Macmillan UK., (2009), 1–23 doi:10.1057/9780230237049_1
 23. Markovic, S., Iglesias, O., Singh, J. J., and Sierra, V., "How does the Perceived Ethicality of Corporate Services Brands Influence Loyalty and Positive Word-of-Mouth? Analyzing the Roles of Empathy, Affective Commitment, and Perceived Quality", *Journal of Business Ethics*, Vol. 148, No. 4, (2018), 721–740. doi:10.1007/s10551-015-2985-6
 24. Arndt, J., "Role of Product-Related Conversations in the Diffusion of a New Product", *Journal of Marketing Research*, Vol. 4, No. 3, (1967), 291–295. doi:10.1177/002224376700400308
 25. Gupta, P., and Harris, J., "How e-WOM recommendations influence product consideration and quality of choice: A motivation to process information perspective", *Journal of Business Research*, Vol. 63, Nos. 9–10, (2010), 1041–1049. doi:10.1016/j.jbusres.2009.01.015
 26. Kim, Y., Chang, Y., Wong, S. F., and Park, M. C., "Customer attribution of service failure and its impact in social commerce environment", *International Journal of Electronic Customer Relationship Management*, Vol. 8, No. 1/2/3, (2014), 136. doi:10.1504/IJECRM.2014.066890
 27. Kumar, V., Aksoy, L., Donkers, B., Venkatesan, R., Wiesel, T., and Tillmanns, S., "Undervalued or Overvalued Customers: Capturing Total Customer Engagement Value", *Journal of Service Research*, Vol. 13, No. 3, (2010), 297–310. doi:10.1177/1094670510375602
 28. Phillips, W. J., Wolfe, K., Hodur, N., and Leistritz, F. L., "Tourist Word of Mouth and Revisit Intentions to Rural Tourism Destinations: a Case of North Dakota, USA", *International Journal of Tourism Research*, Vol. 15, No. 1, (2013), 93–104. doi:10.1002/jtr.879
 29. Mukerjee, K., "The impact of brand experience, service quality and perceived value on word of mouth of retail bank customers: investigating the mediating effect of loyalty", *Journal of Financial Services Marketing*, Vol. 23, No. 1, (2018), 12–24. doi:10.1057/s41264-018-0039-8
 30. Alhulail, H., Dick, M., and Abareshi, A., "The Influence of Word of Mouth on Customer Loyalty to Social Commerce Websites: Trust as a Mediator", (2019), 1025–1033. doi:10.1007/978-3-319-99007-1_95
 31. de Matos, C. A., and Rossi, C. A. V., "Word-of-mouth communications in marketing: a meta-analytic review of the antecedents and moderators", *Journal of the Academy of Marketing Science*, Vol. 36, No. 4, (2008), 578–596. doi:10.1007/s11747-008-0121-1
 32. Ding, C. G., and Tseng, T. H., "On the relationships among brand experience, hedonic emotions, and brand equity", *European Journal of Marketing*, Vol. 49, No. 7/8, (2015), 994–1015. doi:10.1108/EJM-04-2013-0200
 33. Barsky, J., and Nash, L., "Evoking Emotion: Affective Keys to Hotel Loyalty", *The Cornell Hotel and Restaurant Administration Quarterly*, Vol. 43, No. 1, (2002), 39–46. doi:10.1177/0010880402431004

34. Lin, J. C., and Liang, H., "The influence of service environments on customer emotion and service outcomes", *Managing Service Quality: An International Journal*, Vol. 21, No. 4, (2011), 350–372. doi:10.1108/09604521111146243
35. Barger, P. B., and Grandey, A. A., "Service with A Smile and Encounter Satisfaction: Emotional Contagion and Appraisal Mechanisms", *Academy of Management Journal*, Vol. 49, No. 6, (2006), 1229–1238. doi:10.5465/amj.2006.23478695
36. Russell, J. A., and Pratt, G., "A description of the affective quality attributed to environments.", *Journal of Personality and Social Psychology*, Vol. 38, No. 2, (1980), 311–322. doi:10.1037/0022-3514.38.2.311
37. Plutchik, R., "A general psychoevolutionary theory of emotion", In *Theories of Emotion*, Academic press, Elsevier, (1980), 3–33 doi:10.1016/B978-0-12-558701-3.50007-7
38. Izard, C. E., "Differential Emotions Theory", In *Human Emotions*, Boston, MA, Springer US, (1977), 43–66. doi:10.1007/978-1-4899-2209-0_3
39. Yeh, T.-M., Chen, S.-H., and Chen, T.-F., "The Relationships among Experiential Marketing, Service Innovation, and Customer Satisfaction—A Case Study of Tourism Factories in Taiwan", *Sustainability*, Vol. 11, No. 4, (2019), 1041. doi:10.3390/su11041041
40. Richard, J. E., and Zhang, A., "Corporate image, loyalty, and commitment in the consumer travel industry", *Journal of Marketing Management*, Vol. 28, Nos. 5–6, (2012), 568–593. doi:10.1080/0267257X.2010.549195
41. Wikhamn, W., "Innovation, sustainable HRM and customer satisfaction", *International Journal of Hospitality Management*, Vol. 76, (2019), 102–110. doi:10.1016/j.ijhm.2018.04.009
42. Lee, Y.-C., Wang, Y.-C., Lu, S.-C., Hsieh, Y.-F., Chien, C.-H., Tsai, S.-B., and Dong, W., "An empirical research on customer satisfaction study: a consideration of different levels of performance", *SpringerPlus*, Vol. 5, No. 1, (2016), 1–9. doi:10.1186/s40064-016-3208-z
43. Ganesan, S., "Determinants of Long-Term Orientation in Buyer-Seller Relationships", *Journal of Marketing*, Vol. 58, No. 2, (1994), 1–19. doi:10.1177/002224299405800201
44. Sirdeshmukh, D., Singh, J., and Sabol, B., "Consumer Trust, Value, and Loyalty in Relational Exchanges", *Journal of Marketing*, Vol. 66, No. 1, (2002), 15–37. doi:10.1509/jmkg.66.1.15.18449
45. Oliver, R. L., "Whence Consumer Loyalty?", *Journal of Marketing*, Vol. 63, No. 4_suppl1, (1999), 33–44. doi:10.1177/00222429990634s105
46. Lv, H., Yu, G., and Wu, G., "Relationships among customer loyalty, customer satisfaction, corporate image and behavioural intention on social media for a corporation", *International Journal of Information Technology and Management*, Vol. 17, No. 3, (2018), 170–183. doi:10.1504/IJITM.2018.092879
47. Fullerton, G., "When Does Commitment Lead to Loyalty?", *Journal of Service Research*, Vol. 5, No. 4, (2003), 333–344. doi:10.1177/1094670503005004005
48. Yi, Y., and La, S., "What influences the relationship between customer satisfaction and repurchase intention? Investigating the effects of adjusted expectations and customer loyalty", *Psychology and Marketing*, Vol. 21, No. 5, (2004), 351–373. doi:10.1002/mar.20009
49. Sahin, A., Zehir, C., and Kitapçı, H., "The Effects of Brand Experiences, Trust and Satisfaction on Building Brand Loyalty; An Empirical Research On Global Brands", *Procedia - Social and Behavioral Sciences*, Vol. 24, (2011), 1288–1301. doi:10.1016/j.sbspro.2011.09.143
50. Iglesias, O., Singh, J. J., and Batista-Foguet, J. M., "The role of brand experience and affective commitment in determining brand loyalty", *Journal of Brand Management*, Vol. 18, No. 8, (2011), 570–582. doi:10.1057/bm.2010.58
51. Khaleghimoghaddam, N., and Bala, H. A., "The Impact of Environmental and Architectural Design on Users' Affective Experience", *YBL Journal of Built Environment*, Vol. 6, No. 1, (2018), 5–19. doi:10.2478/jbe-2018-0001
52. Murray, J., Elms, J., and Teller, C., "Examining the role of store design on consumers' cross-sectional perceptions of retail brand loyalty", *Journal of Retailing and Consumer Services*, Vol. 38, (2017), 147–156. doi:10.1016/j.jretconser.2017.06.001
53. Gong, T., and Yi, Y., "The effect of service quality on customer satisfaction, loyalty, and happiness in five Asian countries", *Psychology & Marketing*, Vol. 35, No. 6, (2018), 427–442. doi:10.1002/mar.21096
54. Chavoshi, A., and Hamidi, H., "Social, individual, technological and pedagogical factors influencing mobile learning acceptance in higher education: A case from Iran", *Telematics and Informatics*, Vol. 38, (2019), 133–165. doi:10.1016/j.tele.2018.09.007
55. Hsu, S.-H., Chen, W., and Hsieh, M., "Robustness testing of PLS, LISREL, EQS and ANN-based SEM for measuring customer satisfaction", *Total Quality Management & Business Excellence*, Vol. 17, No. 3, (2006), 355–372. doi:10.1080/14783360500451465
56. F. Hair Jr, J., Sarstedt, M., Hopkins, L., and G. Kuppelwieser, V., "Partial least squares structural equation modeling (PLS-SEM)", *European Business Review*, Vol. 26, No. 2, (2014), 106–121. doi:10.1108/EBR-10-2013-0128
57. Japutra, A., and Molinillo, S., "Responsible and active brand personality: On the relationships with brand experience and key relationship constructs", *Journal of Business Research*, Vol. 99, (2019), 464–471. doi:10.1016/j.jbusres.2017.08.027
58. Bagozzi, R. P., and Yi, Y., "On the evaluation of structural equation models", *Journal of the Academy of Marketing Science*, Vol. 16, No. 1, (1988), 74–94. doi:10.1007/BF02723327
59. Cronbach, L. J., "Coefficient alpha and the internal structure of tests", *Psychometrika*, Vol. 16, No. 3, (1951), 297–334. doi:10.1007/BF02310555
60. Moazenzadeha, D., and Hamidi, H., "Analysis and Development of Technology Acceptance Model in Mobile Bank Field", *International Journal of Engineering, Transactions C: Aspects*, Vol. 31, No. 9, (2018), 1521–1528. doi:10.5829/ije.2018.31.09c.07
61. Mohammadi, A., "Analyzing Tools and Algorithms for Privacy Protection and Data Security in Social Networks", *International Journal of Engineering, Transaction B: Applications*, Vol. 31, No. 8, (2018), 1267–1273. doi:10.5829/ije.2018.31.08b.15
62. Fornell, C., and Larcker, D. F., "Evaluating Structural Equation Models with Unobservable Variables and Measurement Error", *Journal of Marketing Research*, Vol. 18, No. 1, (1981), 39–50. doi:10.1177/002224378101800104
63. Hamidi, H., and Chavoshi, A., "Analysis of the essential factors for the adoption of mobile learning in higher education: A case study of students of the University of Technology", *Telematics and Informatics*, Vol. 35, No. 4, (2018), 1053–1070. doi:10.1016/j.tele.2017.09.016
64. Ab Hamid, M. R., Sami, W., and Mohamad Sidek, M. H., "Discriminant Validity Assessment: Use of Fornell & Larcker criterion versus HTMT Criterion", *Journal of Physics: Conference Series*, Vol. 890, (2017), 012163. doi:10.1088/1742-6596/890/1/012163
65. Malekinezhad, F., and Lamit, B., "Investigation into University Students Restoration Experience: The Effects of Perceived Sensory Dimension and Perceived Restorativeness", *Preprints*, (2017). doi:10.20944/preprints201708.0085.v1

66. Zare, M. R., Aghaie, A., Samimi, Y., and Asl Hadad, A., "A Novel Excellence Model of the ICT Industry: Case Study on Telecommunications Backbone Network of Iran", *International Journal of Engineering, Transaction B: Applications*, Vol. 33, No. 10, (2020), 2016–2029. doi:10.5829/ije.2020.33.10a.20
67. Hair, J. F., Ringle, C. M., and Sarstedt, M., "PLS-SEM: Indeed a Silver Bullet", *Journal of Marketing Theory and Practice*, Vol. 19, No. 2, (2011), 139–152. doi:10.2753/MTP1069-6679190202
68. Baron, R. M., and Kenny, D. A., "The moderator–mediator variable distinction in social psychological research: Conceptual, strategic, and statistical considerations.", *Journal of Personality and Social Psychology*, Vol. 51, No. 6, (1986), 1173–1182. doi:10.1037/0022-3514.51.6.1173
69. Zhao, X., Lynch, J. G., and Chen, Q., "Reconsidering Baron and Kenny: Myths and Truths about Mediation Analysis", *Journal of Consumer Research*, Vol. 37, No. 2, (2010), 197–206. doi:10.1086/651257
70. Choi, B., and Choi, B.-J., "The effects of perceived service recovery justice on customer affection, loyalty, and word-of-mouth", *European Journal of Marketing*, Vol. 48, No. 1/2, (2014), 108–131. doi:10.1108/EJM-06-2011-0299

8. APPENDIX: CONSTRUCTS AND ITEMS USED IN THE QUESTIONNAIRE

TABLE A. Constructs and measurement items

Construct	Item	Reference
Sensory experience	SEV.1: The lighting at this store is comfortable	Chen and Lin [6]
	SEV.2: The interior space of this store is clean and tidy	By researchers
	SEV.3: The products arrangement and appearance at this store are attractive	Chen and Lin [6]
	SEA.1: The background music at this store is pleasing	Chen and Lin [6]
	SEA.2: There are no annoying sounds in this store	By researchers
	SES.1: The aroma in this store is pleasant	Kim and moon [19]
	SES.2: I like the aroma in this store	Chen and Lin [6]
	SES.3: The staff at this store are fragrant	By researchers
	SETO.1: It is pleasant for me that touch the products before purchase	Yoganathan et al. [11]
	SETO.2: This store has comfortable indoor temperature and ventilation	Chen and Lin [6]
SETA.1: The food products sold at this store are delicious and quality	By researchers	
Positive emotions	PE.1: Satisfaction (pleasing, fulfilling)	Chen and Lin [6]
	PE.2: Joy (happy, enjoyable)	Chen and Lin [6]
	PE.3: Excitement (appealing, animating)	Chen and Lin [6]
	PE.4: Peacefulness (comfortable, relaxed)	Chen and Lin [6]
	PE.5: Refreshment (fresh, novel)	Chen and Lin [6]
Negative emotions	NE.1: Regret (remorse, penitence)	Liu and Jang [18]
	NE.2: Anger (upsetting, irritating)	Chen and Lin [6]
	NE.3: Sadness (disappointing, gloomy)	Chen and Lin [6]
	NE.4: Fear (frightful, uneasy)	Chen and Lin [6]
	NE.5: Shame (embarrassing, awkward)	Chen and Lin [6]
Satisfaction	SA.1: The performance of this store has fulfilled my expectations	Iglesias et al. [10]
	SA.2: This retail store responds well to my needs	Sahin et al. [49]
	SA.3: I am satisfied with my decision to visit this store	Choi et al. [3]
Loyalty	LO.1: I will continue to visit this store, even if other alternatives are available	Choi and Choi [70]
	LO.2: If the price of products in this store is more than the other stores, I will buy again from this store	By researchers
	LO.3: I purchase from this store again, because it is the best choice for me	Choi et al. [3]
WOM intention	WOM.1: I say positive things about this store to other people	Choi and Choi [70]
	WOM.2: I encourage my friends and relatives to use this store	Choi and Choi [70]
	WOM.3: I would provide my relatives with positive things about this store when deciding to shopping	By researchers

Persian Abstract

چکیده

اگرچه قصد توصیه دهان به دهان (WOM) به عنوان یک متغیر حاصل از سازه‌هایی همچون وفاداری، رضایت و اعتماد در کسب‌وکارهای خرده‌فروشی مورد مطالعه قرار گرفته شده‌است، اما توجه کمتری به بررسی تأثیر تجربه‌حسی بر قصد WOM مشتری در این زمینه شده‌است. از آنجایی که مطالعه همزمان تأثیرات تجربه‌حسی بر احساسات و قصد WOM مشتری در فروشگاه‌های خرده‌فروشی زنجیره‌ای نادر است، هدف این مقاله مطالعه چگونگی تأثیر تجربه‌حسی بر قصد WOM مشتری با در نظر گرفتن متغیر میانجیگر احساسات مشتری در فروشگاه‌های خرده‌فروشی زنجیره‌ای می‌باشد. برای این منظور 306 پرسشنامه معتبر از مشتریان یکی از بزرگترین و قدیمی‌ترین فروشگاه‌های زنجیره‌ای ایران (فروشگاه زنجیره‌ای اتکا) جمع‌آوری و مورد تجزیه و تحلیل قرار گرفته شد. مدل مفهومی پیشنهادی این پژوهش بر مبنای مدل محرک-اورگانیسم-پاسخ توسعه‌یافته و برای بررسی این مدل از روش مدل‌سازی معادلات ساختاری (SEM) و تحلیل رگرسیونی استفاده شده‌است. این مدل به وسیله روش حداقل مربعات جزئی (PLS) و با استفاده از نرم افزار SmartPLS مورد آزمون قرار گرفته شده‌است. نتایج حاصله نشان می‌دهد که تجربه‌حسی تأثیر مستقیم و معتاداری بر احساسات مشتری دارد. علاوه بر این مشخص گردید که تجربه‌حسی تأثیر مستقیم قابل ملاحظه‌ای بر قصد WOM مشتری ندارد ولی به صورت غیرمستقیم و از طریق میانجیگرهای احساسات، رضایت و وفاداری بر قصد WOM مشتری تأثیر می‌گذارد. آنالیز رگرسیونی صورت‌گرفته نشان می‌دهد که در بین پنج تجربه‌حسی (چشایی، لامسه، شنوایی، بینایی و بویایی)، چشایی بیشترین تأثیر را بر احساسات مثبت مشتری دارد. بعد از تجربه‌چشایی، تجربیات لامسه، بینایی و شوایی به ترتیب بیشترین تأثیر را بر احساسات مثبت مشتری می‌گذارند. به صورت مشابه مشخص گردید که تجربیات چشایی و لامسه تأثیر منفی و معتاداری بر احساسات منفی مشتریان دارند، که تأثیر تجربه‌چشایی قوی‌تر از تجربه‌لامسه می‌باشد.



Removing of Sb and As from Electrolyte in Copper Electrorefining Process: A Green Approach

M. R. Shojaei^a, G. R. Khayati^{*b}, N. Assadat Yaghubi^c, F. Bagheri Sharebabaki^d, S. M. J. Khorasani^e

^a Department of Materials Science and Engineering, Sharif University of Technology, Tehran, Iran

^b Department of materials science and Engineering, Shahid Bahonar University of Kerman, Kerman, Iran

^c Research & Development Center, Shahrabak Copper Complex, National Iranian Copper Industries Company, Kerman, Iran

^d Supervisor of Copper Electrorefining Operation, Khatoonabad copper refinery, Shahrehabak copper complex, National Iranian copper industries company, Kerman, Iran

^e Senior metallurgical engineer, Process control unit, Khatoonabad copper refinery, Shahrehabak copper complex, National Iranian copper industries company, Kerman, Iran

PAPER INFO

Paper history:

Received 08 August 2020

Received in revised form 26 September 2020

Accepted 29 October 2020

Keywords:

Antimony

Arsenic Copper

Cooling

Electrorefining

ABSTRACT

Removing of arsenic and antimony from electrolyte of copper electrorefining plant by cooling treatment is the subject of current study. In this regards, the temperature of various electrolyte samples reduce to 5, 10, 15 and 20 °C and hold at different times without any turbulency. Experimental results reveal that decreasing the temperature of the electrolyte, facilitate the deposition of As and Sb in the form of AsO₅Sb, AsO₄Sb and As₂O₃ as the white precipitate at a critical time. Also, in the case of the electrolyte retention times exceed than the critical time, the copper content of electrolyte precipitate as blue phase. Typically, it is possible to remove 27 wt.% of Sb and 6 wt.% of As by the cooling of the electrolyte to 5 °C after 8 h. It seems that due to the biocompatibility, the lack of need to the complex technology and its simplicity, the proposed method is a suitable alternative to the common approaches for the removal of antimony and arsenic from industrial electrolyte.

doi: 10.5829/ije.2021.34.03c.14

1. INTRODUCTION

Electrorefining is one of the most common technique in which the high quality of copper cathode (99.99 wt.%) is produced. In this technique, impure copper cast anodes (about 98.5 wt.%) uses as the source of copper and dissolve electrochemically in H₂SO₄ solution as the electrolyte. Then, the Cu ions selectively electrodeposited on the stainless steel cathode blanks. The impurities in the electrorefining cell can be categorized into two groups:

(i) Au, Os, Ru, Ir, Rh, Pd, Pt, Pb, Te, Se and Sn with a negligible tendency for dissolution in the electrorefining cell. These impurities are not electrodeposited at the stainless cathode blank and in the ideal condition go to the anodic slimes;

(ii) Sb, Bi, As, S, Fe, Co and Ni that dissolve in the electrolyte with the significant tendency for dissolution in the electrolytes.

Due to the deposition of copper at lower potentials than type (ii), these impurities accumulate in the electrolyte. In these conditions fail to remove these impurities from the electrolyte has a detrimental effect on the purity of the cathode produced. As a result, these impurities must be continuously removed from the electrolytes, [1].

Historically, As and Sb have been recognized as two of the most challenging impurities in the copper electrorefining. Typically, the former segregates at the grain boundary and deteriorate the mechanical properties of copper through the drawing. While, the later causes the nodulation of the cathode, lowering of current efficiency and passivation [2, 3]. In this regard, the removal of As and Sb is a hot issue with the significant desirability in

*Corresponding Author Email: mohammadrezashojaei3@gmail.com
(M. R. Shojaei)

the copper electrorefining plants. Numerous methods have been introduced to remove As and Sb from electrorefining copper plants, including the bleeding of electrolyte that strongly dependent on the location of the electrorefining plant [4], usage of liberator cells [3], ion exchange [4], adding the removal agents [5], using of the organic phase by solvent extraction [6], absorption by activated carbon [6], co-precipitation of Bi and Sb by adding of barium or lead carbonates [7], crystallization of As with SO_2 [8], removal of Sb and Bi by titanium (IV) oxysulfate co-precipitation [9] and self-purification of copper electrolyte [10]. To the best of our knowledge, all of above methods are complicated and finding of an eco-friendly way to remove As and Sb from the electrolyte is strongly appreciated. This paper is an attempt to remove As and Sb with a green method to reduce the energy consumption and costs. As a first report, in this paper, a simple method is proposed for the removal of As and Sb ions from the electrolyte of the copper electrorefining plants in the industrial scale.

2. EXPERIMENTAL

The industrial electrolyte (mother sample) is selected from the output of the polishing filter of Khatoon Abad industrial company in Shahrabak, Iran. It is free of suspended and floating slimes and reflects the actual behavior of electrolyte through the cooling treatment. It is necessary to note that the amount of Bi in Sarcheshmeh mine is too low (10-20 ppm). Also, the additives including leveling agent and grain refining agent animal glue and thiourea at the electrolyte have no effect on the removal of As and Sb due to dissociation after about 120 min [11-12]. Since the mole fraction of As/(Bi+Sb) in casting anode of a selected plant is higher than 4, it is possible to provide the possibility of self-purification and caused the errors in the results. Accordingly, the mother sample is holed for 24 h in 62 °C (i.e., the operational temperature of the electrorefining plant) as a first step. Then, four samples selected and cooled until 5, 10, 15, and 20 °C, separately in an incubator (Hanchen Model: ES-60). Figure 1 shows schematic steps of the proposed method for removing the impurities. To determine the critical time required for the removal of arsenic and antimony, all samples were allowed to form a white precipitate (its constituents are As, Sb and O) in selected cooling temperature. It is important to note all samples are quite stagnant until the formation of white precipitate is completed. Also, to determine the critical times for the crystallization of CuSO_4 as a blue precipitate, the cooling process is continued until the crystallization has occurred on the white precipitate. Collected precipitates are washed four times with deionized water and then dried at 50 °C for 60 min. Each experiment is repeated three times and 10 mL of each sample is selected and mixed to make the sample for chemical analysis. A scanning electron

microscope (SEM, VGA, TESCAN, XMU) at 20KV as an accelerating voltage equipped with an EDS detector is used to analyze the chemical component of the precipitates. The X-ray diffraction (XRD) pattern is recorded by Riqaku mini flex diffractometer with Cu-K α X-ray diffraction at 35 kV and 20 mA. The vibration characteristic is determined by IR spectroscopy (Nexus 670, Nicolet crop). ANALYAST DIVISION: WET, AAS, ELECTRO ANALYSE are also employed for chemical analysis of selected electrolytes before and after the cooling treatment.

The density functional theory calculations are performed utilizing the CP2K software package [13]. Double ζ -valence polarized basis set [14], Perdew-Burke-Ernzerhof generalized gradient approximation exchange-correlation functional [15], and Goedecker-Teter-Hutter pseudopotential [16] are used for self-consistent field (SCF) calculations. The charge density cutoff radius of 300 Ry with the convergence limit of 10^{-6} is adopted. The geometries are optimized until the force on each atom is less than 15 meV/Å with a maximum displacement of 0.002 Bohr using the Broyden-Fletcher-Goldfarb-Shanno algorithm [17]. For calculation of the normal modes of the vibrations, the geometries are further optimized until the force on each atom is less than 1 meV/Å. The convergence criterion for SCF calculations is set to 10^{-8} . The structures and the isosurfaces of molecular orbitals are shown using a piece of VESTA software [17].

3. RESULTS AND DISCUSSION

3.1. Selected Cooling Cycles

To determine the critical time for the formation of the white precipitate and crystallization of blue copper sulfates, each sample is kept at the selected temperature until the blue copper sulfates is formed as reported in Table 1. As a first result, there is a significant difference between the critical time

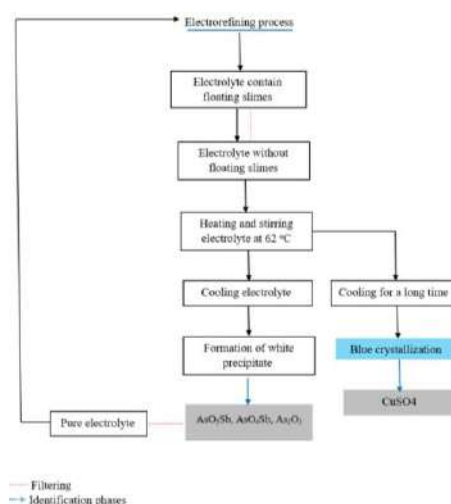


Figure 1. Schematic presentation of the proposed method for the removal of As, Sb

TABLE 1. Temperature and critical time for the precipitation of white and blue type in various samples

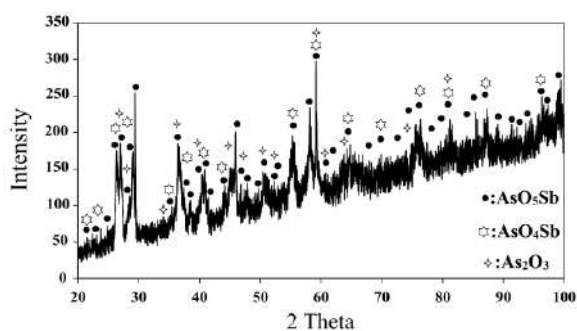
Temperature (°C)	5	10	15	20
Minimum time required for the formation of a white precipitate (h)	8	11	14	16
Minimum time required for the crystallization of copper sulfate as a blue precipitate (h)	12	15	20	24

of the formation of white precipitate and the crystallization of the copper sulfate at the selected cooling temperatures. Typically, this difference from 3 h at 2 °C enhanced to the about 8 h at 20 °C for the formation of white precipitate. The critical times increases at higher temperature for the storage of the electrolyte. Therefore, compared to the temperature, the super saturation due to the decrease in temperature is the administrated factor on the formation of white precipitate. In other words, the higher the degree of saturation is performed at a lower temperature. It is also possible to selectively separate the two phases over a relatively long time for all investigated temperatures.

3. 2. Phase and Structural Analysis of Collected White Precipitates

The phase analysis of a white precipitate is carried out using XRD. All samples showed similar XRD patterns. Figure 2 typically shows the XRD pattern of white precipitate from cooled electrolyte for 8 h at 5 °C. As shown, AsO_5Sb (PDF: 98-001-6465), As_2O_3 (PDF no. 01-083-1548) and AsO_4Sb (PDF no.: 73-0875), respectively are the main phases with relatively crystalline characteristics. Peak broadening can be related to the amorphous characteristics of these phases and/or the ultra-fine particles size of the precipitate. Also, the weight percent of other possible impurities in white precipitates is lower than 5 wt.% and as a consequence there is not any peaks of these impurities.

Figure 3(a) typically illustrates the SEM image (using a backscatter detector) of collected white precipitates after the storage of electrolyte at 5 °C for 8 h.

**Figure 2.** Typically, the XRD pattern of white precipitate after the cooling of electrolyte at 5 °C for 8 h

Accordingly, the presence of three various morphologies including plate-like, rod-like and spherical is obvious. As shown, the sizes of spherical particles are lower than 500 nm and may be one of the reasons of peak broadening in the XRD pattern. Also, due to the different average atomic mass units of observed phases in the XRD pattern ($\text{Amu}_{\text{AsO}_5\text{Sb}}=39.5$, $\text{Amu}_{\text{As}_2\text{O}_3}=39.6$ and $\text{Amu}_{\text{AsO}_4\text{Sb}}=43.5$), it can be concluded that the brighter spherical particles are related to AsO_4Sb due to the higher average atomic mass unit. In this regard, the similar brightness of rod-like and plate-like particles can be related to a similar average atomic mass unit of these phases. The EDS is used to determine the chemical composition of A, B and C points in Figures 3(b), 3(c) and 3(d). As can be seen from the EDS spectrum of point A, As, Sb and O are the main constituents of selected flake particles. Similar elements are also observed in the EDS spectrum of point C at the surface of rod-like particles. While, at the EDS of point B (Figure 3(c)), instead of Sb, there are some minor amounts of Cu and S due to the entrapment of electrolyte at the surface crack of rod-like particles.

To further investigate of these phases, the chemical analysis of electrolyte is determined before and after the cooling and the formation of a white precipitate. Table 1 typically, compares the chemical composition of as received and cooled electrolyte to 5 °C for 8 h.

As the first conclusion of Table 2, the content of Ni, Cu, Bi, Co and Fe are relatively constant for both the electrolytes and strongly rejected the co-precipitation of these ions through the cooling. The concentration of As(III) and Sb(III) experience little change including 0.03 g/L and 0.03 g/L, respectively. While, the maximum decrease in the concentration related to the As(V) and Sb(V) to be about 0.23 g/L and 0.09 g/L after the cooling, respectively.

3. 3. Mechanism of the Removal of Antimony and Arsenic from Electrolyte

The phase analysis of precipitates confirms the presence of crystalline AsO_5Sb , AsO_4Sb and As_2O_3 phases. As shown in Table 2, As(V), As(III), Sb(V), Sb(III) are the main constituents that change their concentration after the cooling. According to the literature, H_3AsO_4 , $\text{AsO}^+/\text{HAsO}_2$, HSb(OH)_6 and SbO^+ are the stable component of these components in the electrolyte [18]. Given that, the pressure, acidity and type of electrolytes are not changed through the cooling. It can be concluded that the temperature has a key role in the ratio of As(V)/As(III) and Sb(V)/Sb(III) through the cooling. An increase in As(III) after the cooling cycle, despite the decrease in As(V), Sb(III) and Sb(V) contents is the other notable concept in Table 1. Ying-Lin Peng et al. [19] showed that the oxidation of As(III) to As(V) facilitates at the higher temperature. They reported that at constant electrolysis time of 168 h, the oxidation rates of As(III) from As(V) at the temperature 75 °C is 2.21 times

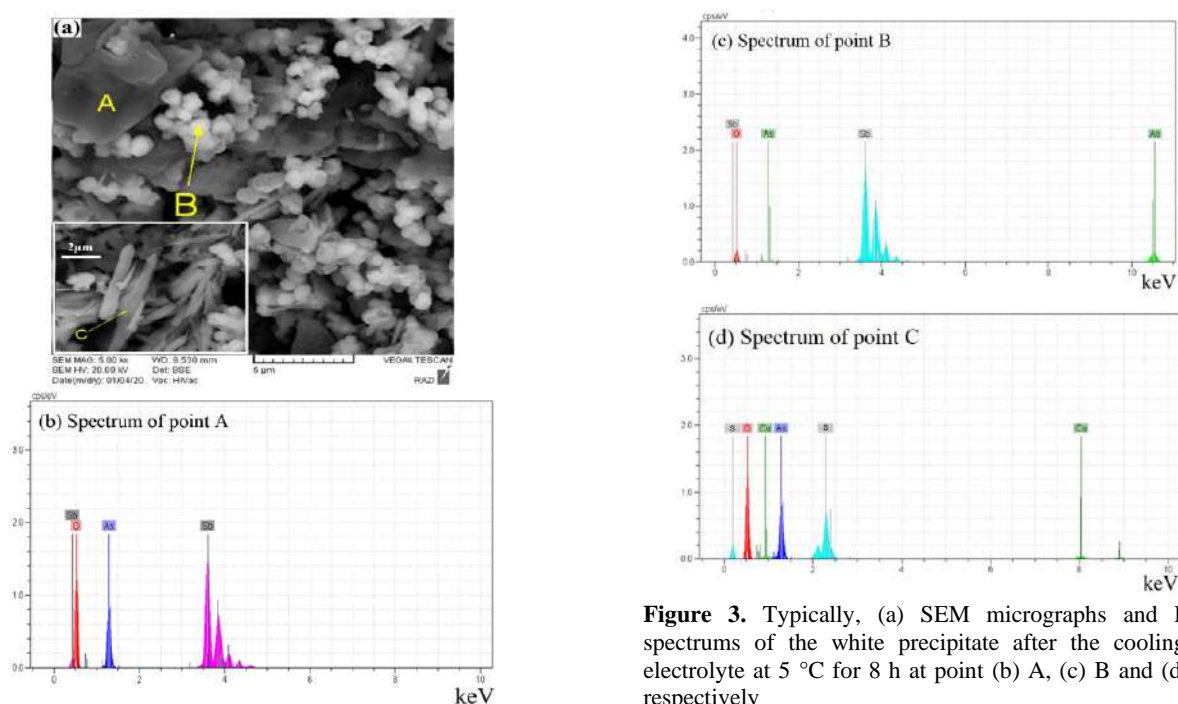
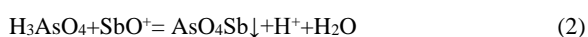


Figure 3. Typically, (a) SEM micrographs and EDS spectra of the white precipitate after the cooling of electrolyte at 5 °C for 8 h at point (b) A, (c) B and (d) C, respectively

TABLE 2. Typically abbreviation of chemical composition of as received electrolyte and cooled electrolyte at 5 °C for 8 h (± 1 ppm or ± 0.001 g/L)

Element/ion	As _t (g/L)	As ⁵⁺ (g/L)	As ³⁺ (g/L)	Sb _t (g/L)	Sb ⁵⁺ (g/L)	Sb ³⁺ (g/L)	Bi (ppm)	Cu (g/L)
As received electrolyte	3.27	3.07	0.20	0.44	0.18	0.26	12	45
After cooling to 5 °C for 8 h	3.07	2.84	0.23	0.32	0.09	0.23	12	45

of its value at 45 °C. Dependency between the temperature and solubility of oxygen is the other factor that must be considered. As a general trend, the solubility of O₂ decreases at the higher temperature. For example, the equilibrium content of O₂ solubility in synthetic electrolyte with 200 g/L H₂SO₄ is to be about 0.72 mM/L at 62 °C and 1.61 mM/L at 5 °C [20]. While, in our experiments, due to the lower retention time (8 h) and being stagnant of the electrolyte there is not sufficient time for the diffusion of O₂ from the atmosphere to the electrolyte. Accordingly, from one hand the lower O₂ content of electrolyte respect to the equilibrium amount and on the other hand the higher stability of As(III) respect to As(V) at lower temperature providing a suitable condition for the conversion of As(III) to As(V). Accordingly, by consideration of the results of the XRD spectra as well as the chemical analysis of filtered electrolytes, it can be concluded that the following reactions (Equations (1)-(4)) are responsible for the removal of As and Sb from the electrolyte.



The mixture of AsO₅Sb and AsO₄Sb is formed and deposits according to reactions (1) and (2). Moreover, the cooling of the electrolyte promoted the reduction of As(V) to As(III) [21] as shown in reaction 3. Then, some amount of As(III) ion oxidized by dissolved oxygen in the electrolyte and produce As₂O₃ as precipitate (reaction 4). Wang et al. [22] proposed that the formation AsO₄Sb as the white powder is possible through the cooling of copper refining electrolyte.

3. 4. Molecular Structures of the Formation Phases

The optimized geometry of the structures is shown in Figure 4. Accordingly, three structures can be considered for As₂O₃. Since, the structure of As₂O₃⁻² in Figure 4(b) has the lowest total energy, it is more probable that this structure is formed. The total energies of the three structures of As₂O₃ are shown in Table 3.

The highest occupied molecular orbital (HOMO) isosurfaces of each structure are shown in Figure 5. For

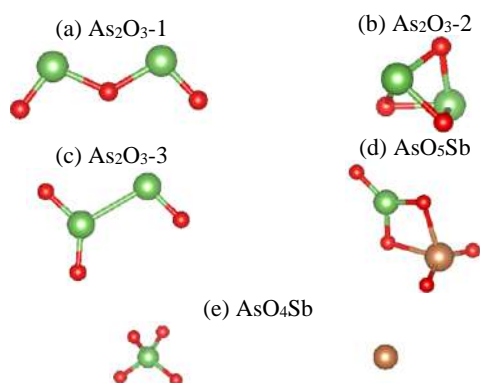


Figure 4. The optimized structures of observed phases including (a-c): As_2O_3 , (d): AsO_5Sb and (e): AsO_4Sb

TABLE 3. Total energies of the three structure of As_2O_3

Structures of As_2O_3	Energy (kJ/mol)
1	-159102.466
2	-159166.75
3	-158953.023

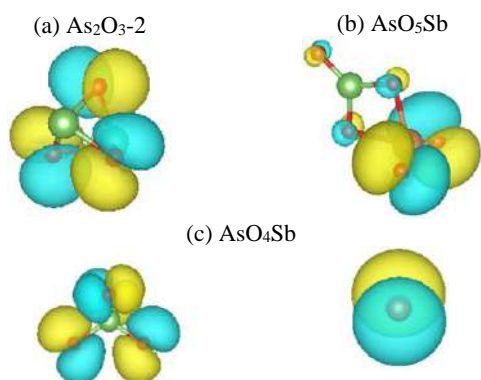


Figure 5. HOMO isosurfaces of the formation phases obtained from DFT calculations

each structure, the HOMO energy levels are mostly localized on oxygen atoms of the structures and have a negligible portion on As and Sb except for AsO_4Sb . This may be indicative of the ionic nature of the structures in which the most of the electron sharing is from As and Sb atoms. Also, for AsO_4Sb structure, the Sb atom is about 12 Å further from the AsO_4 in the simulation cell, which again shows the ionic nature of the structure.

3. 5. FTIR Analysis of White Precipitates

FTIR pattern of the white precipitate is given in Figure 6. There is a vibration bond at 2605.27 cm^{-1} due to the adsorption of CO_2 in the atmosphere to the precipitate. The bond at 1287.43 , 1013.84 , 1071.65 and 1175.67 cm^{-1} are the bending vibration absorption spectrum of As-OH [23-

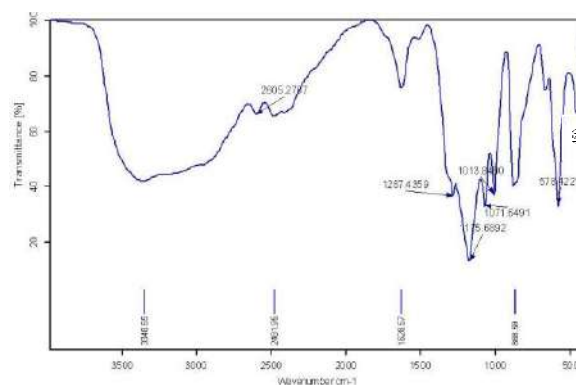


Figure 6. FTIR spectrum of white precipitate that collected from cooled electrolyte at $5\text{ }^\circ\text{C}$ for 8 h

25], the bond at 868.59 cm^{-1} is the anti-stretching vibration absorption spectrum of As-O-Sb and/or As-O-As [26]. The bond at 1287.44 , 878.42 , 1628.57 and 1175.69 cm^{-1} are the anti-stretching vibration absorption spectrum of Sb-OH [23-25], and the bond at 578.42 cm^{-1} is the anti-stretching vibration absorption spectrum of Sb-O-As [27-29], and the bend at 3348.65 and 1628.27 cm^{-1} are the bending vibration absorption spectrum of O-H [23, 24]. The bond at 450.10 cm^{-1} is inferred as the bending vibration absorption spectrum of O-As-O [26]. The presence of these valence bonds confirms the results of the XRD.

4. CONCLUSION

In this study, a green approach is proposed for selective removal of Sb and As from the electrolyte of copper the electrorefining plant. Experimental results showed that the cooling of industrial electrolyte is able to remove about 27 wt.% of Sb, 6 wt.% of As(V) and reactivation of 1 wt.% of As(v) to As(III) by effecting on the solubility of As(V), As(III), Sb(III) and Sb(V). Removing of these impurities is done by the formation of As_2O_3 , AsO_5Sb and AsO_4Sb as white precipitates. The results confirm the need for the storage of electrolyte at any selected temperature for a specified period. Longer storage time results in the precipitation of copper as blue copper sulfates on the primary white precipitate. Accordingly, an efficient approach proposed without using an organic solvent, expensive the raw materials, and complicated equipments for selective removal of Sb and As from the industrial electrolyte.

5. REFERENCES

- Schlesinger, M. E., Sole, K. C., & Davenport, W. G., "Extractive metallurgy of copper", *Elsevier*, Fourth ed., , 2011.

2. Artzer, A., Moats, M. & Bender, "Removal of Antimony and Bismuth from Copper Electrorefining Electrolyte: Part I—A Review", *Jom*, Vol. 70, No. 10, (2018), 2033-2040. <https://doi.org/10.1007/s11837-018-3075-x>
3. Artzer, A., Moats, M., & Bender, "Removal of Antimony and Bismuth from Copper Electrorefining Electrolyte: Part II—An Investigation of Two Proprietary Solvent Extraction Extractants", *Jom*, Vol.70, No. 12, (2018), 2856-2863. <https://doi.org/10.1007/s11837-018-3129-0>
4. Acharya, S., "Copper Refining Electrolyte and Slime Processing-Emerging Techniques", *In Advanced Materials Research*, Vol. 828, (2014), 93-115. <https://doi.org/10.4028/www.scientific.net/AMR.828.93>
5. Zeng, W., Wang, S., & Free, M., L., "Experimental studies of the effects of anode composition and process parameters on anode slime adhesion and cathode copper purity by performing copper electrorefining in a pilot-scale cell", *Metallurgical and Materials Transactions B*, Vol. 47, No. 5, (2016), 3178-3191. <https://doi.org/10.1007/s11663-016-0736-4>
6. Navarro, P., Simpson, J., & Alguacil, F., "Removal of antimony (III) from copper in sulphuric acid solutions by solvent extraction with LIX 1104SM", *Hydrometallurgy*, Vol. 53, No. 2, (1999), 121-131. [https://doi.org/10.1016/S0304-386X\(99\)00033-X](https://doi.org/10.1016/S0304-386X(99)00033-X)
7. Hyvarinen, O., V., 1979. P. *U.S. Patent*, No. 4,157,946. Washington, DC: U.S. Patent and Trademark Office.
8. Wang, X., Wang, X., Liu, B., Wang, M., Wang, H., Liu, X., & Zhou, S., "Promotion of copper electrolyte self-purification with antimonic oxides", *Hydrometallurgy*, Vol. 175, (2018), 28-34. <https://doi.org/10.1016/j.hydromet.2017.10.028>
9. Nie, H., Cao, C., Xu, Z., & Tian, "Novel method to remove arsenic and prepare metal arsenic from copper electrolyte using titanium (IV) oxysulfate coprecipitation and carbothermal reduction", *Separation and Purification Technology*, Vol. 231, (2020), 115919. <https://doi.org/10.1016/j.seppur.2019.115919>
10. Xiao, F. X., Dao, C. A. O., Mao, J. W. Shen, X. N. & Ren, F. Z., "Role of Sb (V) in removal of As, Sb and Bi impurities from copper electrolyte", *Transactions of Nonferrous Metals Society of China*, Vol. 24, (2014), 271-278. [https://doi.org/10.1016/S1003-6326\(14\)63057-0](https://doi.org/10.1016/S1003-6326(14)63057-0)
11. Stantke, P., "Using CollaMat to measure glue in copper electrolyte", *JOM*, Vol.54, (2002), 19-22.
12. Hutter, J., Iannuzzi, M., Schiffmann, F., & VandeVondele, "CP2K: atomistic simulations of condensed matter systems. Wiley Interdisciplinary Reviews", *Computational Molecular Science*, Vol. 4, (2014), 15-25. <https://doi.org/10.1002/wcms.1159>
13. V., Vondele, J. & Hutter, "Gaussian basis sets for accurate calculations on molecular systems in gas and condensed phases", *Chemical Physics*, Vol. 127, No. 11, (2007), 114105. <https://doi.org/10.1063/1.2770708>
14. Perdew, J., P., Burke, K., & Ernzerhof, M., "Generalized gradient approximation made simple", *Physical Review Letters*, Vol. 77, (1996), 3865.
15. Goedecker, S., Teter, M., & Hutter, "Separable dual-space Gaussian pseudopotentials", *Physical Review B*, Vol. 54, (1996), 1703. <https://doi.org/10.1103/PhysRevB.54.1703>
16. Press, W. H., Teukolsky, S. A., Vetterling, W. T., & Flannery, B. P., "Numerical recipes 3rd edition: The art of scientific computing. Third ed", *Cambridge University Press*, 2007.
17. Momma, K., & Izumi, F., "VESTA 3 for three-dimensional visualization of crystal, volumetric and morphology data", *Applied Crystallography*, Vol. 44, (2011), 1272-1276. <https://doi.org/10.1107/S0021889811038970>
18. Xiao, F., X., Cao, D., Mao, J., W., & Shen, X., N., "Mechanism of precipitate removal of arsenic and bismuth impurities from copper electrolyte by antimony", *In Advanced Materials Research*, Vol. 402, (2012), 51-56. <https://doi.org/10.4028/www.scientific.net/AMR.402.51>
19. Peng, Y., L., Zheng, Y., J., & Chen, W., M., "The oxidation of arsenic from As (III) to As (V) during copper electrorefining", *Hydrometallurgy*, Vol. 129, (2012), 156-160. <https://doi.org/10.1016/j.hydromet.2012.06.009>
20. Xing, W., Yin, G., & Zhang, J., "Rotating electrode methods and oxygen reduction electrocatalysts. Elsevier, Fourth (Ed.), (2014).
21. Jergensen, G. V., "Copper leaching", *Solvent Extraction, and Electrowinning Technology*, Third (Ed.) SME, (1999).
22. Xue-Wen, W., Qi-Yuan, C., Zhou-Lan, Y., & Lian-Sheng, X., "Identification of arsenato antimonates in copper anode slimes", *Hydrometallurgy*, Vol. 84, (2006), 211-217. <https://doi.org/10.1016/j.hydromet.2006.05.013>
23. Naili, H., & Mhiri, T., "X-ray structural, vibrational and calorimetric studies of a new rubidium pentahydrogen arsenate $RbH_2(AsO_4)_2$ ", *Alloys and Compounds*, Vol. 315, (2001), 143-149. [https://doi.org/10.1016/S0925-8388\(00\)01309-8](https://doi.org/10.1016/S0925-8388(00)01309-8)
24. Qureshi, M., & Kumar, V., "Synthesis and IR, X-ray and ion-exchange studies of some amorphous and semicrystalline phases of titanium antimonate: separation of VO^{2+} from various metal ions", *Chromatography A*, Vol. 62, (1971), 431-438. [https://doi.org/10.1016/S0021-9673\(00\)91395-5](https://doi.org/10.1016/S0021-9673(00)91395-5)
25. Colomban, P., Doremieux-Morin, C., Piffard, Y., Limage, M. H., & Novak, A., "Equilibrium between protonic species and conductivity mechanism in antimonic acid, $H_2Sb_4O_{11} \cdot nH_2O$ ", *Journal of Molecular Structure*, Vol. 213, (1989), 83-96. [https://doi.org/10.1016/0022-2860\(89\)85108-7](https://doi.org/10.1016/0022-2860(89)85108-7)
26. Zongsheng, Z., "Mechanism of arsenic removal in oxidized Fe-As system". *Journal of China Environmental Science*, Vol. 1, (1995).

Persian Abstract

چکیده

حذف آرسنیک و آنتیموان از طریق سردسازی الکترولیت صنعتی کارخانه پالایش الکتریکی مس صورت گرفت. به عنوان یک مسیر نوین، در پژوهش حاضر، دمای الکترولیت به 5، 10، 15 و 20 درجه سانتی گراد کاهش یافته و در زمان های مختلف بدون تلاطم نگهداری گردید. نتایج تجربی نشان می دهد که کاهش دمای الکترولیت، رسوب As و Sb را به شکل As_2O_3 و AsO_4Sb ، AsO_5Sb به عنوان رسوب سفید در یک زمان بحرانی بوجود می آورد. همچنین، در مواردی که زمان نگهداری الکترولیت در دماهای مذکور بیشتر از زمان بحرانی باشد، محتوای مس الکترولیت به صورت فاز آبی رسوب می کند. به عنوان مثال، می توان 27 درصد وزنی Sb و 6 درصد وزنی As را با خنک سازی الکترولیت تا 5 درجه سانتیگراد پس از 8 ساعت حذف کرد. به نظر می رسد با توجه به سازگاری زیست محیطی، عدم نیاز به فنآوری پیچیده و سادگی، روش پیشنهادی جایگزین مناسبی برای روش های رایج برای از حذف آنتیموان و آرسنیک در مقیاس صنعتی باشد.



Effect of Silver Clusters Deposition on Wettability and Optical Properties of Diamond-like Carbon Films

E. Mohagheghpour^a, M. M. Larijani^b, M. Rajabi^c, R. Gholamipour^c

^a Radiation Applications Research School, Nuclear Sciences and Technology Research Institute, Tehran, Iran

^b Physics and Accelerators Research school, Nuclear Sciences and Technology Research Institute, Tehran, Iran

^c Department of Advanced Materials and Renewable Energy, Iranian Research Organization for Science and Technology (IROST), Tehran, Iran

PAPER INFO

Paper history:

Received 19 November 2020

Received in revised form 18 January 2021

Accepted 03 February 2021

Keywords:

Biomedical Applications

Contact Angle

Diamond-Like Carbon

Hydrophobic

Silver

Surface Treatment

ABSTRACT

In this study, the effect of silver clusters deposition was investigated on optical, wettability and surface properties of diamond-like carbon (DLC) films. Silver clusters and DLC films were deposited on Ni-Cu (70.4-29.6;W/W) alloy substrates by ion beam sputtering deposition (IBSD) technique. Optical and structural properties were measured using UV-visible spectroscopy and Raman spectroscopy, respectively. The wettability and surface free energy of films were determined by the contact angle (CA) measurements. Raman spectra of DLC thin film with 121 ± 6 nm thickness without accumulated Ag showed that the size of the graphite crystallites with sp^2 bands (L_a) was 3.36\AA by the I_D/I_G ratio equal to 0.062 with large optical band gap equal 3eV extracted from Tauc relation. The results of the deposition Ag in the various ion beam energy between 0.6 to 2keV showed the Ag clusters were accumulated uniformly on the surface of DLC films at 0.9keV. The volume percentage of silver clusters was varied from 5.0 ± 2.01 to 16.3 ± 1.4 . The variation was caused by controlling the screen voltage and the deposition time. The CA of the deposited films increases from $79^\circ\pm 2$ to $95^\circ\pm 2$ as well as the reflection values in the visible and near-infrared region due to the increase in the Ag concentration in the surface of DLC films; while the surface free energy decrease from 86 ± 1 to 66 ± 2 mJ/m² and the optical transmittance is almost constant. Our results demonstrate that the deposition of silver particles on DLC films is potentially useful for biomedical applications having good hydrophobic characteristics without causing a destructive effect on the optical properties of DLC films.

doi: 10.5829/ije.2021.34.03c.15

1. INTRODUCTION

Diamond-like carbon (DLC) film is an interesting protective coating for modifying the surface properties of biomedical implants [1-3] due to their excellent mechanical properties such as wear and corrosion resistance, low friction coefficient, excellent chemical inertness and biocompatibility [4, 5]. Also, due to the optical properties, DLC films have widespread application in optical lens, anti-reflection coatings for optical devices, photodiodes and electroluminescence devices [5, 6].

In medical implants, the chemical properties of a protective coating at the interface strongly affect the biological behavior of coating [7]. Thus, controlling the

surface chemistry of an implant and investigation about effective factors on it, for producing a specific surface with a well-defined biological reaction, is very important. On the other hand, there are reports that hydrophobic surfaces are better than hydrophilic ones for coating medical tools such as medical guide-wire and protein absorption, platelet attachment and activation for cardiovascular applications [8].

Doped DLC films have recently attracted a lot of attention [9] because of the addition of the other elements into DLC can change the surface free energy. Among the large number of NPs investigated, Ag is a powerful antibacterial agent that increases surface hydrophobic properties, improves hemocompatibility [10-12] and enhances the electron field emission property with

*Corresponding Author Institutional Email: emohaghegh@aeoi.org.ir
(E. Mohagheghpour)

lowering the work function [13]. Ag incorporation in the DLC films reduces surface free energy [14, 15], decreases the residual stress, improve the wear performance [14-16], and promote faster biointegration of DLC films [17]. Although the surface modification of diamond like carbon film by silver (Ag:DLC) can solve some of the major drawbacks of pure DLC films, this process has a destructive effect on the transparency, optical and structural properties of these films [18] due to the decreasing of the fraction of sp^3 bonds in the carbon structure [14, 16]. Koutsokeras et al. [19] reported that by limiting the interactions between metal (Ag, Cu) and carbon during deposition can retain the transparency level of the hydrogenated diamond like carbon films.

So, it is valuable to find a process that improves the surface properties without changing the DLC film properties. In this research that follows our previous work [20]. We want to introduce a new method for modifying the surface properties of DLC thin films by depositing silver particles without optical properties disturbance.

Although, several researches have been investigated the deposition of silver particles, in the recent years, the synthesis of silver particles is usually done by wet chemical reduction starting from a molecular precursor containing Ag in an oxidized state [21, 22]. This method has several drawbacks such as the presence of impurities, high cost of synthesis process and weak adhesion of the obtained nano particles to the substrate [22, 23]. In addition, Liu et al. [24] have reported the use of silver nano particles to decorate the surface of graphene oxide. In order to enhanced catalytic applications Ag nanoparticles, Jeon et al. [25] and Lim et al. [26] dispersed Ag nanoparticles on graphene oxide nanosheets and reduced graphene oxide, respectively. So, there is lack of systematic studies about of Ag deposition on DLC film and investigation about of the relation between Ag concentration and surface properties of DLC film.

In the present study, we deposited silver clusters via ion beam sputtering deposition (IBSD) method directly on the surface of DLC films which were deposited on the Ni-Cu alloy and microscope slides for studying the optical properties of thin films. IBSD method has been used for silver particles deposition with excellent adhesion to DLC thin film which is a result of controlling energetic particles precisely by adjusting the particle flux, energy and incidence angle, independently [27].

We investigated the effect of Ag concentration on the surface of DLC films on the optical and wetting properties of DLC films deposited on Ni-Cu (70.4-29.6; W/W) alloy by IBSD method. The optical property, the wetting behavior and the surface free energy dependence on the Ag concentration and the existing relations are systematically determined.

2. EXPERIMENTAL

DLC thin films were deposited on the Ni-Cu alloy substrate by ion beam sputtering deposition technique. Nickel with a purity higher than 99% and copper with purity higher than 99.9% produced at Mes Sarcheshmeh (Rafsanjan, Iran) were used to make Ni-Cu (70.4-29.6; W/W) alloy by a vacuum arc remelting (VAR) furnace and were homogenized with four times remelting. After rolling, the samples were cut into pieces with an approximate size of 10×20 mm and 0.5 mm thickness, and then were mechanically wet ground, polished and smoothed with Al_2O_3 to get a finished mirror surface. These substrates were cleaned ultrasonically with acetone, ethanol, and deionized water prior to film deposition.

The carbon source for deposition DLC films was a high purity graphite plate (>99%; $12 \text{ cm} \times 15 \text{ cm}$) produced by SGL carbon group. During the deposition process of DLC film, the pressure was kept constant at 2×10^{-5} Torr by introducing a high purity argon gas. Eight sets of DLC films were prepared under identical conditions. The accelerator voltage, the ion current, the substrate temperature and the deposition time were 2200V, 25 mA, 100 °C, and 30 min, respectively. After that, for determining the appropriate parameters for depositing silver particles, the ion beam energy and deposition time were changed in the ranges of 0.6 to 2 keV and 10 to 90s, respectively. During the deposition of silver particles, the pressure and the ion current were kept constant at 2×10^{-5} and 10 mA, respectively.

The thickness of DLC films as a surface for deposition of Ag was determined by reflection measurement (AvaSpec-2048). The AFM was operated in a tapping mode (DME dual scope DS 95, Danish Micro Engineering, Herlev, Denmark) with a scan rate of approximately 3 Hz and 0.1 nN force in the typical scan area of $1 \times 1 \mu\text{m}^2$. The surface roughness of Ni-Cu alloy substrates was measured by the portable surface roughness tester (TR 200, Time Instruments, Beijing, China). The Raman spectra were measured using the 785 nm excitation wavelength of Nd: YLF laser with a power of 30 mW. The optical properties of DLC films were obtained by simultaneous deposition of the films on the glass substrate (microscope slides). The optical properties were investigated from the reflectance and transmittance data using a UV/visible spectrophotometer (Cary 500, Varian, Palo Alto, and California). The optical microscope (Olympus BX_60), a field emission gun SEM (MIRA3\TESCAN) and scanning electron microscopy (VEGA\TESCAN-LMU, RONTEC) was employed to evaluate the amount and manner of Ag accumulation on the surface of DLC thin films. The amount of Ag on the DLC films was determined by energy dispersive spectrometer (EDS;

VEGA\\TESCAN-LMU, RONTEC). The wetting test was carried out at room temperature by using a contact angle-measuring device (CAM). The contact angle (CA) was determined from digital images taken by a DFK23U618 USB3.0 color industrial camera with the help of an a₂X lens. An open-source image processing software, ImageJ1.46v, was used to measure contact angles.

3. RESULTS AND DISCUSSION

Figure 1 shows the Raman spectra of DLC film deposited on the Ni-Cu (70.4-29.6; W/W) alloy and the glass substrate. The average surface roughness of the Ni-Cu alloy substrates was 272 ± 20 nm before the coating. The accelerator voltage, the ion current and the substrate temperature were 2200V, 25 mA, and 100 °C, respectively. The deposition time was 30 min that generated a DLC thin film with 121 ± 6 nm thickness.

The Raman spectra of the carbon film are mainly composed of two broad peaks that are associated with D and G peaks. The D peak contributed to the disordered graphitic carbon and G peak contributed to the graphite carbon in aromatic (rings) and olefinic (chains) molecules [2, 28].

The spectra were deconvoluted by Gaussian functions to determine the I_D/I_G ratio, as well as D and G peak positions. The data extracted from the Raman deconvolution of DLC film on Ni-Cu alloy and glass substrate are reported in Table S1. It is observed that the integrated intensity ratio I_D/I_G increases from 0.062 to 0.072 while the G peak band shifts from 1577.9 to 1541.7 cm^{-1} due to DLC film deposition on the Ni-Cu alloy and glass substrate, respectively.

According to amorphization trajectory proposed by Ferrari and Robertson [29], structural evolutions from graphite to diamond consist of three stages. When the I_D/I_G ratio is very small and the decrease in the I_D/I_G ratio

associated with the G peak band shifts to the greater values, the structure changes from amorphous carbon to DLC. Therefore, in this research, the structure of the deposited film is diamond-like amorphous carbon with large optical band gap (3 eV) extracted from Tauc relation [2, 30] (Figure 2).

On the other hand, according to this trajectory [29], in very low I_D/I_G ratio, there exists a simple relation between the I_D/I_G ratio and optical band gap given in Equation (1):

$$\frac{I_D}{I_G} = \frac{C}{E_g^2} \quad (1)$$

According to the Raman deconvoluted spectra, since the integrated intensity ratio I_D/I_G is very low- with a small increase from 0.062 to 0.072 which is due to deposition of DLC film on the Ni-Cu alloy and glass substrate, respectively. We can use this equation for predicting the evolution of optical properties of deposited DLC thin film on the Ni-Cu alloy by the optical properties study of the deposited DLC thin film on the glass substrate.

The surface free energy is an important parameter in controlling the adsorption, wetting and surface adhesion of DLC film that depends on the amount and nature of surface bonds. This parameter can be determined by the CA of a surface [31]

Here, we investigated the effect of silver accumulation on the wettability properties of DLC thin film. With the deposition of Ag at 2keV ion beam energy, a continuous thin layer was formed. The microscopic images of accumulated clusters at 1.2 keV ion beam energy (Figure S1) show high percentage coverage of the surface of DLC film by silver clusters with a diameter of about 50-100 microns. In addition, according to FESEM images of deposited Ag at 0.6 keV ion beam energy (Figure S2), the accumulation of SNPs was done only in the surface defect regions that have higher energy levels in comparison with the other parts of the deposited layer. Therefore, the investigation was done at 0.9

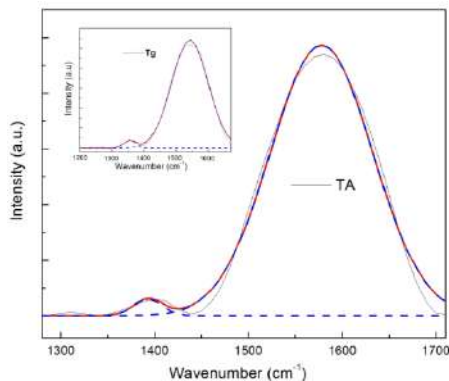


Figure 1. Raman spectra of DLC films deposited on Ni-Cu alloy (TA) and glass substrate (Tg), (— ion beam energy, — Gaussian fit peak, — deconvoluted peaks)

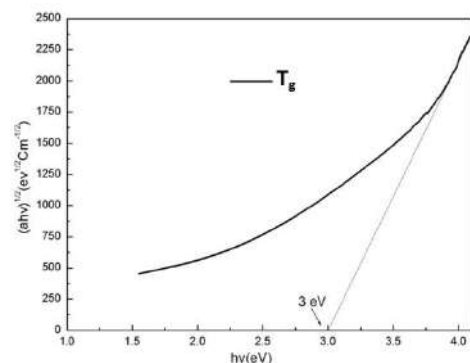


Figure 2. Tauc plot to determine the optical band gap of DLC thin film without accumulation of silver nanoparticles (SNPs)

keV ion beam energy in different deposition times ranging from 10 to 30 s (Figure 3).

Figure 4 shows the profile of the distilled liquid water drop and its contact angle on the DLC thin films as a function of Ag weight percentage in the surface. The corresponding values of the contact angle are presented in Table 1. The CA measurements indicated that the hydrophobicity of the DLC films increased with the silver clusters deposition on its surface.

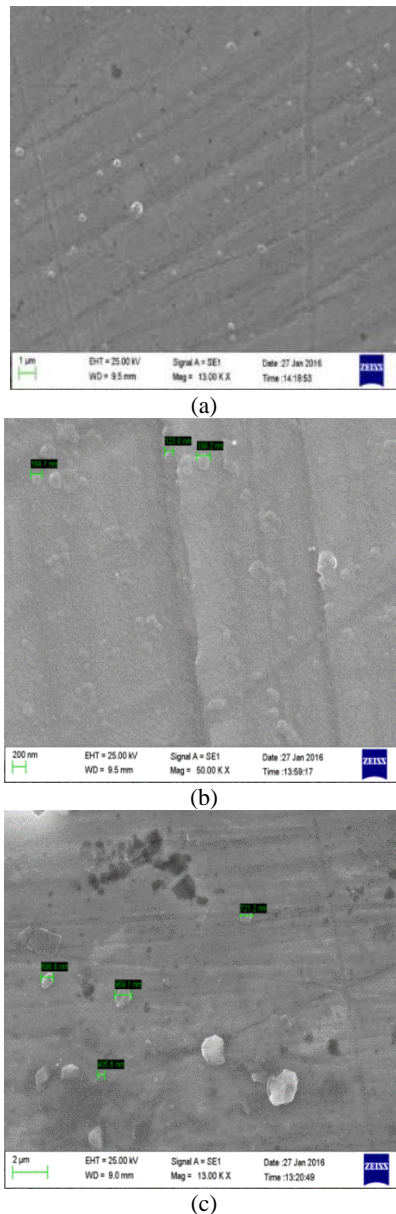


Figure 3. Scanning Electron Microscopy (SEM) image of accumulated SNPs at 0.9 keV ion beam energy (a) after 10s deposition time ($T_A\text{-Ag}_{10}$) with magnification 13KX and 40 KX, (b) after 20s deposition time ($T_A\text{-Ag}_{20}$) with magnification 13KX and 50 KX, (c) after 30s deposition time ($T_A\text{-Ag}_{30}$) with magnification 13KX and 40 KX

Since a hydrophobic surface usually has a contact angle higher than 70° , while a hydrophilic surface has a contact angle lower than 70° [32] and CA of the uncoated substrate (Ni-Cu alloy), shown in our previous work, is around 62° [20], this surface has the hydrophilic nature before coating. By DLC coating of the substrates, the hydrophobic property is induced to the surface due to the hydrophobic nature of the amorphous carbon films [33]. By depositing Ag clusters on the surface of DLC films, the value of the CA will vary between $79^\circ \pm 2 - 95^\circ \pm 2$ by increasing the volume percentage of Ag from 5.0 ± 2.01 to $16.3 \pm 1.4\%$.

The surface free energy can be calculated using Young–Dupre Equation (2) [34]:

$$E = \gamma(1 + \cos \theta) \quad (2)$$

where γ is the surface tension of water at 20°C ($\gamma = 72.8 \text{ mJ/m}^2$), and θ is the contact angle ($^\circ$).

The volume percentage of the DLC films covered by Ag clusters was calculated by image analysis software (Table 1). In addition, the weight percentage of Ag calculated by EDS analysis is reported in Table 1. As expected, the volume percentage and the weight percentage of Ag increase in the surface by increasing the deposition time of SNPs.

The result of calculating surface free energy by Equation 2 shows that the surface free energy decreases with the increase in the volume percentage and the weight percentage of Ag due to the increase in the deposition time on the surface of DLC film (Table 1).

When silver nanoparticles or silver ions accelerate towards the substrate, they first accumulate in high-energy areas of the surface. FESEM images of silver nanoparticles on the surface of DLC thin films (Figure S2) confirm this phenomenon. Therefore, with the accumulation of particles in high-energy areas, the reaction centers (dangling bonds) decrease on the surface, and as a result, the surface free energy decreases.

Since any factor that reduces the surface free energy of the interface increases the wetting angle and hydrophobic property [35, 36], hence, the increase in CA caused by silver particles deposition on the surface of DLC thin films is explained. This trend continues with an increase in concentration of Ag to a point that CA reaches

TABLE 1. The contact angle (CA), surface free energy, weight and volume percentage of accumulated Ag extracted from EDS analysis

Sample code	Contact angle ($^\circ$)	surface free energy (mJ/m^2)	Weight percentage (%)	Volume percentage (%)
T_A	$74^\circ \pm 1$	92 ± 1	0.00	0.0
$T_A\text{-Ag}_{10}$	$79^\circ \pm 2$	86 ± 2	0.29	5.0 ± 2.01
$T_A\text{-Ag}_{20}$	$87^\circ \pm 1$	75 ± 1	0.37	7.4 ± 0.35
$T_A\text{-Ag}_{30}$	$95^\circ \pm 2$	66 ± 2	0.57	16.3 ± 1.4

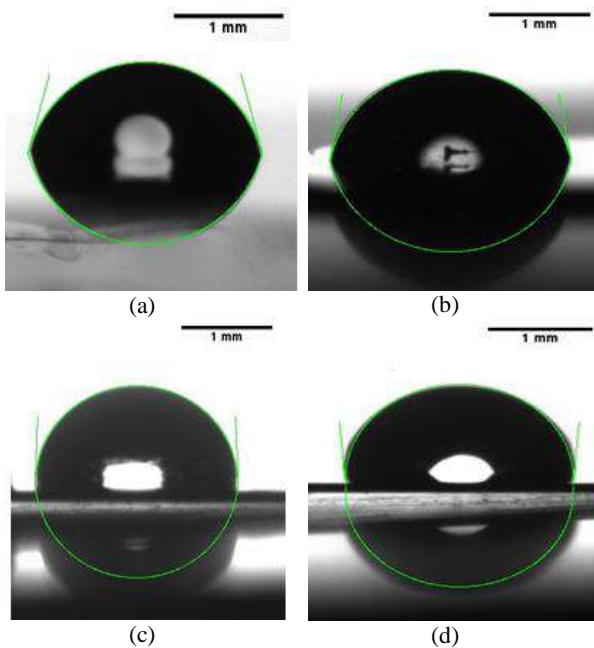


Figure 4. Profiles of the liquid distilled water droplet on DLC films deposited by different SNPs content (a) T_A (b) T_A-Ag_{10} (c) T_A-Ag_{20} and (d) T_A-Ag_{30}

$95^\circ \pm 2$ as a result of the increase in the Ag up to 16.3% volume percentage on the surface of DLC thin films.

Cavaliere et al. [12] deposited highly bactericidal Ag nanoparticle films on the glass by cluster beam deposition method.

Since there are several reports about improving hemocompatibility of the surface with antibacterial properties [32, 37], it can be concluded that with the accumulation of Ag on the surface of DLC film, hemocompatibility of the surface increases as a result of the increased hydrophobicity. The results from the other studies confirm our findings [24, 29, 38-40].

Figure 5 shows the transmittance and reflection spectra of DLC films deposited on a glass substrate at the same condition of Ni-Cu substrates. The values of optical density (OD) of DLC are presented in Figure S3. It was observed that the optical transmittance stays almost constant, but the reflection values increase in the visible and near-infrared region due to Ag deposition on the surface of DLC films. It means that, there are no significant physical changes in DLC films, but with an increase in light reflection from the surface, the amount of light absorption and hence the optical density in the DLC films decreases (Figure S3). We found that in addition to the increase in hydrophobicity of the DLC thin films caused by deposition of Ag, the optical density of DLC increases without any reduction in the transparency of DLC films; while according to the other studies [32] the transparency and optical band gap of DLC film decreased due to Ag incorporation in the film. The reduction in the total

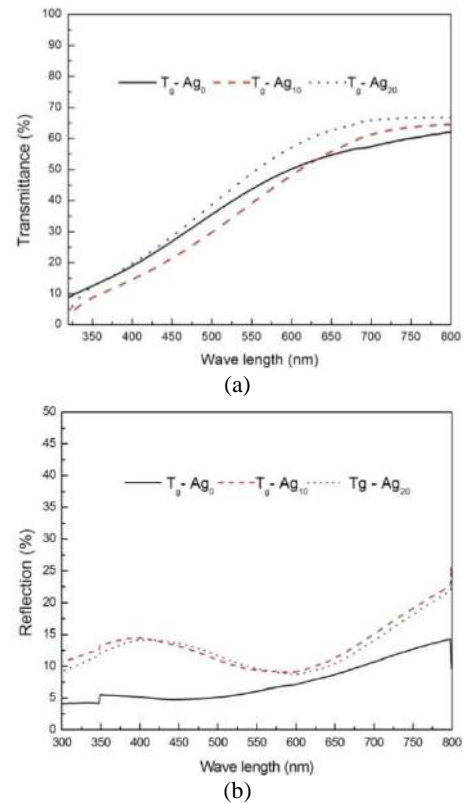


Figure 5. (a) Optical transmission and (b) the reflection of DLC films deposited on glass substrates

surface energy of Ag-incorporated DLC films are attributed to the decrease in both polar and dispersive component [32]; but due to the increase in sp^2/sp^3 ratio of the DLC films and the changes in electronic structure by the incorporation of substitutional defect states in the films, the transparency and optical band gap of Ag:DLC film is lower than pure DLC film [15, 16, 18].

Thus, as noted in the other research [8, 10], the hydrophobic surface is better than the hydrophilic surface for coating on medical device. Similarly, according to the results of this research the hydrophobicity of DLC films improved by accumulation Ag on the surface without destructive effects on the optical properties; it can be said that this coating method is an excellent candidate for a wide variety of engineering applications in optical devices and biomedical implantation.

4. CONCLUSION

Deposition of silver clusters on the DLC films was done uniformly at 0.9 keV ion beam energy by ion beam sputtering method.

The hydrophobicity of the DLC thin film on the Ni-Cu (70.4-29.6; W/W) alloy substrate has improved because of the deposition of silver clusters on the surface

of thin film. The contact angle shifted from $79^{\circ} \pm 2$ to $95^{\circ} \pm 2$ due to the increase in the Ag volume percentage in the surface of DLC films from 5.0 ± 2.01 to 16.3 ± 1.4 .

The reflection values increased in the visible and near-infrared region due to deposition of Ag on the surface of DLC thin films while the optical transmittance stayed almost constant. Therefore, an increase in the hydrophobicity and the optical density of the DLC thin films without any decrease in the transparency of DLC films is due to the deposition of Ag clusters.

In fact, with the accumulation of Ag in the high-energy areas on the surface of the DLC films, the reaction centers (dangling bonds) on the surface reduced and CA increased because of the decrease in the surface free energy. This kind of nanostructured DLC film is an excellent candidate for a wide variety of engineering applications in optical devices and biomedical applications.

5. ACKNOWLEDGMENT

The authors would like to acknowledge Mr. Majid Malek for his kind collaboration while working with IBSD system. Also, we would like to thank Yasser Amoosi for offering help in reviewing and revising the manuscript for grammar and syntax.

6. REFERENCES

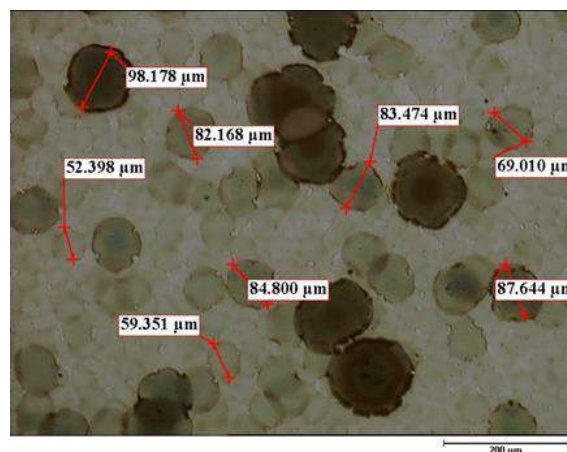
- Zhang, M., Xie, T., Qian, X., Zhu, Y., Liu, X., "Mechanical properties and biocompatibility of Ti-doped diamond-like carbon films." *ACS Omega*, Vol. 5, No. 36, (2020), 22772-22777, <https://doi.org/10.1021/acsomega.0c01715>.
- Robertson, J., "Diamond-like amorphous carbon." *Materials Science and Engineering: R: Reports*, Vol. 37, No. 4-6, (2002), 129-281, [https://doi.org/10.1016/S0927-796X\(02\)00005-0](https://doi.org/10.1016/S0927-796X(02)00005-0).
- Waseem, B.; Alam, S.; Irfan, M.; Shahid, M.; Farooq, M.; Soomro, B. D.; Hashim, S.; Iqbal, R., "Optimization and Characterization of Adhesion Properties of DLC Coatings on Different Substrates." *Materials Today: Proceedings*, Vol. 2, No. 10, Part B, (2015), 5308-5312. <https://doi.org/10.1016/j.matpr.2015.11.041>.
- HABIBI, B. H., GOLAZAR, M., "Morphological Characterization of Combustion Deposited Diamond Crystals and Films." *International Journal of Engineering, Transaction B: Applications*, Vol. 15, No. 3, (2002), 255-260. 2002.
- Peng, K.-Y., Wei, D.-H., Lin, C.-R., Yu, Y.-C., Yao, Y.-D., Lin, H.-M., "Hydrophobic and high transparent honeycomb diamond-like carbon thin film fabricated by facile self-assembled nanosphere lithography." *Japanese Journal of Applied Physics*, Vol. 53, No. 5S1, (2014), 05FC02. <https://doi.org/10.7567/JJAP.53.05FC02>.
- Mednikarov, B., Spasov, G., Babeva, T., Pirov, J., Sahatchieva, M., Popova, C., Kulischa, W., "Optical properties of diamond-like carbon and nanocrystalline diamond films." *Journal of Optoelectronics and Advanced Materials*, Vol. 7, No. 3, (2002), 1407-1413.
- Yang, P., Huang, N., Leng, Y. X., Chen, J. Y., Fu, R. K. Y., Kwok, S. C. H., Leng, Y., Chu, P. K., "Activation of platelets adhered on amorphous hydrogenated carbon (a-C:H) films synthesized by plasma immersion ion implantation-deposition (PIII-D)." *Biomaterials*, Vol. 24, No. 17, (2003), 2821-2829. [https://doi.org/10.1016/S0142-9612\(03\)00091-7](https://doi.org/10.1016/S0142-9612(03)00091-7).
- Jones, M. I., McColl, I. R., Grant, D. M., Parker, K. G., Parker, T. L., "Protein adsorption and platelet attachment and activation, on TiN, TiC, and DLC coatings on titanium for cardiovascular applications." *Journal of Biomedical Materials Research*, Vol. 52, No. 2, (2000), 413-421. [https://doi.org/10.1002/1097-4636\(200011\)52:2<413::AID-JBM23>3.0.CO;2-U](https://doi.org/10.1002/1097-4636(200011)52:2<413::AID-JBM23>3.0.CO;2-U).
- Chen, J. S., Lau, S. P., Sun, Z., Chen, G. Y., Li, Y. J., Tay, B. K., Chai, J. W., "Metal-containing amorphous carbon films for hydrophobic application." *Thin Solid Films*, Vol. 398-399, (2001), 110-115. [https://doi.org/10.1016/S0040-6090\(01\)01455-9](https://doi.org/10.1016/S0040-6090(01)01455-9).
- Juknius, T., Ružauskas, M., Tamulevičius, T., Šiugzdiniienė, R., Jukniene, I., Vasiliauskas, A., Jurkevičiūtė, A., Tamulevičius, S., "Antimicrobial properties of diamond-like carbon/silver nanocomposite thin films deposited on textiles: towards smart bandages." *Materials*, Vol. 9, No. 5, (2016), 371. <https://doi.org/10.3390/ma9050371>.
- Wai, K. P., Koo, C. H., Chong, W. C., Lai, S. O., Pang, Y. L., "Improving Hydrophilicity of Polyethersulfone Membrane Using Silver Nanoparticles for Humic Substances Removal." *International Journal of Engineering, Transactions B: Applications*, Vol. 31, No. 8, (2018), 1364-1372.
- Cavaliere, E., De Cesari, S., Landini, G., Riccobono, E., Palleschi, L., Rossolini, G. M., Gavioli, L., "Highly bactericidal Ag nanoparticle films obtained by cluster beam deposition." *Nanomedicine: Nanotechnology, Biology and Medicine*, Vol. 11, No. 6, (2015), 1417-1423. <https://doi.org/10.1016/j.nano.2015.02.023>.
- Ahmed, S. F., Moon, M.-W., Lee, K.-R., "Enhancement of electron field emission property with silver incorporation into diamondlike carbon matrix." *Applied Physics Letters*, Vol. 92, No. 19, (2008), 193502. <https://doi.org/10.1063/1.2926676>.
- Jastrzębski, K., Jastrzębska, A., Bociąga, A., "A review of mechanical properties of diamond-like carbon coatings with various dopants as candidates for biomedical applications." *Acta Innovations*, Vol. 22, (2017), 40-57.
- Choi, H. W., Choi, J.-H., Lee, K.-R., Ahn, J.-P., Oh, K. H., "Structure and mechanical properties of Ag-incorporated DLC films prepared by a hybrid ion beam deposition system." *Thin Solid Films*, Vol. 516, No. 2, (2007), 248-251. <https://doi.org/10.1016/j.tsf.2007.06.154>.
- Jing, P., Ma, D., Gong, Y., Luo, X., Zhang, Y., Weng, Y., Leng, Y., "Influence of Ag doping on the microstructure, mechanical properties, and adhesion stability of diamond-like carbon films." *Surface and Coatings Technology*, Vol. 405, (2021), 126542. <https://doi.org/10.1016/j.surfcoat.2020.126542>.
- de Oliveira, A., Placias, F., da Silva Sobrinho, A., Leite, D., Miyakawa, W., Neto, J. J., Koh, I., Liberatore, A., dos Santos, M., Matieli, J., "Secondary ion mass spectrometry and atomic force microscopy analysis of silver-doped diamond-like carbon films on titanium alloy (Ti6Al4V) for possible biomedical application." *Thin Solid Films*, Vol. 719, (2021), 138487. <https://doi.org/10.1016/j.tsf.2020.138487>.
- Ahmed, S. F., Moon, M.-W., Lee, K.-R., "Effect of silver doping on optical property of diamond like carbon films." *Thin Solid Films*, Vol. 517, No. 14, (2009), 4035-4038. <https://doi.org/10.1016/j.tsf.2009.01.135>.
- Koutsokeras, L., Constantinou, M., Nikolaou, P., Constantinides, G., Kelires, P., "Synthesis and Characterization of Hydrogenated Diamond-Like Carbon (HDLC) Nanocomposite Films with Metal (Ag, Cu) Nanoparticles." *Materials*, Vol. 13, No. 7, (2020), 1753. <https://doi.org/10.3390/ma13071753>.

20. Mohagheghpour, E., Rajabi, M., Gholamipour, R., Larijani, M. M., Sheibani, S., "Ion beam energy dependence of surface and structural properties of amorphous carbon films deposited by IBSD method on Ni-Cu alloy." *Journal of Materials Research*, Vol. 32, No. 7, (2017) 1258-1266. DOI:10.1557/jmr.2017.43.
21. Rycenga, M., Cobley, C. M., Zeng, J., Li, W., Moran, C. H., Zhang, Q., Qin, D., Xia, Y., "Controlling the Synthesis and Assembly of Silver Nanostructures for Plasmonic Applications." *Chemical Reviews*, Vol. 111, No. 6, (2011), 3669-3712. <https://doi.org/10.1021/cr100275d>.
22. Taglietti, A., Arciola, C. R., D'Agostino, A., Dacarro, G., Montanaro, L., Campoccia, D., Cucca, L., Vercellino, M., Poggi, A., Pallavicini, P., Visai, L., "Antibiofilm activity of a monolayer of silver nanoparticles anchored to an amino-silanized glass surface." *Biomaterials*, Vol. 35, No. 6, (2014), 1779-1788. <https://doi.org/10.1016/j.biomaterials.2013.11.047>.
23. Yliniemi, K., Vahvaselkä, M., Ingelgem, Y. V., Baert, K., Wilson, B. P., Terryn, H., Kontturi, K., "The formation and characterisation of ultra-thin films containing Ag nanoparticles." *Journal of Materials Chemistry*, Vol. 18, No. 2, (2008), 199-206. <https://doi.org/10.1039/B713313H>.
24. Liu, G., Wang, Y., Pu, X., Jiang, Y., Cheng, L., Jiao, Z., "One-step synthesis of high conductivity silver nanoparticle-reduced graphene oxide composite films by electron beam irradiation." *Applied Surface Science*, Vol. 349, (2015), 570-575. <https://doi.org/10.1016/j.apsusc.2015.05.044>.
25. Jeon, E. K., Seo, E., Lee, E., Lee, W., Um, M.-K., Kim, B.-S., "Mussel-inspired green synthesis of silver nanoparticles on graphene oxide nanosheets for enhanced catalytic applications." *Chemical Communications*, Vol. 49, No. 33, (2013), 3392-3394. <https://doi.org/10.1039/C3CC00115F>.
26. Lim, E. J., Choi, S. M., Seo, M. H., Kim, Y., Lee, S., Kim, W. B., "Highly dispersed Ag nanoparticles on nanosheets of reduced graphene oxide for oxygen reduction reaction in alkaline media." *Electrochemistry Communications*, Vol. 28, (2013), 100-103. <https://doi.org/10.1016/j.elecom.2012.12.016>.
27. Yu, X., Qin, Y., Wang, C. B., Yang, Y. Q., Ma, X. C., "Effects of nanocrystalline silver incorporation on sliding tribological properties of Ag-containing diamond-like carbon films in multi-ion beam assisted deposition." *Vacuum*, Vol. 89, (2013), 82-85. <https://doi.org/10.1016/j.vacuum.2011.11.007>.
28. Shin, J.-K., Lee, C. S., Lee, K.-R., Eun, K. Y., "Effect of residual stress on the Raman-spectrum analysis of tetrahedral amorphous carbon films." *Applied Physics Letters*, Vol. 78, (2001), 631-633. <https://doi.org/10.1063/1.1343840>.
29. Ferrari, A. C., "Interpretation of Raman Spectra of Disordered and Amorphous Carbon." *Physical Review B*, Vol. 61, (2000), 14095-14107. <https://doi.org/10.1103/PhysRevB.61.14095>.
30. Sánchez-Vergara, M. E., Alonso-Huitron, J. C., Rodríguez-Gómez, A., Reider-Burstin, J. N., "Determination of the Optical GAP in Thin Films of Amorphous Dilithium Phthalocyanine Using the Tauc and Cody Models." *Molecules*, Vol. 17, No. 9, (2012), . <https://doi.org/10.3390/molecules170910000>.
31. Banerjee, D., Mukherjee, S., Chattopadhyay, K. K., "Controlling the surface topology and hence the hydrophobicity of amorphous carbon thin films." *Carbon*, Vol. 48, No. 4, (2010), 1025-1031. <https://doi.org/10.1016/j.carbon.2009.11.021>.
32. Choi, H. W., Dauskardt, R. H., Lee, S.-C., Lee, K.-R., Oh, K. H., "Characteristic of silver doped DLC films on surface properties and protein adsorption." *Diamond and Related Materials*, Vol. 17, No. 3, (2008), 252-257. <https://doi.org/10.1016/j.diamond.2007.12.034>.
33. Vogler, E. A., "Structure and reactivity of water at biomaterial surfaces." *Advances in Colloid and Interface Science*, Vol. 74, No. 1-3, (1998), 69-117. [https://doi.org/10.1016/S0001-8686\(97\)00040-7](https://doi.org/10.1016/S0001-8686(97)00040-7).
34. Pauleau, Y., "Generation and evolution of residual stresses in physical vapour-deposited thin films." *Vacuum*, Vol. 61, No. 2, (2001), 175-181. [https://doi.org/10.1016/S0001-8686\(97\)00040-7](https://doi.org/10.1016/S0001-8686(97)00040-7).
35. Ostrovskaya, L. Y., Dementiev, A. P., Kulakova, I. I., Ralchenko, V. G., "Chemical state and wettability of ion-irradiated diamond surfaces." *Diamond and Related Materials*, Vol. 14, No. 3, (2005), 486-490. <https://doi.org/10.1016/j.diamond.2004.09.010>.
36. Ostrovskaya, L. Y., "Studies of diamond and diamond-like film surfaces using XAES, AFM and wetting." *Vacuum*, Vol. 68, No. 3, (2002), 219-238. [https://doi.org/10.1016/S0042-207X\(02\)00460-8](https://doi.org/10.1016/S0042-207X(02)00460-8).
37. Kwok, S., Zhang, W., Wan, G., McKenzie, D., Bilek, M., Chu, P. K., "Hemocompatibility and anti-bacterial properties of silver doped diamond-like carbon prepared by pulsed filtered cathodic vacuum arc deposition." *Diamond and Related Materials*, Vol. 16, No. 4-7, (2007), 1353-1360. <https://doi.org/10.1016/j.diamond.2006.11.001>.
38. Aisenberg, S., Chabot, R., "Ion-beam deposition of thin films of diamondlike carbon." *Journal of applied physics*, Vol. 42, No. 7, (1971), 2953-2958. <https://doi.org/10.1063/1.1660654>.
39. Oganov, A. R., Hemley, R. J., Hazen, R. M., Jones, A. P., "Structure, bonding, and mineralogy of carbon at extreme conditions." *Reviews in Mineralogy and Geochemistry*, Vol. 75, No. 1, (2013), 47-77. <https://doi.org/10.2138/rmg.2013.75.3>.
40. Paulmier, T., Bell, J. M., Fredericks, P. M., "Deposition of nanocrystalline graphite films by cathodic plasma electrolysis." *Thin Solid Films*, Vol. 515, No. 5, (2007), 2926-2934. <https://doi.org/10.1016/j.tsf.2006.08.027>.

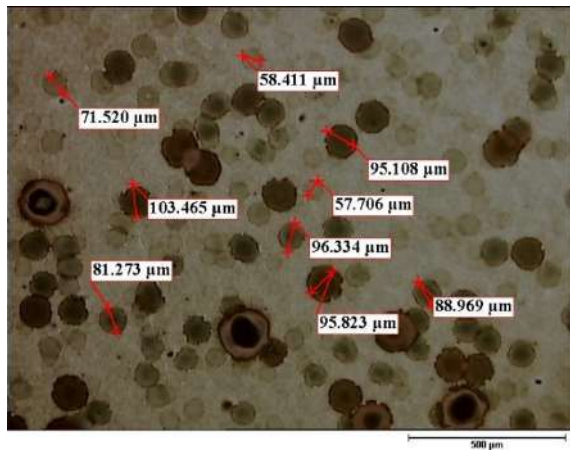
7. APPENDIX

TABLE S1. The data extracted from Gaussian deconvolution of Ramman spectra

Sample code	G- peak (cm-1)	I _D /I _G ratio	La(Å)
Tg	1541.7	0.072	3.62
TA	1577.9	0.062	3.36



(a)



(b)

Figure S1. Microscopic images of accumulated silver cluster at 1.2 keV ion beam energy

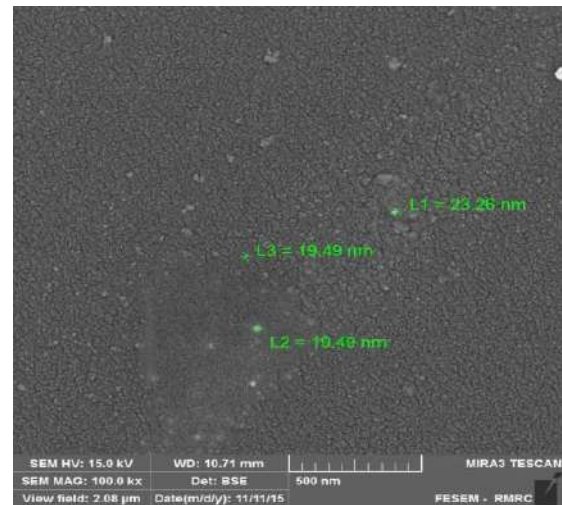


Figure S2. Field Emission Scanning Electron Microscopy (FESEM) image of accumulated silver nano particles at 0.6 keV ion beam energy

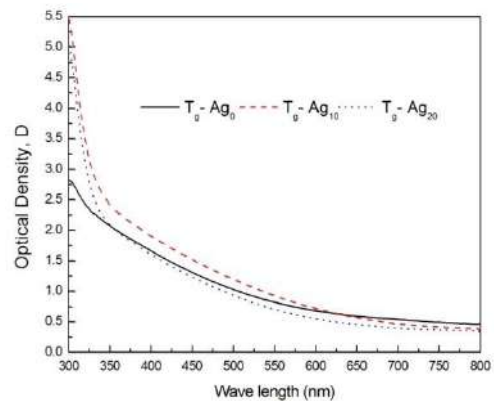
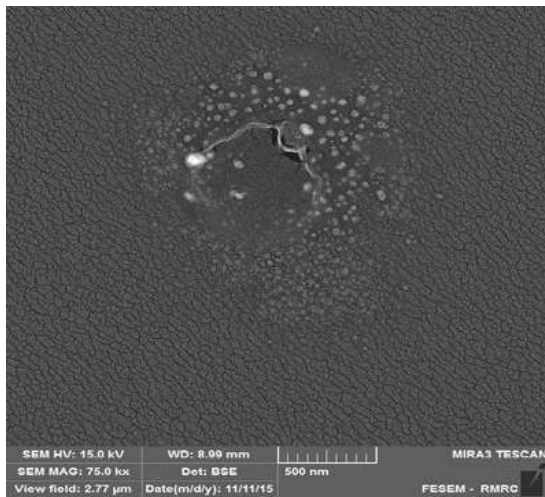


Figure S3. Optical density of DLC films with accumulated SNPs on the surface

Persian Abstract

چکیده

در تحقیق حاضر، تاثیر انباشت خوشه‌های نقره بر خواص نوری، تشرودنگی و خواص سطحی فیلم کربن شبه‌الماسی (DLC) بررسی شده است. نقره و فیلم DLC بر زیرلایه آلایژ نیکل-مس (W/W: 70/4-29/6) با استفاده از روش کندوپاش پرتو یونی (IBSD) انباشت شد. خواص نوری و ساختاری به ترتیب با استفاده از طیف سنجی فرابنفش-مرئی و رامان انجام شد. تشرودنگی و خواص سطحی لایه‌ها با استفاده از زاویه تشرودنگی (CA) اندازه‌گیری شد. طیف رامان فیلم DLC با ضخامت 6 ± 121 nm بدون انباشت نقره نشان می‌دهد که اندازه کریستالهای گرافیت با پیوندهای sp^2 $3/36 \text{ \AA}$ ، نسبت I_D/I_G برابر با 0/062 و انرژی باند گپ 3eV می‌باشد که با استفاده از معادله تاک بدست آمده است. نتیجه انباشت نقره در انرژی یون متفاوت بین 0/6keV تا 2 keV نشان‌دهنده انباشت خوشه‌های نقره به صورت یکنواخت بر روی فیلم DLC در 0/9 keV می‌باشد. درصد حجمی خوشه‌های نقره از $5/0 \pm 2/01$ تا $16/1 \pm 1/40$ تغییر می‌کند. تغییرات با کنترل ولتاژ شتاب‌دهنده و زمان انباشت ایجاد می‌شود. CA در فیلم‌های انباشت شده از $79^\circ \pm 2$ به $95^\circ \pm 2$ افزایش می‌یابد و مقادیر انعکاس در محدوده مرئی و فروسرخ نزدیک در نتیجه افزایش غلظت نقره در سطح فیلم DLC افزایش می‌یابد در حالی که انرژی آزاد سطح از $1 \pm 86 \text{ mJ/m}^2$ به $1 \pm 66 \text{ mJ/m}^2$ کاهش می‌یابد و میزان عبور نور تقریباً ثابت می‌ماند. نتایج نشان می‌دهد که انباشت ذرات نقره بر فیلم‌های DLC با توجه به ویژگی آبگریزی خوب بدون تاثیر مخرب بر خواص نوری فیلم DLC پتانسیل استفاده برای کاربردهای بیوپزشکی را دارا می‌باشد.



Direct Drive Friction Welding Joint Strength of AISI 304

A. Jabbar Hassan^{a*}, T. Boukharouba^a, D. Miroud^b, N. Titouche^c, S. Ramtani^d

^a LMA, USTHB, BP. 32, El-Alia, 16111 Bab-Ezzouar, Algiers, Algeria

^b LSGM, USTHB, BP. 32; El-Alia, 16111 Bab-Ezzouar, Algiers, Algeria

^c DE M E M, DTN, Centre de Recherche Nucléaire de Birine, BP. 180, Ain Oussera, Djelfa, Algeria

^d CSPBAT-LBPS, UMR 7244 CNRS, Paris University, Galilée Institute, Villetaneuse, France

P A P E R I N F O

Paper history:

Received 04 November 2020

Received in revised form 15 December 2020

Accepted 18 January 2021

Keywords:

Austenitic Stainless Steel

Micro-hardness

Ultimate Tensile Strength

A B S T R A C T

The present study describes the effect of friction welding process on mechanical and metallurgical properties of AISI 304 steel. The joints were made by direct drive friction welding (DDFW) machine, while the characteristics of friction welded joints were evaluated by macro-microstructure, microhardness, tensile test with 4 mm and 6 mm effective diameter, and scanning electron microscope (SEM). The results showed severe flash formation at stationary side related to rotating side, highly plastically deformed zone (HPDZ) was revealed at the interface with large dimension of 110 μm . Maximum microhardness values were recorded at welded center and increased from peripheral to central zones. Reducing ratio of ultimate tensile strength (UTS) and ductility for welded joint related to AISI 304 were 86 and 67%, respectively. Tensile fractures occurred adjacent to the interface at thermo-mechanically affected zone (TMAZ). Fracture morphologies by SEM were discovered cleavage features and mostly ductile mode with micro-porosities of different forms and dimensions.

doi: 10.5829/ije.2021.34.03c.16

1. INTRODUCTION

The metal used in the present study is austenitic stainless steel (AISI 304), which has several applications such as in chemical, petrochemical, medical, food processing and pharmaceutical equipment, cryogenic vessels, heat exchangers and corrosive environments. AISI 304 is weldable by fusion processes [1], but fusion welding produces harmful welded joint characterizations such as phase transformation in the welding and heat affected zone. Therefore, to avoid all these problems several studies have attempted to replace fusion welding by modern techniques such as friction welding [2].

Friction welding is one of the solid state welding techniques; it provides welding below melting temperature of the metal being joined. There are two most famous processes: DDFW [3] and friction stir [4-8]. DDFW is a technique which causes joining by heat developed between contact surfaces under effect of rotation speed and applied pressure. In this setup, one part

is stationary, while the other is rotating and the two are still in contact with each other until rotation is stopped abruptly, where the pressure increases to complete welded joint. This technique is preferred because of sub-melting temperature, high reproducibility, low input energy, easy and fast procedure with reduced formation intermetallic compounds [3, 9]. Principle applications of friction welding technology are for fabrication of automobile parts like drive shafts, engine valves, pumps and compressor [10].

Several works have reported the influence of friction welded joint on the characterization of AISI 304. According to earlier studies, Sahin [11] proposed that suitable welding conditions for 10 mm diameter of AISI 304 were 1440 rpm (rotation speed), 60 MPa (friction pressure), 110 MPa (forging pressure) and 9 s (friction time). Bouarroudj et al. [10] also have mentioned and considered these conditions. Sathiya et al. [12] have showed that tensile strength of friction welded joints exhibited equivalent strength with AISI 304. SEM

*Corresponding Author Email: jabbarhassan1973@yahoo.fr (A. Jabbar Hassan)

observations showed ductile mode on the tensile fracture surface morphology without dimples. The impact strength is more or less the same as that of AISI 304 material. Thus, impact fracture surface morphology by SEM also observed ductile mode without dimples. The increase in hardness at the welded joint zone may be credited to the heating temperature of material at the welding region. Hassan et al. [13] have reported the results of compression yield strength with different angles of 0, 45 and 90° under effect of friction time for AISI 304. The values of compression yield strength for AISI 304 reduced with increasing friction time for 0° angle, whilst 45 and 90° angle kept comparatively at the same values. From the compression results, apparent anisotropy of the yield strength of AISI 304 under effect of friction time is obvious.

AISI 304 is one of the most famous steels in manufacturing. It is used fundamentally in applications relating to continuous and alternating high service temperatures. This study is aimed at contributing to understanding of the mechanical and metallurgical behavior of DDFW for AISI 304. The strength of friction welding joints were estimated by macro-microstructure to view physical consideration of welded joint, microhardness examinations for welding region distinguish along the axial direction and variations along with interface. On the other hand, according to the values of microhardness along with interface, which will liable on variation of microstructural and mechanical properties along the interface, tensile tests were carried out for two effective diameters of 4 mm and 6 mm. SEM observation, finally, exposes nature of tensile fracture morphology for welded joint and compared to AISI 304.

2. MATERIALS AND METHOD

Austenitic stainless steels AISI 304 has a Ref. No. of 4301 according to the original technical chart. It received as a long shaft of 6 m length. The metal was cut to small pieces (12 mm diameter and 45 mm length). Microstructural and mechanical tests were carried out in LMA and LSGM, USTHB, Algeria. AISI 304 is a high Cr and Ni steel as shown in Table 1, and it has excellent mechanical properties as revealed in Tables 2. Figure 1 shows the optical microstructure of austenitic equiaxed grains for AISI 304. Figure 2 exposes DDFW conditions variation during time of welding.

Friction welding machine used in the present study was designed and fabricated as a DDFW machine; it is CNC machine as shown in Figure 3. This machine has

TABLE 1. Alloying elements of AISI 304 (wt.%)

C	Mn	Si	P	S	Mo	Cr	Ni
0.070	1.650	0.750	0.045	0.030	0.80	19.00	8.00

TABLE 2. Mechanical properties of AISI 304 (as it is, Ref. No. 4301)

UTS (MPa)	Young's modulus (MPa)	Elongation (%)	Average $H_{V0.1}$
760 - 780	$1.93 \cdot 10^5$	≈ 47	280 - 285

operating speed varied from 0 to 3000 rpm and maximum pressure applied is 300 MPa. Welding conditions were rotation speed 3000 rpm; friction pressure 130 MPa; friction time 10 s; forging pressure 260 MPa and forging time 5 s. These welding conditions depended principally on the type of metal, dimension of specimen and last publication articles [2, 3, 9, 13].

NIKON SMZ 745T device was used for macroscopic observations with a magnification of X 0.67 to evaluate flash formation and macro-graphic of welded joint. NIKON ECLIPSE LV100ND apparatus was utilized for



Figure 1. Optical microstructure of the base metal, AISI 304

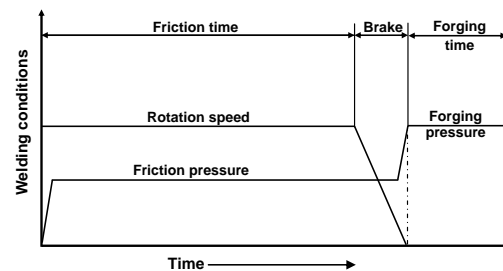


Figure 2. DDFW conditions diagram

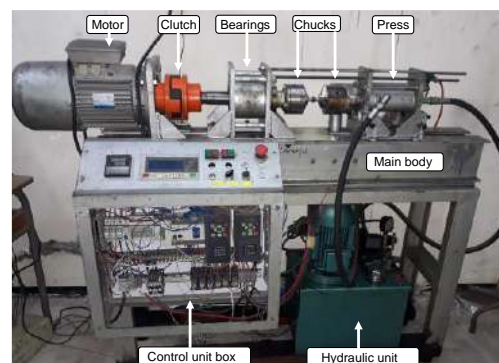


Figure 3. DDFW machine used in the present study

microscopic observations with a magnification of X 50 and X 100. Microstructure test piece was cut by using a Presi mecatome T180 cutting machine. The test pieces were embedded in a cold curing epoxy resin and polished with wet SiC abrasive paper up to 1200 grit and followed by polishing with 1 μm diamond polishing paste. The electrolytic etching of the test pieces was carried out by STRUERS LECTROPOL-5 equipment by 10 g oxalic acid hydrate and 90 ml water at 15 V for period of 300 s. Tensile fracture surface observations were realized by scanning electronic microscopy (SEM) using JEOL JSM-6360 device; the magnification of images were X 50 and X 300.

SHIMADZU HMV tester machine was carried out for microhardness measurements according to ASTM E384 specifications. The tests were achieved at room temperature with 100 gf indentation force and 10 s dwell time. Micro-hardness measurements performed along the axial direction and the interface. The tensile test specimens were cut by the lathe machine in the axial direction under standard specification of ISO 6892-1: 2009 (F) with effective diameter of 4 mm and 6 mm. Tensile tests were achieved by INSTRON 5500 universal testing machine with load capacity of ± 100 kN. The quasi-static strain rate was 0.0016 s⁻¹.

3. RESULTS AND DISCUSSION

During friction welding operation, as the temperature increases due to high rotation speed and pressure, accumulated heat causes the metal to be softened at the interface, and the metal moves toward the peripheral to form flash. Figure 4a reveals large amount of flash formation built up on the rotating side due to mechanical action. AISI 304 contains high amounts of Cr and Ni that make it more refractory, which requires high pressure and temperature during welding process to obtain significant amount of flash [3]. According to previous study, the degree of flash formation depends on the mechanical properties of the metal being welded [14] such as hardness [15] and on the capability of the metal to undergo thermo-plastic deformation [13]. Figure 4b shows macro-graphic view of the welded joint. It shows the amount of thermo-plastic deformation during process, which is responsible for flash formation and large separation of welding line.

Figure 5 demonstrates different magnifications of microscopic investigation for welding center. From this figure, it is possible to find out HPDZ at the interface, with very fine grains and moderately blackish color. The HPDZ is 110 μm ; this zone is created because of period of friction and forging which causes large amount of plastic deformation.

Forging pressure is responsible for dynamic recrystallization at welding interface, that leads to refinement of grains to form HPDZ. While, high plastic

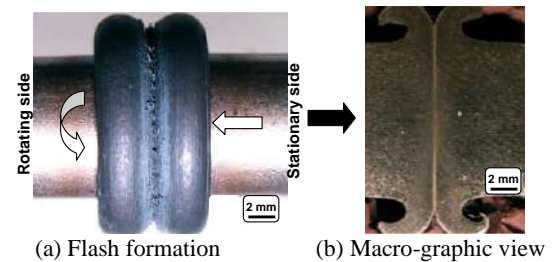


Figure 4. Macro-graphic observation for welded joint

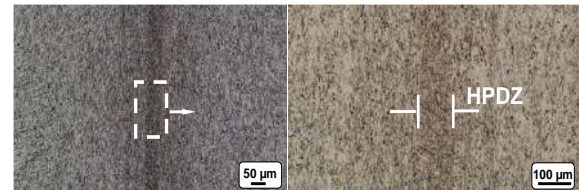


Figure 5. Microstructure of welded joint

deformation and elevated temperature are blaming on this. Grain size, deformation conditions, chemical composition and nature of crystal structure are most important factors that affect dynamic recrystallization [16].

Khidhir and Baban [15] welded AISI 1045 and AISI 316L by DDFW and have found grain refinement at welding joint for side of AISI 316L due to severe plastic deformation of grains because of dynamic recrystallization. Generally, Cr-Ni-Mo austenitic stainless steel improves the microstructure grains and longer friction time obtains high thermo-plastic deformation that control the dimension of HPDZ. Therefore, grain refinement occurs at welding region due to dynamic recrystallization, thermo-mechanical-deformation and quality of welding. HPDZ does not extend to the peripheral because of temperature, dynamic recrystallization and thermo-plastic deformation have not the same effect along the interface [3].

Microhardness profile along the axial direction as demonstrated in Figure 6 explains that there are three basic regions depending on the microhardness variations. The first region is HPDZ; microhardness at this region is very high related to the base metal with average value is 310 $\text{Hv}_{0.1}$ and dimension of 110 μm as mentioned in microscopic investigation. HPDZ is created because of high friction and forging pressure application under effect of input heat during process. Second region is TMAZ at neighboring of the interface of welding joint with low values of microhardness related to AISI 304 with average 270 $\text{Hv}_{0.1}$ and enlarged dimensions of at least of 450 μm . Input heat along the axial direction permits TMAZ to expand due to speed of cooling guides to grain growth [15]. Third region is the base metal or zone which is not affected by heat of welding; average of micro-hardness is 285 $\text{Hv}_{0.1}$.

Figure 7 shows the microhardness profile along the interface with high values of microhardness of AISI 304, highest values recorded at the welding center. However, microhardness decreases when moving from central toward peripheral. This is because the interface is subject to highest changes of pressure and temperature during welding process. P. M. AJITH et al. [17-18] have proposed that the elevation of microhardness is due to high friction pressure. Friction pressure and temperature cause thermoplastic deformation and dynamic recrystallization along the interface resulting in fine grains.

According to Figure 7, and as mentioned previously that the maximum values of micro-hardness were recorded at the welding center, though, these values are falling when moving from central toward peripheral, which will responsible on the variation of micro-structural and mechanical properties along the interface. Therefore, tensile tests were carried out for two effective diameters of 4 mm and 6 mm of welding joint as well as for the AISI 304. The propagation of deformation through the tests were measured locally by the displacement sensor with $19.5 \text{ mm} \pm 2.5$ open space; the sensor was chucked on the tensile piece around the welding interface. The welding line was put at the center of the tensile pieces, which allows to achieve an accurate strain sensor position. Figure 8 illustrates tensile test curves for welding joint with 4 mm and 6 mm related to AISI 304.

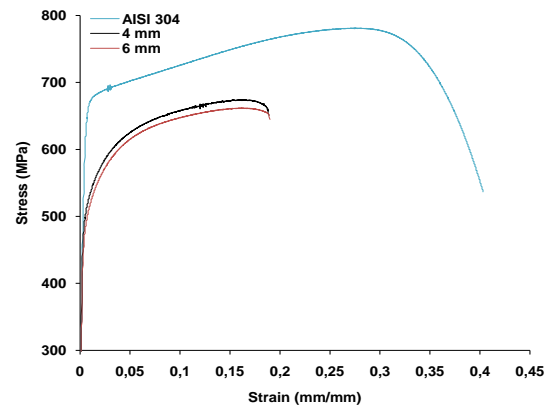


Figure 8. Curves of tensile tests for 4 mm and 6 mm with regard to AISI 304

Table 3 shows tensile tests results. The values of UTS for 4 mm and 6 mm are about 86 and 84% respectively for AISI 304, while, the ductility for 4 mm and 6 mm are approximately 67%. According to previous studies, welding conditions have important effect on UTS and ductility. Kirik and Ozdemir [14] have exposed that UTS related to the amount of input heat and plastic deformation at the interface under effect of high rotation speed. Handa et al. [19] have explained that welding conditions influence the UTS and ductility due to thermoplastic deformation in the bond line which increases during welding process and leads to more mass displaced at the interface.

Figure 9 illustrate tensile specimens after the tests. The position of fracture as shown in the figure in the zone is closer to the welding interface at TMAZ (Figure 10) for both cases of 4 mm and 6 mm. This region as shown in the figure, contains deformed grains due to high rotation speed and severe pressure, that also cause micro defects along grains boundary. In addition, TMAZ absorbs high amount of input heat and causes grain growth as mentioned previously which is responsible for weakness in tension. Table 4 demonstrates the results of necking region, the elongation values for 4 mm and 6 mm are around 22.04 and 22.27%, respectively. The values of reduction in cross sectional area for 4 mm and 6 mm are roughly 25 and 30%, respectively. Consequently, elongation in the gauge length and the necking as shown in the fracture position clarifies the quantity of input heat at TMAZ.

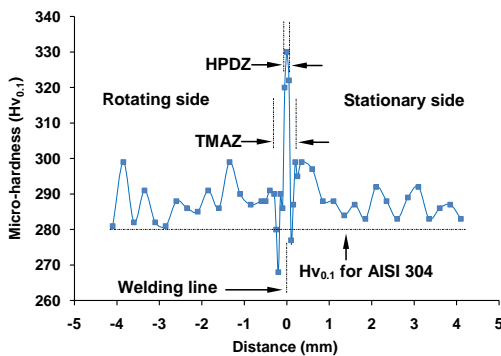


Figure 6. Micro-hardness profile along the axial direction

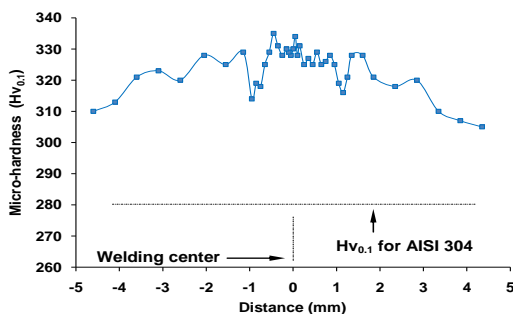


Figure 7. Micro-hardness profile along the interface

TABLE 3. Tensile tests results

Case	UTS (MPa)	ϵ_{max} (mm/mm)	UTSwelded/UTS AISI 304 (%)	$\frac{\epsilon_{max} \text{ welded}}{\epsilon_{max} \text{ AISI 304}}$ (%)
AISI 304	781	0.403	100	100
4 mm	674	0.189	86	67
6 mm	661	0.191	84	67

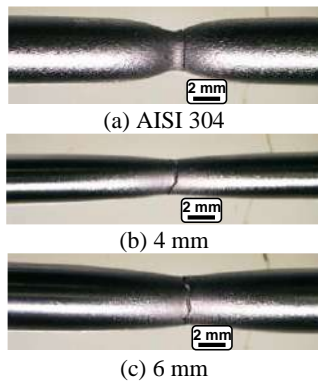


Figure 9. Tensile fracture position for 4 mm and 6 mm diameter with regard to AISI 304

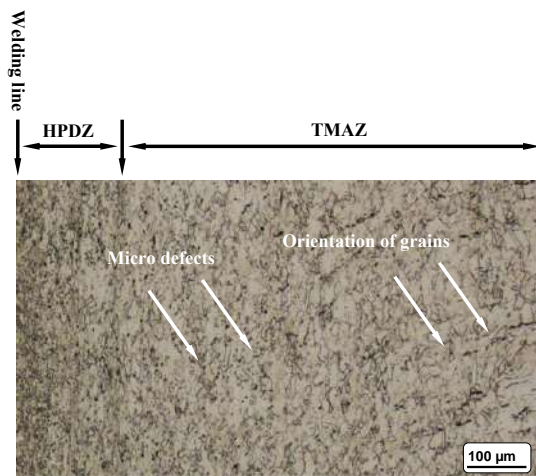


Figure 10. Microstructure of rotating side reveals orientation of grains and micro defects

TABLE 4. Necking results of tensile test pieces

Case	Elongation (%)	Reduction in cross sectional area (%)
AISI 304	47.00	55
4 mm	22.04	25
6 mm	22.27	30

Figure 11 shows nature of fracture morphology as revealed by SEM for 4 and 6 mm as well as AISI 304. Magnification of center region of fracture shows cleavage features with most ductile mode and microporocities of different forms and dimensions. It also reveals some form of fingerprint as a result of large amounts of thermoplastic deformation under influence of high pressure and rotation speed. This guides the soft metal to flow from the center towards the peripheral during welding process [9, 20]. However, fracture mechanism of welded joints and AISI 304 seem clear. For AISI 304 there is a ductile zone of fracture (A), circle

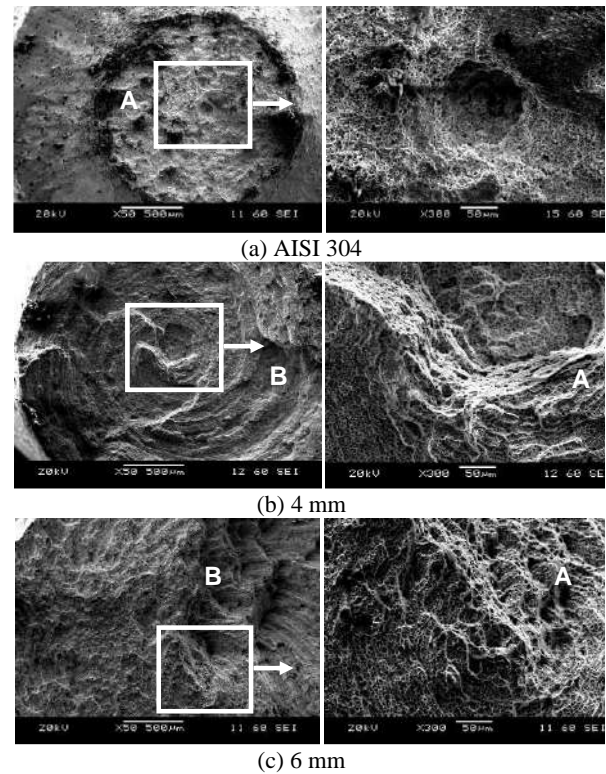


Figure 11. Tensile fracture surface for 4 mm and 6 mm with regard to AISI 304

of deformation determines this nature of fracture. As shown welded joint fracture for 4 mm and 6 mm, there are two important regions, zone (A) clears most ductile and micro deformation, while zone (B) shows fracture propagation with severe deformation through fingerprint. The same opinion was clarified in the microstructure of rotating side, where the fracture occurred, which reveals the orientation of grains and micro defects under influence of rotation speed and high pressure.

4. CONCLUSION

Effect of direct drive friction welding on the evolution of metallurgical and mechanical properties of AISI 304 are summarized as follows:

- Large amounts of flash is built up on the rotating side due to mechanical action,
- High plastic deformation zone (HPDZ) appears at the interface, with very fine grains and moderately blackish color with dimension of 110 μm,
- There are three basic regions depending on the microhardness variations; the first region is HPDZ, with average microhardness value of 310 Hv_{0.1}. The second region is TMAZ at neighboring of welding interface with low average values of micro-hardness of 270 Hv_{0.1}. The

third region is the base metal or zone which is not affected by heat of welding with average of microhardness of 285 Hv_{0.1},

- The values of UTS for 4 mm and 6 mm are about 86 and 84%, respectively for AISI 304. While, the value of ductility for both 4 mm and 6 mm is approximately 67 % for AISI 304,

- The position of fracture in the zone is closer to the welding interface at TMAZ for both cases of 4 mm and 6 mm; this region is absorbing high amount of input heat and that is the reasons for grain growth,

- Fracture morphology shows cleavage features with most ductile mode and micro-porocities mocroporosities of different forms and dimensions.

5. REFERENCES

- Rizvi, S. A., Effect of Heat Input on Microstructural and Mechanical Properties of AISI 304 Welded Joint Via MIG Welding, *International Journal of Engineering, Transactions C: Aspects* Vol. 33, No. 9, (2020), 1811-1816, <https://doi.org/10.5829/IJE.2020.33.09C.16>.
- Titouche, N., Boukharoubab, T., Amzert, S., Hassan, A. J., Lechelal, and R., Ramtani, S., Direct Drive Friction Welding Effect on Mechanical and Electrochemical Characteristics of Titanium Stabilized Austenitic Stainless Steel (AISI 321) Research Reactor Thick Tube, *Journal of Manufacturing Processes*, Vol. 41 (2019), 273-283, <https://doi.org/10.1016/j.jmapro.2019.03.016>.
- Hassan, A. J., Boukharouba, T., Miroud, D, and Ramtani, S., Metallurgical and Mechanical Behavior of AISI 316- AISI 304 during Friction Welding Process, *International Journal of Engineering , Transactions B: Applications*, Vol. 32, No. 2, (2019), 284-291, <https://doi.org/10.5829/ije.2019.32.02b.16>.
- Ethiraj, N., Sivabalan, T., Sivakumar, B., Vignesh Amar, S., N. Vengadeswaran, and Vetrivel K., Effect of Tool Rotational Speed on the Tensile and Microstructural Properties of Friction Stir Welded Different Grades of Stainless Steel Joints, *International Journal of Engineering, Transactions A: Basics*, Vol. 33, No. 1, (2020), 141-147, <https://doi.org/10.5829/ije.2020.33.01a.16>.
- Villegas, J.F., Guarín, A.M., and Unfried-Silgado, J., A Coupled Rigid-viscoplastic Numerical Modeling for Evaluating Effects of Shoulder Geometry on Friction Stir-welded Aluminum Alloys, *International Journal of Engineering, Transactions B: Applications*, Vol. 32, No. 2, (2019), 184-191, <https://doi.org/10.5829/ije.2019.32.02b.17>.
- Hasanzadeh, R., Azdast, T., Doniavi, A., Babazadeh, S., Lee, R. E., Daryadel, M., and Shishavan, S. M., Welding Properties of Polymeric Nanocomposite Parts Containing Alumina Nanoparticles in Friction Stir Welding Proces, *International Journal of Engineering Transactions A: Basics*, Vol. 30, No. 1, (2017): 143-151, <https://doi.org/10.5829/idosi.ije.2017.30.01a.18>.
- Singh, R., Rizvi, S. A., and Tewari, S. P., Effect of Friction Stir Welding on the Tensile Properties of AA6063 Under Different Conditions, *International Journal of Engineering, Transactions A: Basics*, Vol. 30, No. 4, (2017), 597-603, <https://doi.org/10.5829/idosi.ije.2017.30.04a.19>.
- Shishavan, S. M., Azdast, T., Aghdam, K. M., Hasanzadeh, R., Moradian, M., and Daryadel, M., Effect of Different Nanoparticles and Friction Stir Process Parameters on Surface Hardness and Morphology of Acrylonitrile Butadiene Styrene, *International Journal of Engineering Transactions A: Basics*, Vol. 31, No. 7, (2018), 1117-1122, <https://doi.org/10.5829/ije.2018.31.07a.16>.
- Hassan, A. J., Boukharouba, T., and Miroud, D., Characterizations of Friction Welding Joint Interface for AISI 316, *China Welding*, Vol. 28, No. 1, (2019), 42-48, doi: 10.12073/j.cw.20180811001.
- Bouarroudj E., Chikh S., Abdi S., Miroud D., Thermal Analysis During Rotational Friction Welding, *Applied Thermal Engineering*, Vol. 110, (2017), 1543-1553. <https://doi.org/10.1016/j.applthermaleng.2016.09.067>.
- Sahin, M., Evaluation of the Joint-Interface Properties of Austenitic-Stainless Steels (AISI 304) Joined by Friction Welding, *Materials & Design*, Vol. 28, No. 7, (2007), 2244-2250, <https://doi.org/10.1016/j.matdes.2006.05.031>.
- Sathiya, P., Aravindan, S., and Noorul Haq, A., Mechanical and Metallurgical Properties of Friction Welded AISI 304 Austenitic Stainless Steel, *International Journal of Advanced Manufacturing Technology*, Vol. 26, (2005), 505-511, DOI 10.1007/s00170-004-2018-6
- Hassan, A. J., Boukharouba, T., and Miroud, D, Friction Welding of AISI 304: Effect of Friction Time on Micro-structure, Micro-hardness and Tension-Compression Properties, *Acta Metallurgica Slovaca*, Vol. 26, No. 3, (2020), 78-84, <https://doi.org/10.36547/ams.26.3.631>
- Kirik, I., and Ozdemir, N., Weldability and Joining Characteristics of AISI 420/AISI 1020 Steels using friction welding, *International Journal of Materials Research*, Vol. 104, No. 8, (2013), 769-775, <https://doi.org/10.3139/146.110917>.
- Khidhir, G. I., and S. A. Baban, Efficiency of Dissimilar Friction Welded 1045 Medium Carbon Steel and 316L Austenitic Stainless Steel Joints, *Journal of Materials Research and Technology*, Vol. 8, No. 2, (2019), 1926-1932, <https://doi.org/10.1016/j.jmrt.2019.01.010>.
- Hassan, A. J., Boukharouba, T., and Miroud, D., Concept of Forge Application Under Effect of Friction Time for AISI 316 Using Friction Welding Process, *International Journal of Advanced Manufacturing Technology*, Vol. 112, No. 7-8, (2021), 2223-2231, <https://doi.org/10.1007/s00170-020-06421-4>.
- Ajith, P. M., Afsal Husain, T. M., Sathiya, P., and Aravindan, S., Multi-objective Optimization of Continuous Drive Friction Welding Process Parameters Using Response Surface Methodology with Intelligent Optimization Algorithm, *Journal of Iron and Steel Research, International*, Vol. 22, No. 10, (2015), 954-960, [https://doi.org/10.1016/S1006-706X\(15\)30096-0](https://doi.org/10.1016/S1006-706X(15)30096-0).
- Ajith, P.M., Barik, B. K., Sathiya, P., and Aravinda S., Multiobjective Optimization of Friction Welding of UNS S32205 Duplex Stainless Steel, *Defence Technology*, Vol. 11, (2015), 157-165, <https://doi.org/10.1016/j.dt.2015.03.001>.
- Handa, A., and Chawla, V., Mechanical Characterization of Friction Welded Dissimilar Steels at 1000 rpm, *Materials Engineering*, Vol. 20, (2013), 102-111, <http://fstroj.uniza.sk/journal-mi/PDF/2013/14-2013.pdf>.
- Hassan, A. J., Boukharouba, T., Miroud, D, Titouche, N., and R., Ramtani, S., Experimental Investigation of Friction Pressure Influence on the Characterizations of Friction Welding Joint for AISI 316, *International Journal of Engineering, Transactions C: Aspects*, Vol. 33, No. 12, (2020), 2514-2520, <https://doi.org/10.5829/ije.2020.33.12c.12>.

Persian Abstract

چکیده

مطالعه حاضر تأثیر فرایند جوشکاری اصطکاکی بر خصوصیات مکانیکی و متالورژیکی فولاد AISI 304 را توصیف می‌کند. اتصالات توسط دستگاه جوش اصطکاکی درایو مستقیم (DDFW) ساخته شده‌اند. اتصالات جوش داده شده اصطکاکی توسط ریزساختار، ریزسختی، آزمایش کشش با قطر موثر 4 و 6 میلی‌متر و میکروسکوپ الکترونی روبشی (SEM) ارزیابی شده است. نتایج نشان داد که شکل‌گیری شدید پلیسه در سمت ثابت (مربوط به سمت چرخش)، منطقه تغییر شکل یافته (HPDZ) موم‌سان وسیع با ابعاد 110 میکرومتر است. مقادیر حداکثر سختی در مرکز جوش داده شده ثبت شد و از مناطق پیرامونی به مناطق مرکزی افزایش یافت. کاهش استحکام کششی نهایی (UTS) و شکل‌پذیری برای اتصال جوش داده شده به ترتیب 86 و 67٪ برای AISI 304 مشاهده شد. شکستگی‌های کششی در مجاورت رابط در منطقه تحت تأثیر حرارت مکانیک (TMAZ) رخ داده است. مورفولوژی شکست توسط SEM ویژگی‌های رخ‌برگی و حالت عمدتاً شکل‌پذیر با ریزتخلخل‌های با اشکال و ابعاد مختلف مشاهده شد.



Synthesis and Characterization of TiO₂/CuO/WO₃ Ternary Composite and its Application as Photocatalyst

H. Koohestani*, R. Ezoji

Faculty of Materials and Metallurgical Engineering, Semnan University, Semnan, Iran

PAPER INFO

Paper history:

Received 07 October 2020

Received in revised form 29 November 2020

Accepted 21 December 2020

Keywords:

Ternary Composite

TiO₂/CuO

TiO₂/CuO/WO₃

Photocatalyst

ABSTRACT

Photocatalytic removal of water and air pollution has received much attention today. Many photocatalysts based on semiconductors have been developed and used. Binary and even ternary composites have been developed to solve the drawback of semiconductors, including high band gaps and short life time of charge carriers. In this study, a three-component composite of TiO₂/CuO/WO₃ was synthesized by adding WO₃ to TiO₂/CuO. Their structural properties were evaluated by analyzes X-ray diffraction (XRD), field-emission scanning electron microscopy (FESEM), and diffusive reflectance spectra (DRS) and their performance by methylene orange dye removal. The results of XRD and SEM analysis showed purity and uniform distribution of elements. The combination of TiO₂/10%CuO and 15%WO₃ with band gap 2.66 eV showed the highest rate constant of dye removal (0.0301 min⁻¹).

doi: 10.5829/ije.2021.34.03c.17

1. INTRODUCTION

Due to the increasing demand for solar energy, treated water and air, and the removal of hazardous and toxic pollutants, the use of semiconductor photocatalysts that have a wide variety of capabilities in these fields have attracted considerable attention [1-4]. Especially TiO₂, which due to its good photocatalytic activity in the removal of organic pollutants such as rhodamine B [5], tetracycline [6], phenols [7], dye reagents [8], etc., has been further studied under ultraviolet irradiation.

Heterogeneous photocatalysts based on advanced oxidation processes using semiconductor materials such as TiO₂ have been of great interest over the past two decades for the treatment of environmental pollution in water and air. However, this technique can not significantly improve the practical quality of water [9]. Because TiO₂ has drawbacks such as: rapid recombination of photo-excited charge carriers (electron-hole) and extensive band gaps [10-14]. The excited direction of TiO₂ in practical applications, due to its low efficiency in photon utilization and relatively high band gap energy (3.0-3.2 eV), requires a source of ultraviolet

light illumination, which is only a small part of sunlight (3-5%) [15].

Many strategies have been used to solve these problems to develop the TiO₂ photocatalytic system with improved activity under UV-vis irradiation. Some of these strategies include: use of transition metal ions, precious metal deposition, dye sensitized TiO₂ and coupling with other semiconductors such as ZnO, CdS and WO₃ [16, 17]. Among semiconductors, WO₃ and CuO coupling have been extensively studied. WO₃ with band gap energy of 2.5-2.9 eV improves the photocatalytic efficiency of TiO₂ in various ways. It prevents the recombination of e_{cb}⁻/h_{vb}⁺ pairs and transmits the useful region of the excitation beam to the visible spectrum [14, 16]. In addition, the presence of WO₃ increases the surface acidity on TiO₂ particles [18]. They are composed in different ways to adsorb more OH⁻ or H₂O molecules and produce larger amounts of HO[•] radicals [11, 19]. Accordingly, many studies have evaluated the photocatalytic activity of WO₃/TiO₂ to reduce the amount of methylene blue and methyl orange using light irradiation [16, 20].

Another TiO₂ composite, as a successful combination of monoxide properties, is the CuO/TiO₂ composite,

*Corresponding Author Email: h.koohestani@semnan.ac.ir (H. Koohestani)

which is particularly attractive due to its low p-CuO band gap and high n-TiO₂ reactivity [21, 22]. The p-n junction coupling is expected to produce an improved lifetime of the charge carriers with positive effects on photocatalytic activity [23, 24]. The high photocatalytic activity of CuO/TiO₂ has been attributed to the transfer of photo-excited electrons from the TiO₂ conduction band to the CuO conduction band. This accumulation of extra electrons in the CuO conduction band causes a negative shift in Fermi level and thus improves its photocatalytic performance in removing organic pollutants from water as well as hydrogen production from water [25].

Recently, a number of composites with three compounds have been fabricated and their photocatalytic performance has been investigated. Miwa et al. [26] synthesized CuO/Al₂O₃/TiO₂ composite by mechanical method. They showed that the combination of 0.2wt% CuO/0.3wt% Al₂O₃/TiO₂ had a better performance in the photocatalytic production of hydrogen. Yanyan et al. [27] synthesized the WO₃/TiO₂/SiO₂ composite by sol-gel method. The results of photocatalytic performance in photodegradation of Ace showed that 3% WO₃/TiO₂/SiO₂ had the highest efficiency of 88%. Li et al. [28] showed that the simultaneous addition of 15% MoS₂/MoO₃ to TiO₂ produced a fast degradation rate (maximum ~0.138 min⁻¹), of rhodamine B degradation (95%) in 20 min under visible-light irradiation.

Because in the three compounds due to the difference in the edge of the conduction band and the valence band, after the production of photo-excited charge carriers, electrons and holes are transferred at the junction of these semiconductors, the timelife of the charge carriers increases and the chance their participation in oxidation reactions increases. Therefore, in this work, WO₃/TiO₂/CuO ternary nanocomposites are synthesized. The samples were examined by X-ray diffraction (XRD), Field-emission scanning electron microscopy (FESEM) and diffusive reflectance spectra (DRS) analyzes. To study the photocatalytic performance of synthesized composites, methyl orange removal test is performed.

2. MATERIALS AND EXPERIMENTS

2. 1. Materials

In this research, Titanium tetraisopropoxide (TTIP) from Daejung (Korea), hydrochloric acid (HCl), 2-propanol, methyl orange (MeO), WO₃ nanopowder, ascorbic acid and Cupric sulfate pentahydrate (CuSO₄.5H₂O) from Merck (Darmstadt, Germany) were purchased.

2. 2. Synthesis of TiO₂-based Composites

To make the ternary nanocomposite of TiO₂/CuO/WO₃, initially similar to the flowchart of Figure 1 and by adjusting the time and amount of each compound, two solutions were prepared as follows:

Solution A: 6 ml of 2-propanol was mixed with 6 ml of hydrochloric acid and 85 ml of distilled water for 10 min. Then 6 ml of TTIP was added dropwise into the solution and the temperature was slowly raised to 50 °C. The solution was stirred for 60 min.

Solution B: 0.4 g of copper sulfate was dissolved in 100 ml of distilled water and stirred for 20 min. 30 ml of sodium hydroxide 0.05 M was added to the solution. After stirring for 30 min, 30 ml of ascorbic acid 0.05 M was added and stirred for 30 min.

To prepare a ternary composite with a specific composition, certain ratio of solution B were added dropwise into solution A (to achieve a TiO₂ to CuO ratio of 1:9). Also, a certain amount of WO₃ nanoparticle powder was added to it. The resulting solution was stirred for 1 h and then allowed to precipitate for 24 h. The precipitate was calcined after drying for 2 h at 400 °C. The resulting samples were named 5WTC, 10WTC, 15WTC and 20WTC according to the composition of 90TiO₂-10CuO and the amount of WO₃ at 5, 10, 15 and 20%.

2. 3. Characterizations In order to investigate the phases formed in the composite samples, the XRD

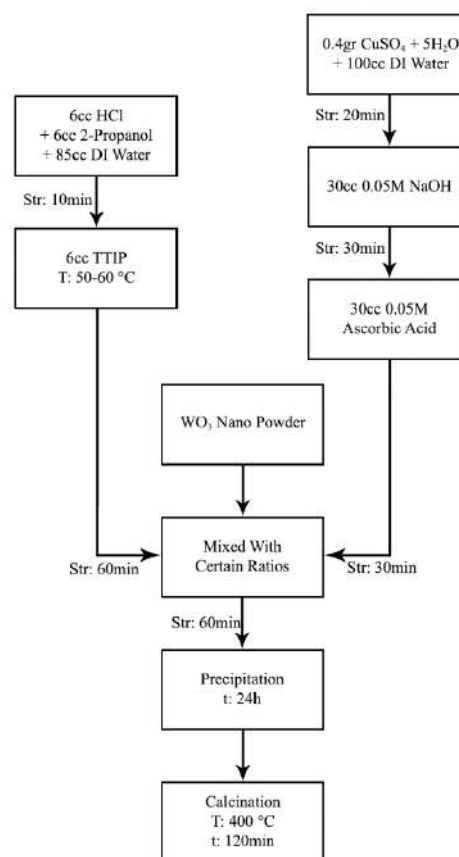


Figure 1. Flowchart of synthesis of TiO₂/CuO/WO₃ ternary composite

diffractometer (Bruker D8) with Cu K_{α} radiation ($\lambda=1.54056 \text{ \AA}$) was used, which shows X-ray diffraction patterns with intensity in terms of diffraction angle (2θ). Field-emission scanning electron microscopy (MAIA3, Tescan) was used to evaluate the microstructure of the samples. EDS and map analyzer capabilities were used to more accurately investigate the presence of elements and how they are distributed. The diffuse reflectance spectra (DRS) of the composites were recorded by a UV-Vis spectrophotometer (Avaspec-2048-TEC) using BaSO_4 as a reference in the region from 200 to 900 nm.

Photocatalytic activities were investigated by adding 150 mg/l of composite to 50 ml solutions of MeO (with 5 mg/l initial concentration). At first, solution was stirred for 60 min in full darkness to achieve adsorption-desorption equilibrium. UV irradiation from two 6 W lamp (Philips) was then applied to the catalyst containing solution. Samples were then taken out for analysis at the intervals of 30 min. The concentration of dye in the solution was measured spectrophotometrically at the wavelength of the maximum absorbance (λ_{max} : 612 nm).

3. RESULTS AND DISCUSSIONS

The diffraction pattern of $\text{TiO}_2/10\%\text{CuO}$ binary samples and 15WTC ternary samples is shown in Figure 2. In both patterns, the anatase (JCPDS 21-1272) and rutile (JCPDS 21-1276) peaks can be seen well. In the binary sample, CuO phase peaks appeared, but in the ternary sample, due to the low CuO value, the peak was not seen. In the pattern of the ternary sample, the peaks of the orthorhombic phase WO_3 (JCPDS 20-1324) are identified. Ke et al. [9] reported that in the TiO_2/WO_3 composite the conversion of the anatase phase to rutile occurs at lower temperatures. WO_3 leads to the formation of W^{+5} and excess oxygen vacancies by the ability to absorb electrons from the TiO_2 conduction band [9, 16]. These oxygen vacancies accelerate the phase transformation in TiO_2 from anatase to rutile. Akhlaghian et al. [29] were observed WO_3 effect in the reduction of anatase phase transformation to rutile phase.

The presence of rutile peaks in Figure 2b may be due to this. On the other hand, the presence of CuO does not cause a significant change in the size of anatase and rutile crystals and their transformation [25].

Figure 3 shows the FESEM and EDS images of TiO_2/CuO binary and 15WTC ternary samples. Figure 3a indicates relatively spherical particles approximately 15-30 nm diameter, and EDS Figure 3c confirms the presence of three elements Ti, Cu, and O. The particle morphology of the 15WTC ternary sample is shown in Figure 3b. As can be seen, TiO_2/CuO nanoparticles have coated the surface of WO_3 coarse particles. EDS in Figure 3d demonstrates the presence of elements W, Ti, Cu and O.

In, The distribution of elements in the ternary sample along with the map images is shown Figure 4. As can be seen, the elements W, Ti and Cu are evenly distributed throughout the sample surface.

Band gap is one of the most important properties of semiconductors in photocatalytic processes and

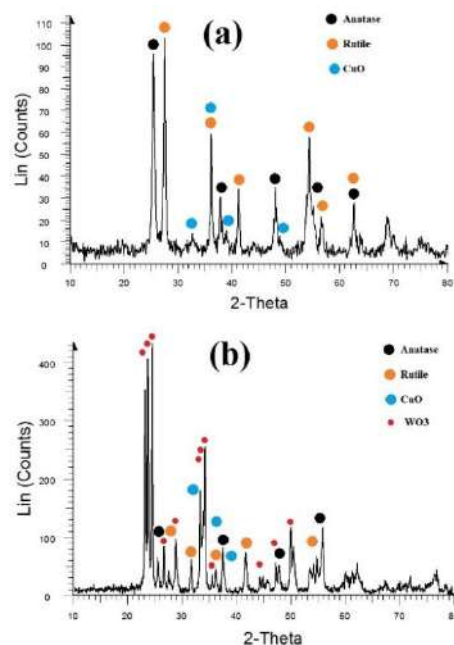


Figure 2. X-ray diffraction pattern of nanocomposite samples (a) binary TiO_2/CuO (b) ternary 15WTC

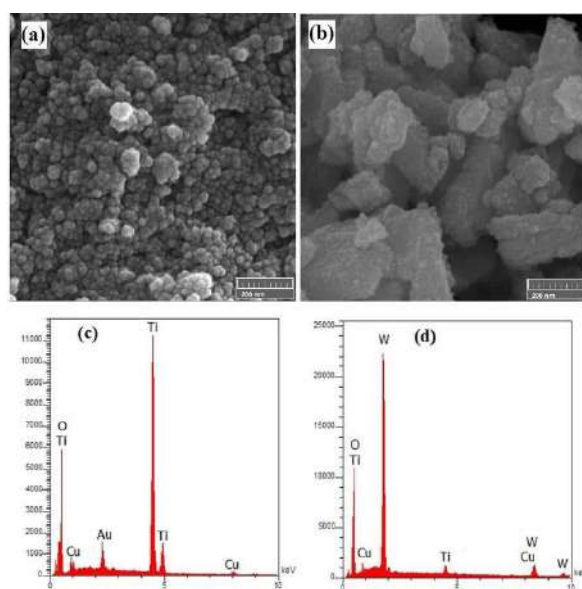


Figure 3. FESEM images of nanocomposite samples (a) binary TiO_2/CuO and (b) ternary 15WTC and EDS spectra of nanocomposite samples (c) binary TiO_2/CuO and (d) ternary 15WTC

applications. Figure 5 shows the DRS analysis results including the absorption spectrum (Figure 5a) and how to determine the band gap (Figure 5b). The value of optical band gap obtained from the diagrams is represented in Table 1. The band gap of the samples was obtained using the Kubelka-Munk relationship from the absorption spectrum [25]:

$$(\alpha hv) = \beta(hv - E_g)^n \tag{1}$$

where E_g is the sample band gap energy (eV), ν is the light frequency (s^{-1}), h is the Planck constant (J.s), β is the absorption constant and α is the absorption coefficient. The value of index n is considered to be 1.2, 3.2 and 2 for direct transition, forbidden direct transition or indirect transition, respectively. The band gap can be determined by extrapolating the linear portion of the $(\alpha hv)^n-hv$ curve. $n=1/2$ value better defines our composites [25].

It should be noted that the band gap energy of TiO_2 , CuO and WO_3 are 3.20, 1.70 and 2.70, respectively [30]. According to the results, the addition of other compounds to TiO_2 has reduced the band gap energy. For example, the band gap value has been reduced to 2.95 eV for $TiO_2/10\%CuO$. A shift in the absorption edge for TiO_2/CuO composites with CuO is shown to be possibly related to the formation of a defect levels in an energy range in TiO_2 [31].

Addition of WO_3 to the binary compound further reduces the band gap. Baia et al. [32] in the presence of WO_3 , were only able to reduce the gap of composite to 3.02 eV. Therefore, in order to further reduce the band gap energy, the presence of both components is required. The lowest band gap energy (2.66 eV) was obtained for

TABLE 1. The band gap of samples

Samples	Band gap energy, E_g (eV)
TiO_2	3.20*
TC	2.95
5WTC	2.70
10WTC	2.68
15WTC	2.66
20WTC	2.71

* ref. [25]

the 15WTC sample, and then by adding more WO_3 value, due to the fact that a higher level of the TC compound was covered; the ability to absorb the compound decreased, resulting in an increase in the band gap.

Table 2 presents the edge of the conduction band and edge of the valance band for TiO_2 , CuO and WO_3 [30]. Because the conduction band of tungsten oxide is lower than that of TiO_2 , electron transfer from titanium particles to WO_3 is possible. This action effectively separates the charge carriers and increases their lifetime. In the case of

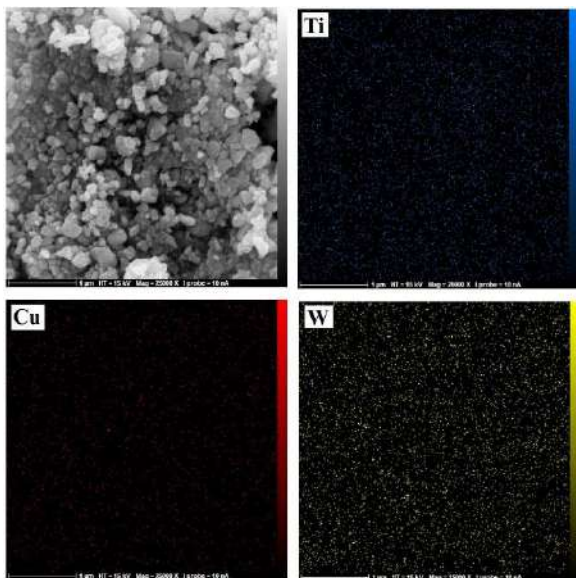


Figure 4. Map images of the distribution of Ti, W and Cu elements in a 15WTC ternary sample

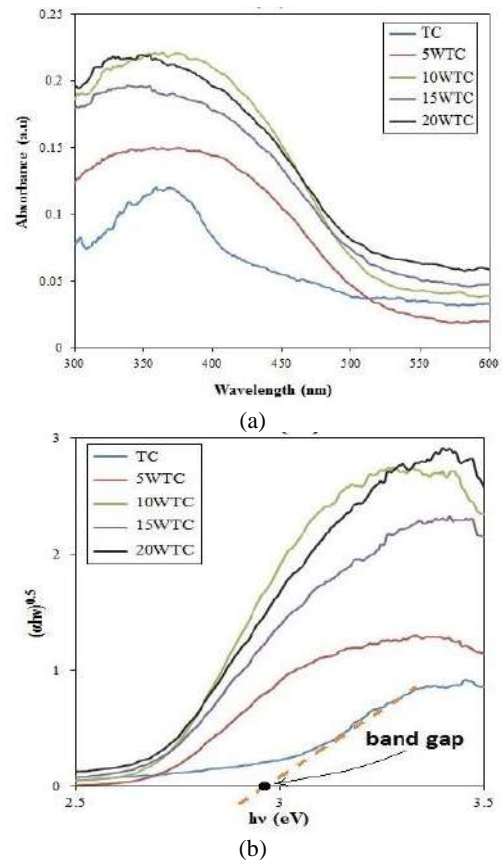


Figure 5. synthesized nanocomposites (a) UV-Vis diffuse reflectance spectra (b) Tauc plot obtained from UV-Vis DRS spectra

TABLE 2. valance and conduction band edge of different semiconductor [30]

	Conduction Band edge (eV)	Valence Band edge (eV)
TiO ₂	-4.21	-1.01
CuO	-4.96	-3.26
WO ₃	-5.24	-2.54

TiO₂/WO₃ composition, due to the lower valance band of WO₃ than TiO₂, the transfer of holes in WO₃ is possible. In the case of CuO, the unequilibrium transfer of charge carriers at the TiO₂/CuO junction causes holes to move from TiO₂ to CuO and electrons to move from CuO to TiO₂.

In the case of the TiO₂/CuO/WO₃ ternary compound, UV light excites electrons in the conduction band WO₃ and CuO, which are transferred to the conduction band TiO₂. On the other hand, the holes travel in the opposite direction and migrate from the TiO₂ valence band to the WO₃ and CuO valence bands. This migrations of charge carriers restrict their recombination rate and thus enhances the separation of electron-hole pair. The photo-generated electrons can be trapped by oxygen molecules in the organic solution to form superoxide radical anions ($\cdot O_2^-$), which can effectively degradate organic pollutants. These holes convert the water molecules into OH \cdot and react with organic pollutants to generate H₂O and CO.

Figure 6 shows the function of the compounds in removing methylene orange dye. The photocatalytic performance kinetics of the samples can be evaluated according to the following relation and rate constant comparison [17]:

$$-\ln\left(\frac{C}{C_0}\right) = k_{app}t \quad (2)$$

where C₀ is the initial concentration of dye, and k_{app} is the apparent constant (min⁻¹). Investigating the changes in ln

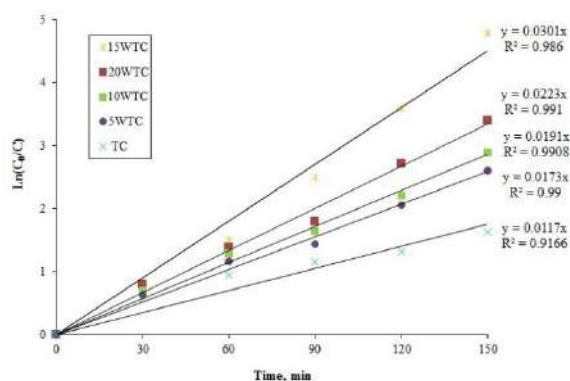


Figure 6. Linear correlation between reaction time and logarithm of relative concentration of methylene orange (ln C₀/C)

(C/C₀) over time for different samples, it is observed that the addition of CuO and WO₃ to the TiO₂ constant speed is improved. The highest rate constant is for the 15WTC sample and is 0.0301 min⁻¹. Akhlaghian et al. [29] in a study showed that the 28.11% CuO/2.1% WO₃/TiO₂ composition was very successful in phenol photodegradation and had a rate constant of 0.0621 min⁻¹. These results indicate that the charge transfer between the compounds and an increase in electron-hole life, their photocatalytic performance is improved.

4. CONCLUSIONS

In this study, ternary TiO₂/CuO/WO₃ composites were synthesized and evaluated by different analyzes (XRD, FESEM, DRS and etc.). The results of XRD and FESEM analysis showed purity and uniform distribution of elements. With the production of the ternary composites, the band gap decreased. Due to the difference in the edge of the conduction band and the valence band, after the production of excited charge carriers with light, electrons and holes are moved at the junction of these semiconductors. This will increase their lifetime and give them a greater chance of participating in redox reactions to remove water pollutions. The results of methylene orange dye removal showed that the ternary composite TiO₂/10%CuO with 15%WO₃ and 2.66 eV band gap, had the highest performance.

5. REFERENCES

- Bi, D. and Y. Xu, "Synergism between Fe₂O₃ and WO₃ particles: Photocatalytic activity enhancement and reaction mechanism". *Journal of Molecular Catalysis A: Chemical*, Vol. 367, 103-107. <https://doi.org/10.1016/j.molcata.2012.09.031>
- Feng, C., S. Wang and B. Geng, "Ti (iv) doped WO₃ nanocuboids: fabrication and enhanced visible-light-driven photocatalytic performance." *Nanoscale*, Vol. 3, No. 9, (2011), 3695-3699. <https://doi.org/10.1039/C1NR10460H>
- Liu, Y., C. Xie, J. Li, T. Zou and D. Zeng, "New insights into the relationship between photocatalytic activity and photocurrent of TiO₂/WO₃ nanocomposite." *Applied Catalysis A: General*, Vol. 433, (2012), 81-87. <https://doi.org/10.1016/j.apcata.2012.05.001>
- Karácsonyi, É., L. Baia, A. Dombi, V. Danciu, K. Mogyorósi, L.C. Pop, G. Kovács, V. Coşoveanu, A. Vulpoi, S. Simon and Zs. Pap, "The photocatalytic activity of TiO₂/WO₃/noble metal (Au or Pt) nanoarchitectures obtained by selective photodeposition." *Catalysis today*, Vol. 208, (2013), 19-27. <https://doi.org/10.1016/j.cattod.2012.09.038>
- Zhuang, J., W. Dai, Q. Tian, Z. Li, L. Xie, J. Wang, P. Liu, X. Shi and D. Wang, "Photocatalytic degradation of RhB over TiO₂ bilayer films: effect of defects and their location." *Langmuir*, Vol. 26, No. 12, (2010), 9686-9694. Doi: 10.1021/la100302m
- Reyes, C., J. Fernández, J. Freer, M.A. Mondac, C. Zaror, S. Malato and H.D. Mansill, "Degradation and inactivation of tetracycline by TiO₂ photocatalysis." *Journal of Photochemistry and Photobiology A: Chemistry*, Vol. 184, No. 1-2, (2006), 141-146. <https://doi.org/10.1016/j.jphotochem.2006.04.007>

7. Laoufi, N., D. Tassalit and F. Bentahar, "The degradation of phenol in water solution by TiO₂ photocatalysis in a helical reactor." *Global NEST Journal*, Vol. 10, No. 3, (2008), 404-418.
8. Kuo, W. and P. Ho, "Solar photocatalytic decolorization of dyes in solution with TiO₂ film." *Dyes and Pigments*, Vol. 71, No. 3, (2006), 212-217. <https://doi.org/10.1016/j.dyepig.2005.07.003>
9. Ke, D., H. Liu, T. Peng, X. Liu and K. Dai, "Preparation and photocatalytic activity of WO₃/TiO₂ nanocomposite particles." *Materials Letters*, Vol. 62, No. 3, (2008), 447-450. <https://doi.org/10.1016/j.matlet.2007.05.060>
10. Iliev, V., D. Tomova, S. Rakovsky, A. Eliyas and G. Li Puma, "Enhancement of photocatalytic oxidation of oxalic acid by gold modified WO₃/TiO₂ photocatalysts under UV and visible light irradiation." *Journal of Molecular Catalysis A: Chemical*, Vol. 327, No. (1-2): (2010), 51-57. <https://doi.org/10.1016/j.molcata.2010.05.012>
11. Li, X., F.B. Li, C.L. Yang and W.K. Ge, "Photocatalytic activity of WO₃-TiO₂ under visible light irradiation." *Journal of Photochemistry and Photobiology A: Chemistry*, Vol. 141, No. (2-3), (2001), 209-217. [https://doi.org/10.1016/S1010-6030\(01\)00446-4](https://doi.org/10.1016/S1010-6030(01)00446-4)
12. Sajjad, A.K.L., S. Shamaila, B. Tian, F. Chen and J. Zhang, "Comparative studies of operational parameters of degradation of azo dyes in visible light by highly efficient WO₃/TiO₂ photocatalyst." *Journal of Hazardous Materials*, Vol. 177, No. 1-3, (2010), 781-791. <https://doi.org/10.1016/j.jhazmat.2009.12.102>
13. Kwon, Y.T., K.Y. Song, W.I. Lee, G.J. Choi and Y.R. Do, "Photocatalytic behavior of WO₃-loaded TiO₂ in an oxidation reaction." *Journal of Catalysis*, Vol. 191, No. 1, (2000), 192-199. <https://doi.org/10.1006/jcat.1999.2776>
14. Leghari, S.A.K., S. Sajjad, F. Chen and J. Zhang, "WO₃/TiO₂ composite with morphology change via hydrothermal template-free route as an efficient visible light photocatalyst." *Chemical Engineering Journal*, Vol. 166, No. 3, (2011), 906-915. <https://doi.org/10.1016/j.cej.2010.11.065>
15. Lv, K., J. Li, X. Qing, W. Li and Q. Chen, "Synthesis and photo-degradation application of WO₃/TiO₂ hollow spheres." *Journal of Hazardous Materials*, Vol. 189, No. 1-2, (2011), 329-335. <https://doi.org/10.1016/j.jhazmat.2011.02.038>
16. Koohestani, H., "Characterization of TiO₂/WO₃ composite produced with recycled WO₃ nanoparticles from W-Ni-Fe alloy." *Materials Chemistry and Physics*, Vol. 229, (2019), 251-256. <https://doi.org/10.1016/j.matchemphys.2019.03.027>
17. Koohestani, H. and S.K. Sadmezhaad, "Improvement in TiO₂ photocatalytic performance by ZrO₂ nanocompositing and immobilizing." *Desalination and Water Treatment*, Vol. 57, No. 58, (2016), 28450-28459. DOI: 10.1080/19443994.2016.1183233
18. Papp, J., B. Podolsky, and N. Rosen, "Surface acidity and photocatalytic activity of TiO₂, WO₃/TiO₂, and MoO₃/TiO₂ photocatalysts." *Chemistry of Materials*, Vol. 6, No. 4, (1994), 496-500. DOI: 10.1021/cm00040a026
19. Sajjad, A.K.L., S. Shamaila, B. Tian, F. Chen and J. Zhang, "One step activation of WO_x/TiO₂ nanocomposites with enhanced photocatalytic activity." *Applied Catalysis B: Environmental*, Vol. 91, No. 1-2, (2009), 397-405. <https://doi.org/10.1016/j.apcatb.2009.06.005>
20. Ramos-Delgado, N., L. Hinojosa-Reyes, I.L. Guzman-Mar, M.A. Gracia-Pinilla and A. Hernández-Ramírez, "Synthesis by sol-gel of WO₃/TiO₂ for solar photocatalytic degradation of malathion pesticide." *Catalysis Today*, Vol. 209, (2013), 35-40. <https://doi.org/10.1016/j.cattod.2012.11.011>
21. Scuderi, V., G. Amiard, R. Sanz, S. Boninelli, G. Impellizzeri and V. Privitera, "TiO₂ coated CuO nanowire array: Ultrathin p-n heterojunction to modulate cationic/anionic dye photo-degradation in water." *Applied Surface Science*, Vol. 416, (2017), 885-890. <https://doi.org/10.1016/j.apsusc.2017.04.229>
22. Sawicka-Chudy, P., M. Sibiński, G. Wisz, E. Rybak-Wilusz and M. Cholewa, "Numerical analysis and optimization of Cu₂O/TiO₂, CuO/TiO₂, heterojunction solar cells using SCAPS." *Journal of Physics: Conference Series*. (2018). IOP Publishing. <https://doi.org/10.1088/1742-6596/1033/1/012002>
23. Zhang, X. and A. Tang, "Novel CuO/TiO₂ nanocomposite films with a graded band gap for visible light irradiation." *Materials Express*, Vol. 2, No. 3, (2012), 238-244. <https://doi.org/10.1166/mex.2012.1069>
24. Koohestani, H. and A. Kheilnejad, "Hydrogen Generation and Pollution Degradation from Wastewater Using TiO₂-CuO Nanocomposite." *Journal of Nanoscience and Nanotechnology*, Vol. 20, No. 9, (2020), 5970-5975. <https://doi.org/10.1166/jnn.2020.18544>
25. Koohestani, H. and S.K. Sadmezhaad, "Photocatalytic degradation of methyl orange and cyanide by using TiO₂/CuO composite." *Desalination and Water Treatment*, Vol. 57, No. 46, (2016), 22029-22038. <https://doi.org/10.1080/19443994.2015.1132395>
26. Miwa, T., S. Kaneco, H. Katsumata, T. Suzuki, K. Ohta, S. Chand Verma and K. Sugihara, "Photocatalytic hydrogen production from aqueous methanol solution with CuO/Al₂O₃/TiO₂ nanocomposite." *International Journal of Hydrogen Energy*, Vol. 35, No. 13, (2010), 6554-6560. <https://doi.org/10.1016/j.ijhydene.2010.03.128>
27. Yanyan, L., T.A. Kurniawan, Z. Ying, A.B. Albadarin and G. Walker, "Enhanced photocatalytic degradation of acetaminophen from wastewater using WO₃/TiO₂/SiO₂ composite under UV-vis irradiation." *Journal of Molecular Liquids*, Vol. 243, (2017), 761-770. <https://doi.org/10.1016/j.molliq.2017.08.092>
28. Li, Z., F. Cao, L. Wang, Z. Chen and X. Ji, "A novel ternary MoS₂/MoO₃/TiO₂ composite for fast photocatalytic degradation of rhodamine B under visible-light irradiation." *New Journal of Chemistry*, Vol. 44, No. 2, (2020), 537-542. <https://doi.org/10.1039/C9NJ04107A>
29. Akhlaghian, F. and A. Najafi, "CuO/WO₃/TiO₂ photocatalyst for degradation of phenol wastewater." *Scientia Iranica*, Vol. 25, No. 6, (2018), 3345-3353. <https://dx.doi.org/10.24200/sci.2018.20611>
30. Xu, Y. and M.A. Schoonen, "The absolute energy positions of conduction and valence bands of selected semiconducting minerals." *American Mineralogist*, Vol. 85, No. 3-4, (2000), 543-556. <https://doi.org/10.2138/am-2000-0416>
31. Lebedev, V., V.V. Sudin, D.A. Kozlov and A.V. Garshev, "Photocatalytic properties of nanocrystalline TiO₂ modified with CuO and WO₃." *Nanotechnologies in Russia*, Vol. 11, No. 1-2, (2016), 20-28. DOI: 10.1134/S1995078016010092
32. Baia, L., E. Orbán, S. Fodor, B. Hampel, E.Z. Kedves, K. Saszet and I. Székely, "Preparation of TiO₂/WO₃ composite photocatalysts by the adjustment of the semiconductors' surface charge." *Materials Science in Semiconductor Processing*, Vol. 42, (2016), 66-71. <https://doi.org/10.1016/j.mssp.2015.08.042>

Persian Abstract

چکیده

حذف فتوکاتالیستی آلودگیهای آب و هوا، امروزه بسیار مورد توجه قرار گرفته است. فتوکاتالیستهای زیادی بر پایه نیمه هادی‌ها تولید شده و مورد استعمال قرار گرفته است. برای رفع مشکلات نیمه هادی‌ها از جمله گاف انرژی بالا و طول عمر پایین حامل‌های بار (الکترون-حفره)، ترکیبات دو جزئی و حتی سه جزئی آنها تولید شده است. در این پژوهش، ترکیب سه جزئی $\text{TiO}_2/\text{CuO}/\text{WO}_3$ ، با افزودن نانوذرات WO_3 به TiO_2/CuO سنتز شده است. خواص ساختاری و عملکرد آنها با حذف رنگ متیلن نارنجی مورد ارزیابی قرار گرفت. نتایج آنالیز پراش پرتو X و میکروسکوپ الکترونی روبشی، خالص بودن و توزیع یکنواخت عناصر را نشان داد. ترکیب $\text{TiO}_2/10\%\text{CuO}$ با $15\%\text{WO}_3$ و گاف انرژی $2/66$ الکترون ولت بیشترین نرخ حذف رنگ را نشان داد.



A Life Clustering Framework for Prognostics of Gas Turbine Engines under Limited Data Situations

A. Mahmoodian^a, M. Durali^{*a}, M. Saadat^b, T. Abbasian^b

^a Mechanical Engineering Department, Sharif University of Technology, Tehran, Iran

^b ECE Faculty, Tehran University, Tehran, Iran

PAPER INFO

Paper history:

Received 23 August 2020

Received in revised form 01 January 2021

Accepted 04 January 2021

Keywords:

Limited Data

Prognosis and Health Management

Remaining Useful Life Estimation

Robustness

ABSTRACT

The reliability of data driven prognostics algorithms severely depends on the volume of data. Therefore in case of limited data availability, life estimations usually are not acceptable; because the quantity of run to failure data is not sufficient to train prognostics model efficiently. To board this problem, a life clustering prognostics (LCP) framework is proposed. LCP regenerates the train data at different ages and outcomes to increment of the training data volume. So, the method is useful for limited data conditions. In this research, initially LCP performance is studied in normal situation is; successively robustness of the framework under limited data conditions is considered. For this purpose, a case study on turbofan engines is performed. The accuracy for the proposed LCP approach is 71% and better than other approaches. The prognostics accuracy is compared in various situations of data deficiency for the case study. The prognostic measures remain almost unchanged when the training data is even one third. Successively, prognostics accuracy decreases with a slight slope; so that when the training data drops from 100 to 5%, the accuracy of the results drops 26%. The results indicates the robustness of the proposed algorithm in limited data situation. The main contribution of this paper include: (1) The effectiveness of life clustering idea for use in prognostics algorithms is proven; (2) A step-by-step framework for LCP is provided; (3) A robustness analysis is performed for the proposed prognostics algorithm.

doi: 10.5829/ije.2021.34.03c.18

1. INTRODUCTION

In recent years, prognostics and health management (PHM) of complex mechanical systems has become more prominent. Prognostic and Remained Useful Life (RUL) prediction has been initialized in medical field [1]; subsequently attracted much attention in engineering issues due to economical and operational considerations [2]. Predicting future behavior of a complex machine such as a gas turbine is a complicated task. Prognostics is currently at the core of systems' health management to achieve reliable and safe operation of machines. In the framework of PHM, many techniques exist which are basically classified into two principal classes: data-driven and model-based prognostics approach [3-4]. The fact that most researches are focusing on data-driven methods shows the desire to work with easily accessible data as

compared to model-based methods, irrespective of the difficulties in gaining accessing statistically significant run-to-failure data. Despite acceptance of data-driven methods, the on-going difficulty with these methods is that they show acceptable RUL estimation only when abundant run-to-failure data are available for training. Although, under the condition of limited failure data, model-based solutions are unsuccessful due to their requirement to large amounts of failure data for validating physical models [5].

In this research, data driven methods are focused and divided mainly in two groups: typical methods and robust methods. A typical prognostics method rely on large amounts of historical failure data (i.e. run-to failure data indicating past degradation patterns) to estimate prognostics model parameters [5]. Otherwise, the predictions may be unreliable and the training can not be

*Corresponding Author Institutional Email: durali@sharif.edu (M. Durali)

carried out. The fact limits the application of typical prognostics methods in problems with small amount of available training data [6]. Failure data are limited in real industrial cases due to some reasons: (1) rare failures; (2) overprotective maintenance and replacement regimes; (3) incomplete reports [7].

Majority of prognostics researches are developed assuming enough run-to-failure data are available for training. Some researchers have used combined regression techniques, including linear and quadratic models to predict the RUL of gas turbine engines [8]. Other methods like particle filter [9], adaptive-order particle filter [10], Kaplan Meier [11] and support vector machine (SVM) [12] have been used for prognostics. Yu et al. [13] have developed a prognostics system for engine health assessment based on logistic regression and state-space-model. Simon et al. [14] have compared the estimation accuracy and computational effort of variants of the Kalman filter like linearized Kalman filter (LKF), extended Kalman filter (EKF), and unscented Kalman filter (UKF) for aircraft engine health estimation. Lu et al. [15] have presented a nonlinear state estimation method based on EKF and obtained a significant improvement in estimation accuracy and robustness. Ding et al. [16] have fused support vector machine and the genetic algorithm and proposed an intelligent prognostics approach. Goebel et al. [17] compared the results of a relevance vector machine (RVM), a Gaussian process regression (GPR), and an artificial neural network (ANN) approach in prognostics.

On the contrary, with the robust methods, the RUL estimation is acceptable despite the lack of abundant trained data. Recently, some novel prognostics methods based on classic algorithms are suggested, such as fusion of prognostics algorithms [18], multistate structure [19], etc. Xu et al. [18] have integrated the strengths of the experience-based prognostics approach and the data-driven approach. The developed fusion prognostics framework has been employed to predict the RUL of a gas turbine engine as an application example [18]. Moghaddass et al. [19] have demonstrated that deterioration process occurs through different levels of health states before failure, leading to a multistate deterioration process in many real-world cases. Xiang et al. [20] have proposed a probabilistic methodology for fatigue prognostics using an inverse first-order reliability method. However, the robustness tests are rarely reported.

In this paper, a novel methodology is presented based on life clustering that allows training datasets to be augmented. Usually, the goal of clustering in literature has been to organize data into homogeneous groups to compact clusters with minimum intra group similarity and to increase separation among clusters with maximized inter group dissimilarity [21]. The proposed method of life clustering prognostics (LCP) is able to

increase the train data set samples; in addition to organize data into homogeneous groups.

The case study is to compare the prognostics accuracy for a robust framework in abundant data and little data condition with for turbofan engines Prognostic Health Management (PHM) Challenge data [22]. For 2008 PHM challenge, many authors have reported the RUL estimation for a given data set. Only typical tests using large scale data have been stated. The best results have been obtained by using RULCLIPPER algorithm [23], EVIPRO algorithm [24] and a similarity-instance based approach [25]. These results are used as the reference point of the current study.

The main contributions of this paper can be summarized as follows. First, the effectiveness of the idea of life clustering for use in prognostics algorithms is proven. Although artificial neural network is used as the main prediction tool in this paper, the idea of LCP can be combined and used with other classical methods of prognostics. Second, a step-by-step framework for prognostics based on life clustering is provided. This method significantly improves the reliability of this algorithm while using all the advantages of a predictive algorithm as the core prediction algorithm. Third, a robustness analysis is performed for the proposed prediction algorithm. This study evaluates the performance of the algorithm in different conditions of lack of sufficient data. Based on the evaluations, the LCP algorithm is robust in limited information conditions and has acceptable results. Robustness of a prognostics algorithm is a critical issue in industrial and real-world cases, where predictive maintenance is required against lack of abundant run-to-failure data.

The outline of this paper is as follows. In section 2 layout of the study is presented. Data processing and prognostics method is explained in section 3. In sections 4, implementation of the proposed method on a case study is described. This paper ends with results and conclusions in two last sections.

2. LAYOUT OF THE STUDY

2.1. Data Description To illustrate the outcomes of this method on prognostics and health monitoring, a case study on turbofan engines from NASA's prognostics Information Repository is performed. The structure of the data set and the effectiveness of the proposed model are presented in this section. The data consists of 21 Measurements, including the measurements listed in Table 1, that are measured during every flight cycle. In the dataset, multiple units operate until failure occurs, providing training set. The other units run to different levels of destruction, forming test set. The challenge is to predict the RUL of test units. This dataset is one of the most widely datasets used for the development and

TABLE 1. List of sensors and Measurements used in this paper [22]

Symbol	Description	Unit
T24	Total temperature at LPC outlet	° R
T30	Total temperature at HPC outlet	° R
P30	Total pressure at HPC outlet	Psia
Nc	Physical core speed	Rpm
Pr	Engine pressure ratio (P50 / P2)	-
Phi	Ratio of fuel flow to Ps30	-
BPR	Bypass ratio	-
BE	Bleed enthalpy	-
T50	Total temperature at LPT outlet	O R
Ps30	static pressure at HPC outlet	Psia
farB	Burner Fuel air ratio	-

validation of prognostics algorithms [2, 18-19]. Figure 1 shows the main components of the aircraft gas turbine engine model.

2. 2. Prognostic Measures In the PHM context, sometimes it is desirable to predict early as compared to predicting late. Therefore, the asymmetric interval $I = [-10, +13]$ around the true RUL is considered to evaluate the performance. Accuracy measure is defined as the percentage of correct estimations which falls within the interval I [25].

Mean square error (MSE) and mean absolute error (MAE) are two other measures which are used to evaluate the performance of LCP method more accurately,

$$e_{mse} = \frac{1}{N} \sqrt{\sum_{t=1}^N (err_t)^2} \quad (1)$$

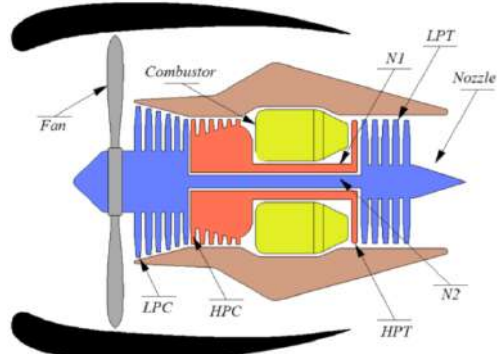
$$e_{mae} = \frac{1}{N} \sum_{t=1}^N |err_t| \quad (2)$$

where error is defined for a given prediction by Equation (2):

$$err = True\ RUL - Estimated\ RUL \quad (3)$$

3. PROGNOSTICS METHOD

In a data-driven PHM process, after data acquisition, the first challenge is how to map the conditions between a complex and interconnected system with its level of the drop; for this purpose, data processing and signal feature extraction should be done. Two general approaches are considered to extract features and design a health indicator (HI). The first approach is to use gas-path parameters such as temperature, vibrations, flow capacity, pressure, compressor efficiency, fan efficiency,

**Figure 1.** Simplified diagram of the gas turbine engine [22]

etc. Vibration and modal analysis is widely used to estimate life of mechanical systems [26-27]. Mohammadi et al. [28] determined performance deterioration according to efficiency and flow capacity as health indicators. The second approach is the combination of functional and performance sensors. In this field, we can mention the works [18, 29, 30], that combine different sensors with different fusion techniques. Diallo [11] has shown in his research that multi-sensor data fusion approach is more reliable. A step by step methodology is indicated in literature [30] to produce a Health Indicator Feature [HIF] vector, which is used in this article.

3. 1. The LCP Prognostic Framework

A prognostics framework based on life clustering is developed as shown in Figure 2. RUL estimation is accomplished through the life clustering of the engines and subsequently construction of a specific prediction module for each cluster. The proposed framework can be implemented as the following phases.

Clustering In the first phase, clustering is performed. The estimation start time of each test engine is shown with symbol tc . In the prognostics issue for a fleet of engines, a range of tc [min (tc): max (tc)] exists. The range must be separated to several divisions in the clustering phase. The cluster width (CW) is defined as follows:

$$CW_i = t_i - t_{i-1}, \sum_{i=1}^n CW_i = t_n - t_0 \quad (4)$$

where t_i s are clustering borders, t_0 is the min (tc), t_n is the max (tc) and n is the number of partitions. In the simple form, clusters widths may be assumed equal. To attain more accurate results, the number of partitions and cluster widths can be found by an optimization process.

Reproduction In the second phase, a time step (ts) is considered so that train data set is observed several times at each time step. Considering maximum observation resolution, each time step is an observation point ($ts=1$). For example, the i^{th} cluster width is m_i ($CW_i = m_i$), so the train data set is reproduced m_i times. For any

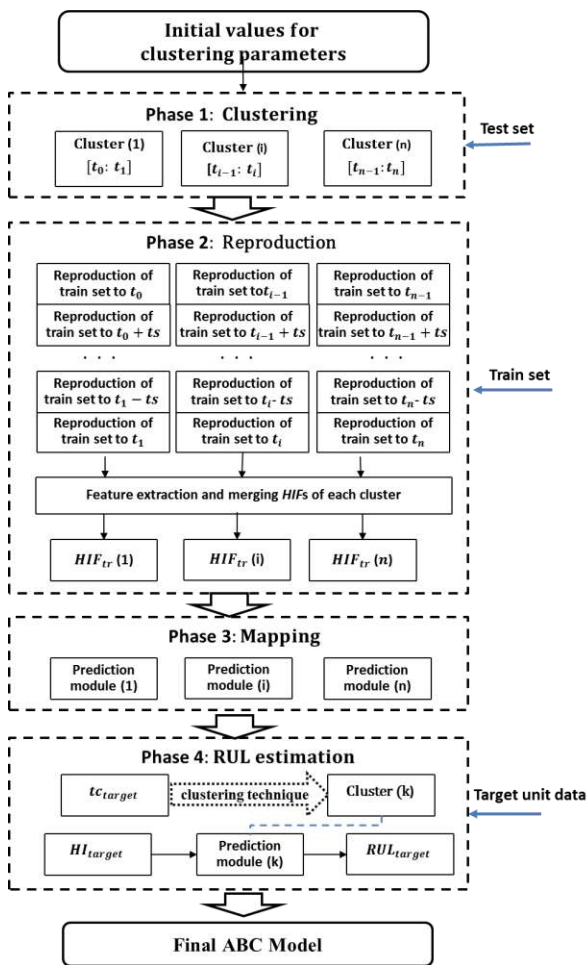


Figure 2. The framework of LCP prognostics

reproduction, units with life lengths less than the relevant observation point are withdrawn; the others are stopped at that point.

Till now, m_i reproductions of train data set are produced for each cluster. Now, data processing of units in each reproduction is performed and m_i vectors HIF are produced. In the last step of this phase, the HIF vectors for each cluster are merged to one and finally n cumulative HIF vectors are remained for n clusters.

Mapping In the previous phase, train data was reproduced several times and n cumulative HIF vectors were resulted. Now in the third phase, a prediction tool such as neural network is used to find a relation between HIFs and RULs for train data. The HIFs are selected as the input, and the corresponding true RUL data are selected as the target values to train the prediction modules. The results of the third phase are n prediction modules for n different life clusters.

RUL estimation In the fourth phase, RUL estimation of the target unit is performed. Initially, signal processing for the device is performed and the relevant HIF vector is calculated. Then, cluster selection must be done

according to the prediction start age (t_c) of the test unit. It can be done in two ways:

1. Classic way, so that each unit belongs to a cluster if its t_c is between the minimum and maximum age of that cluster
2. Fuzzy way, in which each unit belongs to a cluster to some degree that is specified by a membership function.

After cluster selection, the HIF vector of the test unit is inputted to the related prediction module and the device RUL is estimated.

4. CASE STUDY

The steps taken in this study are based on the framework given in Figure 2. The main parameters of the LCP framework are the number of clusters (n), the clusters width (CW) and the observation time step (ts). The optimum values for these parameters are different for each problem and must be optimized. To achieve this goal, various prognostics measures may be defined as the objective function. Sequential phases of the LCP framework are executed and the best parameters are found through an optimization process.

Phase 1 To determine the clustering parameters, four phases of LCP prognostics are implemented and the prognostics measures were compared. For the current case study, prognostics criterions remain almost unaffected while $n > 2$, as shown in Figure 3. Thus, $n = 4$ is chosen to evade costly computations. Sequentially, the optimum clusters widths (CW) are found out by genetic algorithm to maximize the accuracy. The optimal clustering parameters are summarized in Table 2.

Phase 2 Considering observation time step = 1 cycle, the train data set is reproduced at each cycle. For every cycle, for instance the c^{th} cycle, all engines with age longer than c cycles are stopped at the c^{th} cycle. Then data process is performed and health indicator features $HIF_{tr}(c)$ are extracted. Finally relevant HIFs

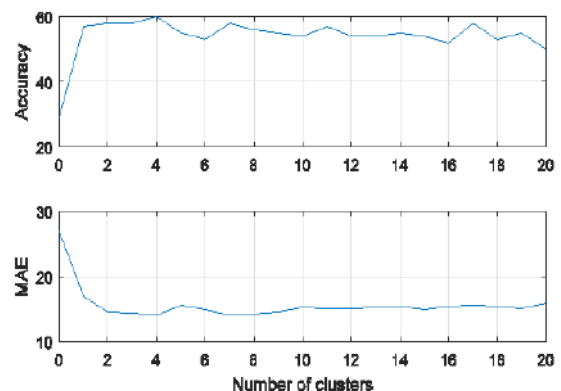


Figure 3. Prognostic measures via. number of clusters

TABLE 2. Summary of optimal clustering scheme

Cluster	Life interval	Cluster width
I	31-75 cycles	45 cycles
II	76-125 cycles	50 cycles
III	126-196 cycles	71 cycles
IV	197-303 cycles	107 cycles

for each cluster are merged to one, for example $HIF_{tr}(31), HIF_{tr}(32) \dots & HIF_{tr}(75)$ are merged to one cumulative vector for the 1st cluster, $HIF_{tr}(76), HIF_{tr}(77) \dots & HIF_{tr}(125)$ are merged to one cumulative vector for the 2nd cluster and so on for other clusters from Table 2. Summary of reproductions of train data set are represented in Table 3.

Phase 3 In the third phase, the algorithm creates a map between HIFs and RULs for each cluster. For this aim, neural network fitting tool is used [31]. In the present study, a forward multilayer perceptron (MLP) with backward propagation Bayesian training algorithm is applied. The network is composed from 10 hidden layers, 70% of data is used for train, 15% for test and 15% for validation. The summary of the formation of four networks is presented in Table 4.

Phase 4 RUL estimation is performed through the following steps:

1. For the j^{th} test engine, tc is considered (tc_j).
2. Depending on its age, the appropriate group from Table 2 is selected (group #k).
3. The relevant HIF vector of j^{th} test engine is extracted ($HIF_{te}(j)$).

TABLE 3. Summary of train data set reproductions

Cluster	length of cumulative HIF
1	4500
2	5000
3	5971
4	2240

TABLE 4. Summary of the formation of the prediction modules

ANN	Input	Target
I	2x4500 matrix, representing 2 features of 4500 HI signals	1x4500 matrix, representing RULs of engines
II	2x5000 matrix, representing 2 features of 5000 HI signals	1x5000 matrix, representing RULs of engines
III	2x5971 matrix, representing 2 features of 5971 HI signals	1x5971 matrix, representing RULs of engines
IV	2x2240 matrix, representing 2 features of 2240 HI signals	1x2240 matrix, representing RULs of engines

4. $HIF_{te}(j)$ is applied as an input to the k^{th} network.
5. The network output is the estimated RUL of the test engine.

5. RESULTS AND DISCUSSION

The performance of the proposed prognostics method is evaluated in two states:

1. Full train data: In this state, all engines (100 units) of train dataset #1 from turbofan engines of the NASA Prognostic Data Repository are utilized to train the LCP algorithm. This is similar to the condition in which most researches have used for training their algorithms and represented their results.
2. Limited train data: In this state, a portion of train dataset #1 is used for training LCP algorithm. Tests are performed with 50, 30, 20 and 10% of train data (equal to 50, 30, 20 and 10 engines). This state is similar to real world in industries when one should deal with a limited train data.

5. 1. LCP Results in Full Train Data Condition To evaluate the effectiveness of the LCP algorithm, a comparison with other approaches is performed as indicated in Table 5. Full testing dataset is used in few papers to our knowledge: Ramasso et al. [23, 24], Khelif et al. [25] and Wang et al. [32] that achieved the best score in PHM challenge 2008. The accuracy for the proposed LCP approach is better in comparison with other approaches.

5. 2. LCP Results under Limited Train Data Condition

It was shown in the previous section that the accuracy of the LCP method is reliable for full data condition in comparison with other methods. In this section a sensitivity analysis is performed under limited data condition. As mentioned earlier, four tests are performed in this section with 50, 30, 20 and 10% of train data. Each test is repeated several times in a way that different portions of the train data are selected. Finally, the mean value of prognostic measures for each test is

TABLE 5. Comparison of accuracy for different methods

Method	Correct %	Early %	Late %
LCP model (using ANN for prediction modules)	71	23	6
Ramasso [24]	67	Nan	Nan
Khelif et al.[25]	54	18	28
Ramasso et al. [23]	53	36	11
Javed et al. [33]	53	27	20
Wang et al. [32]	44	19	37

summarized in Table 6. A comparison of prognostics measures for different sizes of train data is indicated in Figure 4.

While the proposed algorithm reproduces train data several times for each life cluster, the size of the training set is several times larger than the initial train data set. Comparison of results for different numbers of training data showed that when the number of training data decreases, (1) prediction accuracy remains almost unchanged for about 30% of available train data, (2) prediction accuracy decreases about 14% with a slight slope when the available train data falls from 30 units to 10 units and (3) when the available train data goes down from 10 units to 5 units, prediction drops 10% significantly.

Further investigations can be made on the robustness of the proposed algorithm under limited training data condition. Prognostics results of engines in different cycles are studied in this paper. The actual RUL value and the RUL estimate with limited train data (10 units for

TABLE 6. Summary of prognostic measures

Number of train data units	Accuracy (%)		MAE	MSE
	Mean	STD		
100	58 ²	0	14.14	1.97
50	57	3.1	14.5	2
30	56	3.4	14.4	2
20	46.6	3.1	17.3	2.3
10	42	5.7	21.2	2.9
5	32	7.8	31.75	4.4

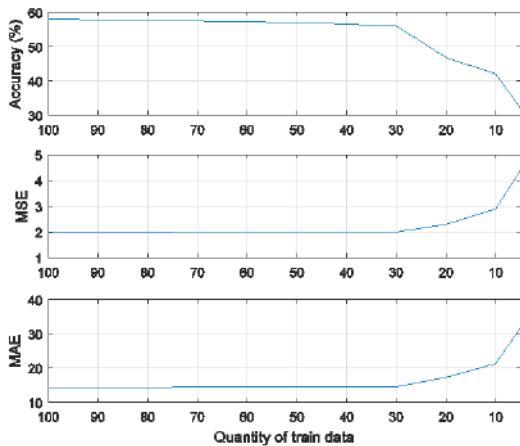


Figure 4. Comparison of prognostics measures for different sizes of train data

² The neural network training multiple times will generate different results due to different initial conditions; Therefore, for sensitivity analysis, the polynomial regression is used for composing prediction

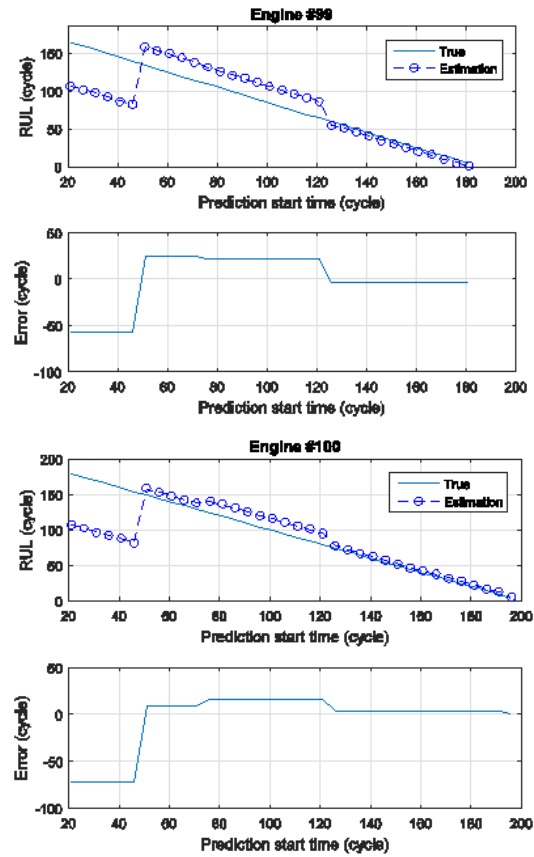


Figure 5. Prognostics results of engines #99-100 in different cycles with limited train data set (10 units for training)

training) are shown in Figure 5 for engines #99-100. Other engines results (#91-98) are shown in Appendix A. The results showed that overall (1) the RUL estimate with small data is reasonably close to the actual RUL especially in large ages, (2) as the engine ages, the prediction error for the RUL gets narrower, means that, the prognostics uncertainty declines, and (3) in some cases, lack of enough data especially in the last cluster, results to increase prediction error. In general, the results indirectly support the hypothesis that, life clustering method leads to acceptable results in condition of train data deficiency (although not necessarily the best method).

6. CONCLUSION

In this paper, a prognostic algorithm is proposed that first classifies the test units in different age groups, then estimates their RUL using predictive techniques. The

modules of the ABC method and the resulted accuracy is different with table 5 (ABC model using ANN)

proposed algorithm uses one of the conventional and available prediction methods (such as ANN as presented in this study) as the core prediction tool and rectifies it with more reliable and robust results .

A case study shows that the results achieved by this method were significantly improved compared to other conventional methods and it was observed that life clustering can be very effective in prognostics. LCP was able to predict with 71% accuracy, a little better than the best published results on the same case study. While the performance of the LCP method was evaluated under normal conditions, its results were examined in the condition of limited training data, which happens frequently in industry .

Comparison of results for different conditions of available training data showed that the prognostic measures remain almost unchanged when the training data is even one third. The reason is that the training data set has been multiplied several times and it compensates the lack of enough training data. Successively, prognostics accuracy decreases with a slight slope; so that when the available training data drops from 30 to 10%, the accuracy of the results drops from 56 to 42%. After that accuracy drops considerably to 32% for 5% of available train data. Although significant accuracy drop is observed below 10% of available train data, it is notable that LCP is using train data of only 5 units to predict remaining life of 100 test units .

In the final stage, more cases were tested and the results of the prognostics algorithm were plotted using a low number of training data (10 engines). The results show that the RUL estimate with small data is rationally close to the actual RUL, although in some cases, severe lack of data especially in the last cluster, results to increase prediction error .

The results of this case study confirmed that the LCP method (1) is a powerful prognostics tool in normal condition and (2) is a robust technique under limited data condition. So the proposed method can be integrated with any classic method to result more accurate and robust RUL estimates for real-world situations. The methodology developed in this paper is not limited to the use with turbojet engine prognostics. It can be extended to other prognostics problems .

Integration and modification of more prediction methods with life clustering idea are to be investigated in future works. However, there are some potential limitations existing in the prediction for the last cluster (in case of severe lack of data) which could be improved with fusion of previous clusters predictions in the future study.

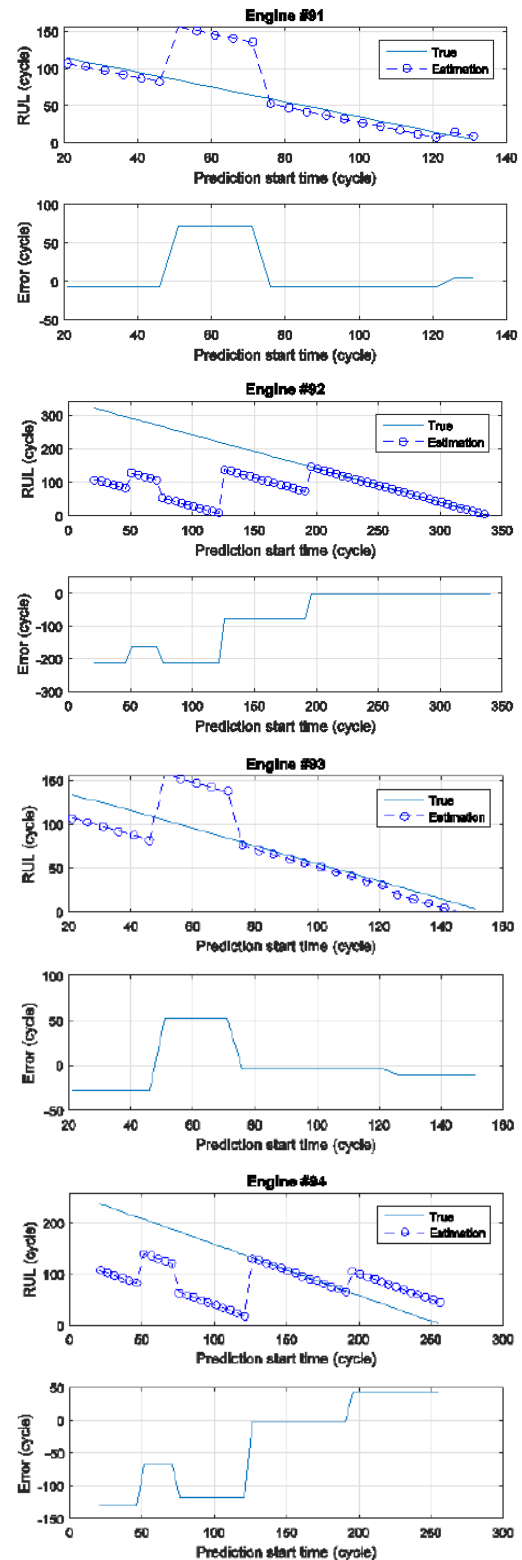
7. REFERENCES

1. Khezri R, Hosseini R, Mazinani M. "A fuzzy rule- based expert system for the prognosis of the risk of development of the breast cancer." *International Journal of Engineering, Transactions A: Basics*. Vol 27, No 10, (2014), 1557-1564. doi: 10.5829/idosi.ije.2014.27.10a.09
2. Hu C, Zhou Z, Zhang J, Si X. "A survey on life prediction of equipment." *Chinese Journal of Aeronautics*. Vol 28, No 1, (2015), 25-33. doi.org/10.1016/j.cja.2014.12.020
3. Hamidi H, Daraee A. "Analysis of pre-processing and post-processing methods and using data mining to diagnose heart diseases." *International Journal of Engineering, Transactions A: Basics* . Vol 29, No 7, (2016), 921-930. doi: 10.5829/idosi.ije.2016.29.07a.06
4. Amini M, Moharrami A, Poursaeidi E. "Failure probability and remaining life assessment of reheater tubes." *International Journal of Engineering, Transactions B: Applications*. Vol 26, No 5, (2013), 543-552. doi: 10.5829/idosi.ije.2013.26.05b.11
5. Peng Y, Dong M, Zuo MJ. "Current status of machine prognostics in condition-based maintenance: a review." *The International Journal of Advanced Manufacturing Technology*. Vol 50, (2010), 297-313. doi.org/10.1007/s00170-009-2482-0
6. Mao R, Zhu H, Zhang L, Chen A. "A new method to assist small data set neural network learning. In Intelligent Systems Design and Applications." *IEEE ISDA'06*. Vol 1, (2006), 17-22. DOI:10.1109/ISDA.2006.67
7. Ranasinghe GD, Lindgren T, Girolami M, Parlikad AK. "A Methodology for Prognostics Under the Conditions of Limited Failure Data Availability". *IEEE Access*. Vol 17, (2019), 173-179. DOI: 10.1109/ACCESS.2019.2960310
8. Li YG, Nilkitsaranont P. "Gas turbine performance prognostic for condition-based maintenance." *Applied Energy*. Vol 86, No 10, (2009), 2152-2161. doi.org/10.1016/j.apenergy.2009.02.011
9. Xiongzi CH, Jinsong YU, Diyin TA, Yingxun WA. "A novel pflssvr-based framework for failure prognostics of nonlinear systems with time-varying parameters." *Chinese Journal of Aeronautics*. Vol 25, (2012), 715-724. doi.org/10.1016/S1000-9361(11)60438-X
10. Tongyang LI, Shaoping WA, Jian SH, Zhonghai MA. "An adaptive-order particle filter for remaining useful life prediction of aviation piston pumps." *Chinese Journal of Aeronautics*. Vol 31, (2018), 941-948. doi.org/10.1016/j.cja.2017.09.002
11. Diallo ON. "A data analytics approach to gas turbine prognostics and health management" (Doctoral Dissertation, Georgia Institute of Technology).
12. Caesarendra W, Widodo A, Yang BS. "Combination of probability approach and support vector machine towards machine health prognostics." *Probabilistic Engineering Mechanics*. Vol 26, (2011), 165-173. doi.org/10.1016/j.probengmech.2010.09.008
13. Huang HZ, Wang HK, Li YF, Zhang L, Liu Z. "Support vector machine based estimation of remaining useful life: current research status and future trends." *Journal of Mechanical Science and Technology*. Vol 29, (2015), 151-163. doi.org/10.1007/s12206-014-1222-z
14. Simon D. "A comparison of filtering approaches for aircraft engine health estimation." *Aerospace Science and Technology*. Vol 12, (2008), 276-284. doi.org/10.1016/j.ast.2007.06.002
15. Lu F, Ju H, Huang J. "An improved extended Kalman filter with inequality constraints for gas turbine engine health monitoring." *Aerospace Science and Technology*. Vol 30, (2016), 36-47. doi.org/10.1016/j.ast.2016.08.008
16. Ding C, Xu J, Xu L. "ISHM-based intelligent fusion prognostics for space avionics." *Aerospace Science and Technology*. Vol 29, (2013), 200-205. doi.org/10.1016/j.ast.2013.01.013
17. Goebel K, Saha B, Saxena A. "A comparison of three data-driven techniques for prognostics." In 62nd Meeting of the Society for Machinery Failure Prevention Technology (Mfpt), (2008), 119-131.

18. Xu J, Wang Y, Xu L. "PHM-oriented integrated fusion prognostics for aircraft engines based on sensor data." *IEEE Sensors Journal*. Vol 14, (2014), 1124-1132. DOI: 10.1109/JSEN.2013.2293517
19. Moghaddass R, Zuo MJ. "An integrated framework for online diagnostic and prognostic health monitoring using a multistate deterioration process." *Reliability Engineering & System Safety*. Vol 124, (2014), 92-104. doi.org/10.1016/j.ress.2013.11.006
20. Xiang Y, Liu Y. "Application of inverse first-order reliability method for probabilistic fatigue life prediction." *Probabilistic Engineering Mechanics*. Vol 26, (2011), 148-156. doi.org/10.1016/j.probengmech.2010.11.001
21. Javed K. "A robust & reliable Data-driven prognostics approach based on extreme learning machine and fuzzy clustering" (*Doctoral Dissertation*).
22. Saxena A, Goebel K, Simon D, Eklund N. "Damage propagation modeling for aircraft engine run-to-failure simulation." *IEEE InPrognostics and Health Management*, (2008). 1-9. DOI:10.1109/PHM.2008.4711414
23. Ramasso E, Rombaut M, Zerhouni N. "Joint prediction of observations and states in time-series: a partially supervised prognostics approach based on belief functions and knn. Networks". (2013). DOI: ff10.1109/TSMCB.2012.2198882
24. Ramasso E. "Investigating computational geometry for failure prognostics." *International Journal of Prognostics and Health Management*. Vol 5, (2014).
25. Khelif R, Malinowski S, Chebel-Morello B, Zerhouni N. "RUL prediction based on a new similarity-instance based approach." *IEEE InIndustrial Electronics (ISIE)*, (2014), 2463-2468. DOI: 10.1109/ISIE.2014.6865006
26. Yakout M, Elkhatib A, Nassef MG. "Rolling element bearings absolute life prediction using modal analysis." *Journal of Mechanical Science and Technology*. Vol 32, (2018), 91-99. doi.org/10.1007/s12206-017-1210-1
27. Prasad SR, Sekhar AS. "Life estimation of shafts using vibration based fatigue analysis." *Journal of Mechanical Science and Technology*. Vol 32, (2018), 4071-4078. DOI: 10.1007/s12206-018-0806-4
28. Mohammadi E, Montazeri-Gh M. "Simulation of full and part-load performance deterioration of industrial two-shaft gas turbine." *Journal of Engineering for Gas Turbines and Power*. Vol 136, (2014), 26-35. DOI: 10.1115/1.4027187
29. Dabaghi E, Kashanian H. "Feature dimension reduction of multisensor data fusion using principal component fuzzy analysis." *International Journal of Engineering, Transactions A: Basics*, Vol 30, No. 4, (2017), 493-499. doi: 10.5829/idosi.ije.2017.30.04a.06
30. Mahmoodian A., Durali M., Abbasain T., Saadat M., "Optimized Age Dependent Clustering Algorithm for Prognosis: A Case Study on Gas Turbines", *ScientiIranica Transaction B: Mechanical Engineering*, (2020), (Articles in Press, Available Online) DOI:10.24200/SCI.2020.53863.3459
31. An D, Kim NH, Choi JH. "Statistical aspects in neural network for the purpose of prognostics." *Journal of Mechanical Science and Technology*. Vol 29, (2015), 1369-1375. DOI: 10.1007/s12206-015-0306-8
32. Wang T, Yu J, Siegel D, Lee J. "A similarity-based prognostics approach for remaining useful life estimation of engineered systems." *IEEE InPrognostics and Health Management*, (2008). 1-6. DOI: 10.1109/PHM.2008.4711421
33. Javed K, Gouriveau R, Zerhouni N., "Novel failure prognostics approach with dynamic thresholds for machine degradation." *IEEE InIndustrial Electronics Society IECON 2013-39th Annual Conference of the IEEE*, (2013) 4404-4409. DOI: 10.1109/IECON.2013.6699844

8. APPENDIX A

Prognostics results of engines #81-96 in different cycles with limited train data set are shown in Figure A-1.



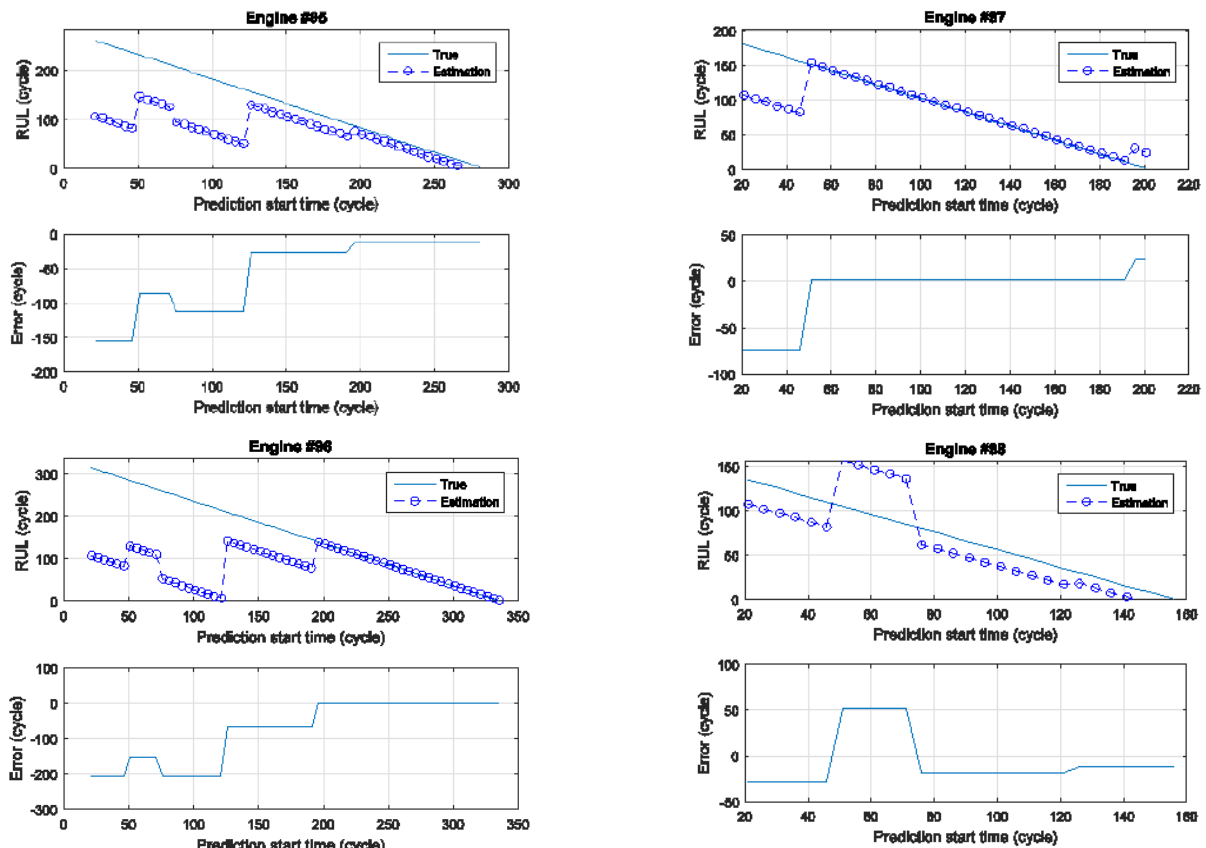


Figure A-1. Prognostics results of engines #91-98 in different cycles with limited train data set

Persian Abstract

چکیده

قابلیت اطمینان الگوریتم‌های پیش‌آگهی داده-پایه به شدت به حجم داده‌ها بستگی دارد. بنابراین در صورت محدودیت داده، برآورد عمر معمولاً قابل قبول نیست. برای حل این مشکل، یک ساختار پیش‌آگهی مبتنی بر خوشه‌بندی عمر پیشنهاد شده است. این ساختار داده‌های آموزش را در سنین مختلف بازسازی کرده و در نتیجه حجم این داده‌ها را افزایش می‌دهد. از این جهت این روش برای مسائلی که با داده محدود مواجه هستند می‌تواند کارآمد باشد. در این تحقیق، ابتدا عملکرد الگوریتم پیشنهادی در شرایط عادی بررسی می‌شود. متعاقباً عملکرد الگوریتم در شرایط محدودیت داده مطالعه می‌شود. برای این منظور، یک مطالعه موردی روی موتورهای توربوفن انجام می‌شود. نتایج حاصل نشان می‌دهد دقت روش پیشنهادی در شرایط عادی 71٪ و بهتر از روش‌های دیگر بوده است. هنگامی که داده‌های آموزش به میزان یک سوم کاهش یافته، دقت پیش‌آگهی تقریباً بدون افت باقی مانده است. وقتی داده‌های آموزش از 100 به 5٪ کاهش یافته، دقت نتایج 26٪ افت کرده است. در مجموع، نتایج بدست آمده حاکی از مقاوم بودن الگوریتم پیشنهادی در شرایط محدودیت داده است.



Introducing an Enhanced Friction Model for Developing Inertia Welding Simulation: A Computational Solid Mechanics Approach

B. Meyghani^{*a}, M. Awang^b, S. S. Emamian^c

^a Institute of Materials Joining, Shandong University, Jingshi Road, Jinan, China

^b Department of Mechanical Engineering, Faculty of Engineering, Universiti Teknologi PETRONAS (UTP), Bandar Seri Iskandar, Perak Darul Ridzuan, Malaysia

^c Center of Advance Manufacturing and Material Processing (AMMP), Department of Mechanical Engineering, Faculty of Engineering, University of Malaya, Malaysia

PAPER INFO

Paper history:

Received 13 December 2020

Received in revised form 01 January 2021

Accepted 15 January 2021

Keywords:

Solid-state Welding

Friction Model

Coulomb Friction Model

Computational Solid Mechanics

ABSTRACT

Numerical simulation of inertia welding attracts enormous research interest during the past decades. Extremely large plastic deformation and complicated frictional behavior make this simulation challenging. In this paper, Norton friction model is modified to be employed in a computational solid mechanics model of inertia welding. A continuous remeshing technique is used to avoid the mesh distortion problem. The results show that after 1.5 (s) the temperature reaches the maximum value of 1200 °C. After that, a decreasing pattern is found for the welding temperature. Moreover, the maximum deformation of 6 mm is obtained. The stress increased to the maximum values of 975 MPa. Consequently, successful prediction of the temperature distribution, thermal history, equivalent plastic deformation, axial shortening and stress distribution is made. The comparisons between the results of this study and the literature showed that implementing the proposed methodology leads to achieving high accuracy results.

doi: 10.5829/ije.2021.34.03c.19

1. INTRODUCTION

Inertia welding or inertia friction welding is a solid-state joining process that is considered as a suitable method for joining different materials together. In this welding, intimate contact of a plasticized at the welding interfaces produces by the frictional heat and the pressure. In order to achieve an accurate finite element modeling of the process, the implementation of the contact interface should be considered as a significant issue. Thus, different available models were presented by researchers [1, 2] for modeling the friction-based joining processes.

Different friction models are proposed by researchers for thermomechanical analysis of the solid-state joining processes such as inertia and friction stir welding (FSW) processes [3-5]. In these models, both computational solid mechanics (CSM) and computational fluid

dynamics (CFD) methods are used in different models. Here, it should be noted that CSM models that are based on finite element methods are mostly used for solving solid mechanics problems, while CFD models are based on finite volume methods and can be appropriate for solving fluid dynamics problems.

In the majority of the proposed CSM based finite element packages, Coulomb friction law is used. In the above-mentioned models, constant or limited ranges for the friction coefficient are employed because the Coulomb friction model is based on the sliding condition [6]. To illustrate the problem, due to the usage of the constant values for the friction coefficient [7, 8], the Coulomb friction model is limited to the sliding frictional condition where the temperature values are low [9]. Based on CSM, Shun et al. [10] employed the Coulomb friction law in DEFORM-3D finite element package for

*Corresponding Author Institutional Email:
Bahman.meyghani@sdu.edu.cn (B. Meyghani)

modeling the inertia welding process. Nimesh et al. used the Coulomb friction model for modeling the dissimilar inertia welding [11] in the Abaqus software environment; however, the model results were limited to the temperature prediction. Constant values of the friction are used in the Coulomb model to simulate FSW process to achieve an accurate prediction of the temperature [12]. From the above-mentioned descriptions, the Coulomb model cannot be accurate to simulate the inertia welding or FSW processes where a partial sliding/sticking condition is available [13]. Consequently, there is a need to use a complicated friction law for simulating the sticking behavior at the tool-workpiece interface.

Although in some limited cases there is an ability (like user-defined subroutines) to modify the package in order to use a more complicated friction model, these modifications are challenging because of the mesh distortion and thereby increasing the computational cost. To explain more, there are different techniques for mesh modeling, Lagrangian, Eulerian and arbitrary Lagrangian-Eulerian (ALE). ALE has been successful in solving the mesh distribution problem which is one of the key and significant difficulties during modeling large plastic deformation processes. However, the computational costs of the ALE method for employing a complicated friction model by user-defined subroutines are high. Norton friction model is proposed by some researchers [13, 14]. In this model, the shear stress is defined to be as a function of relative velocity between the tool velocity and the material velocity. It was claimed that in comparison to the Coulomb friction model, this model has higher accuracy. Another advantage of this model over Coulomb law is the avoidance of a constant value for the friction coefficient. Moreover, in this model the ratio between the shear stress and the pressure is defined as a complicated function of the interface relative velocity (the difference between the velocity of the tool and the material flow velocity). In some model CFD models, Norton friction law is used to achieve a partial sliding sticking condition. They [4, 14] used Norton friction law in the case of sticking condition. These researchers also claim that this formulation can be appropriate for modeling the FSW. As discussed, the majority of the above-mentioned researchers used CFD models, because it can easily handle the distribution of the mesh and its computational costs are low. Here, it should be noted that, the accuracy of the CSM for modeling the inertia welding leads to achieving higher accuracy and efficiency. To illustrate, CSM deals with both mathematical modeling and numerical simulation of solid related phenomena. Thus, these methods can be appropriate for modeling inertia welding. From the above-mentioned descriptions, it can be claimed that accurate implementation of the friction law in the CSM models is mandatory.

Up to now, quite a few models have been developed

to analyze the heat generation, temperature field, plastic deformation and stress in inertia welding quantitatively. Moreover, all proposed models used the Eulerian formulation in CFD models. It should be noted that there are limitations in predicting the strain rate and residual stress for CFD-based models. In the case of using an Eulerian based CSM models, implementing a complicated friction mode, overcoming the mesh distortion and reducing the computational costs are significant challenges.

In this paper, the Norton-Hoff viscoplastic law is modified in order to investigate the relative velocity between the workpieces. Then, a novel method is used to implement this modified friction law to a three-dimensional finite element model (FEM) model. A proper continuous remeshing method is also employed to avoid the distortion of mesh and decreasing the computational costs. Finally, the model is validated by comparing the results of the FE model with experimental tests and the data in the literature.

2. Materials and Methods

2. 1. Interaction Definitions

Five different conditions and one actuator-sensor for the interaction section are defined at the welding interfaces. The constant workpiece is considered to be the master surface and the rotating one is considered to be the slave surface. Two different user-defined subroutines are applied to the model. The first one (Fric) is applied to implement the Norton friction model at the interfaces. A prescribed pressure of 360 MPa is also applied to complete the treatment of friction force. Thus, the generation of the heat is based on the traction and the sliding velocity. The second subroutine UEL is applied as an actuator-sensor. As mentioned, the modified Norton friction model is used in this model that is based on the friction law proposed by Moal and Massoni [15]. Equation 1 shows the general form of the model.

$$\tau = -P \times g(\Delta v_g) \times \frac{\Delta v_g}{|\Delta v_g|} \quad (1)$$

where τ is the shear stress, P is the prescribed pressure and $g(\Delta v_g)$ is the defined function for the ratio between the tool velocity and the material velocity.

It should be noted that Equation 1 is calculated based on the experiments done by Moal and Massoni [15]. In this equation the ratio between the shear stress and the pressure (τ/P) is equal to the relative velocity function. Different conditions are defined for the relative velocity function ($g(\Delta v_g)$) [16, 17]. These conditions are based on the difference between the velocity of the tool and the material velocity at each point and each increment. A sticking condition is proposed near the tool-workpiece interface, where the relative velocity is not high [18]. Far

from the welding tool, a sliding condition is proposed. In this sliding condition, a constant value for the ratio between the shear and the pressure is considered, while a complicated polynominal function is considered for the sticking condition.

2. 1. Finite Element Model Descriptions A fully coupled temperature displacement analysis is selected as the analysis type [19, 20]. Two deformable parts are defined for the workpieces. The element type of CGAX4HT and CGAX3HT are selected for the simulation. The remeshing technique is also employed to avoid mesh distortion [21, 22]. In order to approximate the high-temperature behavior for Astroloy, the Norton-Hoff constitutive law is proposed to explain the complicated temperature and strain rate viscoplastic behavior. It needs to be explained that a rate dependent perfectly plastic material model is also defined [23]. Figure 1 shows a brief explanation for the initial model of the welding in a 2-dimensional viewpoint. Moreover, the room temperature of 20 °C is defined as the initial temperature [24, 25]. The initial rotating velocity for the workpiece is defined to be 48.17 radians per second and the mass moment of inertia of 102,000 Mg mm² is applied to the model.

3. RESULTS AND DISCUSSION

As mentioned earlier, two different subroutines are used to simulate the welding. At each step of the welding, the mesh converts to the geometry, then a new meshing applies for the new geometry (deformed geometry). It should be noted that all of the calculated results (temperature, stress, strains, etc.) at each step will be mapped and considered as new boundary conditions for the next step.

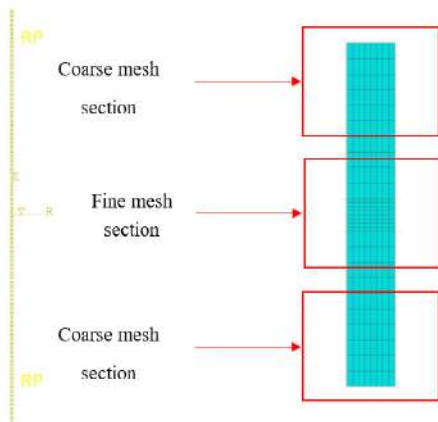


Figure 1. Schematic view and the initial mesh for the workpiece

3. 1. Temperature Distribution The distribution of the temperature in 2 and 3-dimensional viewpoints are shown in Figure 2. As can be seen in Figure 2 section a, the upset is formed successfully and accurately. The contour plot shows the temperature of 1103 °C at the interface between two pipes. The achieved values of the temperature are confirmed by the literature [26]. The temperature decreases along with the fully plastic deformed zone (the maximum temperature of 1011 °C). Far from the welding interface, the temperature has a decreasing rate pattern, because of the distance from the heat source. The main reason for this issue is the conduction, which transfers the heat along with the welding interface [27]. Moreover, due to the continuous remeshing, the mesh distortion problem is solved properly. From Figure 2, it can be seen that there is an extrude flash near the welding interface. This issue is also reported in the literature [27].

Figure 3 indicates the relationship between the time and the temperature at the welding interface. As can be seen, the temperature values sharply increase up to 1200 °C after 1.5 (s) of the welding. This indicates that the main source for the generating of the heat is the frictional force at the welding interface. Due to the implementation of an accurate frictional model in this study, the temperature pattern is in line with the literature [28]. This sharp increase in the values of temperature softens the

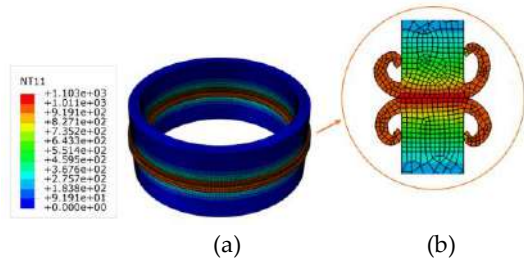


Figure 2. The temperature distribution a) three dimensional and the welding zone b) cross section of the welding

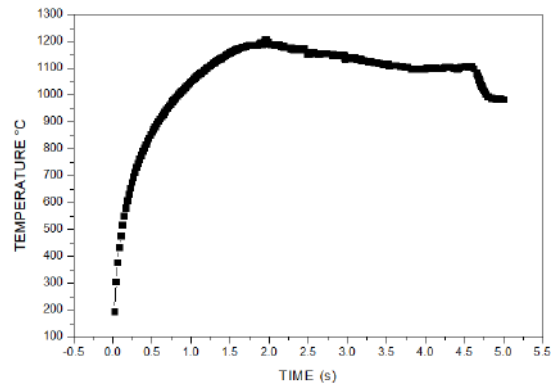


Figure 3. Temperature history at the welding interface

material, and make the deformation of the interface material easier. It can also be observed that a periodic fluctuation of temperature has happened during welding.

The contour plots of the temperature history are shown in Figure 4. As can be seen, after starting the welding (Figure 4-a), the temperature increases to the maximum value of 1178 °C. Applying a high pressure at the beginning of the welding can be the main reason for this sharp increasing rate for the temperature. Figure 4-b shows that with increasing the welding time, the temperature values decrease to 1150°C. It is obvious from Figure 4-c (at 1109 °C) and Figure 4-d (at 1150 °C) that the temperature is decreased as the welding continues. This is happening because of the increase in the amount of the transferred heat from radiation and convection. It should be noted that as the area of the fully plastic deformed zone increases, the heat transfer by radiation and convection increases as well, thus the welding interface temperature decreases. This phenomenon is also reported in the literature [29], which shows the accuracy of the results of this study.

3. 2. Equivalent Plastic Strain

Figure 5 shows the relationship between the shortening of the welding interface and time. As can be seen, before achieving the peak temperature, the workpiece did not deform significantly. After 1.5 (s) the deformation begins and followed a sharp increasing pattern. To illustrate, the deformation sharply increased from 0 to 5 mm until the step time of 4.5 (s) (where the pressure is relieved from the pipes). This issue means that the length of the pipes decreases almost around 5 mm. From the welding time of 4.5 (s) to 5 (s) the deformation rate becomes constant, due to decreasing the pressure on the pipes. Comparisons with the data in literature show that the results of this section are in good agreement with the literature [30].

The equivalent plastic strain during the welding in 2 and 3 dimensions are shown in Figure 6-a. It is obvious

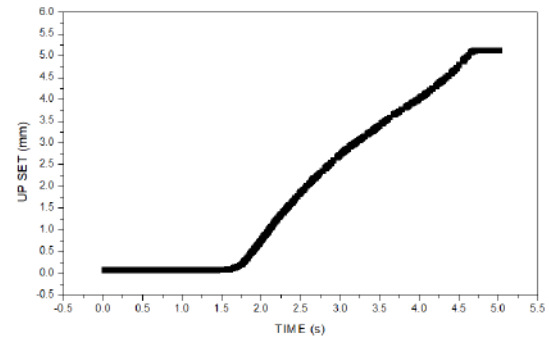


Figure 5. The relationship between the shortening and the time at the welding interface

that the maximum plastic strain is happening at the center of the welding, where two plates are joining together. Achieving the highest plastic deformation in this area is happening because the maximum temperature is located in this area. The plastic deformation decreases far from the welding interface (where the temperature drops gradually). This shows that there is a proportional relationship between plastic deformation and temperature. Figure 6 also indicates plastic deformation history. The results show that with increasing the welding time, the equivalent plastic deformation increases as well. As can be seen in Figure 6-e the maximum plastic deformation is happening in the peripheral regions. An almost asymmetric pattern for the upper and lower surfaces is achieved at the equilibrium stage. From the results of the fully plastic deformation zone, it is obvious

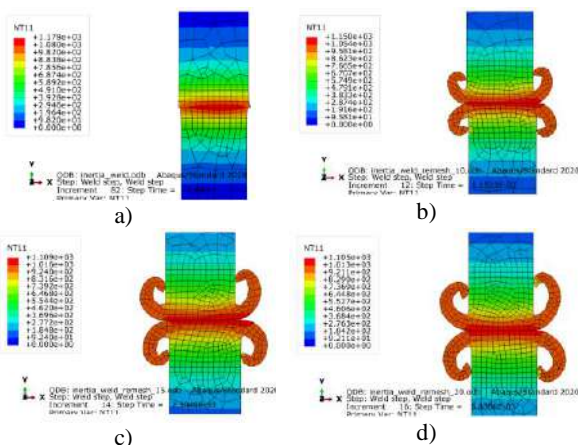


Figure 4. Contour plot of the temperature distribution history

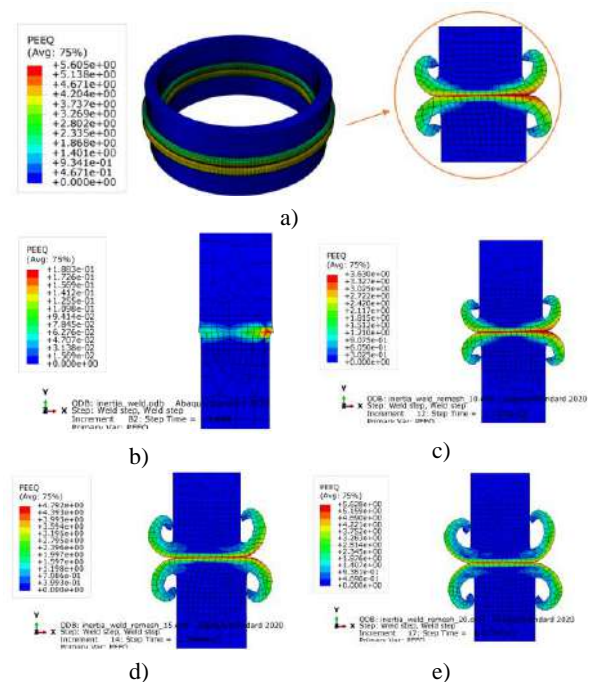


Figure 6. Equivalent plastic strain distribution

that the remeshing technique could accurately handle the mesh distortion problem.

3.3. Stress Distribution The stress distribution is one of the most significant issues during inertia welding, thus in the last part of the results and discussion section, this issue is addressed. Figure 7-a shows the distribution of the stress field in 2 and 3-dimensional viewpoints. The stress history also can be seen from Figure 7-b to Figure 7-e. The decreasing values of the stress at the welding are caused because of the decrease in the temperature. This matter indicates that, like the plastic deformation, there is a proportional relationship between the stress and the temperature. The stress distribution has an almost symmetrical pattern at the welding interface. As the distance from the welding interface increases, this symmetrical pattern changes to an almost asymmetrical shape. The maximum values of the stress are observed to be around 975 MPa (at the fully plastic deformed zone). It should be noted that the stress behavior is in good agreement with the achieved results in the literature [31].

4. CONCLUSIONS

In this paper, a modified Norton friction model is proposed for finite element modeling of the inertia welding process. A continuous remeshing technique is also employed to avoid mesh distortions.

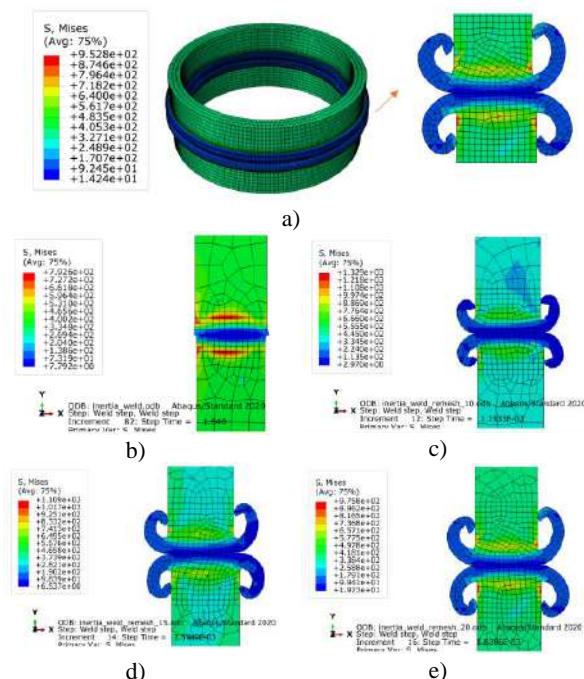


Figure 7. The distribution of the stress during welding

The summary of the findings can be concluded as below:

- The maximum temperature of 1200 °C is reached at the welding interface (at the welding time of 1.5 seconds).
- After that, the temperature decreased due to the increase of the radiation and convection heat transfer from the workpiece to the outside region.
- At the welding interface, the maximum deformation of 6 mm is observed.
- The maximum values of 975 MPa for the stress is achieved.
- Equivalent plastic deformation and stress are found to have an almost symmetrical pattern.
- A proportional relationship between the temperature and both the plastic deformation and stress is obtained.
- Comparisons showed a good agreement between the results of this study and the previous literature.

5. REFERENCES

1. Buffa, G., Fratini, L., Impero, F., Masnata, A., Scherillo, F. and Squillace, A., "Surface and mechanical characterization of stationary shoulder friction stir welded lap joints: Experimental and numerical approach", *International Journal of Material Forming*, Vol., (2020), 1-12. <https://doi.org/10.1007/s12289-020-01574-9>
2. Sun, Z., Wu, C. and Kumar, S., "Determination of heat generation by correlating the interfacial friction stress with temperature in friction stir welding", *Journal of Manufacturing Processes*, Vol. 31, (2018), 801-811. <https://doi.org/10.1016/j.jmapro.2018.01.010>
3. Meyghani, B., Awang, M.B., Emamian, S.S., Mohd Nor, M.K.B. and Pedapati, S.R., "A comparison of different finite element methods in the thermal analysis of friction stir welding (fsw)", *Metals*, Vol. 7, No. 10, (2017), 450. <https://doi.org/10.3390/met7100450>
4. Meyghani, B. and Wu, C., "Progress in thermomechanical analysis of friction stir welding", *Chinese Journal of Mechanical Engineering*, Vol. 33, No. 1, (2020), 12. <https://doi.org/10.1186/s10033-020-0434-7>
5. Miles, M., Nelson, T., Gunter, C., Liu, F., Fourment, L. and Mathis, T., "Predicting recrystallized grain size in friction stir processed 304l stainless steel", *Journal of Materials Science & Technology*, Vol. 35, No. 4, (2019), 491-498. <https://doi.org/10.1016/j.jmst.2018.10.021>
6. Meyghani, B., Awang, M.B., Momeni, M. and Rynkovskaya, M., "Development of a finite element model for thermal analysis of friction stir welding (fsw)", in IOP Conference Series: Materials Science and Engineering, IOP Publishing. Vol. 495, (2019), 012101. Doi:10.1088/1757-899X/495/1/012101
7. Meyghani, B., Awang, M. and Emamian, S., "A mathematical formulation for calculating temperature dependent friction coefficient values: Application in friction stir welding (fsw)", in Defect and Diffusion Forum, Trans Tech Publ. Vol. 379, (2017), 73-82. <https://doi.org/10.4028/www.scientific.net/DDF.379.73>
8. Meyghani, B., Awang, M.B., Poshteh, R.G.M., Momeni, M., Kakooei, S. and Hamdi, Z., "The effect of friction coefficient in thermal analysis of friction stir welding (FSW)", in IOP Conference Series: Materials Science and Engineering, IOP

- Publishing. Vol. 495, (2019), 012102. Doi:10.1088/1757-899X/495/1/012102
9. Dialami, N., Cervera, M., Chiumenti, M. and de Saracibar, C.A., "Local-global strategy for the prediction of residual stresses in fsw processes", *The International Journal of Advanced Manufacturing Technology*, Vol. 88, No. 9, (2017), 3099-3111. <https://doi.org/10.1007/s00170-016-9016-3>
 10. Ji, S.-d., Liu, J.-g., Yue, Y.-m., Zan, L. and Li, F., "3d numerical analysis of material flow behavior and flash formation of 45# steel in continuous drive friction welding", *Transactions of Nonferrous Metals Society of China*, Vol. 22, (2012), s528-s533. [https://doi.org/10.1016/S1003-6326\(12\)61756-7](https://doi.org/10.1016/S1003-6326(12)61756-7)
 11. NIMESH, P., "Simulation of inertia friction welding of mild steel and aluminium 6061 using finite element method on abaqus", (2016).
 12. Meyghani, B., Awang, M. and Wu, C., "Thermal analysis of friction stir welding with a complex curved welding seam (technical note)", *International Journal of Engineering, Transactions A: Basics*, Vol. 32, No. 10, (2019), 1480-1484. <https://dx.doi.org/10.5829/ije.2019.32.10a.17>
 13. Dialami, N., Cervera, M., Chiumenti, M., Segatori, A. and Osikowicz, W., "Experimental validation of an fsw model with an enhanced friction law: Application to a threaded cylindrical pin tool", *Metals*, Vol. 7, No. 11, (2017), 491. <https://doi.org/10.3390/met7110491>
 14. Dialami, N., Cervera, M., Chiumenti, M. and de Saracibar, C.A., "A fast and accurate two-stage strategy to evaluate the effect of the pin tool profile on metal flow, torque and forces in friction stir welding", *International Journal of Mechanical Sciences*, Vol. 122, (2017), 215-227. <https://doi.org/10.1016/j.ijmecs.2016.12.016>
 15. Moal, A. and Massoni, E., "Finite element simulation of the inertia welding of two similar parts", *Engineering Computations*, (1995). <https://doi.org/10.1108/026444409510799730>
 16. MEYGHANI, B., "Thermomechanical analysis of friction stir welding (fsw) on curved plates by adapting calculated temperature dependent properties", Universiti Teknologi PETRONAS, (2018),
 17. Meyghani, B. and Awang, M., "A comparison between the flat and the curved friction stir welding (fsw) thermomechanical behaviour", *Archives of Computational Methods in Engineering*, (2019), 1-14. <https://doi.org/10.1007/s11831-019-09319-x>
 18. Meyghani, B., Awang, M. and Wu, C., "Finite element modeling of friction stir welding (fsw) on a complex curved plate", *Journal of Advanced Joining Processes*, Vol. 1, (2020), 100007. <https://doi.org/10.1016/j.jajp.2020.100007>
 19. Meyghani, B., Awang, M., Emamian, S. and Akinlabi, E., "A comparison between temperature dependent and constant young's modulus values in investigating the effect of the process parameters on thermal behaviour during friction stir welding: Vergleich zwischen den temperaturabhängigen und konstanten elastizitätsmodulwerten in der untersuchung der prozessparameter auf die wärmewirkung beim rührreibschweißen", *Materialwissenschaft und Werkstofftechnik*, Vol. 49, No. 4, (2018), 427-434. <https://doi.org/10.1002/mawe.201700255>
 20. Meyghani, B., Awang, M., Emamian, S. and Khalid, N.M., "Developing a finite element model for thermal analysis of friction stir welding by calculating temperature dependent friction coefficient", in 2nd International Conference on Mechanical, Manufacturing and Process Plant Engineering, Springer. (2017), 107-126. https://doi.org/10.1007/978-981-13-8297-0_64
 21. Meyghani, B., Awang, M., Emamian, S. and Nor, M.K.B.M., Thermal modelling of friction stir welding (FSW) using calculated young's modulus values, in The advances in joining technology. 2018, Springer.1-13. https://doi.org/10.1007/978-981-10-9041-7_1
 22. Meyghani, B., Awang, M. and Emamian, S., "A comparative study of finite element analysis for friction stir welding application", *ARP Journal of Engineering and Applied Sciences*, Vol. 11, No. 22, (2016), 12984-12989.
 23. Meyghani, B., Awang, M. and Wu, C., "Thermal analysis of friction stir processing (FSP) using arbitrary lagrangian-eulerian (ALE) and smoothed particle hydrodynamics (SPH) meshing techniques", *Materialwissenschaft und Werkstofftechnik*, Vol. 51, No. 5, (2020), 550-557. <https://doi.org/10.1002/mawe.201900222>
 24. Meyghani, B. and Awang, M., "A novel tool path strategy for modelling complicated perpendicular curved movements", *Key Engineering Materials*, Vol. 796, (2019), 164-174. <https://doi.org/10.4028/www.scientific.net/KEM.796.164>
 25. Meyghani, B. and Awang, M., "Developing a finite element model for thermal analysis of friction stir welding (fsw) using hyperworks", in Advances in Material Sciences and Engineering, Singapore, Springer Singapore., (2020), 619-628. https://doi.org/10.1007/978-981-13-8297-0_64
 26. Wang, K., "Transient temperature distribution in inertia welding of steels", *Welding Journal*, Vol. 49, (1970), 419s-426s.
 27. Qin, G., Geng, P., Zhou, J. and Zou, Z., "Modeling of thermo-mechanical coupling in linear friction welding of ni-based superalloy", *Materials & Design*, Vol. 172, (2019), 107766. <https://doi.org/10.1016/j.matdes.2019.107766>
 28. Okeke, S., Harrison, N. and Tong, M., "Thermomechanical modelling for the linear friction welding process of ni-based superalloy and verification", *Proceedings of the Institution of Mechanical Engineers, Part L: Journal of Materials: Design and Applications*, Vol. 234, No. 5, (2020), 796-815. <https://doi.org/10.1177/2F1464420719900780>
 29. Mohammed, M., Bennett, C., Shipway, P. and Hyde, T., "Optimization of heat transfer in the finite element process modelling of inertia friction welding of scmv and aermet 100", *WIT Transactions on Engineering Sciences*, Vol. 68, (2010), 253-265.
 30. Meyghani, B., Awang, M. and Wu, C., "Thermal analysis of friction stir welding with a complex curved welding seam", *International Journal of Engineering, Transactions A: Basics*, Vol. 32, No. 10, (2019), 1480-1484. Doi: <https://dx.doi.org/10.5829/ije.2019.32.10a.17>
 31. Meyghani, B. and Awang, M.B., "Prediction of the temperature distribution during friction stir welding (FSW) with a complex curved welding seam: Application in the automotive industry", MATEC Web Conference, Vol. 225, (2018), 01001. <https://doi.org/10.1051/mateconf/201822501001>

Persian Abstract

چکیده

شبیه سازی عددی جوشکاری اینرسی در دهه های گذشته مورد توجه تحقیقاتی زیادی قرار گرفته است. تغییر شکل مومسان بسیار بزرگ و رفتار اصطکاکی پیچیده این شبیه سازی را به چالش می کشد. در این مقاله مدل اصطکاک نورتون اصلاح شده است تا در یک مدل مکانیکی جامد محاسباتی جوشکاری اینرسی استفاده شود. برای جلوگیری از مشکل واپیچش مش از یک روش بازسازی مداوم استفاده می شود. نتایج نشان می دهد که بعد از 1.5 ثانیه دما به حداکثر مقدار 1200°C می رسد. پس از آن، الگوی کاهشی برای دمای جوش بروز می کند علاوه بر این، حداکثر تغییر شکل 6 میلی متر به دست می آید. مقادیر تنش به حداکثر 975 مگاپاسکال افزایش یافت. در نتیجه، پیش بینی موفقیت آمیز توزیع دما، تاریخچه حرارتی، تغییر شکل مومسان معادل، انقباض محوری و توزیع تنش ممکن می شود. مقایسه بین نتایج این مطالعه و اطلاعات گزارش شده در ادبیات نشان داد که اجرای روش پیشنهادی منجر به دست یابی به نتایج با دقت بالا می شود.



Size-dependent Vibration Analysis of Stepped Nanobeams Based on Surface Elasticity Theory

A. Assadi*, M. Nazemizadeh

Faculty of Mechanics, Malek Ashtar University of Technology, Tehran, Iran

PAPER INFO

Paper history:

Received 12 September 2020

Received in revised form 22 November 2020

Accepted 04 December 2020

Keywords:

Vibration
Nanobeams
Stepped
Size-dependent
Surface Effect

ABSTRACT

This paper investigates size-dependent vibrations of stepped nanobeams taken into account surface elasticity theory. To do this, the nanobeams are modeled as stepped beams and size-dependent governing vibration equations are derived considering compatibility conditions in stepped sections. Then, an analytical solution is developed to simulate natural frequencies and mode shapes of the nanobeam with various surface properties. Also, a backward procedure is proposed to verify the obtained results and calculate size-dependent effective surface modulus. The results indicate that surface effects and appropriate steps selection have noticeable impact on natural frequencies of non-uniform nanobeams. Also, the stepped modeling of the nanobeam became more important for longer and slender ones. Moreover, despite uniform nanobeams, the mode shapes of the non-uniform nanobeams are also extremely dependent on the surface effects.

doi: 10.5829/ije.2021.34.03c.20

NOMENCLATURE

		Greek Symbols	
E	Young's modulus of the nanobeam	ρ	Mass density
E^s	Surface Young's modulus of the nanobeam	ε	Strain components
EI_{eff}	Effective bending rigidity	σ	Stress components
L_i	Length of i th section	σ^o	Residual normal stress
d^p	Particle diameter (μm)	σ^s	Surface stress components
w	transverse deflection of the nanobeam		

1. INTRODUCTION

In the recent years, remarkable developments in science and technology have afforded the ability to fabricate small size structures with micron to nano dimensions [1-2]. Among these novel structures, micro/nanobeams have recognized as important components of micro/nano systems such as micro/nano resonators, atomic force microscopes (AFM), etc [3-4]. Therefore, development of advanced micro/nano systems requires proper prediction of their mechanical behavior. Korayem et al. [5] presented dynamic modeling of an atomic force beam for micro/nano manipulation in

which the beam was modeled as a lumped mass. However, lumped mass modeling cannot be approved as an accurate model for a continuous beam, especially in the nano-scale.

On the other hand, the capability of classical continuum theory to model micro/nano systems is strongly doubted through conducting experimental tests and molecular simulations. Accordingly, various analytical higher-order theories have been established to fix the problem. Bakhtiari-Nejad et al. [6] studied size-dependent free vibrations of piezoelectric nanobeams based on the nonlocal elasticity theory. Also, they [7] developed a general formulation of linear natural frequencies and corresponding quality factors for micro/nano composite beams having arbitrary laminated layers based on the nonlocal elasticity theory. Beni [8]

*Corresponding Author Institutional Email: assadi@mut-es.ac.ir (A. Assadi)

employed couple stress theory to model and analyze an isotropic Euler-Bernoulli nano-beam. Nazemizadeh et al. [9] studied size-dependent nonlinear free vibration of a pizeolectric-laminated nanobeam considering the nonlocal elasticity theory. Also, they [10] investigated size effects on the nonlinear dynamic modeling and vibration analysis of a nanobeam at higher modes of vibration.

Furthermore, among the higher-order mechanics theories, the theory of surface elasticity initiated by Gurtin and Murdoch [11] has attracted great interests in nanotechnology. Jiang and Yan [12] employed the surface elasticity theory for static bending of shear deformable nanobeams. They derived the governing equation of the nanobeam and analytically solved the problem. Farshi et al. [13] presented size effects of vibration of the nanobeams taken into account the surface elasticity theory. Assadi and Nazemizadeh [14] presented size-dependent static bending of a Nanobeam based on the surface elasticity theory. They developed Euler nanobeam model to derive the differential equation and used a theoretical solution for the static behavior of the nanobeam.

According to the literature review, there is a need to take into account size-dependent vibration characteristic of the surface parameters. So in this paper, an inverse procedure is proposed to verify the obtained results and calculate size-dependent effective surface modulus of the nanobeam. To do this, the nanobeams are modeled as stepped beams and size-dependent governing vibration equations are derived considering compatibility conditions in stepped sections. Then, an analytical solution is developed to simulate natural frequencies and mode shapes of the nanobeam with various surface properties.

2. PROBLEM FORMULATION

In this section, the governing equation of the size-dependent vibration of the nanobeam is presented. Figure 1 shows a nanobeam with non-uniform cross section and its equivalent stepped beam. For analysis of the problem here it is intended to find the generalized governing equations in the presence of any type of external loadings. For more information, every section

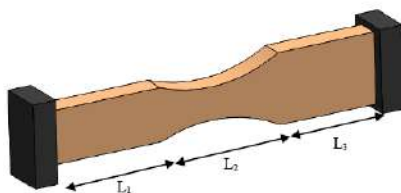


Figure 1. A non-uniform nanobeam

of the beam follows this general equation but we have to satisfy the relating boundary conditions in each case which will be explained in the next section. According to the Euler-Bernoulli beam theory, the strain field of a beam is given as follows:

$$\epsilon_{xx} = -z \frac{\partial^2 w}{\partial x^2}; \quad \epsilon_{xz} = 0 \tag{1}$$

In this relation, w is the transverse deflection of the nanobeam. Also, ϵ_{xx} and ϵ_{xz} are the normal and tangential strains. Moreover, x and z are the coordinate selections across the nanobeams' length and thickness, respectfully. It is to be noted that the origin of z is the nanobeams' neutral axes. The stress field of the deflected nanobeams can be given as follows:

$$\sigma_{xx} = \sigma_{xx}^o - Ez \frac{\partial^2 w}{\partial x^2} \tag{2}$$

In this equation σ^o is the residual normal stress induced in nanobeams by surface residual stresses. According to generalized Gurtin-Murdoch relation [14], it will be obtained for Euler-Bernoulli beam model:

$$\begin{aligned} \sigma_{xx}^s &= \tau^s - E^s z \frac{\partial^2 w}{\partial x^2} \Big|_s \\ \sigma_{xz}^s &= \tau^s \frac{\partial w}{\partial x} \end{aligned} \tag{3}$$

Accordingly, the bending moment of the cross section will be obtained from the following integral equation:

$$\begin{aligned} M &= \iint_A \sigma_{xx} z dA + \int_z \sigma_{xx}^s z dS = \\ &\left(\iint_A z \sigma_{xx}^o dA + \int_z \tau^s z dS \right) - EI_{eff} \frac{\partial^2 w}{\partial x^2} \end{aligned} \tag{4}$$

While the effective bending rigidity EI^{eff} is obtained from the following relation:

$$EI_{eff} = \iint_A Ez^2 dA + \int_z E^s z^2 dS \tag{5}$$

In the above equation, the effective bending rigidity is a combination of bulk and surface elasticity rigidity. In fact, the surface rigidity is originated from the surface effects at nano scales.

On the other hand and according to the self-equilibrating condition, the integral relations in the right hand side of Equation (4) cancel each other and the bending moment is obtained as follows:

$$M = -EI_{eff} \frac{\partial^2 w}{\partial x^2} \tag{6}$$

Finally the governing general differential equation for the deflected nanobeams with consideration of surface effects as follows:

$$EI_{eff} \frac{\partial^4 w}{\partial x^4} + F \frac{\partial^2 w}{\partial x^2} + \rho A \frac{\partial^2 w}{\partial t^2} = 2\tau^s b \frac{\partial^2 w}{\partial x^2} \tag{7}$$

where b is the length of the nanobeams' neutral axis.

3. PROBLEM SOLUTION

The general solution of Equation (7) is taken as $w(x,t)=W(x).sin(\omega_n t)$ from simple variable separation method. Therefore, the following equation must be satisfied for each section of the nanobeams for $W(x)$:

$$EI_{eff} \frac{\partial^4 W}{\partial x^4} - 2\tau^s b \frac{\partial^2 W}{\partial x^2} - \rho A \omega_n^2 W = 0 \tag{8}$$

For simplicity of the problem, another form of Equation (8) is given in bellow:

$$\frac{\partial^4 W}{\partial x^4} - \alpha^2 \frac{\partial^2 W}{\partial x^2} - \eta_n^4 W = 0$$

$$\alpha^2 = \frac{2\tau^s b}{EI_{eff}} \quad \eta_n^4 = \frac{\rho A \omega_n^2}{EI_{eff}} \tag{9}$$

Next, Equation (9) is separated as two 2nd order independent differential equations from which the summation of the solutions represents the general solution of Equation (9):

$$\left. \begin{aligned} \frac{\partial^2 W_I}{\partial x^2} + \zeta_n^2 W_I = 0 \quad \zeta_n^2 = \frac{\alpha^2 + \sqrt{\alpha^4 + 4\eta_n^4}}{2} \\ \frac{\partial^2 W_{II}}{\partial x^2} + \psi_n^2 W_{II} = 0 \quad \psi_n^2 = \frac{\alpha^2 - \sqrt{\alpha^4 + 4\eta_n^4}}{2} \end{aligned} \right\} \tag{10}$$

$$\Rightarrow W = W_I + W_{II}$$

In this equation, W_I is the shape function at the first section of the beam and W_{II} is the shape function at the second section of the nanobeam. Also, it is seen that ζ_2 is a positive definite parameter but ψ_2 is always negative. On the other hand, in order to reduce the number of unknowns of the problem, the following relation governs between these parameters:

$$\zeta_n^2 + \psi_n^2 = \alpha^2 \tag{11}$$

From solving Equation (10), the general solution for W in the case of free vibration is given by the following equation:

$$W = C_1 \sin(\zeta_n x) + C_2 \cos(\zeta_n x) + C_3 \sinh(\psi_n x) + C_4 \cosh(\psi_n x) \tag{12}$$

Next, the boundary conditions of Equation (12) must be satisfied to valid the eigenvalue problem of free vibration for each sets of boundary conditions. Here the whole nanobeam is assumed to be simply supported. Similar to the buckling analysis, the following matrix

equation is obtained for the common boundary conditions of i -th and $(i+1)$ -th sections:

$$\begin{bmatrix} f_n^i & g_n^i & h_n^i & l_n^i & 0 & -1 & 0 & -1 \\ \zeta_n^i g_n^i & -\zeta_n^i f_n^i & \psi_n^i h_n^i & \psi_n^i l_n^i & -\zeta_n^{i+1} & 0 & -\psi_n^{i+1} & 0 \\ -\zeta_n^{i2} f_n^i & -\zeta_n^{i2} g_n^i & \psi_n^{i2} h_n^i & \psi_n^{i2} l_n^i & 0 & \phi_i(\zeta_n^{i+1})^2 & 0 & -\phi_i(\psi_n^{i+1})^2 \\ -\zeta_n^{i3} g_n^i & \zeta_n^{i3} f_n^i & \psi_n^{i3} h_n^i & \psi_n^{i3} l_n^i & \phi_i(\zeta_n^{i+1})^3 & 0 & -\phi_i(\psi_n^{i+1})^3 & 0 \end{bmatrix} \tag{13}$$

$$f_n^i = \sin(\zeta_n^i L_i); \quad g_n^i = \cos(\zeta_n^i L_i); \quad h_n^i = \sinh(\psi_n^i L_i); \quad l_n^i = \cosh(\psi_n^i L_i); \quad \phi_i = \frac{EI_{eff}^{i+1}}{EI_{eff}^i}$$

On the other hand, the boundary conditions for the left side of the first section and the right side of the last section make the problem to follow the given relations in Equation (14):

$$C_2^1 + C_4^1 = 0;$$

$$C_2^1 (\zeta_n^1)^2 - C_4^1 (\psi_n^1)^2 = 0$$

$$\left\{ \begin{aligned} C_1^N f_n^N + C_2^N g_n^N + C_3^N h_n^N + C_4^N l_n^N \\ + C_1^N (\zeta_n^N)^2 f_n^N + C_2^N (\zeta_n^N)^2 g_n^N \\ - C_3^N (\psi_n^N)^2 h_n^N - C_4^N (\psi_n^N)^2 l_n^N \end{aligned} \right\} = 0 \tag{14}$$

Finally, all the matrixes of Equation (13) for $i = 2 \dots N$ together with Equation (14) must be merged to give the general matrix equation of a step-wised nanobeam with N sections. It is seen that if all the material and geometric parameters are given, then the only unknown parameter in the coefficient matrix of Equation (13) is the natural frequency ω_n .

4. SIMULATION RESULTS

In this section, a wide range of vibration simulations are presented for aluminum and silicon-100 nanobeams with the following material parameters (see Table 1) [14].

To verify the proposed method, in Figure 2, the obtained results for vibration analysis of a uniform nanobeam are compared with experiment results presented by He and Lilley [15].

From this figure it is observed that, satisfactory agreement is achieved between the results of this work and those of experimental investigations of other references.

For other simulations, the problem is solved once for nanobeams with surface effects, then for nanobeams without surface effects and the results are comprehensively compared. For this purpose the

TABLE 1. Material properties of the nanobeam

Material	E(Gpa)	ν	E ^s (N/m)	τ^s (N/m)
Al	68.50	0.35	6.090	0.910
Si [100]	130.0	0.24	-11.50	-0.505

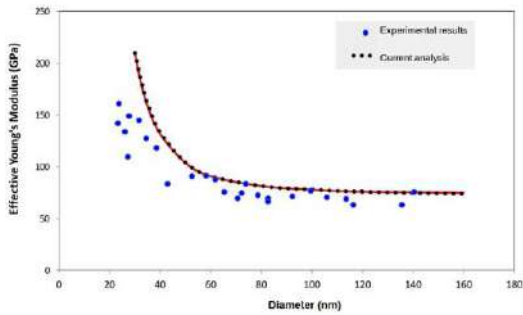


Figure 2. Comparison of effective Young's modulus between the present work and experiment results given by He and Lilley [15]

parameter of NNF (normalized natural frequency) is introduced which the ratio of natural frequency ω_n to that of nanobeams without surface effects. Figure 3 gives the results for size dependent behavior of NNF for one-step nanobeams.

According to Figure 3, it is seen that as D_2 gets higher, the surface effects reduce. In addition, the surface effects on the natural frequency are higher at longer nanobeams. The positive surface residual stress increases the natural frequency but the negative one decreases. Moreover, sensitivity of the problem to D_2/D_1 is higher for longer nanobeams. Also, in the cases of nanobeams with total lengths lower than 30 nm, the whole structure may be modeled as a uniform nanobeam with a simple solution with errors less than %15. In addition, in general the nanobeams with negative surface effects must be modeled more precisely since their natural frequency extremely depend on the magnitude of D_2 .

Next, the vibration problem is solved for two-step nanobeams with the numerical results given in Figure 4.

From this figure, it is seen that, for the constant length of the nanobeams, NNF can be taken independent of D_3 but with an engineering approximation. Moreover, it is observed that thickening and shortening of one section of the step-wised

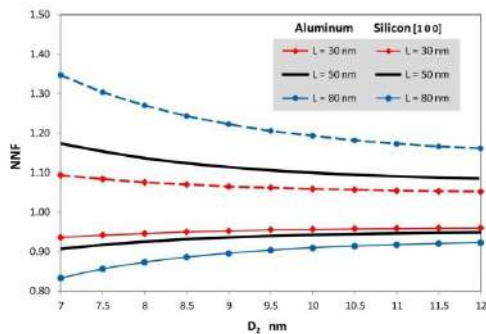
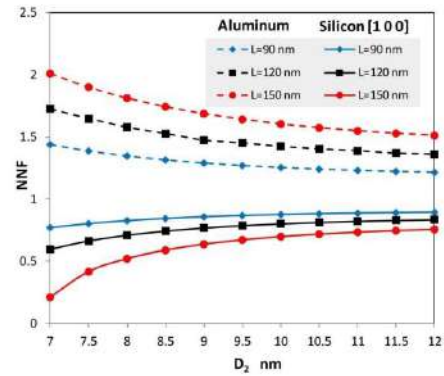


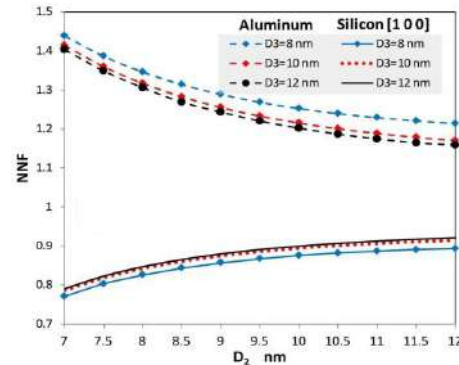
Figure 3. NNF of the one-step nanobeams based on different beam theories ($D_1 = 10$ nm, $L_1 = L_2$)

nanobeams reduces the effect of surface properties on the fundamental natural frequency.

For the next simulation, it is tried to clarify the effect of proper modeling of the non-uniform nanobeam on its vibration analysis. For this purpose, a non-uniform nanobeam is once solved by the developed method in this section and again is considered as a uniform nanobeam with mean diameter. The ratio of the results of this analysis is plotted versus D_2 in Figure 5.



(a)



(b)

Figure 4. NNF of the two-step nanobeams (a): $D_3 = 8$ nm, $D_1 = 10$ nm and (b): $L = 90$ nm, $D_1 = 10$ nm

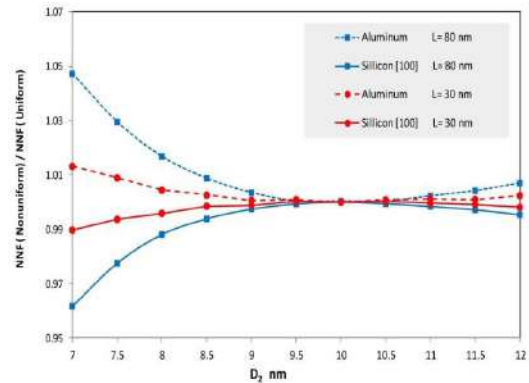


Figure 5. Significance of modeling for proper prediction of NNF for non-uniform nanobeams ($D_1 = 10$ nm)

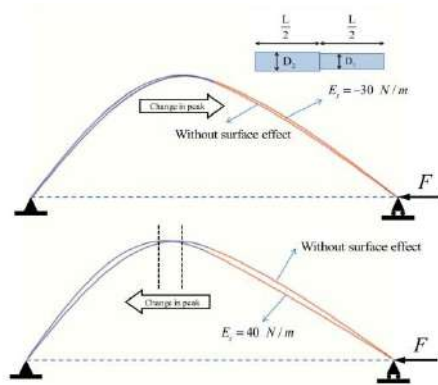


Figure 6. First mode shape of the one-step nanobeams

From this figure, it is observed that in the vibration analyses when the diameters of two adjacent sections differ only in %20, the non-uniform nanobeam can be treated as uniform ones. Otherwise, it is preferred to solve the problem properly.

Furthermore, it is tried to investigate size effects on the mode shapes of the nanobeam. Figure 6 shows the surface effects on the first mode shapes of the nanobeam.

From Figure 6 it is seen that even though large values of surface parameters are examined, but the mode shape is not dependent on their value either the surface parameters be positive or negative. However, it is observed that location of the peak of the principal mode shape depends on the value of surface effects but its magnitude is not changed by variation of these parameters. Also, it should be mentioned that force F is an axial force.

Also, Figure 7 shows the surface effects on the second mode shape of the one-step nanobeam:

In spite of the principal mode shape, Figure 6 illustrates extreme dependence of the second mode shape of a non-uniform nanobeam on the magnitude of surface properties. Generally it is observed that the thinner section is more affected in this case but it is to be noted that the mode shape must be interpreted for the whole structure. From Figure 7 it is seen that location of nodes and peaks of the mode shape changes considerably with changes of surface parameters. It can be interpreted that the surface parameter causes considerable changing of the beam rigidity. In addition, the amplitude of the mode shape in this case is highly dependent on the surface properties. It is to be noted, more variation in the nanobeam's cross section, more changes in mode shapes by surface effects. In addition, the location of peaks and nodes is pushed toward the thinner section for negative values of surface effects and conversely toward the thicker section for positive ones.

Furthermore, Figure 8 shows the effect of surface properties on the second mode shape of the two-step nanobeam.

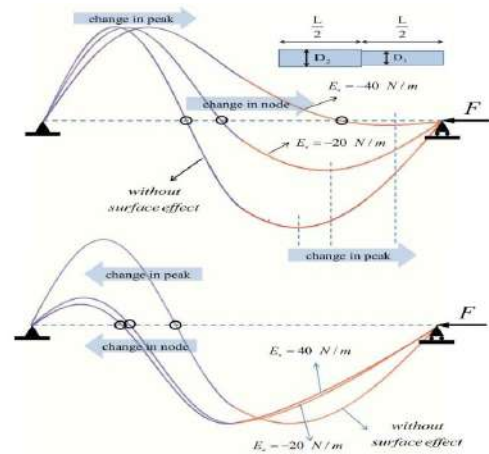


Figure 7. Second mode shape of the one-step nanobeams

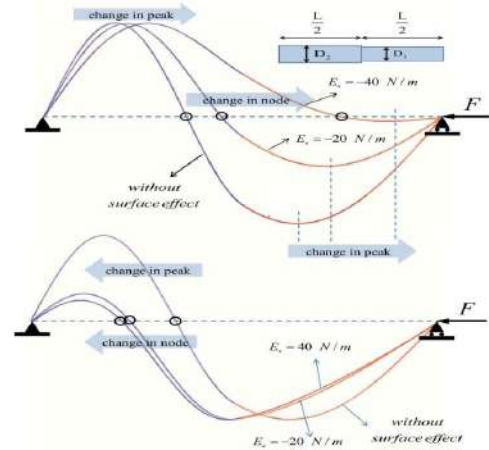


Figure 8. Second mode shape of the two-step nanobeams

It is seen that the surface effects are less than the previous case of Figure 7 since the relative length of the thinner section is reduced but generally the shape of the thinner section is changed considerably. As an important conclusion, it is observed, positive surface parameters make the mode shape more uniform and reduce its amplitude. In this case, it is observed that the location of peaks is not so dependent on the magnitude of surface properties.

5. CONCLUSION

In this paper, size-dependent vibrations of stepped nanobeams have been studied with consideration of the surface elasticity theory. The nanobeams are modeled as stepped beams and size-dependent governing vibration equations have been derived considering compatibility conditions in stepped sections. Then, an analytical solution has been developed to simulate natural frequencies and mode shapes of the nanobeam with

various surface properties. The obtained results indicate that as one section of a step-wised nanobeam gets shorter; the effect of surface properties on the natural frequency of the nanobeam reduces considerably. In addition, the nanobeams with negative surface effects must be modeled more precisely since their natural frequency extremely depend on the diameter magnitude. In fact, proper modeling and choosing the number of steps plays important roles in proper determination of the vibration behavior of non-uniform nanobeams. Moreover, it is seen that the corresponding mode shapes of the nanobeam in some case are extremely dependent on the magnitude of surface effects while their amplitude and locations of nodes and peaks varies a lot by changes of surface effects. It is observed that the thinner section is more affected in this case but it is to be noted that the mode shape must be interpreted for the whole structure. Finally, the obtained results illustrate the capability of the proposed method to model and analyze the size-dependent vibration of the nanobeams

6. REFERENCES

1. Akbari, G., Nikraves, M., Poladi, A. "Mechanical Properties and Microstructural Evolution of Ta/TaNx Double Layer Thin Films Deposited by Magnetron Sputtering." *International Journal of Engineering, Transactions B: Applications*, (2017), Vol. 30, No. 2, 288-293. DOI: 10.5829/idosi.ije.2017.30.02b.16.
2. Mofidian, R., Barati, A., Jahanshahi, M., Shahavi, M. H. "Generation Process and Performance Evaluation of Engineered Microsphere Agarose Adsorbent for Application in Fluidized-bed Systems." *International Journal of Engineering, Transactions B: Applications*, (2020), Vol. 33, No. 8, 1450-1458. DOI: 10.5829/ije.2020.33.08b.02
3. Bagheri, M., Sangpour, P., Badii, E., Pazouki, M. "Graphene Oxide Antibacterial Sheets: Synthesis and Characterization (RESEARCH NOTE)." *International Journal of Engineering Transactions C: Aspects*, (2014), Vol. 27, No. 12, 1803-1808. DOI: 0.5829/idosi.ije.2014.27.12c.01
4. Bakhtiari-Nejad, F., Nazemizadeh, M. "Size-dependent dynamic modeling and vibration analysis of MEMS/NEMS-based nanomechanical beam based on the nonlocal elasticity theory." *Acta Mechanica*, Vol. 227, No. 5, 1363-1379. DOI: 10.1007/s00707-015-1556-3
5. Korayem, M. H., Taheri, M., Korayem, A. H. "Manipulation with atomic force microscopy: DNA and yeast micro/nanoparticles in biological environments", *Proceedings of the Institution of Mechanical Engineers, Part K: Journal of Multi-body Dynamics*, (2014), Vol. 228, No. 4, 414-425. DOI: 10.1177/1464419314542544.
6. Nazemizadeh, M., Bakhtiari-Nejad, F. "Size-dependent free vibration of nano/microbeams with piezo-layered actuators", *Micro & Nano Letters*, (2015), Vol. 10, No. 2, 93-98. DOI: 10.1049/mnl.2014.0317
7. Nazemizadeh, M., Bakhtiari-Nejad, F., "A general formulation of quality factor for composite micro/nano beams in the air environment based on the nonlocal elasticity theory", *Composite Structures*, (2015), Vol. 132, 772-783. DOI: 10.1016/j.compstruct.2015.05.070
8. Beni, Y. T. "A nonlinear electro-mechanical analysis of nanobeams based on the size-dependent piezoelectricity theory". *Journal of Mechanics*, (2017), Vol. 33, No. 3, 289-301. DOI: 10.1017/jmech.2016.65.
9. Nazemizadeh, M., Bakhtiari-Nejad, F., Assadi, A., Shahriari, B., "Size-dependent nonlinear dynamic modeling and vibration analysis of piezo-laminated nanomechanical resonators using perturbation method", *Archive of Applied Mechanics*, (2020), 1-14. DOI: 10.1007/s00419-020-01678-3
10. Nazemizadeh, M., Bakhtiari-Nejad, F., Assadi, A., Shahriari, B., "Nonlinear vibration of piezoelectric laminated nanobeams at higher modes based on nonlocal piezoelectric theory" *Acta Mechanica*, (2020), Vol. 231, No. 10, 4259-4274. DOI: 10.1007/s00707-020-02736-1
11. Gurtin, M. E., Murdoch, A. I. "A continuum theory of elastic material surfaces". *Archive for Rational Mechanics and Analysis*, (1975), Vol. 57, No. 4, 291-323. DOI: 10.1007/BF00261375
12. Jiang, L. Y., Yan, Z. "Timoshenko beam model for static bending of nanowires with surface effects", *Physica E: Low-dimensional Systems and Nanostructures*, (2010), Vol. 42, No. 9, 2274-2279. DOI: 10.1016/j.physe.2010.05.007
13. Farshi, B., Assadi, A., Alinia-Ziazi, A. "Frequency analysis of nanotubes with consideration of surface effects", *Applied Physics Letters*, (2010), Vol. 96, No. 9, 093105. DOI: 10.1063/1.3332579
14. Assadi, A., Nazemizadeh, M. "Size effects on stability and self-instability of non-uniform nanobeams with consideration of surface effects" *Micro & Nano Letters*, (2020), Vol. 15, No. 12, 858-862. DOI: 10.1049/mnl.2020.0262
15. He, J., Lilley, C. M. "Surface effect on the elastic behavior of static bending nanowires". *Nano Letters*, (2008), Vol. 8, No. 7, 1798-1802. DOI: 10.1021/nl0733233

Persian Abstract

چکیده

این مقاله به بررسی ارتعاش وابسته به ابعاد نانوتیرهای پله ای با در نظر گرفتن تئوری الاستیسیته سطحی می پردازد. برای این منظور، نانوتیر به عنوان تیر پله ای مدل سازی شده و معادلات حاکم ارتعاشی آن با در نظر گرفتن شرایط سازگاری بدست می آید. سپس یک حل تحلیلی برای شبیه سازی فرکانسهای طبیعی و شکل مودهای نانوتیر با در نظر گرفتن اثرات سطح، گسترش داده می شود. همچنین، یک رویکرد بازگشتی برای صحت سنجی نتایج و محاسبه مدول الاستیسیته وابسته به ابعاد پیشنهاد می شود. نتایج نشان می دهد که اثرات سطح و انتخاب مناسب پله ها، اثر چشمگیری بر فرکانس طبیعی نانوتیر غیریکنواخت دارد. همچنین، برخلاف تیرهای یکنواخت، شکل مودهای نانوتیرهای غیریکنواخت به شدت وابسته به اثرات سطح است.



Experimental Investigation of the Change of Elastic Moduli of Clastic Rocks under Nonlinear Loading

M. A. Guzev, E. V. Kozhevnikov*, M. S. Turbakov, E. P. Riabokon, V. V. Poplygin

Department of Oil and Gas Technologies, Perm National Research Polytechnic University, Russia

PAPER INFO

Paper history:

Received 29 October 2020

Received in revised form 26 December 2020

Accepted 18 January 2021

Keywords:

Nonlinear Dynamic Loads

Clastic Rock

Elastic Moduli

Dispersion

ABSTRACT

This paper presents an experimental investigation on the nonlinear nature of the dynamic geomechanical characteristics of a clastic rock (sandstone). Rock samples of 7.5 mm in diameter and 15.6 mm in length were prepared. Rock properties were identified. Firstly, the limits of the rock linear elasticity zone were defined during quasistatic loading and uniaxial compressive strength determination at the Tinius Hounsfield rig. Secondly, the small experimental custom-built rig was designed to study the nonlinear nature of the Young's modulus in the zone of linear elasticity. At the rig the sample was stationary preloaded. The dynamic load was generated by a piezoelectric actuator powered with a signal generator. The displacement of rock sample surfaces was recorded by a laser sensor and an eddy current probe. The dynamic experiments were conducted at the load amplitude ranging from 50 to 250 N for each of frequencies of 25 Hz and 40 Hz. It was found that the dynamic Young's modulus increased with amplitude for all the frequencies studied. The newly developed experimental rig allows to investigate elastic moduli dispersion of rocks at the strain up to 10^{-3} under vibrations with frequency up to 40 Hz.

doi: 10.5829/ije.2021.34.03c.21

NOMENCLATURE

d	Sample's diameter (m)	l_0	Sample's length at preloading (m)
d_0	Sample's diameter at preloading (m)	t	Time (s)
E	Young's modulus (GPa)	ε	Strain
E_{dyn}	Dynamic Young's modulus (GPa)	ε_{ax}	Axial strain
f	Frequency of the dynamic load (Hz)	ε_{rad}	Radial strain
F_{dyn}	Dynamic load (N)	ν	Poisson's ratio
F_{max}	Maximum load applied to a sample (N)	σ	Stress (MPa)
F_{min}	Minimum load applied to a sample (N)	$\sigma_{lim,low}$	Lower limit of the linear elasticity zone (MPa)
F_{st}	Preload value (N)	$\sigma_{lim,up}$	Upper limit of the linear elasticity zone (MPa)
l	Sample's length (m)	$\sigma_{UCS,av}$	Average uniaxial compressive strength (MPa)

1. INTRODUCTION

Elastic moduli of rocks are not constant and have nonlinear nature under the influence of the dynamic loading [1]. The phenomenon of the dispersion of elastic moduli under vibrations is considered while geotechnical engineering in such fields as mining [2], modelling the tunnels constructed in liquefiable soil rock [3], cutting

and blasting [4, 5], construction in limestone sands [6], well drilling and completion [7] and reservoir engineering [8]. Experimental studies of clastic rocks elastic moduli dispersion can be differentiated in two groups in accordance with rock saturation during the investigation. In the first group, dynamic elastic moduli are studied on rocks saturated with a fluid (e.g., brine). A study of Opalinus clay in literature [9, 10] and Mancos

*Corresponding Author Email: kozhevnikov_evg@mail.ru (E. V. Kozhevnikov)

shale by Szweczyk et al. [11], showed an increase in the Young's modulus and a decrease in Poisson's ratio with an increase in frequency of the dynamic loading from 1 to 100 Hz at the strain of 10^{-6} . Similar dispersion of the Young's modulus was also reported in literature [12, 13] for Fontainebleau sandstone for frequency ranging from 1 to 100 Hz at the strain lower than 10^{-5} . An increase in Young's modulus was also reported in literature [14] while studying the Berea sandstone in the range of frequencies from 1 to 100 Hz. A schematic nonlinear relation among clastic rock elastic moduli and load frequency is given by Batzle et al. [15]. A strong frequency and rate amplitude dependent elastic behavior over variety of sandstones was reported in literature [16]. Based on these and other works, a number of poroelastic mechanisms have been proposed and modelled on the nonlinear nature of the Young's modulus while studying saturated rocks. Those models characterize in saturated porous media global inertia mechanisms [17], local mechanisms [18, 19], both global and local mechanisms [20] and other (see literature [21]).

In the second group, the studies are performed on dry rocks. It was exhibited in literature [22] that with an increase of frequency from 1 to 100 Hz for samples with a strain range between 10^{-8} and 10^{-6} , the Young's modulus and Poisson's ratio of Donnybrook sandstone are nearly constant, i.e. no dispersion of the Young's modulus is observed. Earlier, it was reported in literature [23] that Young's moduli of Navajo sandstone, Spergen limestone and Oklahoma granite do not depend on frequency of the dynamic loading at the strain of 10^{-7} in the frequency range from 4 to 400 Hz. Similarly, studies conducted by Winkler [24] on vacuum dry sandstones Massillon, Berea and Boise at frequencies up to 0.1 MHz did not reveal any relationship between attenuation and frequency at small strain, which is also relevant for man-made rocks with no intergranular cement. However, the phenomenon of dispersion of elastic moduli in dry clastic rocks is still exists and can be captured by hysteresis loop on the strain–stress diagram as shown in literature [16]. Manifestation of dispersion in dry clastic rocks is accompanied by the phenomenon when the dynamic Young's modulus exceeds the static one which is directly related to a strain rate and a loading path [25, 26]. There is a number of models designed to describe the nature of dynamic elastic characteristics observed under high strain by, for example, inertial approach (see literature [27]). Nevertheless, the mechanism of the dynamic dispersion of elastic moduli under vibrations is still open for research.

Since the standard loading rigs allow us to perform linear loading of rocks at frequency ranging from 0.1 to 2 Hz and strain up to 10^{-3} [26-28], it is practically not possible to use such the rigs to study the effect of nonlinear dynamic loads (vibrations) on rocks. As is shown in literature [4, 29] studying of the dynamic elastic

characteristics of rocks at high strain is limited by the complexity of experiments and data processing. It is possible to study the effect of nonlinear dynamic loads on rocks in the range of seismic frequencies from 1 to 100 Hz at the strain of 10^{-8} .. 10^{-6} using custom-built experimental set-ups, described in literature [10, 12, 15, 30-32]. Recently, Borgomano et al. [33] have built the experimental apparatus able to measure the dynamic rock elastic characteristics at frequencies up to 1 kHz and strain up to 10^{-5} . However, considering that during mining (e.g., well drilling and perforation [34]) the rocks experience much higher strain ($\geq 10^{-2}$) the capacity expansion of existing rigs is required. Studying of the effect of significant dynamic loads up to 10^1 - 10^4 is possible using the Kolsky-Hopkinson bar machines [35, 36], but those machines do not allow to create cyclic (harmonic) loads on rock samples. Therefore, to study the elastic moduli under high strain nonlinear dynamic loads new experimental techniques are necessary. The aim of this paper is to study the nonlinear nature of the dynamic elastic moduli of a dry clastic rock being in the zone of the linear elasticity using a small custom-built experimental rig.

The paper is organized as follows. In Section 2, the experimental methodology, details on samples preparation procedure, quasistatic and nonlinear dynamic experiments are described. The obtained experimental results and its discussion are given in Section 3, followed by the conclusion in Section 4.

2. MATERIALS AND METHODS

2. 1. Description of Rock Samples

A clastic Permian age rock (sandstone) was used for this study. The properties of the rock are given in Table 1 and Figure 1. Each sample was 7.5 mm in diameter d and 15.6 mm in length l . The samples were prepared in accordance with industrial standards [37, 38].

TABLE 1. Properties of the studied rock

Property	Value	Study rig
Porosity, fr. units	11.7	Helium porosimeter PHI-220
Gas permeability, μm^2	0.353	Benchtop Permeability Sistem BPS-805
Pore size, mm	0.02-0.24	
Pore distribution	uniform	
Fracturing	no	Microfocus X-ray tomography rig, Nikon Metrology XT H 225
X-ray density composition	nonuniform (0.05 mm high-density inclusions)	

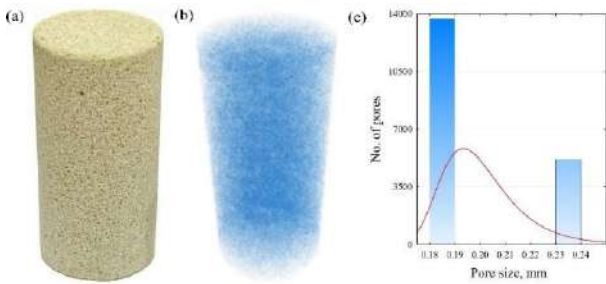


Figure 1. Characteristics of the prepared samples: (a) a photograph depicting a sandstone sample; (b) a sample’s pore space model; (c) a diagram for pore distribution

Using diamond drill bits Tacklife AHS02C the samples were cored from rock blocks with water flush, then cut, washed and dried. In total there were 18 samples prepared. For both quasistatic tests and dynamic experiments there were 9 samples used in order to ensure reliable results.

2. 2. Methodology of Nonlinear Loading Since the elastic moduli, and the dynamic ones in particular, have to be studied in the state when a rock experiences elastic deformation (the Young’s modulus can be determined as $E = \sigma/\epsilon_l$) the limits of the linear elasticity zone should be defined prior to the dynamic experiments. In order to obtain the repeatable dependencies of elastic moduli the experiments on nonlinear dynamic loading were performed on 9 samples (Figure 2).

Elastic limits of the studied clastic rock were defined during quasistatic loading of prepared samples at the Tinius Hounsfield rig. Quasistatic loading was performed at the loading rate of displacement plate of 0.05 mm/min. As a result, the standard diagram of loading–displacement was obtained for all the samples tested which comprised compaction, elastic deformations, irreversible deformations and fracture. Figure 3 shows the limits of the linear elasticity zone equal to $\sigma_{lim,low} = 10.2$ MPa and $\sigma_{lim,up} = 31.7$ MPa defined as average values of limits of the linear section according to literature [39].

After the elasticity zone being determined in order to study the nonlinear behaviour of elastic moduli under dynamic loads at the strain up to 10^{-3} the small experimental rig was built. In the rig (see Figure 4) the rock sample was installed at a load table, below which load sensor Kistler 9027C was mounted. There was a piezoelectric actuator Extrema Model 250 μ located on top of the sample through the metal dist. Above the actuator there was a static load ensuring sample’s preloaded (compacted) state. The actuator was powered with a signal generator Manual MOS-01 able to set the amplitude and frequency of the actuator operation and produce axial-stress oscillations.

During the dynamic experiment the sample was experiencing stationary load F_{st} equal to 700 N and

periodic dynamic load F_{dyn} the amplitude of which was varied between 50 N and 250 N at two frequencies f such as 25 Hz to 40 Hz. At stationary load F_{st} the sample’s length was equal to l_0 and sample’s diameter was equal to d_0 (see Figure 5). The largest $F_{max} = F_{st} + F_{dyn,max}$ and the smallest $F_{min} = F_{st} - F_{dyn,min}$ load applied to a sample corresponded to maximum distance between the sensors and samples top and side surfaces (see Figure 4) and consequently the sample’s strain. The radial displacement

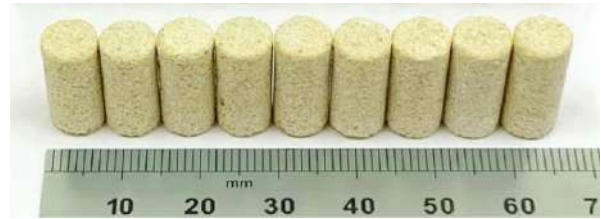


Figure 2. Prepared nine samples of a clastic rock

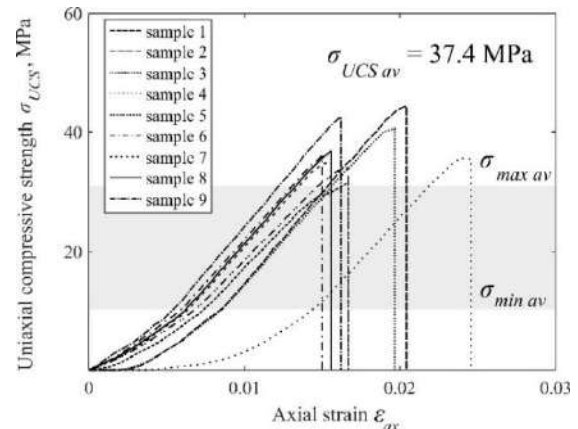


Figure 3. The zone of linear elasticity determined during UCS tests of nine samples



Figure 4. A clastic rock sample at the small experimental rig

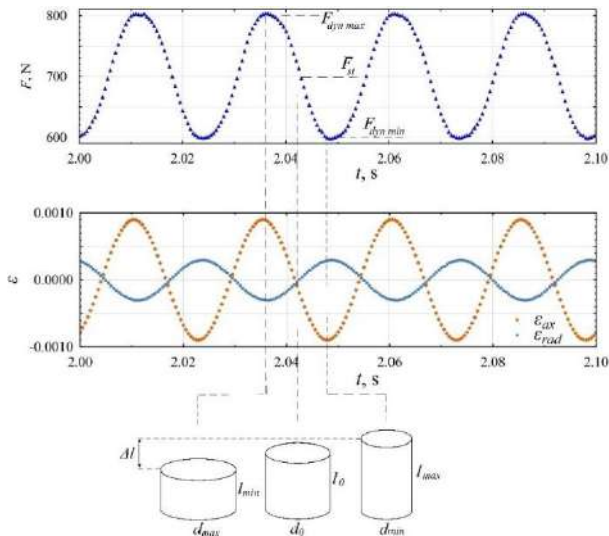


Figure 5. An example of the dynamic loading experiment at frequency of 40 Hz and dynamic load amplitude of 100 N characterizing sample' deformation

of the sample's side surface was recorded by Micro-epsilon. The axial displacement was recorded by an eddy current probe (ECP).

The data from the sensors went to a PC. After the signals of three sensors were acquired and processed in LabView and Matlab the data then was used to calculate the dynamic Young's modulus and Poisson's ratio by using the Equations (1) and (2):

$$E_{dyn} = \frac{\Delta\sigma}{\varepsilon_{ax}} \quad \Delta\sigma = \frac{F_{max}-F_{min}}{S} \quad \varepsilon_{ax} = \frac{l_{max}-l_{min}}{l} \quad (1)$$

$$\nu = \frac{\varepsilon_{rad}}{\varepsilon_{ax}} \quad \varepsilon_{rad} = \frac{d_{max}-d_{min}}{d} \quad (2)$$

3. RESULTS AND DISCUSSIONS

It was obtained during experiments that the elastic moduli of the clastic rock change under dynamic loading depending on frequency and amplitude of the load. Figure 6a demonstrates that at frequency of $f = 25\text{Hz}$ the Poisson's ratio ν increases from 0.4 to 0.58 when dynamic load F_{dyn} on piezoelectric actuator is increased from 100 N to 250 N. At the same time the dynamic Young's modulus E_{dyn} increases up to 2.57 GPa (see Figure 6c). It is also noted that if frequency of dynamic loading is increased up to 40 Hz the Poisson's ratio ν increases from 0.52 to 0.6 (see Figure 6b), while the dynamic Young's modulus E_{dyn} increases up to 3.0 GPa (see Figure 6c). With an increase in the amplitude of dynamic load from 100 N to 250 N the value of E_{dyn} increased from 0.75 GPa to 0.86 GPa. After normalization the strain cycles (shown on Figures 6a and 6b) narrowed to the dashed lines.

The dispersion of the dynamic Young's modulus (see Figures 6c and 6d) corresponds to the varying in a loading cycle rock density. This fact may lead to a perception of rock hardening and softening under vibration. Another possible explanation for the phenomenon of rock elastic

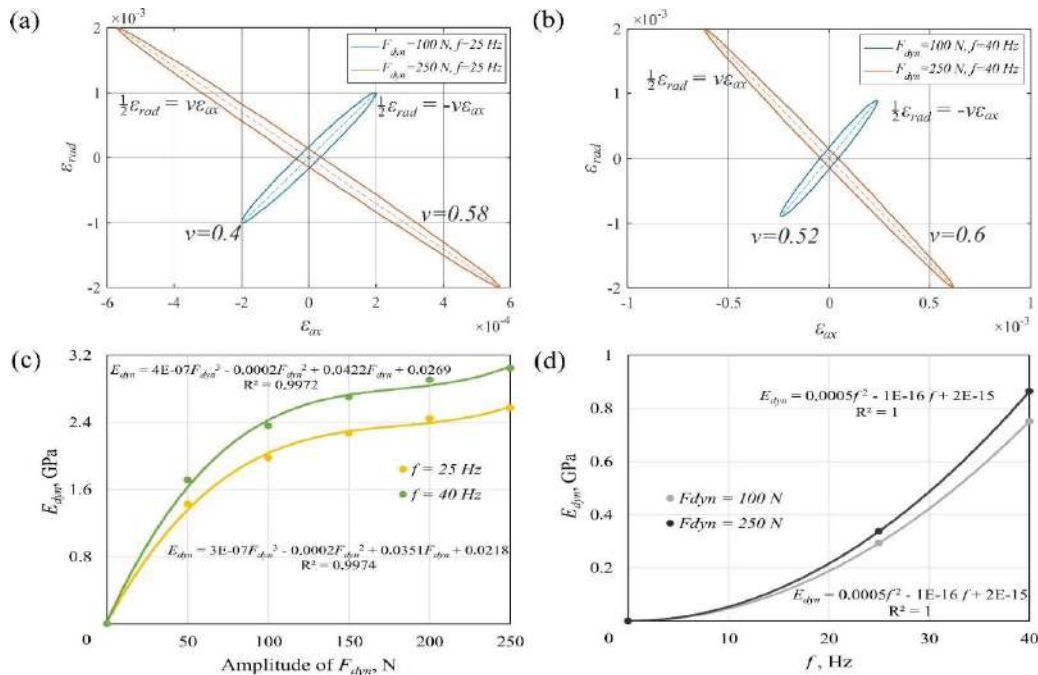


Figure 6. Dependence of strain and elastic moduli on dynamic loading parameters: (a) and (b) dependence of the sample's strain at frequency f of 25 Hz and 40 Hz; (c) and (d) dependence of the dynamic Young's modulus on frequency f of 25 Hz and 40 Hz and amplitude of dynamic load F_{dyn} of 100 N and 250 N

moduli dispersion under high strain vibrations can be inertial resistance of the rock to the dynamic load applied.

However, the experimental results represent a basis for further elastic moduli mathematical models' formulations. The phenomenon of dispersion of the dynamic elastic moduli under high strain vibrations has to be conceptualized, and further developed mathematical models needs to be verified.

4. CONCLUSION

In this work, we present the results of investigation of the nonlinear nature of clastic rock (sandstone) elastic moduli obtained during the series of experiments. The investigation was conducted in two phases. First, the limits of the zone of linear elasticity of samples of 7.5 mm in diameter were determined in quasistatic loading. Then, at the second stage, the experiments on dynamic loading were performed with help of a custom-built small experimental rig. During the course of dynamic loading experiments elastic properties were studied at two frequencies f such as 25 Hz and 40 Hz. At both these frequencies amplitude of nonstationary load varied from 50 N to 250 N. The nonlinear nature of the Poisson's ratio and the dynamic Young's modulus was revealed as a result of the study. The dispersion of elastic moduli values under dynamic loading was observed at each amplitude of the load for both frequencies at the strain up to 10^{-3} . The obtained results confirm the nonlinear nature of the dynamic elastic moduli of a clastic rock shown in the similar mentioned researches on dry rocks but at smaller strain. The newly developed experimental rig allows to investigate elastic moduli dispersion of rocks at the strain up to 10^{-3} under vibrations with frequency up to 40 Hz.

5. ACKNOWLEDGEMENTS

This work was financially supported by the Russian Science Foundation (project No. 19-19-00408).

6. REFERENCES

1. He, M., Li, N., "Experimental research on the non-linear energy characteristics of granite and sandstone", *Geotechnique Letters*, Vol. 10, No. 3, (2020), 385-392. doi: 10.1680/jgele.19.00117
2. Geranmayeh Vaneghi, R., Ferdosi, B., Okoth, A. D., Kuek, B., "Strength degradation of sandstone and granodiorite under uniaxial cyclic loading", *Journal of Rock Mechanics and Geotechnical Engineering*, Vol. 10, No. 1, (2018), 114-126. doi: 10.1016/j.jrmge.2017.09.005
3. Marandi, S. M., Rasti, A. R., "Parametric study of the covering soil of tunnels constructed in liquefiable soil", *International Journal of Engineering, Transactions A: Basics*, Vol. 25, No. 4, (2012), 375-388.
4. Xia, K., Yao, W., Wu, B., "Dynamic rock tensile strengths of Laurentian granite: Experimental observation and micromechanical model", *Journal of Rock Mechanics and Geotechnical Engineering*, Vol. 9, No. 1, (2017), 116-124. doi: 10.1016/j.jrmge.2016.08.007
5. Jiang, Y.-Z., He, K.-F., Dong, Y.-L., Yang, D.-L., Sun, W., "Influence of load weight on dynamic response of vibrating screen", *Shock and Vibration*, Vol. 2019, (2019), 4232730. doi: 10.1155/2019/4232730
6. Lv, Y., Liu, J., Xiong, Z., "One-dimensional dynamic compressive behavior of dry calcareous sand at high strain rates", *Journal of Rock Mechanics and Geotechnical Engineering*, Vol. 11, No. 1, (2019), 192-201. doi: 10.1016/j.jrmge.2018.04.013
7. LeCompte, B., Franquet, J. A., Jacobi, D., "Evaluation of Haynesville Shale vertical well completions with a mineralogy based approach to reservoir geomechanics", in SPE Annual Technical Conference and Exhibition 2009, Vol. 3, (2009), 1417-1430. doi: 10.2118/124227-ms
8. Behnoud far, P., Hassani, A. H., Al-Ajmi, A. M., Heydari, H., "A novel model for wellbore stability analysis during reservoir depletion", *Journal of Natural Gas Science and Engineering*, Vol. 35, (2016), 935-943. doi: 10.1016/j.jngse.2016.09.051
9. Lozovyi, S., Bauer, A., "Static and dynamic stiffness measurements with Opalinus Clay", *Geophysical Prospecting*, Vol. 67, No. 4, (2018), 997-1019. doi: 10.1111/1365-2478.12720
10. Lozovyi, S., Bauer, A., "From static to dynamic stiffness of shales: Frequency and stress dependence", *Rock Mechanics and Rock Engineering*, Vol. 52, (2019), 5085-5098. doi: 10.1007/s00603-019-01934-1
11. Szewczyk, D., Bauer, A., Holt, R. M., "A new laboratory apparatus for the measurement of seismic dispersion under deviatoric stress conditions", *Geophysical Prospecting*, Vol. 64, No. 4, (2016), 789-798. doi: 10.1111/1365-2478.12425
12. Pimienta, L., Fortin, J., Guéguen, Y., "Bulk modulus dispersion and attenuation in sandstones", *Geophysics*, Vol. 80, No. 2, (2015), A25-A30. doi: 10.1190/geo2014-0335.1
13. Pimienta, L., Fortin, J., Guéguen, Y., "Effect of fluids and frequencies on Poisson's ratio of sandstone samples", *Geophysics*, Vol. 81, No. 2, (2016), D183-D195. doi: 10.1190/geo2015-0310.1
14. Tisato, N., Quintal, B., "Measurements of seismic attenuation and transient fluid pressure in partially saturated Berea sandstone: Evidence of fluid flow on the mesoscopic scale", *Geophysical Journal International*, Vol. 195, (2013), 342-351. doi: 10.1093/gji/ggt259
15. Batzle, M. L., Han, D.-H., Hofmann, R., "Fluid mobility and frequency-dependent seismic velocity - Direct measurements", *Geophysics*, Vol. 71, No. 1, (2006), N1-N9. doi: 10.1190/1.2159053
16. Tutuncu, A. N., Podio, A. L., Gregory, A. R., Sharma, M. M., "Nonlinear viscoelastic behavior of sedimentary rocks, Part I: Effect of frequency and strain amplitude", *Geophysics*, Vol. 63, No. 1, (1998), 184-194. doi: 10.1190/1.1444311
17. Biot, M. A., "Theory of propagation of elastic waves in a fluid-saturated porous solid II. Higher frequency range", *The Journal of the Acoustical Society of America*, Vol. 28, No. 179, (1956), 179-191. doi: 10.1121/1.1908241
18. O'Connell, R. J., Budiansky, B., "Viscoelastic properties of fluid-saturated cracked solids", *Journal of Geophysical Research*, Vol. 82, No. 36, (1977), 5719-5735. doi: 10.1029/JB082i036p05719
19. Mavko, G., Nur, A., "Melt squirt in the asthenosphere", *Journal of Geophysical Research*, Vol. 80, No. 11, (1975), 1444-1448. doi: 10.1029/JB080i011p01444

20. Dvorkin, J., Nur, A., "Dynamic poroelasticity: a unified model with the squirt and the Biot mechanisms", *Geophysics*, Vol. 58, No. 4, (1993), 524-533. doi: 10.1190/1.1443435
21. Müller, T. M., Gurevich, B., Lebedev, M., "Seismic wave attenuation and dispersion resulting from wave-induced flow in porous rocks: A review", *Geophysics*, Vol. 75, No. 5, (2010), X75A147-75A164. doi: 10.1190/1.3463417
22. Mikhaltsevitch, V., Lebedev, M., Gurevich, B., "A laboratory study of the elastic and anelastic properties of the sandstone flooded with supercritical CO₂ at seismic frequencies", *Energy Procedia*, Vol. 63, (2014), 4289-4296. doi: 10.1016/j.egypro.2014.11.464
23. Spencer Jr, J. W., "Stress relaxations at low frequencies in fluid-saturated rocks: attenuation and modulus dispersion", *Journal of Geophysical Research*, Vol. 86, No. B3, (1981), 1803-1812. doi: 10.1029/JB086iB03p01803
24. Winkler, K. W., "Frequency dependent ultrasonic properties of high-porosity sandstones", *Journal of Geophysical Research*, Vol. 88, No. B11, (1983), 9493-9499. doi: 10.1029/JB088iB11p09493
25. Peng, K., Zhou, J., Zou, Q., Song, X., "Effect of loading frequency on the deformation behaviours of sandstones subjected to cyclic loads and its underlying mechanism", *International Journal of Fatigue*, Vol. 131, (2020), 105349. doi: 10.1016/j.ijfatigue.2019.105349
26. Khosroshahi, A. A., Sadrejad, S. A., "Substructure model for concrete behavior simulation under cyclic multiaxial loading", *International Journal of Engineering, Transactions A: Basics*, Vol. 21, No. 4, (2008), 329-346.
27. Zhang, Q. B., Zhao, J., "A review of dynamic experimental techniques and mechanical behaviour of rock materials", *Rock Mechanics and Rock Engineering*, Vol. 47, (2014), 1411-1478. doi: 10.1007/s00603-013-0463-y
28. Zheng, Q., Liu, E., Sun, P., Liu, M., Yu, D., "Dynamic and damage properties of artificial jointed rock samples subjected to cyclic triaxial loading at various frequencies", *International Journal of Rock Mechanics and Mining Sciences*, Vol. 128, (2020), 104243. doi: 10.1016/j.ijrmms.2020.104243
29. Subramaniyan, S., Quintal, B., Tisato, N., Saenger, E. H., Madonna, C., "An overview of laboratory apparatuses to measure seismic attenuation in reservoir rocks", *Geophysical Prospecting*, Vol. 62, (2014), 1211-1223. doi: 10.1111/1365-2478.12171
30. Szweczyk, D., Holt, R. M., Bauer, A., "The impact of saturation on seismic dispersion in shales - laboratory measurements", *Geophysics*, Vol. 83, No. 1, (2018), 15-34. doi 10.1190/geo2017-0169.1
31. Tisato, N., Madonna, C., "Attenuation at low seismic frequencies in partially saturated rocks: Measurements and description of a new apparatus", *Journal of Applied Geophysics*, Vol. 86, (2012), 44-53. doi: 10.1016/j.jappgeo.2012.07.008
32. Szweczyk, D., Bauer, A., Holt, R. M., "A new laboratory apparatus for the measurement of seismic dispersion under deviatoric stress conditions", *Geophysical Prospecting*, 64, (2016), 789-798. doi: 10.1111/1365-2478.12425
33. Borgomano, J. V. M., Gallagher, A., Sun, C., Fortin, J., "An apparatus to measure elastic dispersion and attenuation using hydrostatic- and axial-stress oscillations under undrained conditions", *Review of Scientific Instruments*, Vol. 91, No. 3, (2020), 034502. doi: 10.1063/1.5136329
34. Riabokon, E., Turbakov, M., Kozhevnikov, E., Poplygin, V., Wiercigroch, M., "Rock Fracture During Oil Well Perforation", *Lecture Notes in Mechanical Engineering*, (2020), 185-192. doi: 10.1007/978-3-030-49882-5_18
35. Yan, Z., Dai, F., Liu, Y., Du, H., "Experimental investigations of the dynamic mechanical properties and fracturing behavior of cracked rocks under dynamic loading", *Bulletin of Engineering Geology and the Environment*, Vol. 79, No. 10, (2020), 5535-5552. doi: 10.1007/s10064-020-01914-8
36. Li, X. B., Lok, T. S., Zhao, J., "Dynamic characteristics of granite subjected to intermediate loading rate", *Rock Mechanics and Rock Engineering*, Vol. 38, No. 1, (2005), 21-39. doi: 10.1007/s00603-004-0030-7
37. ASTM (2001). ASTM D4543: Standard practices for preparing rock core specimens and determining dimensional and shape tolerances. West Conshohocken, PA, USA: ASTM International.
38. Brown E. T. Suggested Methods for Determining the Uniaxial Compressive Strength and Deformability of Rock Materials. ISRM. Brown E. T., editor. Oxford: Pergamon Press; 1981.
39. Jaeger, J. C., Cook, N. G. W., Zimmerman, R. W. Laboratory testing of rocks. In *Fundamentals of Rock Mechanics*, 4th ed.; Blackwell Publishing: Malden, MA, USA, 2007, 145-167.

Persian Abstract

چکیده

در این مقاله یک تحقیق تجربی در مورد ماهیت غیر خطی ویژگی های ژئومکانیکی دینامیکی یک سنگ آواری (ماسه سنگ) ارائه شده است. نمونه سنگهای قطر 7.5 و طول 6.6 میلی متر تهیه شد. خواص سنگ شناسایی شد. در مرحله اول، محدوده منطبقه کنش خطی سنگ در هنگام بارگذاری کوآیستاتیک و تعیین مقاومت فشاری تک محوری در دکل Tinus Hounsfield تعریف شد. در مرحله دوم، دکل کوچک سفارشی ساخته شده برای آزمایش ماهیت غیرخطی مدول Young در منطقه کشش خطی طراحی شده است. در دکل نمونه از قبل ثابت مانده بود. بار دینامیکی توسط یک محرک پیزوالکتریک که از یک مولد سیگنال تغذیه می کند تولید شد. جایجایی سطوح نمونه سنگ توسط یک سنسور لیزر و یک پروب جریان گردابی ثبت شد. آزمایش های پویا در دامنه بار از 50 تا 250 N برای هر یک از فرکانس های 25 هرتز و 40 هرتز انجام شد. مشخص شد که مدول جوان پویا با دامنه برای تمام فرکانسهای مورد مطالعه افزایش می یابد. دکل آزمایشی تازه توسعه یافته امکان بررسی پراکنندگی مدول الاستیک سنگها را در فشار تا 10-3 تحت ارتعاشات با فرکانس تا 40 هرتز فراهم می کند.

AIMS AND SCOPE

The objective of the International Journal of Engineering is to provide a forum for communication of information among the world's scientific and technological community and Iranian scientists and engineers. This journal intends to be of interest and utility to researchers and practitioners in the academic, industrial and governmental sectors. All original research contributions of significant value focused on basics, applications and aspects areas of engineering discipline are welcome.

This journal is published in three quarterly transactions: Transactions A (Basics) deal with the engineering fundamentals, Transactions B (Applications) are concerned with the application of the engineering knowledge in the daily life of the human being and Transactions C (Aspects) - starting from January 2012 - emphasize on the main engineering aspects whose elaboration can yield knowledge and expertise that can equally serve all branches of engineering discipline.

This journal will publish authoritative papers on theoretical and experimental researches and advanced applications embodying the results of extensive field, plant, laboratory or theoretical investigation or new interpretations of existing problems. It may also feature - when appropriate - research notes, technical notes, state-of-the-art survey type papers, short communications, letters to the editor, meeting schedules and conference announcements. The language of publication is English. Each paper should contain an abstract both in English and in Persian. However, for the authors who are not familiar with Persian, the publisher will prepare the latter. The abstracts should not exceed 250 words.

All manuscripts will be peer-reviewed by qualified reviewers. The material should be presented clearly and concisely:

- *Full papers* must be based on completed original works of significant novelty. The papers are not strictly limited in length. However, lengthy contributions may be delayed due to limited space. It is advised to keep papers limited to 7500 words.
- *Research notes* are considered as short items that include theoretical or experimental results of immediate current interest.
- *Technical notes* are also considered as short items of enough technical acceptability with more rapid publication appeal. The length of a research or technical note is recommended not to exceed 2500 words or 4 journal pages (including figures and tables).

Review papers are only considered from highly qualified well-known authors generally assigned by the editorial board or editor in chief. Short communications and letters to the editor should contain a text of about 1000 words and whatever figures and tables that may be required to support the text. They include discussion of full papers and short items and should contribute to the original article by providing confirmation or additional interpretation. Discussion of papers will be referred to author(s) for reply and will concurrently be published with reply of author(s).

INSTRUCTIONS FOR AUTHORS

Submission of a manuscript represents that it has neither been published nor submitted for publication elsewhere and is result of research carried out by author(s). Presentation in a conference and appearance in a symposium proceeding is not considered prior publication.

Authors are required to include a list describing all the symbols and abbreviations in the paper. Use of the international system of measurement units is mandatory.

- On-line submission of manuscripts results in faster publication process and is recommended. Instructions are given in the IJE web sites: www.ije.ir-www.ijeir.info
- Hardcopy submissions must include MS Word and jpg files.
- Manuscripts should be typewritten on one side of A4 paper, double-spaced, with adequate margins.
- References should be numbered in brackets and appear in sequence through the text. List of references should be given at the end of the paper.
- Figure captions are to be indicated under the illustrations. They should sufficiently explain the figures.
- Illustrations should appear in their appropriate places in the text.
- Tables and diagrams should be submitted in a form suitable for reproduction.
- Photographs should be of high quality saved as jpg files.
- Tables, Illustrations, Figures and Diagrams will be normally printed in single column width (8cm). Exceptionally large ones may be printed across two columns (17cm).

PAGE CHARGES AND REPRINTS

The papers are strictly limited in length, maximum 6 journal pages (including figures and tables). For the additional to 6 journal pages, there will be page charges. It is advised to keep papers limited to 3500 words.

Page Charges for Papers More Than 6 Pages (Including Abstract)

For International Author ***	\$55 / per page
For Local Author	100,000 Toman / per page

AUTHOR CHECKLIST

- Author(s), bio-data including affiliation(s) and mail and e-mail addresses).
- Manuscript including abstracts, key words, illustrations, tables, figures with figure captions and list of references.
- MS Word files of the paper.



THOMSON REUTERS
WEB OF SCIENCE



Scopus®



CAS®
A DIVISION OF THE
AMERICAN CHEMICAL SOCIETY



Scientific Indexing Services

Google
Scholar